Characterization of low conductivity wide band gap semiconductors

by

Gunnar Kusch

University of Strathclyde

A thesis submitted to
the Department of Physics
University of Strathclyde
for the degree of
Doctor of Philosophy

October 11, 2016

Declaration of author's right

This thesis is the result of the author's original research. It has been composed by the author and has not been previously submitted for examination which has lead to the award of a degree.

Signed: Date:

Abstract

This thesis covers research on low electric conductivity wide band gap semiconductors of the group-III nitride material system. The work presented focussed on using multi-mode scanning electron microscope (SEM) techniques to investigate the luminescence properties and their correlation with surface effects, doping concentration and structure of semiconductor structures.

The measurement techniques combined cathodoluminescence (CL) for the characterization of luminescence properties, secondary electron (SE) imaging for imaging of the morphology and wavelength dispersive X-ray (WDX) spectroscopy for compositional analysis. The high spatial resolution of CL and SE-imaging allowed for the investigation of nanometer sized features, whilst environmental SEM allowed the characterisation of low conductivity samples.

The investigated $Al_xGa_{1-x}N$ samples showed a strong dependence on the miscut of the substrate, which was proven to influence the surface morphology and the compositional homogeneity. Studying the influence of the $Al_xGa_{1-x}N$ sample thickness displayed a reduced strain in the samples with increasing thickness as well as an increasing crystalline quality. The analysis of $Al_xGa_{1-x}N$:Si samples showed the incorporation properties of Si in $Al_xGa_{1-x}N$, the correlation between defect luminescence, Si concentration and resistivity as well as the influence of threading dislocations on the luminescence properties and incorporation of point defects.

The characterization of UV-LED structures demonstrated that a change in the band structure is one of the main reasons for a decreasing output power in $Al_xGa_{1-x}N$ based UV-LEDs. In addition the dependence of the luminescence properties and crystalline quality of $In_xAl_{1-x}N$ based UV-LEDs on various growth parameters (e.g. growth temperature, quantum well thickness) was investigated.

The study of nanorods revealed the influence of the template on the compositional homogeneity and luminescence of $In_xGa_{1-x}N$ nanorod LEDs. Furthermore, the influence of optical modes in these structures was studied and found to provide an additional engineering parameter for the design of nanorod LEDs.

Acknowledgements

I wish to express my gratitude to all those who helped me during the course of my PhD. First I would like to thank Prof. Robert W. Martin for the opportunity to pursue a PhD and the extraordinary supervision. His encouragement, patience, advice and continued support were more than than I ever expected and helped me greatly; without him this work would not have been possible.

Secondly, I wish to thank Dr. Paul R. Edwards for sharing his extensive cathodoluminescence knowledge, training me in the use of the SEM, helping me with all the big and small problems regarding CL, for improving my grasp of the English language as well as his vigilant proof reading skills. I am also thankful for the times we shared, drinking a few pints and discussing non physics related topics.

Another thank you goes to Dr. Carol Trager-Cowan, who often provided valuable scientific discussions and the necessary social warmth by making sure no one left a group meeting with an empty stomach.

Also I would like to thank everyone in the group for all the interesting lunch conversations.

I would like to thank all my collaborators at the Tyndall National Institute and TU-Berlin for providing me with the samples onto which this thesis builds. From the collaborators at Tyndall I want to express my gratitude especially to Prof. Peter J. Parbrook, Haoning Li and Michele Conroy, for the many interesting discussions, their help in understanding the MOVPE growth of $In_xAl_{1-x}N$ and the pecularities of $In_xGa_{1-x}N$ nanorods. From the collaborators at TU-Berlin I want to express my gratitude to my friends Dr. Tim Wernicke and Frank Mehnke, for their continued friendship, support and valuable scientific discussions and Prof. Michael Kneissl who arranged for me to meet Prof. Robert W. Martin.

A great thank you goes to Elena Pascal, Stefano Vespucci, David Thomson and Chiara Angelozzi who all provided me with an open ear for complaints, opportunities to go for a beer, terrific food and overall with an alternative family in a far away, cold and rainy country.

I would like to thank my family for their constant support during my PhD, their belief in myself kept me going when I was in doubt. Their frequent questions about my completion date and the general state of my thesis also gave a gentle push in accelerating my progress.

Finally I want to thank someone very dear to me, who tirelessly and mercilessly corrected my writing, made my last year especially enjoyable and brings a smile on my face each time I see her.

List of Publications

First authored

1. **Influence of substrate miscut angle on surface morphology and luminescence properties of AlGaN**
   Kusch, Gunnar; Li, Haoning; Edwards, Paul R.; Bruckbauer, Jochen; Sadler, Thomas C.; Parbrook, Peter J.; Martin, Robert W.
   In: Applied Physics Letters, Vol. 104, No. 9, 092114 , 2014.

2. **Spatial clustering of defect luminescence centers in Si-doped low resistivity $Al_{0.82}Ga_{0.18}N$**
   Kusch, Gunnar; Nouf-Allehiani, M.; Mehnke, Frank; Kuhn, Christian; Edwards, Paul R.; Wernicke, Tim; Knauer, Arne; Kueller, Viola; Naresh-Kumar, G.; Weyers, Markus; Kneissl, Michael; Trager-Cowan, Carol; Martin, Robert W.
   In: Applied Physics Letters, Vol. 107, No. 7, 072103, 2015.

3. **Multi-wavelength emission from a single InGaN/GaN nanorod analyzed by cathodoluminescence hyperspectral imaging**
   Kusch, Gunnar; Conroy, Michele; Li, Haoning; Edwards, Paul R.; Zhao, Chao; Ooi, S.; Pugh, Jon; Cryan, Martin J.; Parbrook, Peter J.; Martin, Robert W.
   In preparation

4. **Compositional analysis of silicon-doped wide bandgap AlGaN by wavelength dispersive X-ray spectroscopy**
   Kusch, Gunnar; Mehnke, Frank; Enslin, Johannes; Edwards, Paul R,; Wernicke, Tim; Kneissl, Michael; Martin, Robert W.
   In preparation

Co-authored

1. **Site controlled Red-Yellow-Green light emitting InGaN Quantum Discs on nano-tipped GaN rods**
   Conroy, Michele Ann; Li, Haoning; Kusch, Gunnar; Zhao, Chao; Ooi, Boon S.; Edwards, Paul and Martin, Robert and Holmes, Justin D. and Parbrook, Peter
   In: Nanoscale, 2016, accepted

2. **Self-Healing Thermal Annealing: Surface Morphological Restructuring Control of Nanorods**
   Conroy, Michele; Li, Haoning; Zubialevich, Vitaly Z.; Schmidt, Michael; Collins, Timothy; Morris, Michael; Glynn, Colm; O'Dywer, Colm; Kusch, Gunnar; Martin, Robert W.
   In: Nano Letters, submitted

3. **Quantitative analysis of threading dislocations in $Al_{0.82}Ga_{0.18}N$:Si layers grown on laterally overgrown AlN/sapphire template**
   M. Nouf-Allehiani; G. Kusch; G. Naresh-Kumar; P. R. Edwards; E. Pascal; R. Johnston; S. Kraeusel; B. Hourahine; F. Mehnke; T. Wernicke; C. Kuhn; and J. Enslin; M. Kneissl; C. Trager-Cowan; R. W. Martin
   In preparation

Contents

Chapter 1

Introduction

Access to clean drinking water is for many of us a given; we go to the tap and fill a glass. Our largest water safety worry is whether or not its hardness will damage our appliances in the long term. Imagine living in an area of the world where the access to clean drinking water is one of the biggest problems of daily life, where people have to walk hours in order to get access to a clean source of water in order to provide for their family.

According to the UN MDG report and assessment (2015) 663 million people or 9% of the world's population have no direct access to an improved water source (e.g. tap water, protected wells) but can only use water sources from unprotected dug wells, springs or surface water. The lowest level of access was found for the 48 least developed countries, especially in the sub-Saharan region. The unprotected water sources as well as some water from improved sources can be contaminated by harmful substances and bacteria (like *faecal streptococcus*). Among other things these can cause cholera, dysentry, typhoid and hepatitis A, strongly endangering the life of those who have to rely on this water.

In urban areas the contaminated drinking water can be filtered by massive systems. However, most of the people that have no access to clean drinking water are living in rural areas, often without a functioning power grid, strongly limiting the equipment choices.

The working principle of one common approach for water treatment is based on radiating the water with UV light which was found to efficiently destroy the DNA or RNA of the most common bacteria found in the water, making them unable to reproduce [1]. DNA absorbs UV light in the 200 to 300 nm regime, with the maximum absorption depending on the organism [2]. For the *Bacillus subtilis* it was found that the maximum absorption lies below 240 nm and at about 270 nm [2].

At the moment the most widely used light sources for UV light are mercury discharge lamps, which do offer high output power at a comparatively low cost. But these lamps have the disadvantage of emitting at a fixed wavelength (254 nm) and being large, bulky and fragile as well as needing access to a power grid or a bulky power source. This is unfortunate for something containing mercury which itself can cause serious harm.

The most promising alternative to the mercury lamps is the application of UV light emitting devices (LEDs) based on the group-III nitrides. These are small, compact and low power consumption devices.

The properties of the group-III nitrides allows the precise tailoring of the emission wavelength of an LED device to the optimum wavelength. This allows an array of different UV-LEDs to potentially cover a range of emission wavelengths in order to efficiently destroy the DNA of different bacteria types.

UV-LEDS are a scalable technology which can be used to disinfect water from a tap as easily as from a large canister. UV-LEDs also do not contain toxic material which would pose a risk on disposal at the end of their life and as they consume only a low amount of power can be operated by solar cells. Furthermore, UV-LEDs have a lower warm up time and can be operated on high frequency, allowing for direct at-point and on-demand water treatment.

The potential for UV-LEDs is not limited to application in water treatment. UV-LEDs are also a promising light source for: treatment of psoriasis, which is an auto-immune disease; gas sensing; medical diagnostics; lithography; communication technology and security technology, like testing banknotes.

However, at the moment UV-LEDs still suffer from an array of drawbacks, limiting their applicability. These drawbacks include the low power output, the high manufacturing costs and the still short lifetimes. The low power output is due to the extremely low external quantum efficiencies of only 2-3% while the short lifetimes are partially due to current crowding effects which heat the LED up, eventually damaging it [3].

To overcome these challenges considerable research effort is being put into these devices, optimising the different processes needed for the fabrication of these LEDs. In the first two experimental chapters of this thesis I present the results of my research efforts to improve the quality of UV-LEDs.

In the chapter (Chapter 4) “Analysis of AlGaN layers” I present my findings on the influence of the miscut angle on the morphology of AlGaN layers; the behaviour of AlGaN layers grown with different thicknesses and the silicon doping of high bandgap (Al% $>$ 80%) AlGaN.

In the chapter (Chapter 5) "UV-LED structures" I present my research performed on UV-LED structures. The first section deals with the reduction in emission intensity with decreasing emission wavelength in AlGaN based UV-LEDs, while the second section focusses on the influence of three growth parameter (temperature, QW thickness and buffer and barrier composition) on the optical properties of InAlN UV-LEDs, which are a promising alternative to the more studied AlGaN UV-LEDs.

In the third experimental chapter (Chapter 6) "Low dimensional semiconductor structures" the results of my investigation on nanorods for solid state lightning (SSL) are shown. SSL is the umbrella term for the application of semiconductor light emitting devices for ambient lighting. Utilizing the advantages of LEDs for ambient lighting has many benefits over using incandescent light bulbs or compact flourescent light bulbs. LEDs not only offer a significant increase in light bulb lifetime, but also a strongly reduced power consumption for the same light output.

The reduced power consumption compared to traditional light sources comes from the inefficient conversion of electricity to light in these devices. Reducing the power consumption for ambient lighting worldwide, by replacing old light bulbs for LEDs, can not only greatly reduce the CO_2 output and help fight climate change, but can also allow people without access to a regular power grid to benefit from ambient lighting.

The far-reaching significance of SSL was honoured in 2014 by the award of the Nobel price in physics to Shuji Nakamura, Hiroshi Amano and Isamu Akasaki for their role in realizing blue light emitting diodes.

Despite light emitting diodes, based on the research of these three Nobel laureates, now being commercially available and found in many devices (e.g. mobile phones, LED TVs), research still continues to achieve higher efficiencies and cheaper devices. One of these research efforts focusses on utilizing nano-structures for LEDs which offer increased light output for the same area. This can potentially lead to a cost reduction in the fabrication of LEDs and thus further the availability of low power consumption ambient light sources.

Chapter 2

Background

In this chapter a short overview of the background of group-III nitride based light emitting diodes (LEDs) is given onto which the rest of the thesis builds. The physical properties of group-III nitrides, the role of crystal defects, the fabrication of LED structures by metal organic vapour phase epitaxy (MOVPE), the structure of LEDs and doping concepts are explained.

2.1 Physical properties of Group-III Nitrides

All samples investigated in this thesis are fabricated using semiconductors from the group-III nitride group, consisting of alloys of nitrogen(N) with the group-III elements indium(In), gallium(Ga) and aluminium(Al). The group-III elements form sp3-hybridized covalent bonds with nitrogen; it is these bonds that are defining the crystal structure. The large difference in the covalent radii of the different elements–1.44 Å for In, 1.22 Å for Ga, 1.21 Å for Al–results in strongly different physical properties like band gap and lattice parameter for the binary III-V alloys (see table 2.1).

2.1.1 Crystal structure

These semiconductors can crystallize in different crystal structures, cubic zinc blende, NaCl and hexagonal wurtzite structure. Out of these three the most common and thermodynamically most stable crystal structure for the group-III nitrides is the hexagonal wurtzite structure (see Fig. 2.1). By choosing special substrates or high reactor pressure during growth it is possible to grow group-III nitrides in NaCl or cubic zinc blende structures. As these two are thermodynamically unstable they are of lesser interest in research efforts aimed to grow light

emitting devices [4, 5, 6].

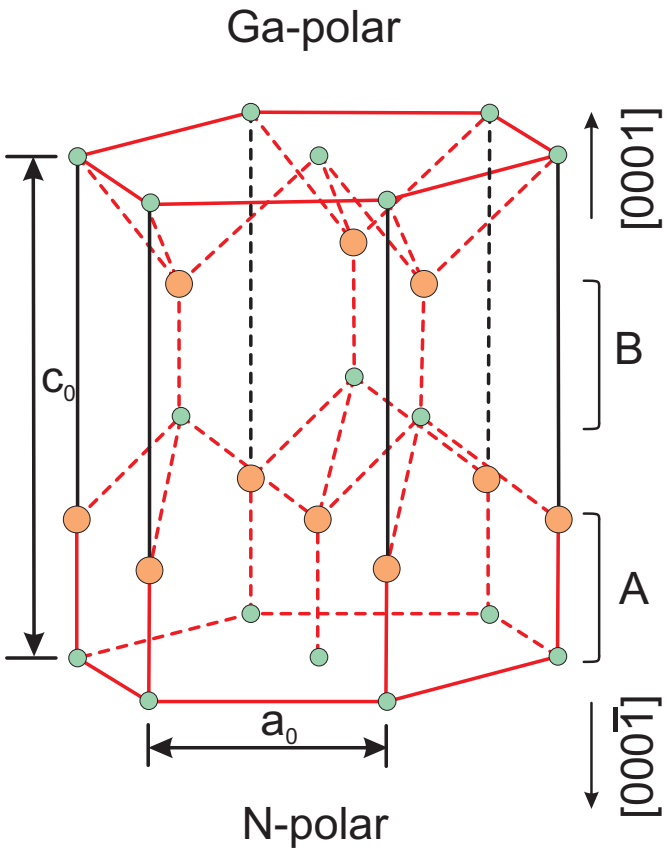

Figure 2.1: The hexagonal unit cell of GaN, Ga-atoms are pictured in orange, nitrogen atoms in green. Both stacks are marked with A and B, c_0 and a_0 are the lattice parameters. With the permission of M. Frentrup [7]

Because all samples investigated in this thesis have a hexagonal structure the properties of this structure will be explained in more detail. The hexagonal unit cell of GaN is shown in Fig. 2.1. The unit cell is described by the lattice parameters c_0 and a_0. The c-axis is perpendicular to the hexagonal base area which is also called basal face.

The lattice parameters for different alloys are given in Tab. 2.1. The wurtzite structure of GaN consist of hexagonal sub lattices for nitrogen and gallium, which are depicted coloured (green for nitrogen and orange for gallium) in Fig. 2.1, with a stacking sequence ABABAB... . Due to the sp3-hybridization the covalent bonds are ordered in a tetragonal structure so that each Ga atom has 4 nitrogen atoms as next neighbours and vice versa.

	c_0[Å]	a_0[Å]	c_0/a_0	E_g 300 K [eV]
GaN	5.185	3.189	1.626	3.40
AlN	4.978	3.111	1.600	6.02
InN	5.718	3.544	1.613	0.70

Table 2.1: Lattice parameter of binary nitride alloys.[8, 9, 10]

2.1.2 Bandgap

Semiconductor materials can be divided into two classes depending on their band gap, which can be direct or indirect. In an indirect band gap semiconductor the valence band maximum (VB_{max}) and the conduction band minimum (CB_{min}) are not at the same position the reciprocal space. For an electron and a hole to recombine in an indirect band gap semiconductor a third particle is needed, a phonon, in order to conserve momentum. In a direct bandgap semiconductor on the other hand, the valence band maximum and the conduction band minimum are at the same position in reciprocal space allowing electrons and holes to recombine radiatively without the assistance of a phonon, leading to an increased recombination probability of direct band gap materials which makes them more suitable for the growth and fabrication of LEDs.

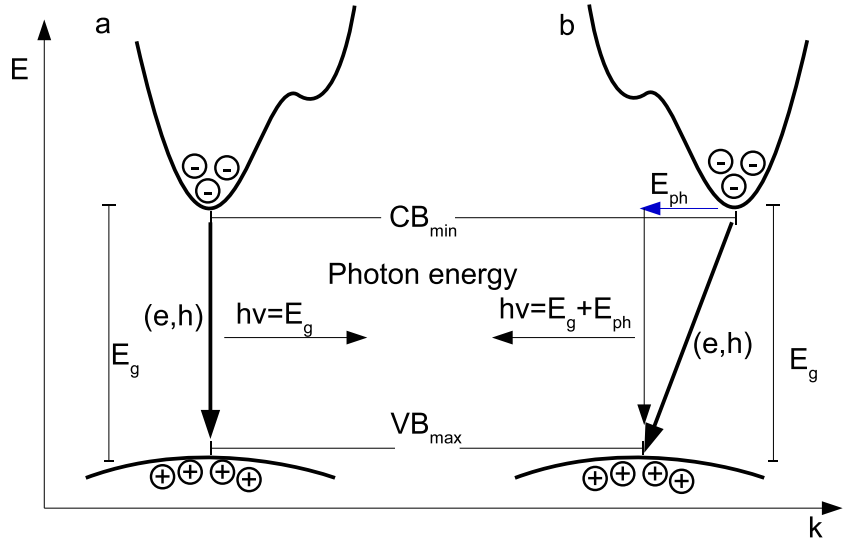

Figure 2.2: Energy band diagram of a direct (a) and an indirect (b) semiconductor in the reciprocal space. k is the reciprocal space vector, E_g the band gap, (e,h) denotes an electron hole recombination process, CB_{min} is the conduction band minimum, VB_{max} is the valence band maximum, E_{ph} is the phonon energy

The group-III nitrides with wurtzite structure always exhibit a direct band

gap of 0.7 eV [9] and 3.4 eV for InN and GaN and 6.02 eV for AlN [10] respectively at room temperature. By changing the composition of ternary ($Al_xGa_{1-x}N$, $In_yGa_{1-y}N$, $In_zAl_{1-z}N$) or quaternary (AlInGaN) alloys each band gap and also each emission wavelength between infra-red and ultraviolet is accessible using the group-III nitrides.

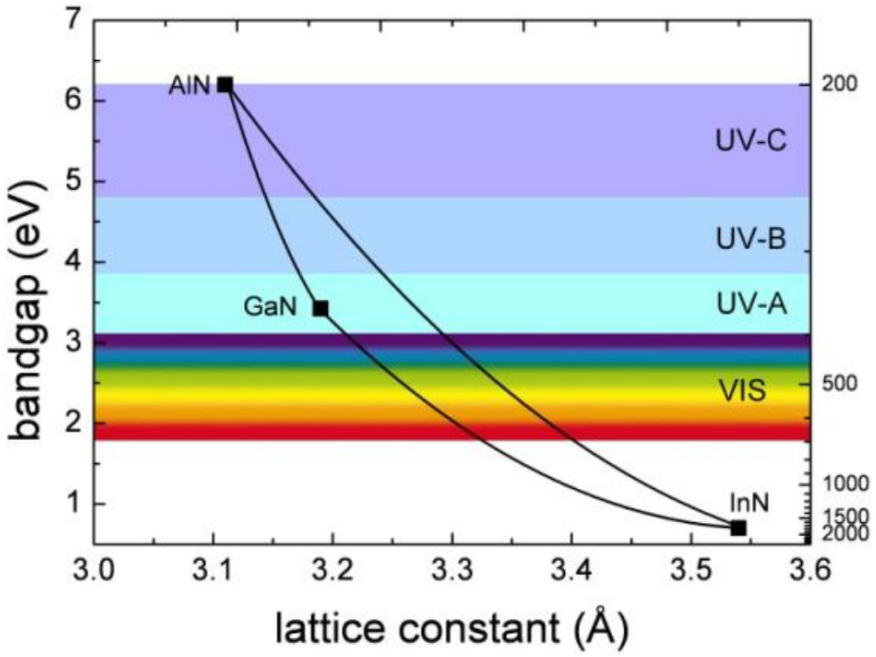

Figure 2.3: Band gap of the group-III nitrides over the a_0 lattice constant. With permission of Frank Mehnke from TU-Berlin.

The bandgap of a ternary semiconductor can be calculated using Vegards Law [11]. For the group-III nitrides this has to be adjusted with the bowing parameter due to a non linear change in the bandgap with the composition (see equation 2.1). The bowing parameters used in this thesis can be found in table 2.2, the bandgap over the lattice constant of the group-III nitrides and their ternary alloys is shown in Fig.2.3.

$$E_g^{InAlN} = (1-x) \times E_g^{InN} + x \times E_g^{AlN} - b_{InAlN} \times x(1-x) \tag{2.1}$$

With E_g the bandgap, x the amount of AlN and b_{InAlN} the bowing parameter of $In_{1-x}Al_xN$.

ternary alloy	b
$Al_xGa_{1-x}N$	1
$In_xAl_{1-x}N$	3
$In_xGa_{1-x}N$	1.43

Table 2.2: Bowing parameter of the ternary group-III nitride alloys [12, 13]

2.2 Growth

All samples presented in this thesis were fabricated by metal organic vapour phase epitaxy (MOVPE). We give here an overview over the technique and the reactor. MOVPE is an epitaxy technique in which crystal layers are fabricated on a substrate from a gas-phase, the requirements needed for such a growth technique lead to the development of two different reactor designs. These commonly used reactors are the horizontal reactor, where the gas flows horizontally over the substrate and the shower head reactor, in which the gas inlet is vertical over the substrate. The reactor used by the Tyndall National Institute and TU-Berlin (who supplied all investigated samples) are close coupled shower head reactors. The setup of that reactor will be discussed next and is schematically shown in Fig. 2.4.

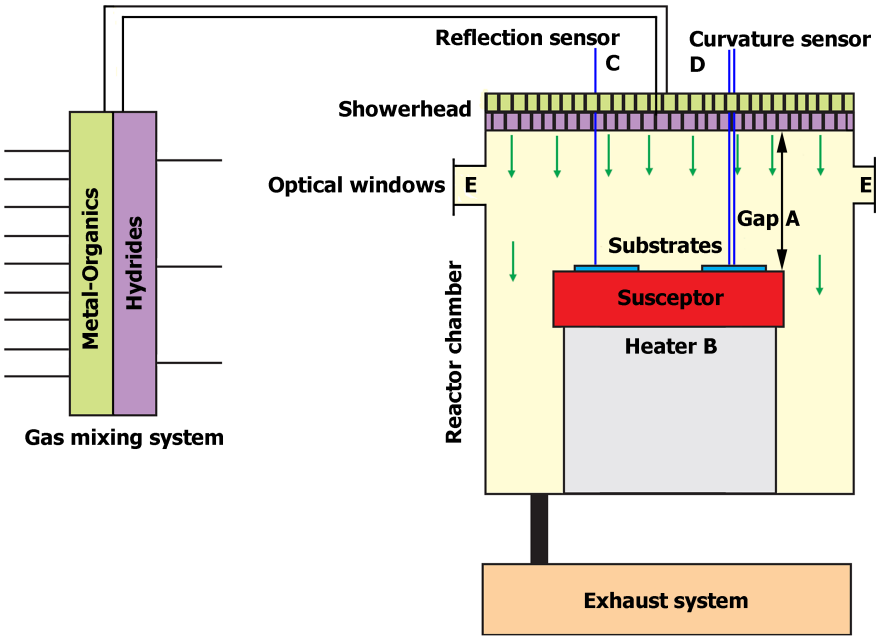

Figure 2.4: Schematic of a close coupled shower head reactor. From the Aixtron manual [14].

Close coupled shower head reactors consist of a reactor lid (the shower head), a rotatable susceptor and resistivity heating elements. A typical growth reactor also employs optical windows in the shower head in order to allow in-situ measurements; e.g. reflectivity measurements. The shower head acts as the gas inlet for these reactor types, where the gas mixture, containing the chemical compounds (precursors) needed for the growth, enter the reactor chamber. In modern shower head reactors the gas flow system is designed so that the group-III precursors and the nitrogen precursor first mix in the reactor chamber in order to prevent unwanted pre-reactions.

Typical precursors for the growth of the group-III nitrides are trimethylindium (TMIn), trimethylgallium (TMGa), trimethylaluminium (TMAl), biscyclopentadienylmagnesium (Cp_2Mg), silane (SiH_4) and ammonia (NH_3). Some of these precursors (TMIn,TMGa,TMAl) are available in liquid form or as a dry chemical (Cp_2Mg), stored in bubblers, while others (SiH_4, NH_3) are available in gaseous form. All of these precursors are mixed with a carrier gas (N_2, H_2) and transported to the reactor. The amount of material that is transported can be influenced by various parameters, like pressure and temperature in the bubbler.

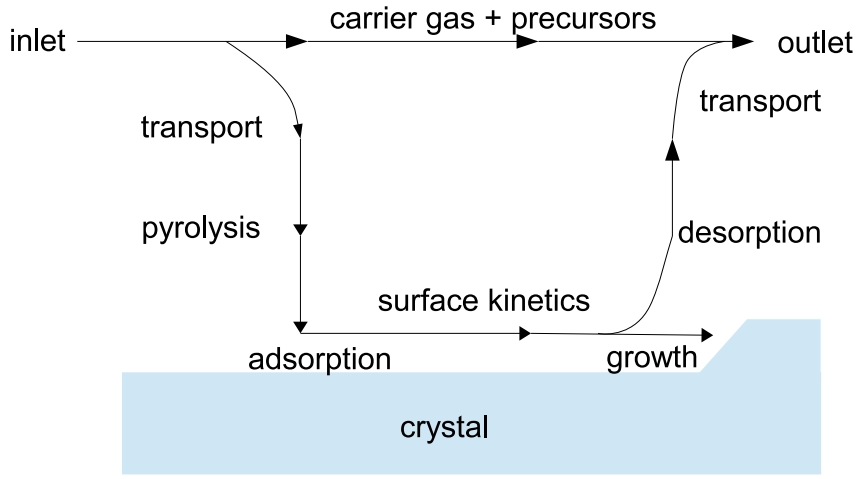

Figure 2.5: Schematic diagram of the relevant growth steps.

The growth process is schematically drawn in Fig. 2.5. During growth the precursors stream through the openings of the shower head over the susceptor and the substrates. The precursors disassemble in a thin layer over the substrates (by pyrolysis) due to the high temperature into their component parts. This process occurs in the gas-phase (homogeneous reactions) and in the boundary layer between the gas-phase and the substrate (heterogeneous reactions). During the growth inside the reactor chamber a pressure between 10^3 Pa and 10^5Pa is

maintained. Low pressure growth is being employed more frequently as it is found that most semiconductors grow more uniform at this pressure.

The pyrolysis of the precursors depends exponentially on the growth temperature. In general the pyrolysis is not yet completely understood, but the decomposition of TMGa should be dominated by the following processes [15]:

$$\begin{aligned} Ga(CH_3)_3 &\rightarrow Ga(CH_3)_2 + CH_3 \\ Ga(CH_3)_2 &\rightarrow GaCH_3 + CH_3 \\ GaCH_3 &\rightarrow Ga + CH_3 \\ Ga + H &\rightarrow GaH \\ GaH + H &\rightarrow Ga + H_2 \end{aligned}$$

After the pyrolysis of the precursors the chemical components of the semiconductor are adsorbed (ad-atoms) by the surface of the substrate. The ad-atoms can then diffuse over the substrate surface until they are either desorbed and thus lost for the growth or absorbed and incorporated into the growing crystal structure.

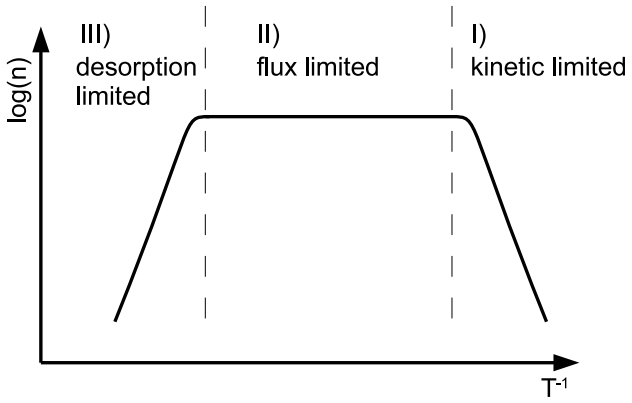

Figure 2.6: Temperature dependence of the growth rate n. Three different areas can be distinguished: I) kinetic limited II) flux limited and III) desorption limited

The growth rate n, when using MOVPE, can be divided into three different regions depending on the growth temperature: I) kinetic limited II) flux limited and III) desorption limited (shown in Fig. 2.6).

In the first region, at low growth temperatures, the temperature is not high enough to decompose all of the precursors. In this region the growth rate depends

exponentially on the growth temperature.

Increasing the temperature will eventually lead to a temperature high enough to decompose all of the precursors, only limiting the growth rate by the influx of the material.

Increasing the growth temperature even further leads to an increase in the desorption rate. This means that even though all of the precursors are being decomposed and the chemical components of the semiconductor are adsorbed unto the growing layer, most of them are being desorbed again, reducing the effective growth rate. In this region the growth rate exponentially decreases with increasing temperature.

2.2.1 Substrates

In the growth of any semiconductor device the choice of the substrate is crucial for the production of high crystalline quality. It is self-evident, that growth on homo-substrates (e.g. GaN on GaN or AlN on AlN) provides the best results in terms of crystalline quality, but for the group-III nitrides this is often not feasible due to the high price of bulk GaN or AlN substrates and the limited range of orientations and sizes.

This lack of homo-substrates led to the investigation of other materials as a substrate for the group-III nitride growth. The most important parameters for a substrate are the mismatch in lattice parameter and thermal expansion between the substrate and the material grown on top of it. Typical substrates used for the growth of the group-III nitrides are Al_2O_3 (sapphire), Si and SiC with sapphire being the most commonly used. In this work all samples were grown using an Al_2O_3 substrate which is why the following discussion will be focused on sapphire substrates.

Material	c_0 [Å]	a_0 [Å]	Lattice mismatch to Al_2O_3 $\Delta a/a$[%]	Difference in thermal expansion coefficient to Al_2O_3 $\Delta\alpha/\alpha$ [%]
Al_2O_3	12.991	4.758		
GaN	5.185	3.189	13.9	-34.2
AlN	4.978	3.111	13.3	-28

Table 2.3: Lattice parameter of GaN,AlN and Al_2O_3 as well as lattice mismatch and difference in thermal expansion coefficient of GaN and AlN to Al_2O_3 [15] [16].

Sapphire substrates are the most commonly used for the group-III nitride

growth due to their high availability, low price, good thermal and chemical stability. The largest drawback for sapphire substrates is the difference in lattice constants to the group-III nitrides which leads to a large lattice mismatch of ∼14% (see Tab. 2.3). This large lattice mismatch would result in a critical thickness of less than a mono layer after which plastic relaxation occurs in the GaN layer grown on top of the substrate . A critical thickness this low would mean that no epitaxial growth of GaN on Al_2O_3 would be possible. Instead of growing directly with this large a lattice mismatch, GaN forms a coincidence lattice [17] when grown on top of sapphire in which every 9th GaN lattice atom matches with every 8th atom of the substrate. The formation of this coincidence lattice reduces the lattice mismatch to 3%. The lattice mismatch of 3% is still rather high and would result in a critical thickness of only a few mono layer.

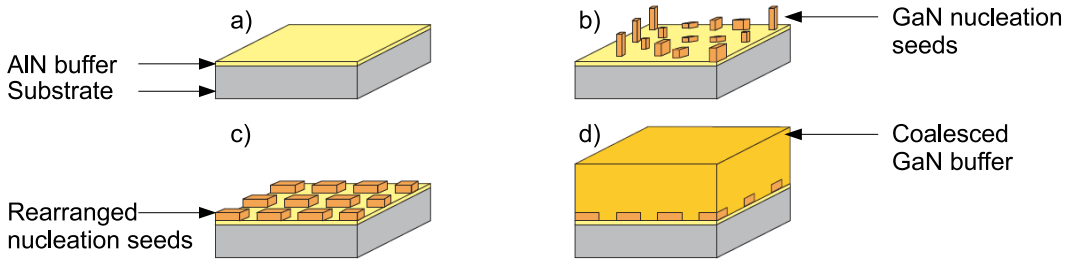

Figure 2.7: Schematic of the four step growth of GaN on a sapphire substrate. With the four steps: a) deposition of a thin AlN buffer; b) growth of GaN nucleation seeds; c) rearranging of the nucleation seeds, d) growth of a coalesced GaN buffer layer.

To reduce the lattice mismatch between the substrate and GaN a four step (sometimes called two step) growth method is employed [18, 19]. In the first step the substrate is heated up under an ammonia flux with H_2 as a carrier gas. The ammonia is, due to the temperature, decomposed into its chemical compounds of nitrogen and hydrogen. The hydrogen etches the sapphire surface and binds the desorping oxygen atoms, while the nitrogen atoms bond to the dangling bonds of the Al atoms of the substrate, thus forming a thin layer of AlN on the surface of the substrate (Fig. 2.7a).

In the next step a GaN nucleation layer is grown on top of the thin AlN layer on top of the substrate. The Ga and N ad-atoms only have a very limited mobility in this step due to the low temperature employed and do not form a homogeneous layer but rather polycrystalline nucleation seeds. These nucleation seeds are random in size and distribution over the substrate surface and allow for

defects to form in order to minimize the lattice mismatch to the substrate (Fig. 2.7b).

In the third step the reactor is heated up to an elevated temperature which leads to the nucleation seeds rearranging themselves in an ordered hexagonal (0001) structure (Fig. 2.7c). After this, in the last step, a thick GaN buffer is grown. The growth of this buffer originates from the GaN nucleation seeds. The buffer grows in a 3D growth mode, eventually leading to coalescence between the nucleation seeds, forming a homogeneous smooth layer (Fig. 2.7d). During the 3D growth some of the threading dislocations that formed in the nucleation seeds bend, which can lead to an annihilation of dislocations, reducing the overall defect density. GaN layers grown with this process usually show a dislocation density of approximately $5 \times 10^8\, cm^{-2}$ [20].

2.2.2 Defects and defect reduction techniques

Semiconductor layers and device structures usually contain crystalline defects. These defects can originate from a number of sources, they can form in order to reduce strain resulting from lattice mismatch or form due to the random movement and incorporation of the ad-atoms [21, 22, 23]. Understanding the physical properties of these defects is of vital interest for optimizing semiconductor devices as they can have a detrimental influence on the function of these devices. In this section a short overview on point defects and dislocations is given, followed by a discussion of defect reducing growth techniques.

Point defects

Point defects are defects in a crystal lattice that can be inscribed by a small sphere. It is possible to distinguish between two types of point defects, intrinsic and extrinsic point defects. *Intrinsic point defects* are defects that involve only atoms of the crystal. These can be vacancies, when one crystal atom is missing from its lattice site, self interstitials, when an atom is placed in between lattice sites, anti sites, which is when an atom is incorporated on a lattice site of another atom (e.g. Ga occupying a N site in GaN) and Frenkel pairs, which is when a lattice atom moves from a lattice site to an interstitial site, leaving behind a vacancy (see Fig. 2.8).

Extrinsic point defects are caused by atoms foreign to the crystal lattice. These atoms are provided either as impurities in the carrier gas (e.g. Oxygen), as by-products from the decomposition of the precursors (e.g. H, C) or are intentionally

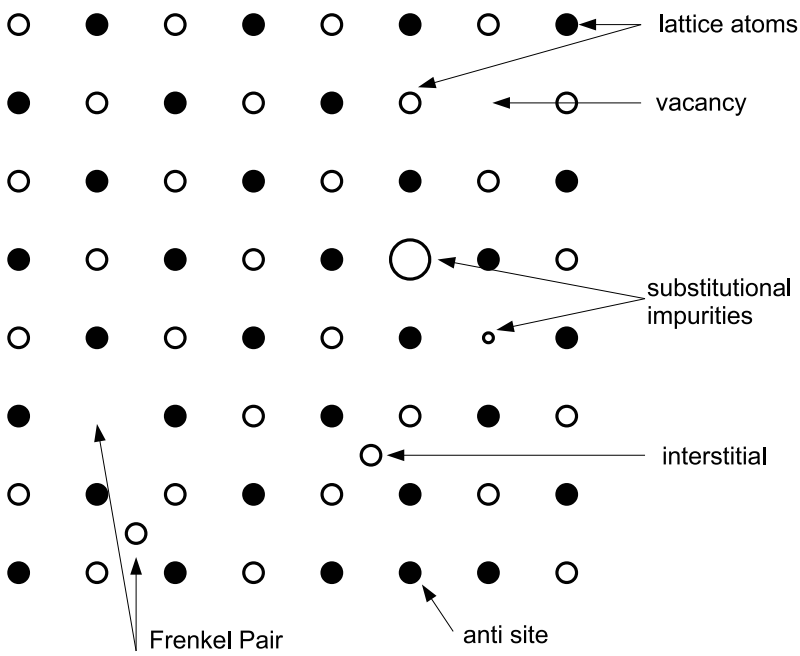

Figure 2.8: Point defects in a crystal lattice.

provided as dopants (Si, Mg, Eu). These atoms can be incorporated on a crystal lattice site, replacing the the intrinsic crystal atom or as interstitials (see Fig. 2.8).

Point defects can incorporate luminescence centres in semiconductor layers and have a strong influence on the electric properties of doped layers.

Dislocations

A dislocation is a line defect in a crystal and characterized by a vector **l**, which defines locally the direction of the dislocation line, and by a vector **b**, called the Burgers vector, which defines the atomic displacement needed to generate the dislocation from a perfect crystal lattice.

A feature of dislocations is the elastic strain field associated with them, allowing dislocations to be visible in an electron microscope. The perfect order of the atomic planes is distorted around a dislocation, changing the diffraction condition for electrons and X-rays around the dislocation which in turn provides a contrast around the dislocation line, allowing dislocations to be measured by diffraction techniques, such as high resolution X-ray diffraction (HR-XRD), electron channelling contrast imaging (ECCI) or in a transmission electron microscope (TEM).

Dislocations can be differentiated by the relation between the dislocation line

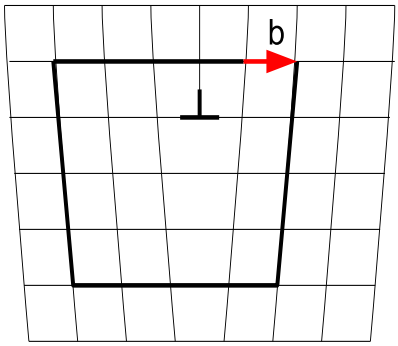

Figure 2.9: Schematic of an edge dislocation, the Burgers vector is drawn in red

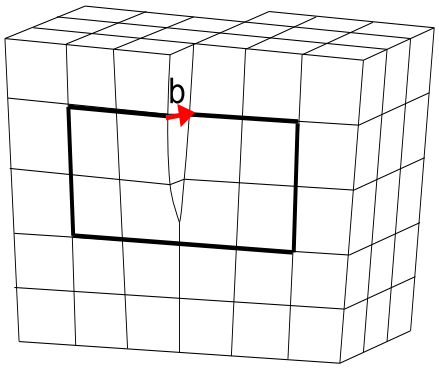

Figure 2.10: Schematic of a screw dislocation, the Burgers vector is drawn in red

and the Burgers vector. One of these dislocations is an *edge dislocation*, where an additional row of atoms is inserted into the crystal lattice (see Fig. 2.9) for these dislocations the Burgers vector **b** is perpendicular to the direction of the dislocation line.

The other main dislocation type is *screw*. For these dislocations the Burgers vector **b** is parallel to the dislocation direction **l**. A screw dislocation is formed when one part of the crystal is sheared to the other part, the dislocation line is where the half plane terminates (see Fig. 2.10). The shearing of one part of the crystal relative to the other is such that it forms a step, pinned at the dislocation core.

A mixture of both dislocation types is possible and is called a *mixed dislocation* when **b** is neither parallel nor perpendicular to the dislocation line. All of these dislocations can have a detrimental effect on the optical and electrical properties as well as the morphology of the grown semiconductor structure. Dislocations can act as non-radiative recombination centres [24, 25], agglomeration sites for point defects [25, 26], as a channel for carriers in transistors, eventually reducing the transistor quality [27], and cause surface modulations like hillocks or V-pits [28, 29, 30].

Imaging of Threading dislocations

The diffraction of electrons at crystal planes is one mechanism that is sensitive to the lattice distortion caused by threading dislocation and thus allows for their imaging. Transmission electron microscopy (TEM) and electron channelling con-

trast imaging (ECCI) are two techniques utilizing this mechanism. Out of these two, TEM is the more established technique and the imaging process will be discussed here briefly, the discussion follows closely the discussion in "Introduction to Dislocations" by Hull et al. [31]. A TEM image is produced by Bragg diffraction of high energy electrons (E $\sim$ 100 kV) in a thin sample (d $\sim$ 100 nm to 1000 nm) and produces an intensity map as a function of the crystal lattice. It can be seen from Fig. 2.9 and Fig. 2.10 that a threading dislocation induces a bending of the crystal planes close to the dislocation, with decreasing bending the farther away from the dislocation the plane is located. If these planes are bent into a strongly diffracting position the intensity of the direct transmitted beam in the TEM will be strongly reduced and the dislocation generates contrast on the detector. Threading dislocations can also be identified by TEM analysis due to the invisibility criterion which states that a *screw dislocation* is invisible in the TEM contrast if the diffraction vector g is perpendicular to the burgers vector of the dislocation $g \cdot b = 0$. Thus by tilting the sample to analyse different diffraction vectors *screw dislocations* can be identified. For the invisibility criterion of *edge dislocation* both $g \cdot b = 0$ and $g \cdot (b \times t) = 0$, with t a vector along the line, must be true. For mixed dislocations there is no diffraction vector for which the dislocation would appear to be invisible.

Defect reduction techniques

Due to the undesired effects of dislocations, growth techniques have been developed which reduce the defect density in a grown semiconductor. One of these techniques will be discussed here in more detail and the fabrication steps and physical mechanisms leading to a reduced defect density will be explained.

Epitaxial lateral overgrowth (ELO) is a widely used techniques to reduce the defect density in hetero-epitaxial grown group-III nitride semiconductors [32]. In this technique a thick buffer layer is grown on top of the substrate and subsequently removed from the growth reactor (Fig. 2.11a). A mask material, acting as an anti surfactant, (e.g. SiO_2 or SiN_x) is then deposited onto the buffer layer (Fig. 2.11b). In the next step the mask is structured, giving regions which are covered by the mask and window regions without a mask (Fig. 2.11c). The sample is then reinserted into the growth reactor and the growth is commenced. During the following growth the buffer material will not grow on the masked area, ad-atoms adsorbed on the masked area will either diffuse onto an unmasked area or desorp from the sample surface. This guarantees that the buffer layer only grows out of the unmasked area (Fig. 2.11d) and eventually coalesces with the

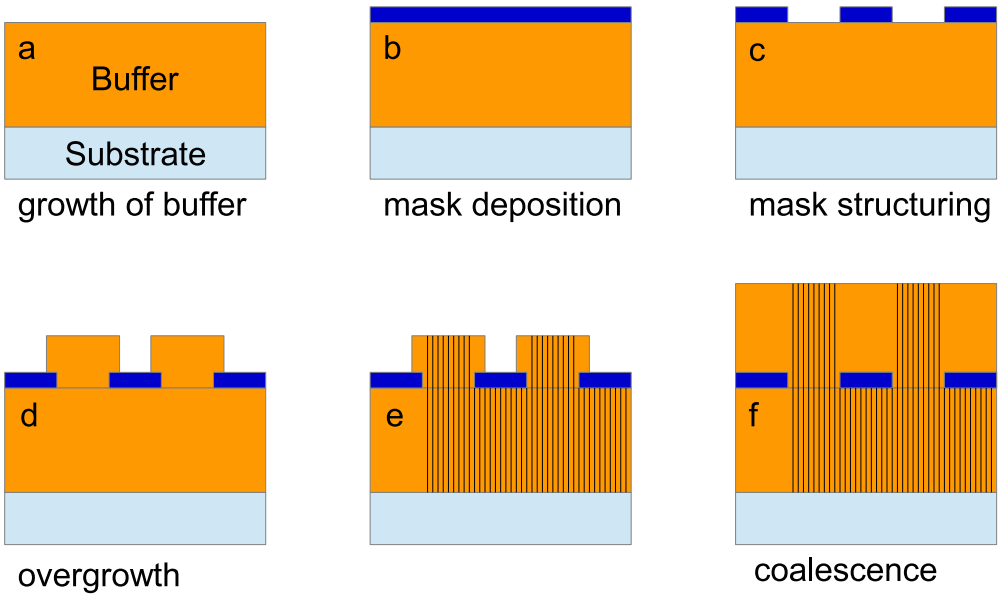

Figure 2.11: Schematic of the epitaxial lateral overgrowth process with: a) growth of a buffer layer; b) deposition of an anti-surfactant mask; c) structuring of the mask; d) overgrowth of the mask; e) dislocations (shown as black lines) terminate at the mask; f) coalescence of the overgrown material.

growth out of other unmasked areas (Fig. 2.11f). In this manner all dislocations directly underneath the masked area are terminated at the mask (Fig. 2.11e), reducing the resulting dislocation density on the coalesced buffer material with reported defect densities as low as $2 \times 10^7\, cm^{-2}$ [33].

2.3 Light emitting diodes

LEDs and laser diodes (LDs) are p/n diodes with an active region, which emit light if an external current is applied. The active region is the area of the device where the light is emitted. The wavelength of the emitted light depends on the band gap of the active region of the devices. In LEDs most of the light emission comes from spontaneous recombination which differentiates them from LDs where most of the emitted light comes from stimulated emission. This means that the structure of LEDs is simpler in design as no carrier inversion or wave-guiding is necessary. Most of the information provided in this section can be found in the book “Light-Emitting Diodes” by Schubert [34].

Recombination mechanics and efficiencies

In general the recombination rate R consist of three different terms expressed by the following equation:

$$R = \frac{dN}{dt} \approx An + Bn^2 + Cn^3 \tag{2.2}$$

Here $\frac{dN}{dt}$ is the change in carrier density with time, A is the non-radiative Shockley-Read-Hall constant, B the radiative recombination constant and C the non-radiative Auger recombination constant, n is the carrier density. The external quantum efficiency (EQE) of a light emitting device is defined by:

$$EQE = \eta_{inj}\eta_{IQE}\eta_{extr.} \tag{2.3}$$

With η_{inj} as injection efficiency, η_{IQE} as internal quantum efficiency and the extraction efficiency $\eta_{extr.}$.

Carriers in a semiconductor device can interact with photons in three different ways. A photon with an energy larger than the band gap (E_g) can be absorbed by an electron in the valence band which lifts it from the valence band into the conduction band. Furthermore, photons with an energy $\hbar\omega = E_g$ can be emitted by optical transitions. This process can be differentiated between spontaneous and stimulated emission. Stimulated emission means that a photon stimulates an electron in the conduction band to emit a photon by recombining back into the valence band. The generated photon has the same properties as the inducing photon. In LEDs the dominant process of generating light is spontaneous emission in which an electron and spontaneously recombine. The spontaneous emission rate (R) depends on the carrier density in the valence (p) and conduction band (n) and a proportionality factor B in the following way:

$$R = Bnp \tag{2.4}$$

This means that increasing the carrier density in the valence and conduction band increases the rate of spontaneous emission as long as $\tau_{nr} \propto n$ (with τ_{nr} the non-radiative recombination rate). Thus the portion of carriers recombining non-radiatively is reduced and the internal quantum efficiency (IQEQ) increased. The internal quantum efficiency describes the ratio between radiative and non-radiative recombination.

$$\eta_{IQE} = \frac{\tau_r^{-1}}{\tau_{nr}^{-1} + \tau_r^{-1}} \tag{2.5}$$

Active Zone

The active zone of an LED can be designed in different ways: it can be a simple p/n junction, a double hetero-structure, quantum wells (QW), quantum wires or quantum dots. The design is decisive for the carrier confinement and thus for the internal quantum efficiency of a light emitting device. All LED samples investigated in this thesis were designed to have an active region consisting of multiple QWs, which we will give a brief presentation of.

The QW is a hetero-epitaxial active zone design in which the optical active region is intended to have a thickness smaller than the deBroglie wavelength of the electrons in this material. This causes discrete energy levels to arise due to the wave-particle nature of both carriers. This is combined with quantum barriers (QB) on both sides of the QW, consisting of a material with a higher bandgap, which causes the carriers to experience a potential barrier between the QW and the QB. Because of this and the reduction of one degree of freedom due to the nature of the quantum wells, carriers accumulate in the quantum wells which leads to carrier inversion. The confinement provided by a QW design, with a QW thickness of L_{QW} and $n = \frac{n^{2D}}{L_{QW}}$ ($p = \frac{p^{2D}}{L_{QW}}$), changes the recombination rate to:

$$R = B\frac{n^{2D}}{L_{QW}}\frac{p^{2D}}{L_{QW}} \tag{2.6}$$

This shows one of the main advantages of QW active zone designs. A decrease of the QW thickness increases the 3D carrier concentration which reduces the radiative recombination time, increasing the internal quantum efficiency. The emission energy of photons generated from carriers recombining in a QW is blue shifted compared to the emission energy from the same material in a bulk crystal. This is due to the discrete energy levels in the QW, which can be approximated by the particle in a box model and provides a fine tuning of the emission energy utilizing the QW width and the barrier height of the QBs.

Electric fields

An intrinsic property of the group-III nitride semiconductors, grown in wurtzite crystal structure, is the presence of polarisation fields [35, 6]. These fields can have a detrimental effect on LED structures, causing high radiative recombination times and reducing the internal quantum efficiency (IQE) by separating the electron and hole wave-functions.

These polarisation fields are the spontaneous polarisation and piezoelectric

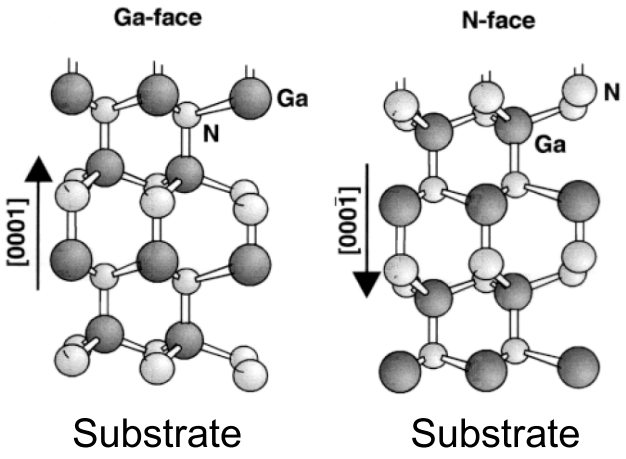

Figure 2.12: Ga and N polarity of GaN. Taken from Ambacher et. al. [6]

polarisation. The *spontaneous polarisation* is caused by the lack of an inversion symmetry of the wurtzite crystal structure, the polarity of the group III-N bond and the unequal bonding lengths between the metal and N atoms in the c_0 and a_0 directions [6]. The ideal axis ratio in an hexagonal crystal is $c_0/a_0 = \sqrt{8/3} = 1.63$. The axis ratio of the group-III nitrides differs from this as the bonds are more strongly oriented along the c-axis. This induces a spontaneous polarisation along the c-axis. The direction of the spontaneous polarisation depends on whether the layer is grown Ga-faced or N-faced (Fig. 2.12) [6]. The strength of the spontaneous polarisation depends on the deviation of the axis ratio from the ideal axis ratio [35]. By comparing the axis ratios for the three binary group-III compounds (see table 2.1) it is possible to determine, that the strength of the spontaneous polarisation increases from GaN to InN and is highest for AlN.

Piezoelectric polarisation occurs when the lattice constants of a crystal are changed due to an applied force. This can happen when a layer is grown pseudomorphically on another layer in hetero-epitaxy. For example, during pseudomorphic growth of $Al_xGa_{1-x}N$ on GaN, the $Al_xGa_{1-x}N$ will experience tensile strain by adapting to the a_0 lattice constant of the GaN layer. This adaptation also changes the bond length along the c-direction, further deviating the c_0/a_0 ratio and causing a piezoelectric polarisation field. This field is, due to the wurtzite symmetry, always oriented along the c-direction [6].

These two polarisation fields will, in a quantum well structure, result in the *quantum confined Stark effect* (QCSE) [36], which strongly influences the carrier recombination rate and emission energy of the QW. In an ideal QW without any electric fields (shown in Fig. 2.13a) the electron and hole wave-function have

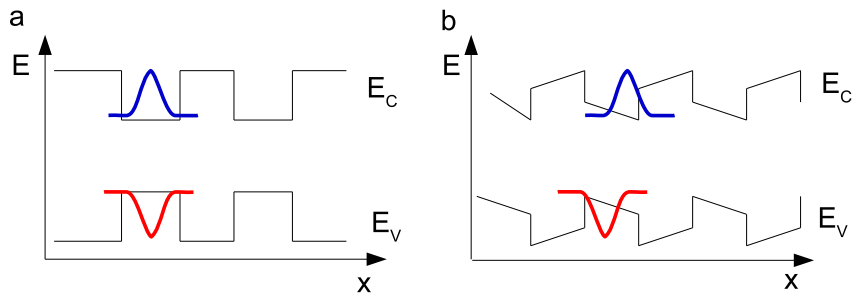

Figure 2.13: Schematic drawing of the electron (blue) and hole (red) wave-function in a quantum well without piezoelectric fields (a) and with piezo electric fields (b).

a strong overlap due to the conduction band minimum and the valence band maximum being at the same position. In a QW structure with piezoelectric fields on the other hand, the polarisation fields cause a tilt of the band structure due to space charges generated at the hetero-interfaces between the QW and the quantum barrier. The tilted bands will then induce a separation of the electron and hole wave-function as the conduction band minimum is no longer at the same point as the valence band minimum (shown in Fig. 2.13b). Due to this separation the the radiative recombination time strongly increases, reducing the internal quantum efficiency of the device. The tilt of the valence and conduction band also induces a red-shift of the QW emission. The tilt of the bands can be reverted by applying an external electric field or by generating carriers which can screen the polarisation fields in the QW structure. This will also cause a blue-shift of the emission energy, which makes it necessary for *c*-plane LEDs to be optimized for specific running conditions.

2.4 Doping

Electric and optical semiconductor devices require a high and controllable conductivity in order to be operated electrically. To achieve the necessary conductivity most of these devices need to be doped. Doping defines the process in which a foreign atom (the dopant) is incorporated into the crystal, substituting one of the native crystal atoms. Depending on the electric configuration of the substituting atom one can distinguish between n-doping and p-doping. Most of the presented discussion can be found in the book “Einführung in die Festkörperphysik” by Ch. Kittel [37].

If a lattice atom is substituted by a dopant with extra electrons in the outer

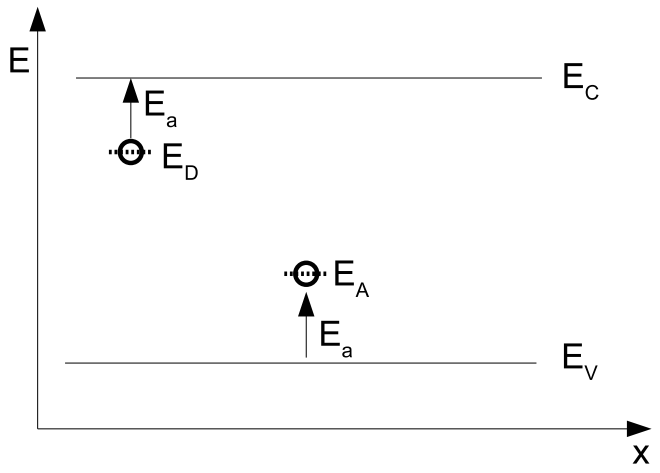

Figure 2.14: Schematic diagram of doping levels in the bandgap. E_C and E_V are the conduction- and valence band edges. E_D is the donor level and E_A the acceptor level, E_a denotes the activation energy of the dopants.

shell it is called a donor and the process is called n-doping. The extra electron induces a donor energy level (E_D) below the conduction band (E_C). If the electron gains energy greater than the activation energy (E_a) it can be excited into the conduction band where it can contribute to the conduction of the semiconductor. The activation energy E_a determines how much energy is needed to ionize an acceptor or donor.

If an atom with fewer electrons in the outer shell than the substituted atom is incorporated into the crystal lattice, it acts as an acceptor and the process is called p-doping. The acceptor atom induces an acceptor energy level (E_A) above the valence band. This can be occupied by an electron from the valence band (E_V) which induces a hole in the valence band, which then can contribute to the conduction of the semiconductor.

The general behaviour of the free carrier concentration, on the inverse temperature, in a doped semiconductor is depicted in Fig. 2.15. Depending on the temperature three distinct areas can be distinguished: I) freeze out II) extrinsic T-region and III) intrinsic T-region.

At T=0 K no acceptor or donor is ionized and there are no free carriers in the semiconductor which means that at this temperature the semiconductor acts as an insulator. For temperatures $0 < T < E_a/k_B$ only a certain number of acceptors and donors are ionized, this area is called freeze out. The carrier concentration in this area increases exponentially with the temperature as described by the Boltzman distribution. An increase in the carrier concentration, at a constant

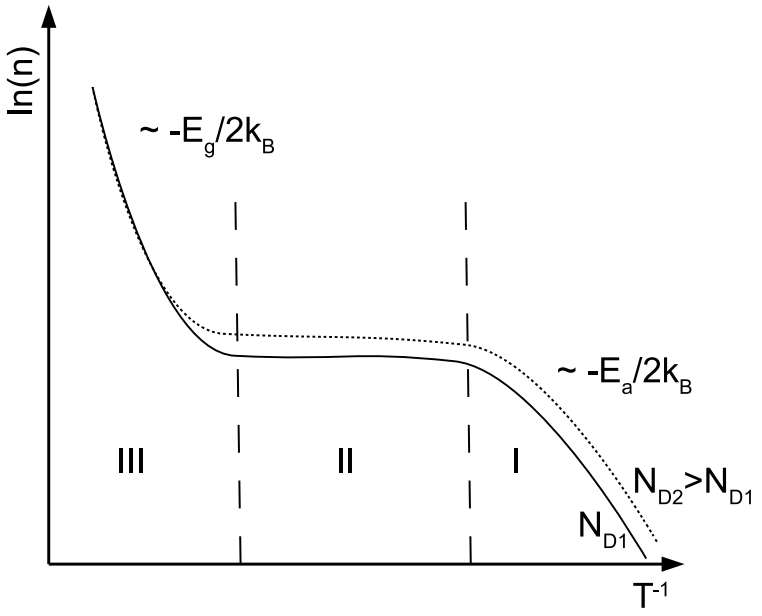

Figure 2.15: Carrier concentration (n) of a doped semiconductor in dependence on the inverse temperature for two doping concentrations ($N_{D1} < N_{D2}$). E_g is the band-gap of the semiconductor and E_a is the activation energy. There are three distinct areas I) freeze out II) extrinsic T-region and III) intrinsic T-region.

temperature, in this area can only be achieved by using a dopant with a lower activation energy or a higher doping concentration.

In the extrinsic T-region all acceptors or donors are ionized, which means that the carrier concentration in this region remains constant and is independent of the temperature. An increase of the carrier concentration in this region can only be achieved by increasing the doping concentration, as the activation energy has no longer influence on the carrier concentration.

In the intrinsic T-region the thermal energy is high enough to excite electrons from the valence band into the conduction band. The carrier density increases exponentially with the temperature. At room temperature none of the group-III semiconductors show intrinsic conductivity, making doping a necessity to achieve a conductivity sufficient enough to operate devices based on these semiconductors.

When choosing a dopant the activation energy, the covalent radius and the formation energy have to be taken into account. For a given temperature the percentage of active dopants (N) can be estimated:

$$N \cong exp(-E_a/2k_BT) \tag{2.7}$$

where k_B is the Boltzman constant, T the temperature in Kelvin and E_a the activation energy.

The value of the activation energy has a significant impact on the number of ionized acceptors and donors. For an activation energy $E_a = 150\,meV$ only 5.5% of the dopants are active at room-temperature, while for an activation energy of $E_a = 20\,meV$ 68% of the dopants are active. The activation energy strongly depends on the intrinsic properties of the doped semiconductor like effective masses of holes and electrons and dielectric constant. A good dopant is usually characterized by an activation energy $< 25\,meV$, which means that at room-temperature most of the incorporated acceptors and donors are ionized.

The difference in the covalent radii between the dopant and the substituted atom dictates the magnitude of the distortion of the perfect crystal by the dopant. The dopant can be incorporated on a lattice place of an intrinsic atom or as an interstitial with both forms distorting the ideal crystals lattice.

Apart from the activation energy and the covalent radius, which are parameters of the dopant, there are further fundamental challenges which limit the achievable doping concentrations in a semiconductor. These are compensating and self-compensating effects which we discuss below.

Compensation by native point defects

Native point defects like vacancies, interstitials and anti-sites are usually incorporated during the growth of a semiconductor. These native defects provide a background doping in some semiconductors; e.g. GaN which even when undoped has light n-type behaviour [38]. They are problematic for the doping of the semiconductor if they can be incorporated in a charged state due to two distinct properties. Firstly, their formation cannot be fully suppressed, native defects will always form during growth. Secondly, their incorporation ratio increases with increased doping concentration, as their formation energy decreases with increasing/decreasing Fermi level (for n-doping/p-doping) in the semiconductor (see Fig. 2.16).

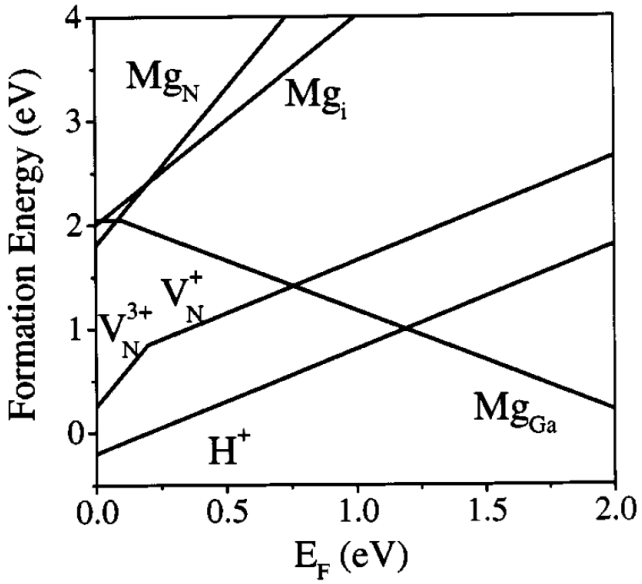

Figure 2.16: Formation energy as a function of the Fermi energy for Mg in GaN, the nitrogen vacancy (V_N^+) and the hydrogen interstitial (H_i^+). Taken from Van de Walle et. al. [39]. The zero of the Fermi energy is set at the valence band maximum.

An example of this behaviour is the formation energy of the nitrogen vacancy (V_N^+) in GaN:Mg (shown in Fig. 2.16). This nitrogen vacancy acts as a singly charged donor in GaN, each vacancy effectively compensating one active Mg acceptor. From first-principles calculations, reported by Van de Walle et. al. [39], shown in Fig. 2.16, it can be seen that with increasing Mg concentration and thus decreasing Fermi energy the formation energy of the nitrogen vacancy decreases. A decreasing formation energy will lead to an increased incorporation

rate, causing a higher vacancy concentration in the semiconductor and thus a higher compensation rate of the Mg acceptors.

Compensation by foreign impurities

During MOVPE growth not only crystal atoms are available for incorporation but also impurities which are either provided as by-products from the precursors (such as C and H from TMGa) or as impurities from the carrier gas (e.g. O). These foreign atoms can be incorporated into the semiconductor during growth and can act as either acceptors or donors; e.g. O incorporated during the growth of GaN acts as a donor causing the n-type behaviour of nominally undoped GaN.

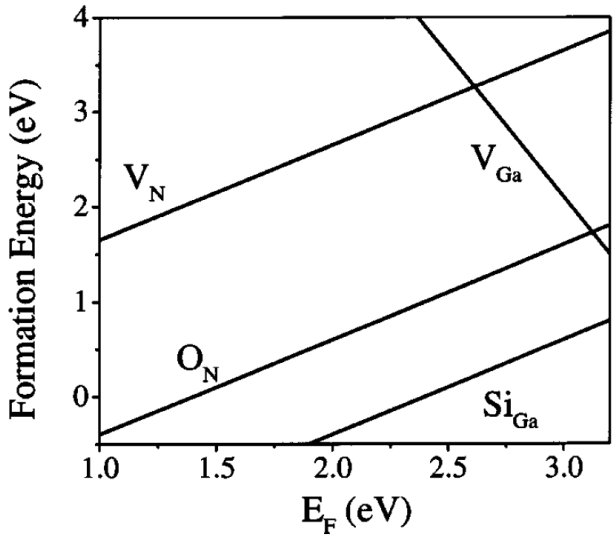

Figure 2.17: Formation energy as a function of the Fermi energy for O in GaN, the nitrogen vacancy and Si. Taken from Van de Walle et al. [39]. The zero of the Fermi energy is set at the valence band maximum.

Impurities that act as acceptors or donors can also compensate intentionally incorporated dopants. For example in GaN:Mg oxygen atoms in the crystal will compensate some of the active Mg acceptors, reducing the carrier concentration. The incorporation ratio of these impurities changes with the formation energy, which depends on the Fermi energy in the crystal. This means that by doping GaN with Mg the Fermi energy is reduced which leads to a reduction of the formation energy of oxygen atoms and thus to an increased incorporation of oxygen in the crystal and an increasing compensation for the Mg acceptors (Fig. 2.17). Thus, it is of utmost importance to reduce the availability of impurity atoms during the growth by choosing ultra pure carrier gases and precursors.

Historically, for many years no p-doping could be achieved for GaN, despite incorporating enough Mg into the semiconductor material. This was found to be due to the concomitant introduction of hydrogen (H) atoms into the grown material, which forms a magnesium-hydrogen-nitrogen vacancy (Mg-H-V_N) complex, compensating the Mg acceptor. This complex can be broken by either thermally treating the material or by irradiating it with a low energy electron beam [40, 41], introducing a necessary extra step into the fabrication of group-III based devices.

Self-compensation

Self-compensation describes a compensating mechanism induced by the dopant itself. That can be the solubility limit of the dopant or a change in the behaviour of a compensating centre due to the high doping. Both effects are observable in the Mg doping of GaN. With sufficiently high Mg doping the solubility limit of Mg in GaN can be reached, changing the incorporation of the dopant from being incorporated on a Ga lattice sites to being incorporated in Mg_3N_2 clusters. These clusters can not only compensate the Mg dopant but also lead to an increased surface roughness of Mg doped GaN layers [42, 43, 44, 45].

Furthermore, with sufficiently high Mg doping a shift in the behaviour of the nitrogen vacancy can be observed. The nitrogen vacancy switches from a singly charged donor to a triply charged donor, which means that each nitrogen vacancy can compensate three active Mg acceptors. This is accompanied by a strong decrease in the formation energy of the nitrogen vacancy strongly increasing its incorporation ratio (Fig. 2.16).
Overall, compensation by foreign impurities and native point defects provides a lower limit on the necessary dopant concentration for achieving conductivity by the chosen carrier type, while self-compensation provides the upper limit on the achievable carrier concentration in a semiconductor.

Doping for group-III nitrides

The n-type doping of the group-III nitrides is usually conducted using silicon (Si) or germanium (Ge), with Si being the more widely used donor. Silicon is amphoteric meaning that Si can be both an acceptor or a donor depending on the atom it substitutes. In GaN the incorporation of Si on a Ga site has the lowest formation energy and Si acts as a donor. The formation energy for incorporating Si on a Ga site is small because the covalent radii of Si and Ga atoms are similar. The incorporation of Si on nitrogen (N) sites or as an interstitial are energetically

unfavourable as the difference in the covalent radii would lead to a relatively large distortion of the crystal lattice, inducing elastic strain in the grown material.

Silicon has an activation energy of 12–17 meV in GaN [46], resulting in 70–80% of the donors being active at room temperature. The doping in GaN is well understood and carrier concentrations between 1×10^{17} and $4 \times 10^{19} cm^{-3}$ [47] with mobilities of $100 - 450\, cm^2/Vs$ can be achieved, which is sufficient for the operation of devices. The Si doping of wide bandgap $Al_xGa_{1-x}N$ layers will be investigated in section 4.4.

The p-doping of group-III nitrides is still one of the main challenges in the fabrication of group-III nitride devices. This is partially due to the limited availability of possible dopants which have either a large difference in the covalent radius or a high activation energy.

Dopant	r_{cov}[Å]	theoretical E_a[meV]
Ga	1.26	
Be	0.9	209
Mg	1.36	224
Ca	1.74	302
Zn	1.25	652

Table 2.4: Covalent radius and activation energy of possible p-dopants on group-III lattice sites in GaN. [39, 48, 49]

Table 2.4 presents an overview of the covalent radius and the activation energy of possible p-dopants in GaN. The covalent radius of Zn is the closest to the Ga atom, allowing the incorporation of Zn with the smallest possible distortion of the crystal. However, with an activation energy of 652 meV only an extremely small number of the Zn atoms would be active acceptors at room-temperature making Zn a very poor donor. The lowest activation energy was found for Be with 209 meV, but Be also has a large difference in covalent radius to Ga possibly introducing large distortions of the GaN crystal lattice.

The most common p-dopant for GaN is Mg which offers both a reasonably low activation energy as well as a covalent radius that is close to the covalent radius of Ga. Due to the similar covalent radii Mg is preferably incorporated on Ga lattice sites (Mg_{Ga}). The activation energy of Mg (224 meV) is considerably higher than the activation energy of Si (12–17 meV) and only 1.3% of the incorporated Mg atoms are active at room temperature. This means that in order to achieve the same carrier concentration with Mg doping as with Si doping a significantly higher number of Mg has to be incorporated into the material.

Chapter 3

Experimental techniques

In this chapter cathodoluminescence (CL) imaging and wavelength dispersive X-ray (WDX) measurements will be discussed in detail as these technique were primarily used to acquire the data presented in this thesis. The chapter starts by introducing the two different scanning electron microscopes (SEM) used for CL imaging and X-ray measurements respectively. Afterwards the CL system and its special feature, hyperspectral acquisition, will be presented and an overview over electron-hole recombination processes and the type of information one can gather from CL will be given. In the last section the generation of X-rays by electron bombardment, the WDX measurement setup and the general principles of operation of WDX spectroscopy are being discussed. Most of the details presented here can be found in the book "Electron Microscopy and Analysis" by Goodhew et al. [50].

3.1 The scanning electron microscope

A SEM is a measurement device utilizing a beam of accelerated electrons for the imaging and characterization of organic and inorganic materials on a mm to nm scale. The SEM consists of an electron gun, where electrons are generated and accelerated (to an energy between 200 eV and 30 keV), electron lenses and the specimen chamber where the specimen and detectors are located. Usually the whole system is under high vacuum in order to minimize electron-gas interactions. Two different scanning electron microscopes have been used in this thesis, a FEI Quanta FEG 250 and a Cameca SX100 electron microprobe analyser (EPMA). The working principle of both is the same and a schematic diagram of the EPMA can be found in Fig. 3.1.

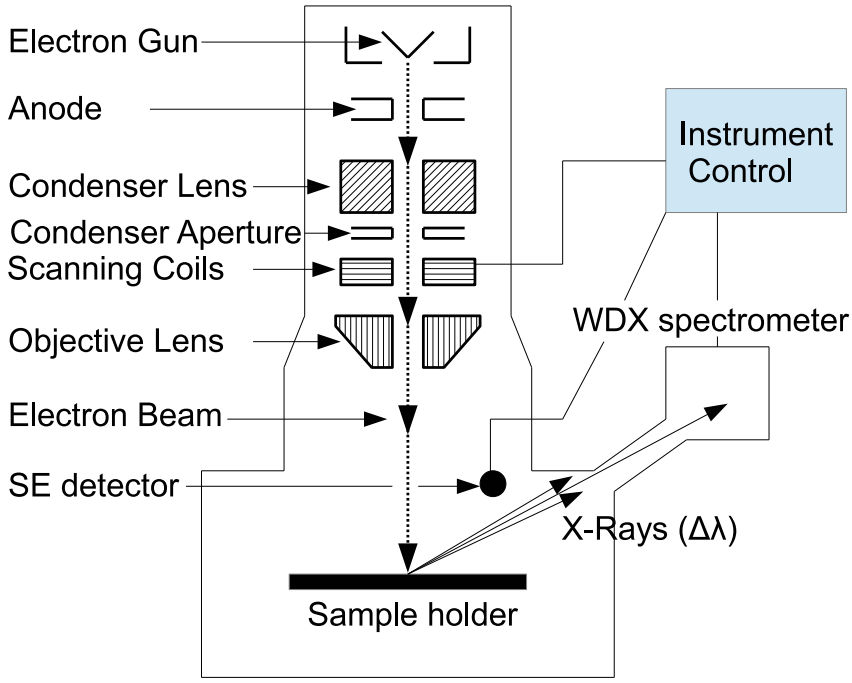

Figure 3.1: Schematic diagram of the main features of an EPMA. Drawn after original from [51]

Electron sources

Two general types of electron sources can be employed in order to generate an electron beam: thermionic electron guns and field emission electron guns.

A thermionic electron gun (shown in Fig. 3.2a) consists of a tungsten wire filament, usually bent into a pin, acting as a cathode. The filament is heated to an elevated temperature ($\geq 2800\,\mathrm{K}$) causing a thermionic emission of electrons from the filament. By holding the filament on a large negative potential (between 200 V and 30 kV) in respect to the anode, the emitted electrons are accelerated towards the anode, generating a beam of high energy electrons. A Wehnelt cap is positioned between the filament and the anode and held at a slightly more negative potential than the filament, which allows better control over the diameter of the area of the filament from which the electrons are emitted. This type of electron gun is employed by the EPMA used in this thesis as the thermionic electron gun can produce higher currents, which is desirable for WDX measurements.

A field emission gun (shown in Fig. 3.2b) consists of a tungsten wire with a sharp tip a few in nm size to which a high electric field is applied from the extraction anode. The electric field applied by the extraction anode reduces the work function for electrons in the tungsten tip. This strongly increases the

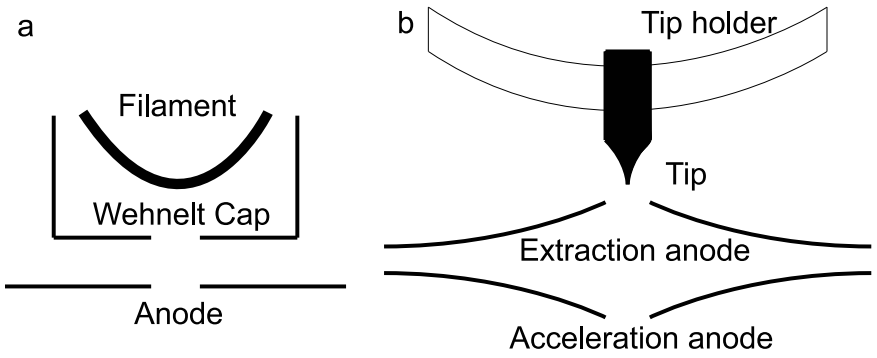

Figure 3.2: Schematic diagram of a thermionic electron gun (a) and a field emission electron gun (b). Drawn after original from [51]

tunnel probability of the electrons, allowing them to leave the tip without being provided the energy needed to overcome the work function. The so generated electrons are then accelerated by the large electric field between the cathode filament and the acceleration anode (between 200 V and 30 kV). The SEM used in this thesis employs a Schottky field emission gun, which is additionally coated with ZrO_2 further reducing the work function. This electron gun can provide a beam diameter on the sample surface as low as 1 nm allowing for high spatial resolution measurements.

The generated beam of high energy electrons is inserted into the beam column, where it is subject to electromagnetic lenses. These lenses demagnify the electron beam from the electron gun crossover diameter to the spot size on the sample (down to 1 nm, depending on the electron source).

Electron-sample interactions

When the electron beam hits the sample the electrons can interact with the sample atoms. The interaction between the electron beam and a sample can be classified in terms of energy lost by two processes; elastic and inelastic scattering. Both processes will be shortly described here, following the description provided by Goodhew et al. [50] Elastic scattering is the deflection of incident beam electrons by sample atoms while the kinetic energy of the incident electron is conserved.This type of scattering occurs as a result of Coulombic interaction between the beam electron and both the nucleus and the electrons surrounding it. This is also known as Rutherford scattering and gives rise to the forward scattered electron signal. The probability p(ϕ) for and electron with energy E_0 to be scattered through an angle ϕ can be described by:

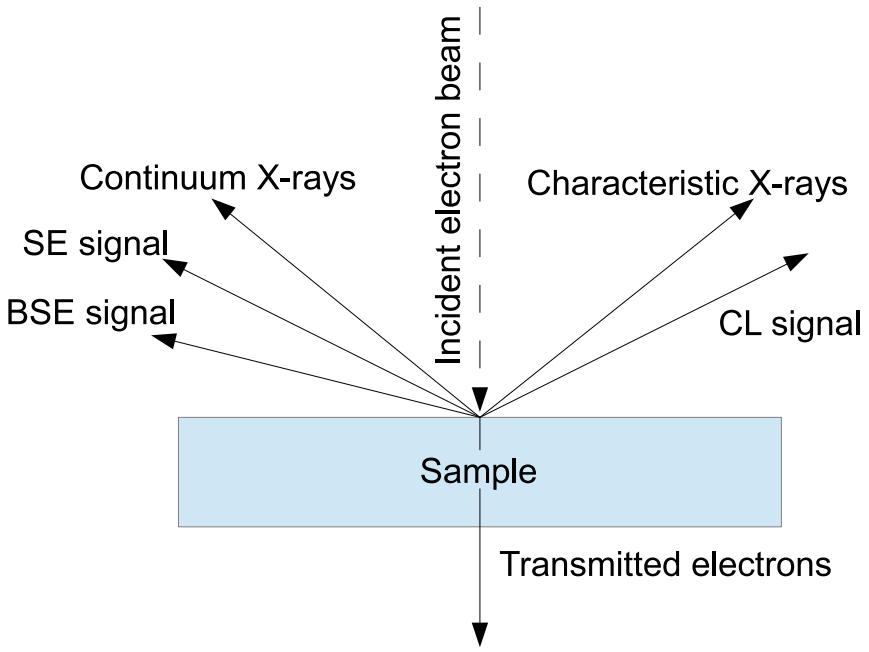

Figure 3.3: Exemplary measurable signals from the electron-sample interactions.

$$p(\phi) \sim \frac{1}{E_0^2 sin^4 \phi} \tag{3.1}$$

From that can be seen that the probability of small angle scattering is much higher than that of a large angle. Furthermore, the scattering probability decreases as the beam electron energy increases. The mean free path for elastic scattering also strongly depends on the atomic number Z of the scattering atoms.

In inelastic scattering processes, electrons lose a measurable part of their kinetic energy. There are many interaction processes which could cause electrons to losse energy and the most probable ones will be briefly discussed. *Phonon scattering* is the process in which beam electrons lose energy by exciting a phonon in the sample material and thus heating it slightly. The amount of energy lost in this process is generally less than 1 eV and the mean free path of high energy beam electrons for this process is quite large ($\sim 1\,\mu$m). *Plasmon scattering* is another inelastic scattering process in which the beam electron excites a plasmon and typically looses between 5 to 30 eV of energy. The mean free path for this effect is rather short (~ 100 nm) and it was found that this effect dominates the energy loss spectrum. *Single valence electron excitation* is a scattering process similar to plasmon scattering, with the difference that instead of transferring the energy to the "sea" of electrons, the energy is transferred to a single valence electron.

The typical energy transferred is about 1 eV and the mean free path of beam electrons to undergo this scattering process is large ($\sim 1\,\mu$m). *inner shell excitation* is another form of elastic scattering, by which the beam electron knocks out an electron from an inner atomic shell. because the binding energies of inner shell electrons is high, the energy loss of the beam electrons in this scattering effect is significant (e.g. 283 eV for a Carbon K electron).

Both processes give rise to various measurable signals, for example secondary electrons (SE) from loosely bound valence band electrons, backscattered electrons (BSE), characteristic X-rays from inner shell electrons and CL, providing valuable information for the characterization of the sample properties (see Fig. 3.3).

3.1.1 The environmental SEM

To prevent samples from charging under the electron beam of the SEM, they are connected to earth. While this is enough for samples with a high electron mobility (metals, certain semiconductors), this is insufficient for samples with a low electron mobility (organic samples, insulators, certain semiconductors). Low mobility samples will charge under the electron beam, which can influence measurements or prevent measurements at all. In order to be able to measure these samples different techniques can be applied.

The most common technique is to coat the surface with a thin conducting layer, usually Au. This allows the surface of the samples to be imaged on a low magnification; for higher magnifications the surface features of the sample might be invisible due to the Au layer or surface features of the Au layer might be visible, indistinguishable from the features of the sample. Furthermore, the coating of the sample surface can reabsorb light generated in the sample, preventing the investigation of the optical properties of the sample in the SEM.

Another technique to measure low mobility samples is to employ an environmental SEM (ESEM). In an ESEM it is possible to release small amounts of gas into the sample chamber, acting as a transport for the accumulated surface charges, thus allowing measurement of low conductivity samples without preparation. Because the inserted gas is effectively lowering the quality of the vacuum an ESEM also employs a pressure-limiting aperture which allows a high vacuum in the beam column and limits the influence of the gas to the specimen chamber, which reduces the electron-gas interaction.

The electrons can interact with the gas in the chamber the same way they interact with the specimen, namely by elastic and inelastic scattering. These effects are not desired as they lead to a broadening of the spot size of the electron

beam and thus a decrease of the spatial resolution of the measurements. The effect of the electron-gas interaction depends on the electron energy and the number of gas atoms in the path between the electron source and the sample. The acceleration energy can seldom be varied in order to reduce the interaction because it also determines the interaction volume and thus the spatial resolution of some of the measurements. The number of gas atoms between the electron source and the sample can be varied by two parameters.

The first is the distance the electrons have to travel through the gas filled atmosphere, by the incorporation of a pressure-limiting aperture which keeps the electron column under high pressure and just the specimen chamber filled with the gas one can reduce the path through the gas from ca. 30 cm to 1 cm.

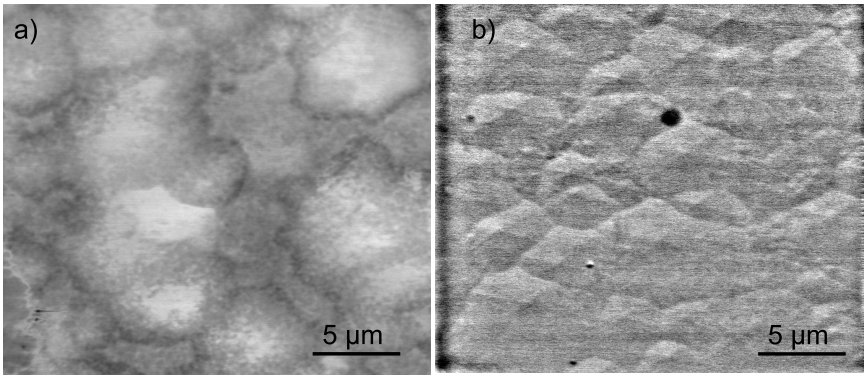

Figure 3.4: SE images of an $Al_xGa_{1-x}N$ same sample in high vacuum a) and low vacuum b) conditions.

Another way is to change the amount of gas released in the specimen chamber. This is limited by the charging of the sample and should always be reduced as much as possible, while still preventing the sample from charging.

The difference in imaging between the low vacuum ESEM mode and the high vacuum mode can be seen in Fig. 3.4. The SE-image a) shows that the spatial resolution of the SEM is strongly reduced, no small features are visible and the larger features are blurred. In the second image b) the spatial resolution was restored, the boundaries of the large features are imaged clearly and small features can be found on the sample surface.

3.2 Cathodoluminescence spectroscopy

Cathodoluminescence is the general term used for the emission of light from a material after irradiation with electrons from an electron source. When an elec-

tron from the electron beam interacts with the sample in the sample chamber, it can generate electron-hole pairs due to inelastic scattering processes. In contrast to photoluminescence where each photon, from the light source (e.g. a laser), can only generate one electron-hole pair, each electron in the electron beam can generate multiple electron-hole pairs while gradually loosing energy. The main advantages of CL spectroscopy compared to photoluminescence spectroscopy (PL) or electroluminescence (EL) spectroscopy are the high spatial resolution, the wide range of excitation energy and the possibility to perform depth resolved measurements. All of this is crucial in underpinning the optimization of wide band gap semiconductor structures.

3.2.1 Electron-hole recombination processes

To understand which kind of information about a semiconductor can be obtained from CL measurements, one has to take a closer look at the recombination processes in a direct band gap semiconductor. The basic recombination processes are shown in Fig. 3.5.

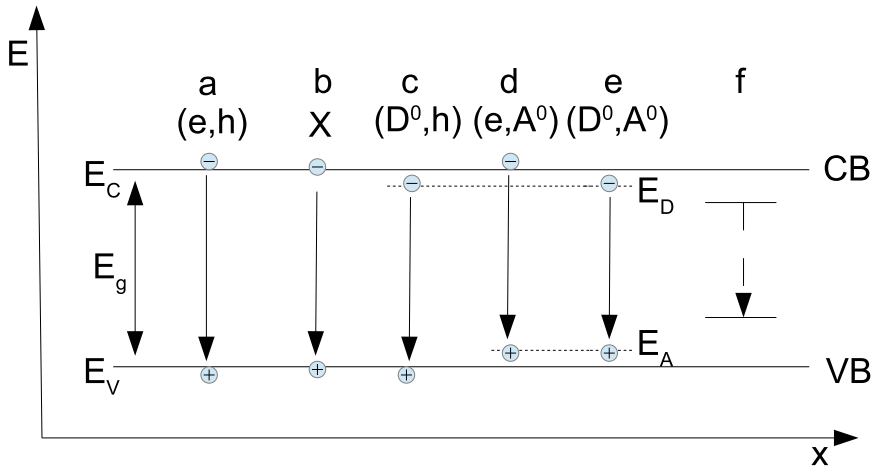

Figure 3.5: Recombination processes in a semiconductor. With E_C the conduction band energy level; E_V the valence band energy level and E_g the band gap ($E_C - E_V$); E_D and E_A the donator and acceptor energy level respectively. a) shows an electron-hole recombination; b) the recombination process of a free exciton; c) the recombination between a donator bound electron and a hole in the valence band; d) the recombination of an electron in the conduction band with an acceptor bound hole; e) the recombination between a donator bound electron and an acceptor bound hole; f) the non-radiative recombination via defect states in the band gap. Redrawn after original from [52]

In semiconductors and insulators the filled valence band and the empty con-

duction band are separated by an energy gap $E_g = E_C - E_V$. Electrons can be excited, by inelastic scattering processes, from the valence band into the conduction band. Electrons which are excited above the conduction band minimum will lose excess energy by non-radiative phonon and electron excitations. From the bottom of the conduction band electrons can recombine with holes in the valence band by different radiative and non-radiative mechanisms.

One of these mechanisms is the direct electron-hole recombination as shown in Fig. 3.5a . In this recombination process a photon with an energy $E_{ph} = E_g = hf$ will be emitted. This emission process is influenced by temperature variations: higher temperatures affects the line width of the emission due to the occupation of higher states in the conduction and valence band as well as a decreasing band gap energy due to increasing inter-atomic spacing, as described by the Varshni expression [53]:

$$E_g(T) = E_g(0) - \frac{\alpha T^2}{T + \beta} \tag{3.2}$$

with E_g the band gap energy, $E_g(0)$ the band gap energy at 0 K, T the temperature and α,β constants. If these influences are taken into account one can derive a variety of information from measuring the band gap energy. For GaN, InN and AlN the strength of electric fields in the grown layer may be estimated. For ternary semiconductors like $Al_xGa_{1-x}N$ the composition of the layer can be calculated if the strain state is known.

At low temperatures, before recombination, electrons and holes can form electron-hole pairs called excitons. This reduces the emission energy of the radiative recombination by the exciton binding energy, which is in the range of 5 meV up to 50 meV [54], depending on the effective mass of the particles and the dielectric constant (Fig. 3.5b).

Radiative emission of trapped electrons and holes at donor(e,A°) or acceptor(D°,h) states in the conduction band is called extrinsic emission (Fig. 3.5c and d). These donor and acceptor states can result from the intentional and unintentional incorporation of extrinsic atoms. The emission energy observed from these lines is reduced compared to the band gap energy, by the activation energy of the respective donor or acceptor, $\Delta E = E_g - E_a$. At certain doping concentrations radiative recombination between neutral donors and acceptors become identifiable (Fig. 3.5e). This process is called donor acceptor pair recombination (DAP) and it can lead to a series of emission lines emerging and possibly merging into a broad band, due to Coulomb interaction between ionized donors and acceptors [52].

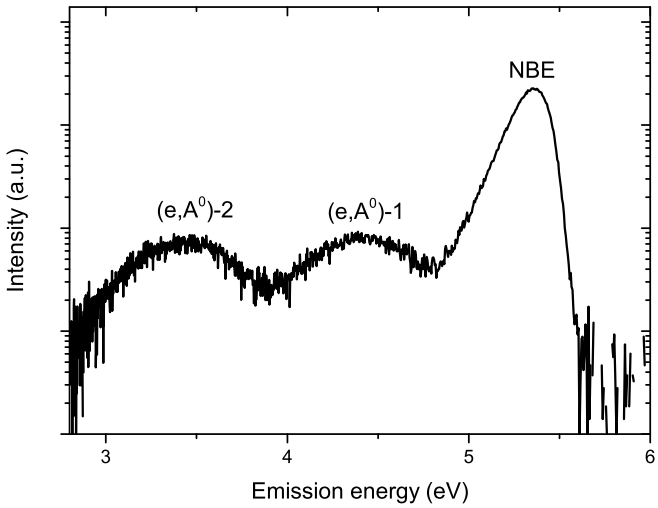

Figure 3.6: Example CL spectra of a Si doped $Al_{0.82}Ga_{0.18}N$ layer. The near band edge (NBE) emission and two extrinsic emission peaks can be distinguished.

Localized transition levels in the band gap can be caused by point or extended defects. Point defects can be vacancies, interstitials or extrinsic atoms while dislocations are the most prominent extended defects (see section 2.2.2). These localized transition levels behave as non-radiative recombination centres, where electrons and holes can recombine by releasing a cascade of phonons. These defect centres can be identified in CL measurements by a strongly reduced luminescence intensity and can provide information about the defect concentration and distribution.

A CL example spectra, of a Si doped $Al_{0.82}Ga_{0.18}N$ layer, in which three different peaks can be distinguished, is shown in Fig. 3.6. The near band edge (NBE) peaks arises due to recombination from the conduction band to the valence band of the $Al_{0.82}Ga_{0.18}N$ layer. The other two peaks arise due to the recombination from an electron in the conduction band with a hole in two different acceptor states in the sample.

3.2.2 Cathodoluminescence setup

In order to measure the generated light a CL-detection system needs a highly efficient system to collect and transmit the light and a detector in order to measure the intensity of the CL signal. The specific requirements for the setup of the CL system depend on which kind of CL measurement is desired to be performed. The three basic CL measurements are panchromatic CL, monochromatic CL and

hyperspectral CL.

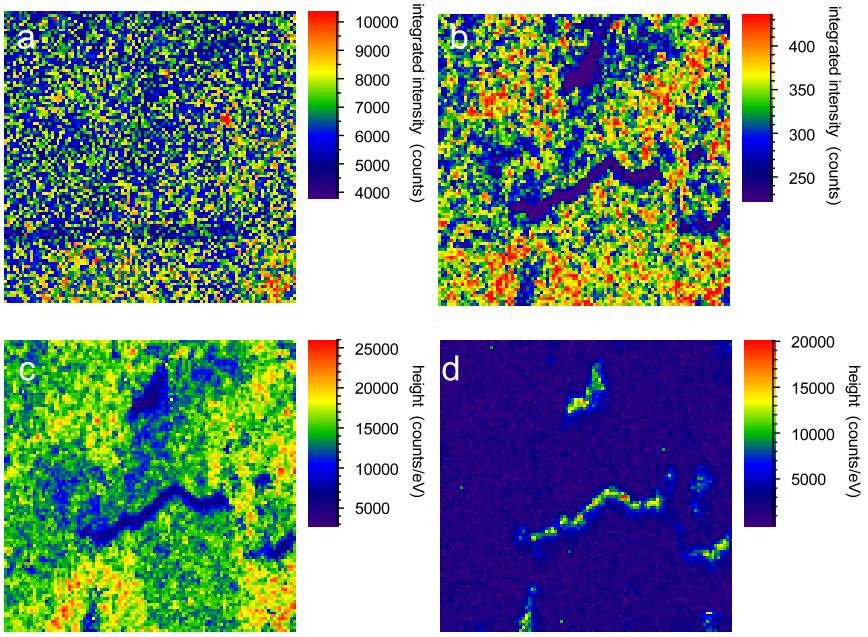

Figure 3.7: Comparison of the same area, imaged with different CL techniques. Image a) shows panchromatic CL; b) Monochromatic CL, c) and d) intensity maps extracted from a hyperspectral CL map.

Panchromatic CL is the most basic of CL measurements. The photons generated by the electron beam are being collected and focused onto a detector which gives a signal proportional to the photon flux. This setup is capable of measuring the intensity over the whole spectrum which allows the user to identify areas of non-radiative recombination. However, as panchromatic CL only measures the intensity, the whole spectral information of the emitted light is lost.

The second widespread CL technique is *monochromatic CL*. In this setup the collected light is passed through a monochromator, producing a measurement of the intensity in only a small spectral range, losing all intensity variation of the rest of the spectrum in the process. This technique allows the analysis of different peaks in the CL spectrum and their spatial intensity variation. Small variations in the emission behaviour of each single peak are lost in this measurement due to the predefined investigated wavelength.

Utilizing the scanning capabilities of an SEM both of these measurement techniques are capable of producing CL maps, three dimensional data arrays containing the intensity information of the whole spectra or just one wavelength over the mapped area.

The third measurement technique is *CL hyperspectral imaging*, which was the

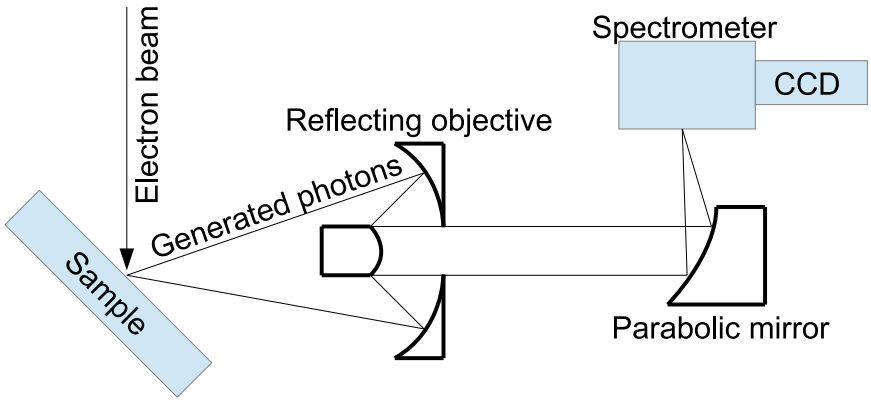

Figure 3.8: Schematic of the used CL setup. Generated photons are collected by the reflecting objective. The collected photons are transmitted and focused onto the entrance slit of the spectrometer by a reflecting mirror. In the spectrometer the wavelength dispersive element disperses the photons onto the different channels of the CCD, where they are collected.

main setup used to acquire the CL data shown in this thesis. CL hyperspectral imaging is the logical advancement of pan- and monochromatic CL. By using a wavelength dispersive element in the optical path of the generated light and a CCD detector it is possible to measure the intensity of each wavelength (limited by the spectral resolution of the setup) while retaining the spectral information of the emitted light. Thus allowing for example, to determine whether a defect only affects certain emission wavelengths or all, or to monitor the spectral behaviour of a single peak; e.g. measuring whether it blue or red shifts.

In Fig. 3.7 a comparison of the different measurement techniques on the same sample area is shown. Image a) shows a panchromatic CL intensity map, no features can be seen. Image b) shows a monochromatic CL map, features with a strongly reduced intensity can be found. Images c) and d) show two maps at different wavelength extracted from a CL hyperspectral image, it can be seen that the feature that is dark in image c) shows up as a bright feature in image d) indicating a local composition variation at the feature.

The setup of the CL system used in this thesis to acquire CL hyperspectral images is schematically shown in Fig. 3.8 and the working principle of CL hyperspectral imaging in Fig. 3.9.

3.2.3 Data treatment

As CL hyperspectral imaging creates a multidimensional data array a treatment of the data is necessary in order to obtain 3D information for further processing. For

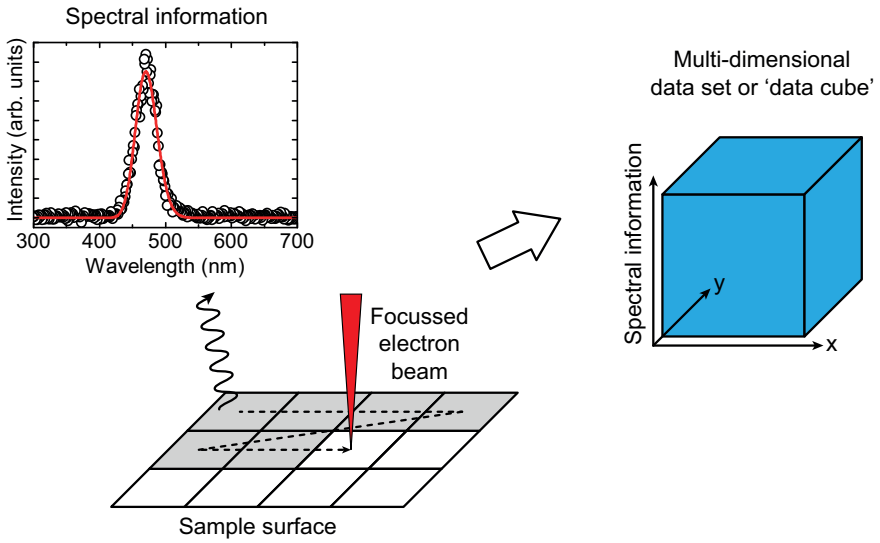

Figure 3.9: The principle for the hyperspectral CL mapping. The focused electron beam rasters the surface, while at each measurement spot a full spectrum is recorded. The spectral information together with the spatial information creates a multidimensional data set. *With permission of Paul R. Edwards*

this data treatment the analysis software: Cathodoluminescence Hyperspectral Imaging and Manipulation Program (CHIMP) developed by Dr. Paul R. Edwards is used. This software allows the mathematical treatment of the collected data by fitting a curve defined by user specified parameters (intensity range, peak position range, FWHM range, peak type) to the data. Another analysis tool provided by the software is the principal component analysis (PCA). PCA finds the main contributing factors of a data set (the principal components) and allows to re-plot the data set as a function of these components. This effectively reduces the dataset containing some thousand entries to a few components which can then be more easily analysed. PCA is especially useful for treating datasets with a low signal to noise ratio. Important to note is, that the original data set can be recalculated by a linear combination of all principal components. Additionally, some of the "spectra" obtained for a principal component can have negative intensity values at areas where another component has a high positive value, due to an adjustment of each data point for the mean.

3.2.4 Spatial resolution of Cathodoluminescence

The high spatial resolution of CL spectroscopy is one of its main advantages compared to other spectroscopy techniques such as PL and EL, allowing the study of the luminescence properties of a semiconductor on a nano-meter scale.

The spatial resolution of the CL signal depends on three parameters: I) the beam diameter, II) the interaction volume in which photons are generated and III) the diffusion length of minority carriers. The beam diameter is in the range of 1-10 nm and only a limiting factor for the spatial resolution when very low acceleration energies are used. The dimensions of the interaction volume strongly depend on the penetration depth of the electron beam, ranging from a few nanometer up to 2 μm. Utilizing the Monte Carlo Casino software [55] the interaction volume can be inferred.

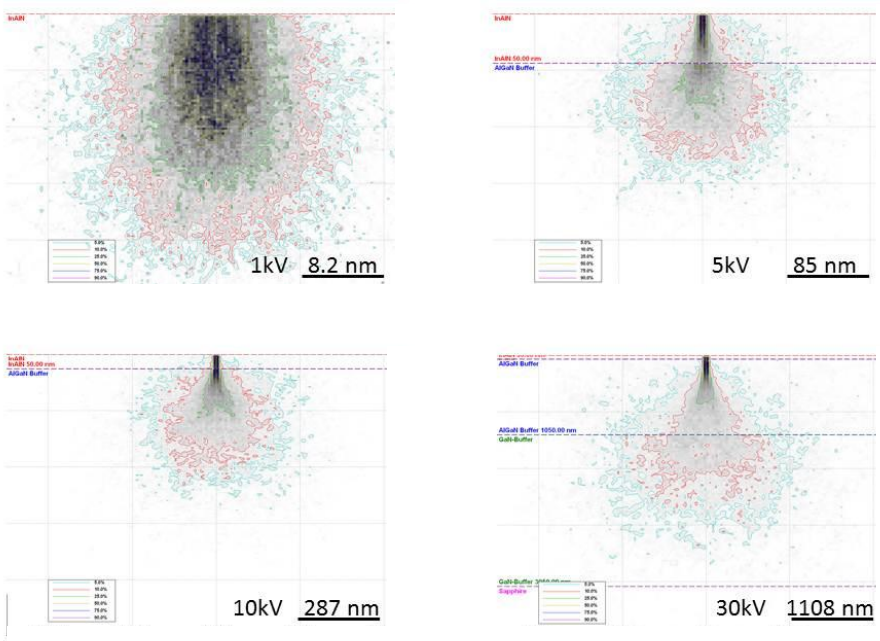

Figure 3.10: Monte Carlo simulation of the energy distribution by position for different electron energies with a spot size of 10 nm. For higher energies the typical light bulb shape of the energy distribution is visible. The simulation was performed with the Monte Carlo Casino software [55].

The Monte Carlo calculation shown in Fig. 3.10 depicts the predicted interaction volume in a semiconductor structure of 50 nm $In_{0.15}Al_{0.75}N$ on top of 1 μm $Al_{0.5}Ga_{0.5}N$ on top of 1 μm GaN on a sapphire substrate. It can be seen that the interaction volume strongly increases with increasing beam energy, from a few nm at a beam energy of 1 keV to more than 2 µm for a beam energy of 30 keV, decreasing the spatial resolution of the CL measurement.

The diffusion length of minority carriers depends on sample parameters like doping concentration and defect density and can not be externally controlled [56].

3.2.5 Depth resolved Cathodoluminescence

Another advantages of CL measurements, compared to photoluminescence (PL) or electroluminescence (EL), is the potential to perform non destructive depth resolved studies of the luminescence properties of a semiconductor. This is especially an advantage in studying devices structures where often underlying layers exert a strong influence on the properties of later grown layers. Excitation and study of these layers can be crucial in underpinning the optimization of device structures, a task CL is very well suited to.

For depth resolved studies the penetration depth of the primary electrons provided by the SEM electron source has to be controlled. The penetration depth of the primary electrons (r) depends on inelastic scattering processes and can be approximated by [57]:

$$r(\mu m) = \frac{2.76 \cdot 10^{-2} A}{\rho Z^{0.89}} E^{\alpha} \tag{3.3}$$

With A being the atomic mass, ρ the density, Z the atomic number, α a value from 1.67 to 1.75 and E the energy of electrons. From this expression it can be seen that the information depth of CL measurements depends on the acceleration energy. To get a better idea of the sampling depth, Monte Carlo calculations are performed. The employed program (CASINO) is documented in reference [55]. In Fig. 3.11 the results for Monte Carlo calculations of the CL intensity for different acceleration energies are shown. Demonstrating the different depth from which the CL signal can be acquired by varying the acceleration energy of the primary beam electrons. For example for an acceleration energy of 5 keV one can only expect to sample the luminescence properties of the first ∼200 nm of the $Al_{0.5}Ga_{0.5}N$ layer, while for an acceleration energy of 30 kV the full 1500 nm of the layer are being sampled as well as parts of the underlying substrate (Al_2O_3).

Results for Monte Carlo calculations of the CL intensity for different acceleration energies are shown in Fig. 3.11.

Depth resolved CL studies are especially suitable to investigate hetero-structures, to characterize variations in the emission energy of the different layers which will provide information about possible compositional inhomogeneities. Studies of the intensity distribution of buried layers or in homo-structures require that re-absorption effects are taken into account as these can strongly influence the intensity and shape of an observed luminescence peak. Re-absorption is a process in which a photon generated at a certain depth is getting re-absorbed by the material, which can potentially change the shape of luminescence peaks. It

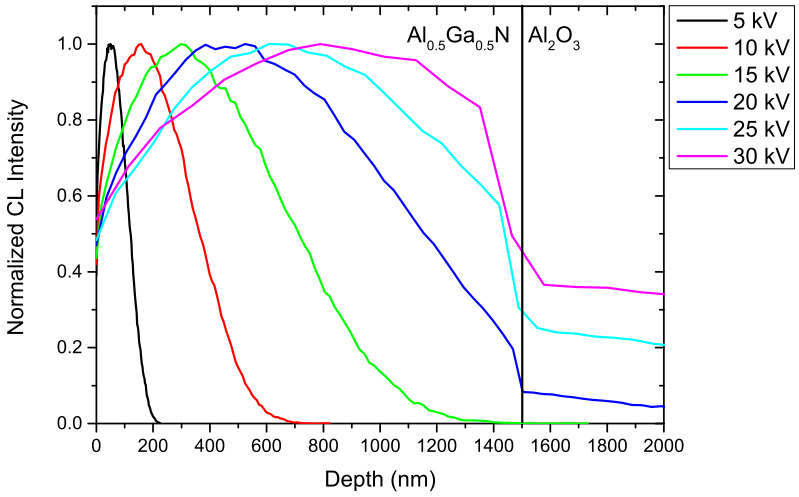

Figure 3.11: Depth dependent CL intensity distribution for an 1.5 µm thick $Al_{0.5}Ga_{0.5}N$ layer on top of an Al_2O_3 substrate. The calculation was performed with the Monte Carlo Casino software [55].

is obvious that in a heterostructure in which a low bandgap material A is on top of a high bandgap material B the photons generated in material B can be reabsorbed by material A, artificially increasing the intensity of material A and potentially reducing the intensity of material B to zero.

This effect can also occur in a thick homo-epitaxial layer. It was found by Knobloch et al. [58] that with increasing probing depth the line shape of the GaN NBE peak strongly changed as can be seen in Fig. 3.12.

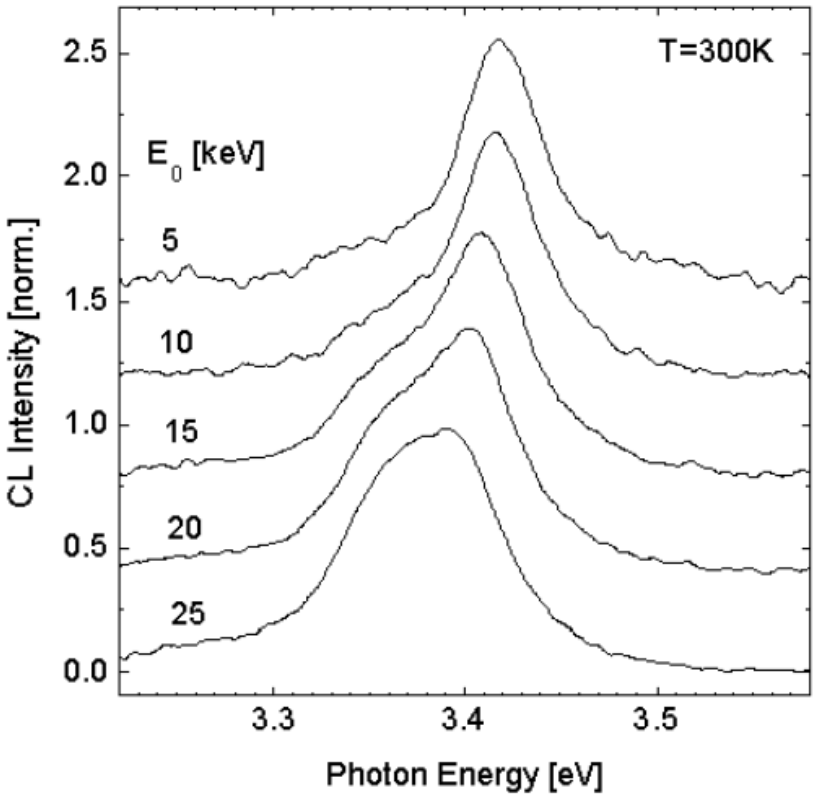

Figure 3.12: Change in the line shape of the GaN NBE peak with increasing measurement depth. Taken from Knobloch et al. [58]

3.3 Wavelength dispersive X-ray spectroscopy

When the beam electron interact with a sample, they can generate X-rays. The emitted X-rays can be divided into two classes, a) characteristic X-rays, related to the sample elements and b) continuous Bremsstrahlung produced by electrons decelerating in the sample. The characteristic X-rays can be identified by their energy or wavelength forming the basis of the two most common detectors found in an EPMA, the wavelength dispersive X-Ray (WDX) spectrometer and the energy dispersive X-ray (EDX) spectrometer. The EPMA used for measurements presented in this thesis utilised a WDX system, consisting of three WDX spectrometers, which will be explained in more detail.

3.3.1 Generation of X-rays

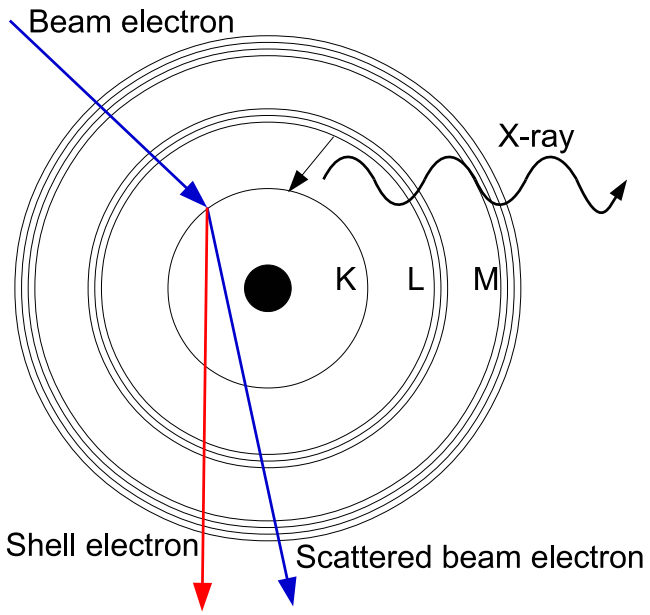

Figure 3.13: Schematic of the generation of characteristic X-rays. A beam electron knocks out an electron from the K shell of the atom, an electron from the L shell relaxes onto the vacant space, emitting an X-ray in the process. Redrawn after original from [50]

Characteristic X-rays can be generated by impact ionisation, causing a beam's electron to knock out an electron from an inner shell of the sample atom. The vacant space left by the electron will be filled by an electron recombining from one of the outer shells onto the hole state in the inner shell, emitting the excess energy as an characteristic X-ray. This process is schematically shown in Fig. 3.13. The characteristic X-rays are named after the shell the electron recombines

to, e.g. a K_α X-ray is an X-ray generated by an electron recombining onto the K shell and a L_α X-ray is an X-ray generated by electrons recombining to the L shell.

3.3.2 WDX setup

When electrons interact with a sample, generating X-rays, a narrow cone of X-rays is detected by the WDX spectrometer. The spectrometer consists of a diffraction crystal, which can be set to specific angles, in order to let through only those X-rays which fulfil the Bragg equation:

$$n\lambda = 2d\sin\theta \tag{3.4}$$

with d the lattice spacing of the diffraction crystal, θ the angle of incidence, λ the X-ray wavelength and n an integer. The diffraction crystal can be rotated, in order to maximize the intensity of the incident X-ray beam as well as to scan through a large area of angles, detecting all possible characteristic X-rays. This setup allows to calculate the wavelength λ of the incident characteristic X-rays which can be used to determine which elements are found the investigated sample. A schematic of the collection mechanism is shown in Fig. 3.14.

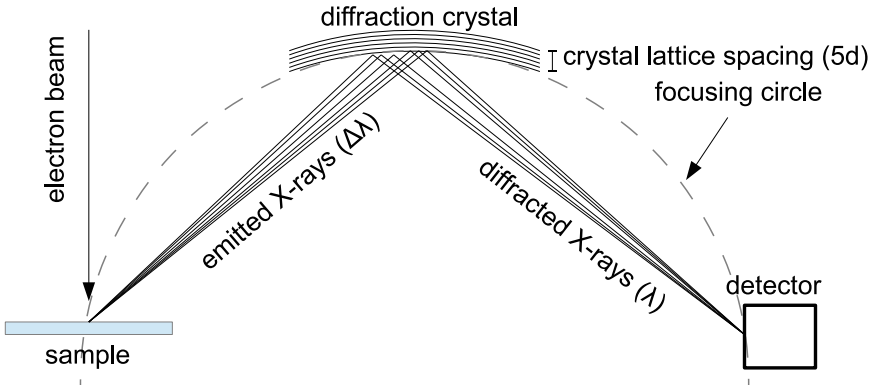

Figure 3.14: Collection of X-rays by the WDX spectrometer. The X-ray spectrum emitted from the sample consists of a range of wavelengths ($\Delta\lambda$) but only those fulfilling the Bragg condition at the crystal (λ) are being diffracted to the detector. Redrawn after original by [51]

The range of characteristic wavelengths that can be found in this way, depends on the lattice spacing of the detector as well as the possible angles it can reach. This limited detection range necessitates that a range of crystals is available in the WDX spectrometer in order to be capable of detecting all desired elements.

An overview of the diffraction crystals used in the employed EPMA is given in table 3.1.

Crystal	lattice spacing d [nm]	K-lines	L-lines	M-lines
LiF	0.4207	21 – 37	52 – >90	
PET	0.8742	14 – 25	38 – 65	73 – >90
TAP	2.576	9 – 15	25 – 41	57 – 80
PC0	4.5	7 – 11		
PC1	6	6 – 9		
PC2	10	5 – 8		
PC3	20	4 – 5		

Table 3.1: Lattice spacing and element numbers of the detectable X-rays of the different employed diffraction crystals. Taken from the Cameca manual.

The spatial resolution of the WDX analysis is governed by the interaction volume of the incident electron beam in the sample material and does thus depend on the energy of the electron beam and the material density of the investigated sample. Details on how the interaction volume changes with the energy of the electron beam has been given earlier in this chapter. It has to be noted here, that the beam energy can not be chosen randomly but must always be above the minimum energy necessary to excite X-rays from the elements to be investigated. An overview of the minimum energies needed to excite X-rays for elements typically investigated in the group-III nitride system can be found in table 3.2.

Element	Minimum energy [keV]
Ga	L_α 1.098
Al	K_α 1.486
N	K_α 0.392
In	L_α 3.286
Si	K_α 1.739
O	K_α 0.525
C	K_α 0.277
Mg	K_α 1.253

Table 3.2: Minimum needed energy for the generation of X-rays of an specific X-ray line, for elements typically investigated in the group-III nitrides. Values obtained from the IMIX software manual.

Quantitative WDX analysis

Quantitative element analysis of a sample requires that the X-ray intensities for each element are converted into weight percent. This can be achieved by comparing the intensity of a measured element (I_A) with the intensity measured for a standard (I_{A^*}) containing a known amount of that element, which can either be a pure sample or a well characterised compound. The weight fraction can than be calculated using an approximate proportional relationship between the intensity ratio and the weight fraction (C_A) for an element A using the following equality:

$$\frac{I_A}{I_{A^*}} = (ZAF)C_A \tag{3.5}$$

with Z the atomic number, A the absorption correction and F the fluorescence correction.

Chapter 4

Analysis of AlGaN layers

4.1 Introduction

In this chapter the optical and structural properties of wide bandgap $Al_xGa_{1-x}N$ layers are investigated. Wide bandgap $Al_xGa_{1-x}N$ layers are used as buffer layers on top of which the active region of UV-LEDs is grown and can therefore have a strong influence on the performance of the resulting devices [59, 60]. Thus, understanding and controlling the growth of $Al_xGa_{1-x}N$ is one of the key challenges for the successful growth of UV LEDs.

The morphology, defect density and the doping concentration of wide bandgap $Al_xGa_{1-x}N$ buffer layers are parameters which significantly influence the quality of an LED. The morphology of $Al_xGa_{1-x}N$ layers can lead to compositional inhomogeneities [61], broadening the emission peak of the active region, while most of the defects present in the $Al_xGa_{1-x}N$ layer will propagate into the active region where they will promote non-radiative recombination of carriers, leading to a reduction of the internal quantum efficiency of the active region [24, 25]. In terms of doping, the n- and p-type carrier concentrations in the $Al_xGa_{1-x}N$ layer will directly influence the injection efficiency and thus have a strong influence on the output power of the grown device.

Despite the importance of the $Al_xGa_{1-x}N$ layers, the growth and application of such structures has not been fully explored, and remains one of the key challenges in the III-nitride material system. This is due to the complicated growth mechanics which can potentially lead to phase separation and compositional inhomogeneity [62, 63, 64]. Minimization of these effects in the active region requires the growth of $Al_xGa_{1-x}N$ buffer layers with high crystalline quality.

The structure of this chapter follows the study of the above mentioned effects. In the next section the influence of the substrate miscut on the optical and mor-

phological properties of $Al_xGa_{1-x}N$ buffer layers is investigated with the optimization of its crystalline quality and the reduction of compositional inhomogeneity as its goal. We then examine the influence of the $Al_xGa_{1-x}N$ layer thickness on the quality of $Al_xGa_{1-x}N$ layers. In the last part of the chapter Si-doping and its effect on the morphology and luminescence properties of $Al_xGa_{1-x}N$ layers is studied.

4.2 Influence of miscut angle on AlGaN layers

The miscut angle describes the deviation of the substrate orientation from a specific crystallographic orientation as shown in Fig. 4.1.

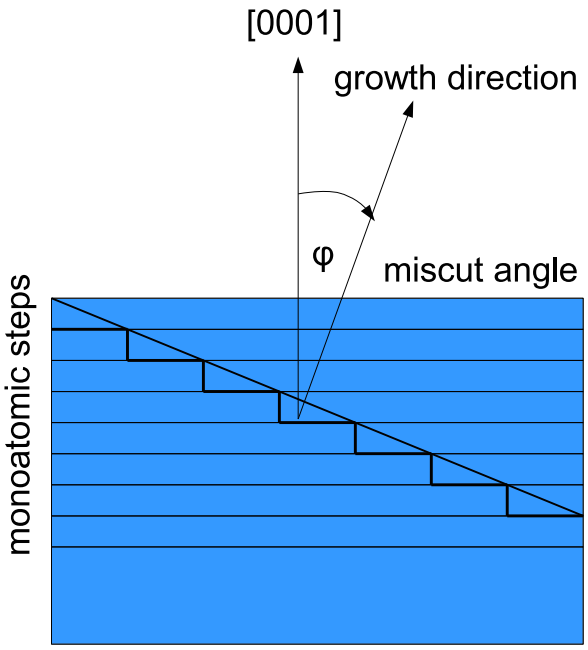

Figure 4.1: Schematic representation of the substrate miscut, after Perlin et al. [65]

The morphology of a substrate with a miscut angle greater than (smaller than) 0° consist of an array of mono-atomic steps, where the step width decreases with increasing miscut angle. The step width and direction significantly influences the growth conditions of semiconductors as shown by Kueller et. al. [66] and Someya et. al. [67]. For example Kueller et. al. [66] showed that a change of the miscut direction from 0.25° towards m-plane to 0.25 ° towards a-plane strongly influences the coalescence of ELO grown AlN and Someya et. al. [67] found that

a miscut angle of 0.25° towards $[10\bar{1}0]$ resulted in the smoothest morphology for the growth of GaN layers on a-plane sapphire substrates. In order to investigate the influence of the miscut angle on the optical and morphological properties of $Al_{0.47}Ga_{0.53}N$ layers, two samples of different miscut were studied.

Both samples were grown under the same growth conditions at the Tyndall National Institute, on *c*-plane sapphire substrates with a miscut of 0.1° (sample A) and 0.4° (sample B) towards the *m*-plane, using an Aixtron close-coupled shower-head 3×2" metal-organic vapour phase reactor. Trimethylgallium (TMGa), trimethylaluminium (TMAl) and ammonia (NH_3) were used as precursors, while the carrier gas was hydrogen (H_2). The samples consist of a 1 µm AlN layer grown on the sapphire substrate, followed by a 1 µm GaN layer and 2-period insertion layers of high temperature (HT)-GaN (10 nm) and low temperature (LT)-AlN (1 nm). On top of this structure 2 µm of nominally undoped $Al_{0.47}Ga_{0.53}N$ was deposited.

High resolution X-ray diffraction (HR-XRD) scans were performed at Tyndall to determine the composition and showed an AlN content of approximately 47% for both samples. Reciprocal space maps indicate that the $Al_xGa_{1-x}N$ layer in both samples is fully relaxed. In order to investigate the surface morphology SE-imaging in low vacuum mode and atomic force microscopy (AFM) in tapping mode were used. Low vacuum mode was necessary due to charging effects preventing a clear image to be obtained in high vacuum mode.

AFM measurements performed in the Tyndall National Institute by the group of Prof. P. J. Parbrook over 10×10 μm^2 areas (Fig.4.2) show distinctive differences between the two samples. Sample A with a miscut of 0.1° shows the formation of different hillocks with an RMS roughness of 4 nm while sample B (0.4° miscut) shows step bunches with a height of 5 nm and an RMS roughness of 5.3 nm in addition to the hillocks.

Step bunches are known to be generated during growth on miscut substrates where the miscut of the substrate results in the formation of a considerable number of mono-atomic steps. Step bunches are surfaces features which consist of surface steps of multiple atomic layers height. The development of a morphology from mono-atomic steps to step bunches can be driven by a number of factors, including the relief of stress from the as grown material, the presence of an Ehrlich-Schwoebel barrier and surface electro-migration [68, 69, 70]. During the *c*-plane growth of III-nitrides these step edges are non *c*-plane facets which can locally influence the material quality by offering semi and non-polar surfaces.

In order to investigate the surface morphology on a larger scale and probe

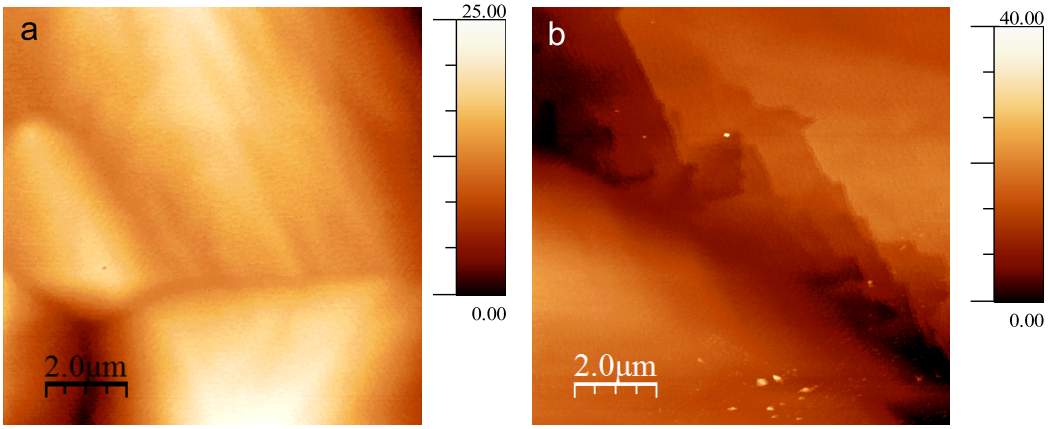

Figure 4.2: AFM images of sample A (a) with a miscut of 0.1° and B (b) with a miscut of 0.4°. The morphology of sample A shows hillocks seperated by valleys, while the morphology of sample B shows step bunching.

the luminescence properties of the $Al_xGa_{1-x}N$ layer, CL hyperspectral imaging was conducted in the ESEM with the setup described in section 3.2.2. The measurements were performed at room temperature with an acceleration voltage of 5 kV and a beam current of 2.9 nA. At this acceleration voltage 90% of the beam energy is deposited within a depth of approximately 90 nm according to Monte Carlo simulations using CASINO software [55] (see Section 3.2.5). A beam energy of 5 keV was chosen as it provides a good compromise between spatial resolution and CL signal. Gaussian functions were fitted to the generated data set (see section 3.2.3) to extract information about the emission energy as well as the intensity of each of the peaks. The measurements were performed at a chamber pressure of 0.1–0.3 mbar which effectively reduced the charging effects observed at high vacuum.

SE-imaging of sample A (shown in Fig. 4.3a) in the ESEM reveals a crack-free morphology consisting of several areas with a different size and shape distribution, separated by valleys. This is consistent with measurements performed by AFM (Fig. 4.2a). Figure 4.3b shows the mean emission spectrum over the measured area. Figure 4.3c and 4.3d show the $10 \times 10\,\mu m^2$ maps of the fitted CL peak energy and intensity of the $Al_xGa_{1-x}N$ near band edge (NBE) peak respectively, which were acquired from the centre of the SE-image in Fig. 4.3a.

The CL energy map reveals domains between which there are notable shifts in the $Al_xGa_{1-x}N$ NBE emission energy. For example, the energy map in Fig. 4.3b shows different regions with CL peaks centred at various values staying between 4.53 eV and 4.58 eV. Within each domain the peak energy remains fairly

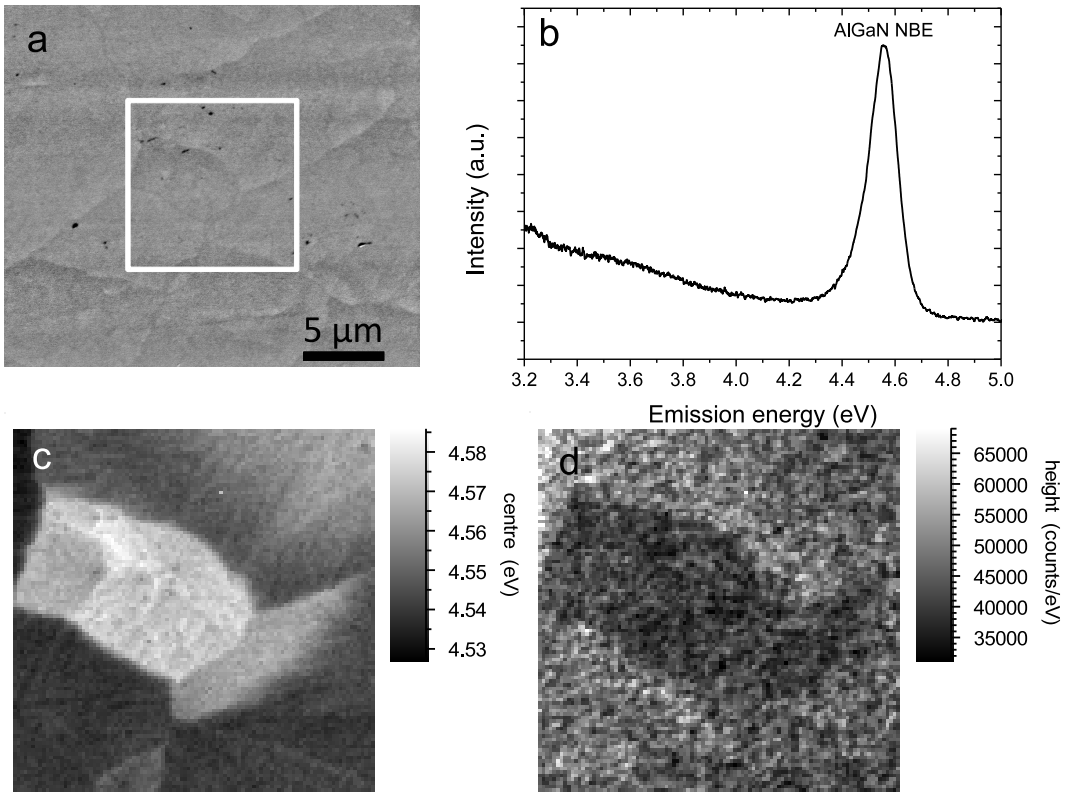

Figure 4.3: SE-image (a) and mean room temperature spectrum over the mapped area (b) as well as fitted $10 \times 10\,\mu m^2$ CL-maps of the NBE peak energy (c) and intensity (d) of sample A. The CL hyperspectral image was acquired in the boxed area in the SE-image.

constant. Comparing this with the CL intensity map in Fig. 4.3d, we can observe a clear correlation between the intensity distribution and the emission energy. The intensity is highest for low emission energies and decreases with increasing energy. The variation in the emission energy could be caused by various effects.

One phenomenon which could be causing both the observed morphology and luminescence is a compositional pulling effect. This effect causes a gradual compositional variation in the epitaxial layer due to compressive biaxial strain generated by the lattice mismatch between buffer and the overgrown layer [71, 72] which can lead to lateral compositional variations. Another effect might be the growth of $Al_xGa_{1-x}N$ micro-crystallites with slightly different orientations and composition [73]. Furthermore, the large difference in the mobility of Ga and Al atoms [74] during the growth can lead to the nucleation of islands during the initial growth stage. Due to their higher mobility Ga atoms contribute more to the growth of the islands while Al atoms are incorporated more randomly. The effect of this initial behaviour lessens with subsequent growth but can still produce a significant $Al_xGa_{1-x}N$ compositional inhomogeneity [75]. The observed behaviour could also be explained by spiral growth, driven by threading dislocations with a screw component, where the energy shift between the domains would be explained by a different Ga incorporation due to different step densities [25].

The first two effects are unlikely for our sample series as XRD measurements do not show any signs of micro-crystallites and also show that the layer is fully relaxed. Thus spiral growth is suggested as the most likely cause, but further measurements which allow the direct measurement of dislocation type and location, like electron channelling contrast imaging (ECCI), have to be performed for confirmation. If the effect is caused by a change in the composition alone it would correspond to a decrease in the AlN content by about 2%.

The SE-images of the second sample (sample B) in Fig. 4.5a and Fig. 4.6a reflect the topography in the corresponding AFM measurement in Fig. 4.2b. The surface is smooth apart from large steps. The steps direction follows an underlying association with the miscut orientation while the step length varies greatly. The steps are, as discussed earlier , formed during growth by step bunching.

CL hyperspectral imaging of a $10 \times 10\,\mu m^2$ area in the centre of the SE-images reveals two $Al_xGa_{1-x}N$ NBE peaks at 4.41 eV and 4.54 eV (see Fig. 4.4) whose distribution strongly depends on the morphology. The intensity of the 4.54 eV peak (black line in Fig. 4.4 and map in Fig. 4.5b) is mostly constant over the measured area with a large drop in intensity along the step edges seen in the SE-image, while there is only a small variation of the emission energy over the

scanned area (not shown).

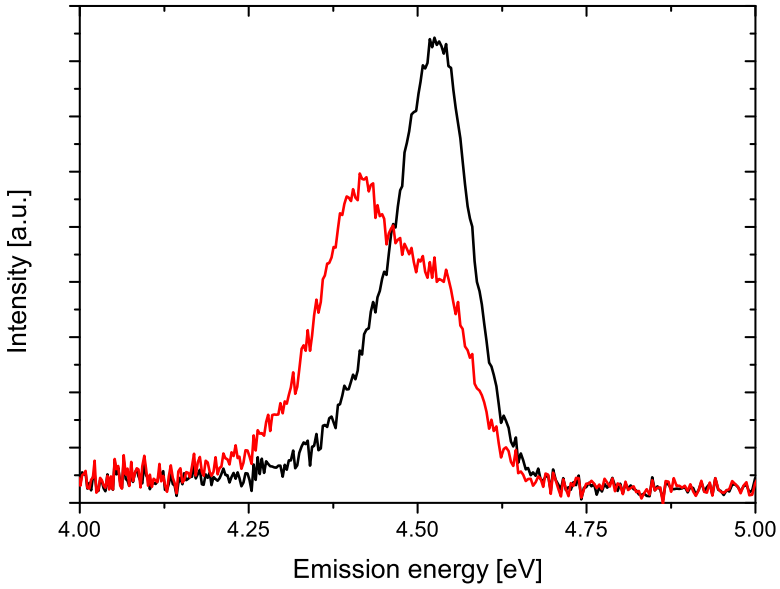

Figure 4.4: Room temperature CL spectra of sample B acquired in an area without step bunches (black) and centred on a step bunch (red).

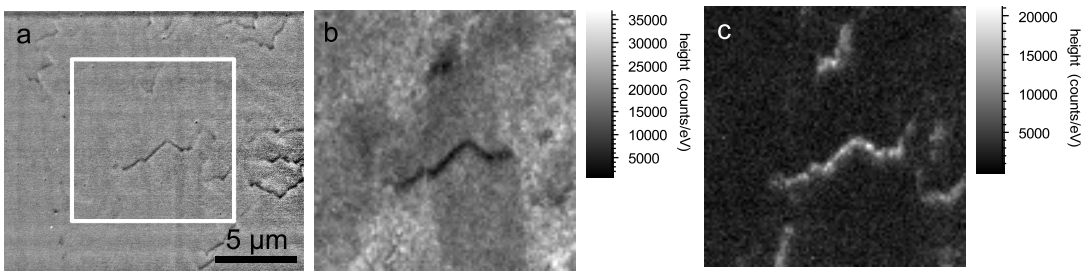

Figure 4.5: SE-image (a) and fitted $10 \times 10\,\mu m^2$ room temperature CL intensity maps of the 4.54 eV peak (b) and the 4.41 eV peak (c) of sample B. The CL hyperspectral image was acquired in the boxed area in the SE-image.

The 4.41 eV luminescence Fig. 4.5c is highly localized and occurs along the step edge. This observation is strengthened by the CL hyperspectral images taken at a higher magnification from a different area (Fig. 4.6) in which the intensity of the lower energy peak (Fig. 4.6c) perfectly matches the step edge imaged in the SE-image. This indicates that along step edges the growth conditions of $Al_xGa_{1-x}N$ are different than on the otherwise smooth sample surface.

Comparing between the intensity maps of both peaks an inverse relationship can be observed. This suggests that the 4.41 eV peak is not an additional peak

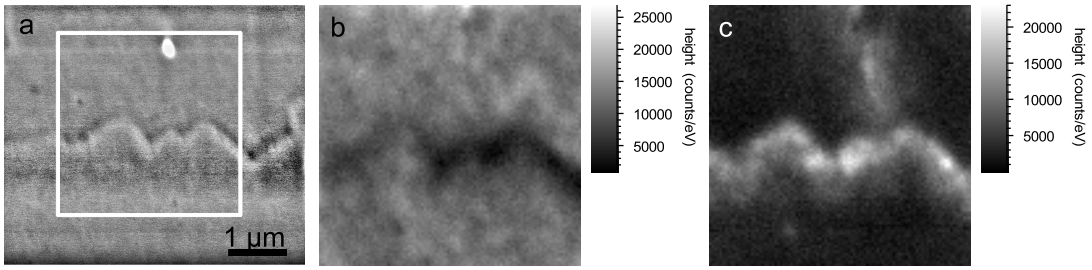

Figure 4.6: SE-image (a) and fitted $3 \times 3\,\mu m^2$ room temperature CL intensity maps of the 4.54 eV peak (b) and the 4.41 eV peak (c) of sample B. The CL hyperspectral image was acquired in the boxed area in the SE-image.

but instead a peak of the NBE emission of an $Al_xGa_{1-x}N$ layer with a lower AlN content (Fig. 4.4). The shift in emission energy corresponds to a change in the AlN content by about 5 atomic %. This behaviour was previously seen by Chang et. al. [76] and attributed to the lower surface mobility of Al during the growth which decreases the incorporation probability of Al along step edges. The additional bright area running vertically in Fig. 4.6c, which does not correlate with the SE-image, is believed to originate from an overgrown step bunch.

Direct comparison of the SE-images of both samples at the same magnification (Fig. 4.3a for A and Fig. 4.5a for B) emphasizes the differences shown in the AFM measurement. While sample A shows the formation of domains on the surface, no such domains are present in sample B; instead step bunches can be seen on the surface. The same differences are visible in the CL peak intensity maps of both samples. These differences can be explained by the different miscut angle of the substrate: a high miscut angle promotes the formation of step bunches [77] which may be assisting in the relief of stress [69].

The formation of step edges on $Al_{0.5}Ga_{0.5}N$ has already been reported on epitaxial lateral overgrown (ELO) samples in Ref. [78]. Those samples showed step bunches with a height of either 70 nm or 2–4 nm, along with a change in the composition between the flat terraces (50% AlN) and step edges (34% or 41% AlN), depending on the thickness of the $Al_xGa_{1-x}N$ layer (0.7 µm or 3.5 µm). On the ELO samples the non *c*-plane facets form during the overgrowth of the pattern etched into the substrate. The formation of the non *c*-plane facets in the samples presented in this chapter is due to the miscut of the substrate. The step bunches seen in the 0.7 µm thick sample in Ref. [78] are continuous and their spacing and direction are aligned with the underlying ELO pattern. The step bunches seen in our investigation and their 3.5 µm thick sample are of varying length and exhibit a zigzag pattern with the main orientation following the miscut orientation or

underlying ELO pattern (Ref. [78]) respectively.

Conclusion

The characterization of the two samples showed that the miscut of the substrate has a great influence on the surface morphology and luminescence homogeneity of the $Al_{0.47}Ga_{0.53}N$ buffer layer. For the growth of an active region on top of the high miscut sample, the effect of the step edges on the sample has to be taken into account. For the growth on the low miscut sample the effect of the different domains has to be understood in order to prevent inhomogeneities in the active zone and a resulting broadening of the emission band.

4.3 Influence of AlGaN layer thickness

In order to investigate the influence of the $Al_xGa_{1-x}N$ layer thickness on the layer properties three different samples were grown by MOCVD at the Tyndall National Institute by the group of Prof. P. J. Parbrook. Trimethylgallium (TMGa), trimethylaluminium (TMAl) and ammonia (NH_3) were used as precursors, while hydrogen (H_2) was used as carrier gas. The sample structure consists of a nominally undoped $Al_{0.53}Ga_{0.47}N$ layer which was deposited on an AlN template, grown on a *c*-plane sapphire substrate. For the sample with the lowest thickness a 10 nm thick low temperature AlN interlayer was inserted between the AlN template and the $Al_xGa_{1-x}N$ layer. The thickness of the $Al_{0.53}Ga_{0.47}N$ layer was varied between 800 nm and 1500 nm.

Room temperature CL spectra of all three samples were measured with a beam energy of 5 keV, resulting in 90% of the beam energy being deposited in the first 90 nm, confining the interaction volume into the $Al_{0.53}Ga_{0.47}N$ layer. The normalized spectra are shown in Fig. 4.7. All three spectra show a strong high energy $Al_xGa_{1-x}N$ NBE emission peak around 4.7 eV and defect luminescence peaks at 3.74 eV and 3 eV. The measured NBE peak position red-shifts with the layer thickness, from 4.75 eV for the 800 nm thick sample to 4.65 eV for the 1500 nm sample. For further analysis a Gaussian function was fitted to the $Al_xGa_{1-x}N$ NBE peak of each of the samples, in order to extract the FWHM and the emission energy. The obtained values are shown in Fig. 4.8.

Fig. 4.8 shows a clear linear correlation between the layer thickness and the NBE emission energy as well as a non linear reduction of the FWHM of the NBE peak. The most likely reasons for the linear red-shift of the NBE emission energy are either a gradual increase in the relaxation of the compressive strain of

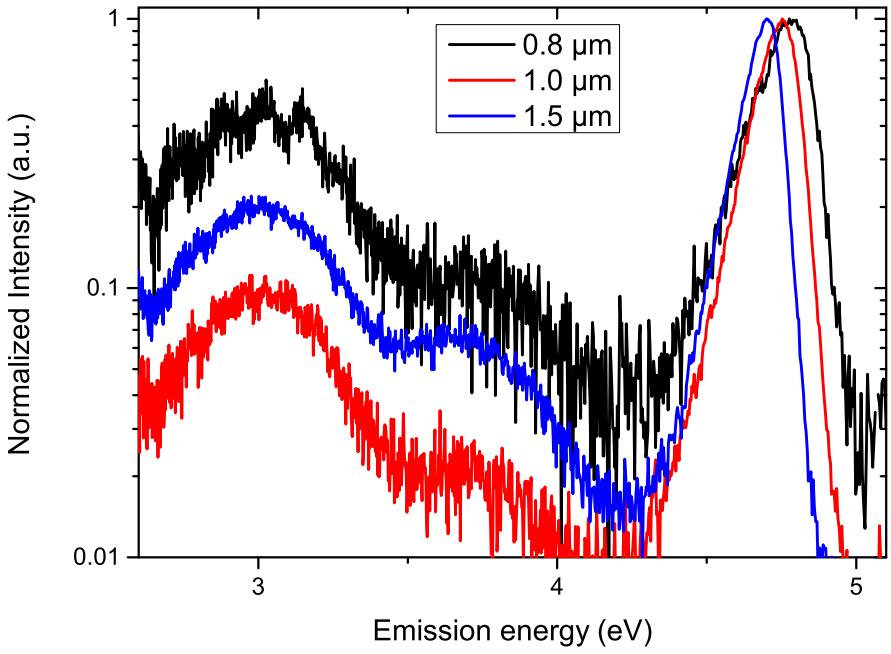

Figure 4.7: Normalized CL spectra of the three investigated samples of different thicknesses. A strong NBE peak at around 4.70 eV and two defect peaks at 3.74 eV and 3.00 eV were measured.

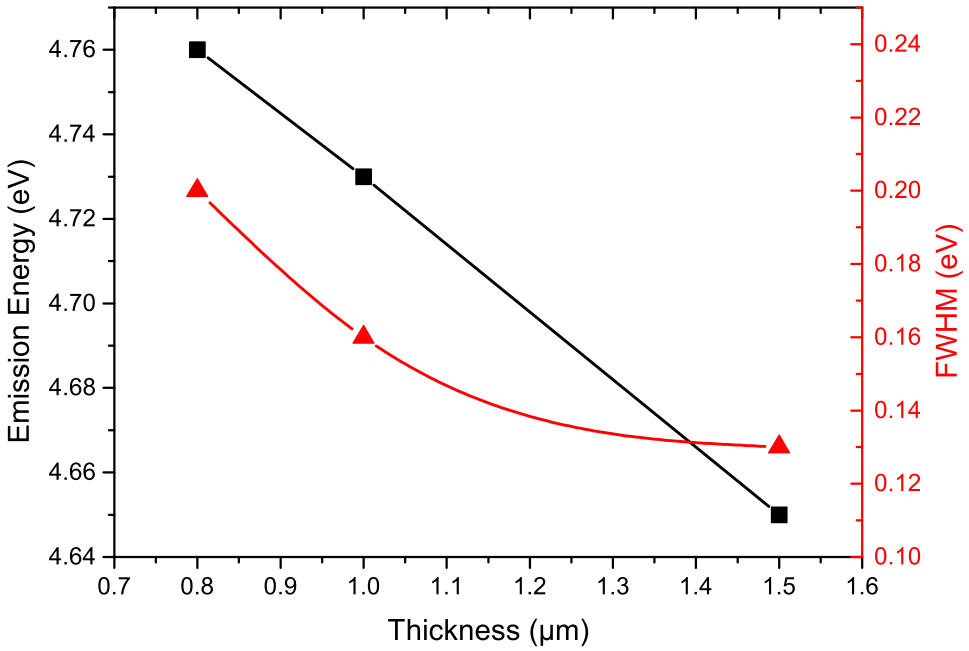

Figure 4.8: Extracted emission energy (black) and FWHM (red) of the $Al_xGa_{1-x}N$ NBE emission. A clear decrease in both parameters with increasing thickness can be observed. The lines are guides to the eye only.

the $Al_{0.53}Ga_{0.47}N$ layer with increasing layer thickness or a compositional pulling effect as was observed for the growth of $Al_xGa_{1-x}N$ on GaN by Lin et al. [71]. Both effects are related to hetero-epitaxy of non lattice matched semiconductors. Growing a layer with a different lattice constant from the underlying layer will force the grown layer to adapt the crystal structure of the underlying layer, thus deforming the lattice of the grown layer. This deviation of the grown lattice from the ideal lattice structure of the semiconductor will lead to compressive or tensile strain, depending whether the underlying layer has a smaller or greater a_0 lattice constant (in c growth direction) than the grown layer. Strain incorporated in a semiconductor can affect the the bandgap energy, compressive strain leading to a blue-shift and tensile strain to a red-shift of the bandgap energy. The magnitude of these shifts depends on the magnitude of the incorporated strain field as shown by Shikanai et al. [79].

The presence of a strain field during growth can have multiple effects, including a compositional pulling effect. For the growth of an $Al_xGa_{1-x}N$ layer on an AlN layer a biaxial strain field is present, to reduce this field Ga atoms can be pulled out of the layer. This results in the growth of an $Al_xGa_{1-x}N$ film with an higher AlN% and a reduced strain field. During subsequent growth fewer and fewer Ga atoms are being expelled, increasing the GaN% in the layer despite an constant TMGa/TMAl ratio in the gas-phase. This leads to a decreasing bandgap energy for thicker layers as was observed for this sample series.

Another effect that can occur during the growth of a strained layer is the relief of strain due to the inclination of threading dislocations. This was first observed by Cantu et al. [80] for $Al_xGa_{1-x}N$:Si and later by Ren et al. [81] and Follstaedt et al. [82] for nominally undoped $Al_xGa_{1-x}N$ layers. A model for the relaxation process was proposed by Romanov et al. [83]. In this model, the edge dislocations in the over-layer are inclined to project along one of the three <1-100> line directions in the (0001) inter-facial plane. The bent dislocations relax the over-layer because their Burgers vectors have an a component in this plane [82]. The model also predicts, that the relaxation of the layer increases linearly with thickness. This linear increase in relaxation will lead to a linear decrease in the emission energy in a compressive strained layer, as observed for these samples.

To investigate which of these mechanics causes the red-shift observed in the CL spectra for the three samples, depth resolved CL was performed on the sample with the highest layer thickness. The results are shown in Fig. 4.9. The depth resolved CL shows a small red-shift of the NBE emission peak with increasing

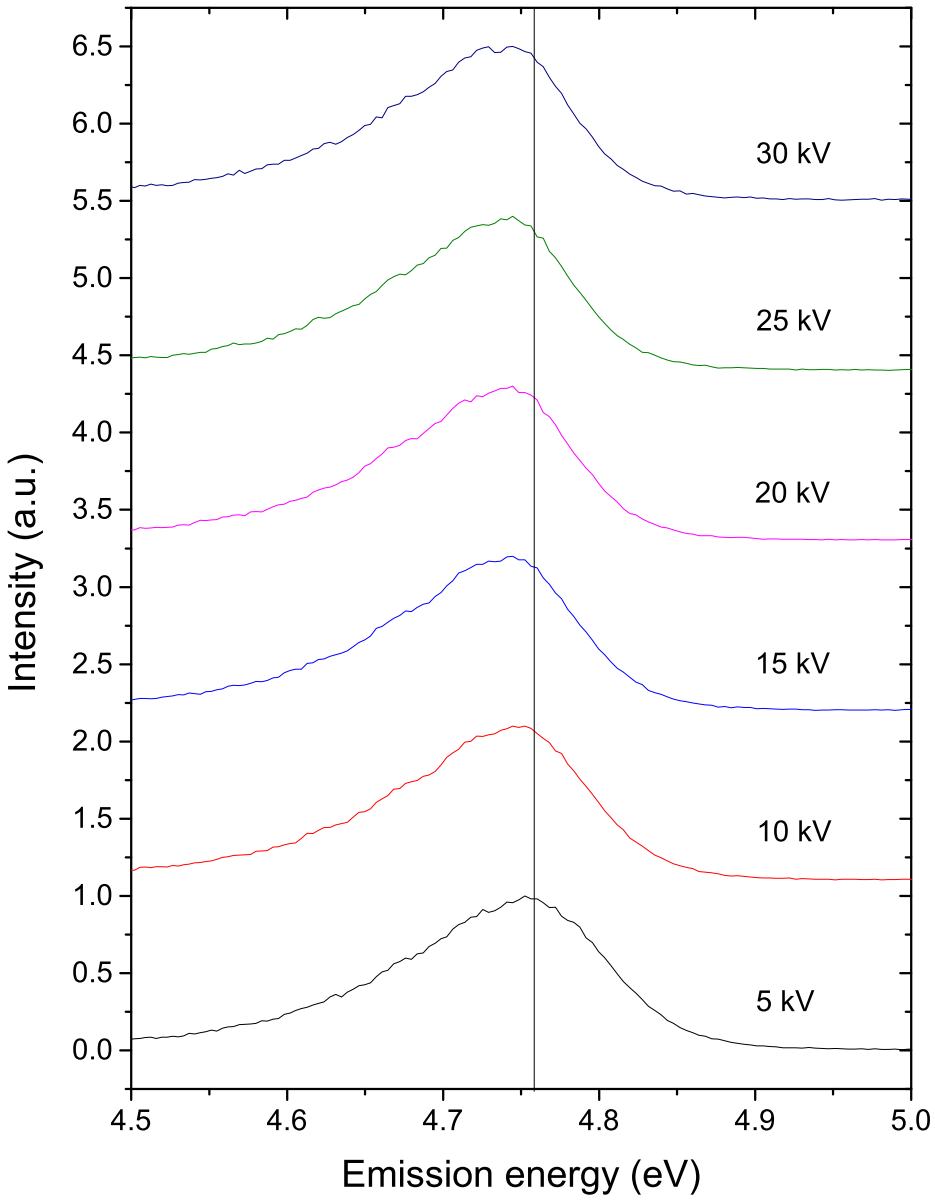

Figure 4.9: Recorded spectra of Al_xGa_{1-x} NBE emission peak of the 1500 nm thick sample at different acceleration voltages.

sampling depth. This is opposed to the effect of the composition pulling effect, from which a blue-shift of the NBE emission peak with sampling depth would be expected, as the AlN% is expected to be higher the closer one probes to the interface between the $Al_xGa_{1-x}N$ layer and the AlN buffer. This means that the observed red-shift with sample thickness is most likely caused by a relaxation of the $Al_xGa_{1-x}N$ layer, possibly due to inclined dislocations. The small red-shift observed in the depth resolved CL is caused by re-absorption, where photons from the high energy shoulder of the emission peak get reabsorbed while travelling through the material, evident from the change in the high energy shoulder (see Section 3.2.5).

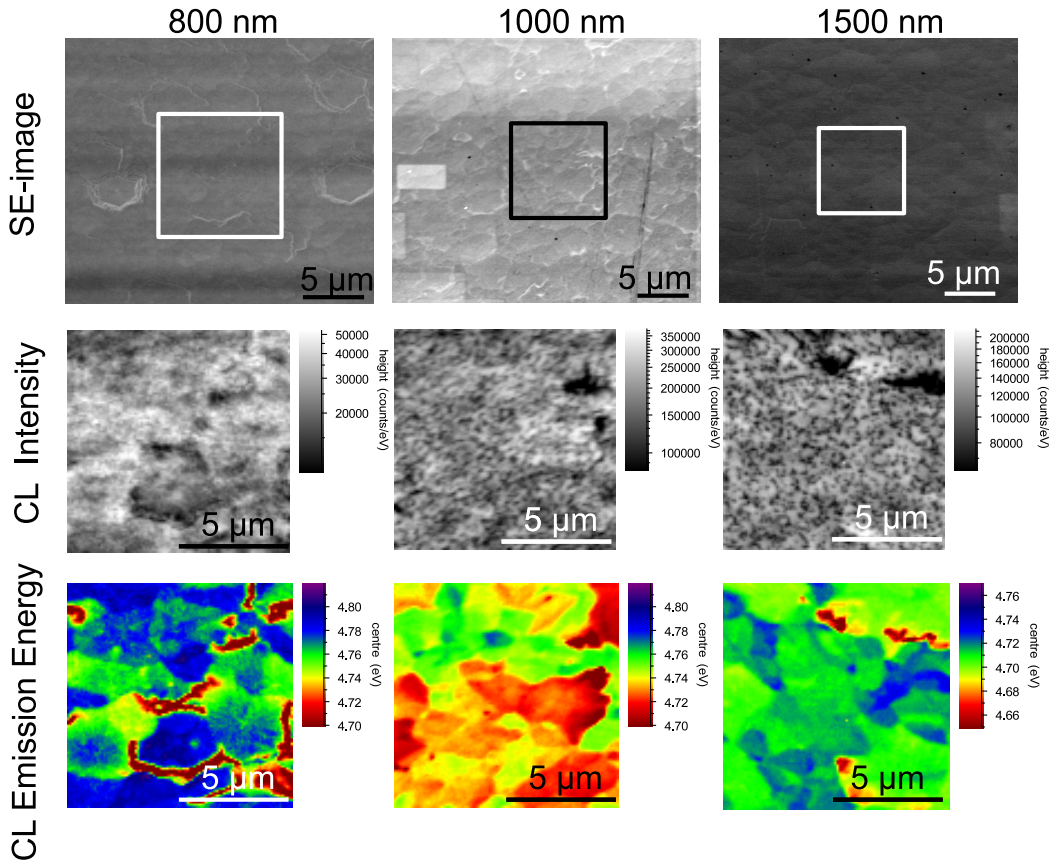

Figure 4.10: SE-images and $10 \times 10\,\mu m^2$ CL intensity and emission energy maps for each of the samples with different $Al_xGa_{1-x}N$ layer thicknesses (values given at top of image). The CL hyperspectral images were recorded in the boxed area in the SE-images.

To investigate the behaviour of the NBE FWHM with the increasing layer thickness, CL hyperspectral imaging and SE-imaging were performed. For these

samples the CL imaging was done with an acceleration energy of 5 keV a beam current of 5.6 nA and a chamber pressure of 0.4 mbar. The chamber pressure had to be increased as room temperature CL imaging was not possible under high vacuum conditions due to charging effects. The results of the measurements are shown in Fig. 4.10.

Analysing the SE-images shows a clear change in the surface morphology. The morphology of the 800 nm thick sample consists of hexagonal platelets with a diameter of several µm and a considerable height difference to the surrounding material. Between these platelets smaller domains are visible. With increasing layer thickness the hexagonal platelets begin to coalesce, reducing the height difference between the platelets and the surrounding area. This is clearly visible in the 1000 nm thick sample where the height of the platelets is reduced yet it is still possible to distinguish between different features. For the thickest sample the overall density of these large structures is strongly reduced and the surface morphology mainly consists of different, smaller domains.

The influence of these morphological features on the luminescence properties can be directly seen in the corresponding CL images. The large platelet features seen in the image for the 800 nm thick sample show a strong reduction in emission energy along the edges of the feature. This indicates that the edges of these large features exhibit a similar behaviour to the step bunches observed in the previous section (section 4.2), namely an increased GaN incorporation due to a higher Ga ad-atom mobility. Due to these features and the accompanying compositional inhomogeneity the emission energy variation in the 800 nm thick sample is around 100 meV.

This emission energy variation is reduced for the higher layer thicknesses as the coalescence of the hexagonal platelet causes the compositional inhomogeneity to be reduced. The remaining emission energy variation observed in the CL map for the 1500 nm thick sample is caused by the domains observable in the SE-image, similar to those observed in the previous section (section 4.2).

This does explain the behaviour of the FWHM observed in the CL spectra in Fig. 4.8. The observed FWHM has two main components which are the emission energy variation due to compositional inhomogeneity, caused by the hexagonal platelets and the variation in the emission energy between different domains. With increasing layer thickness the platelets coalesce and the component caused by these features is strongly reduced, thus a decrease in the observed FWHM is observed. The remaining FWHM is mainly caused by the variation in the emission energy between the domains. This variation can have multiple reasons, for

example differences in the tilt and twist of the domains or small scale compositional variations as observed around spiral growth hillocks (discussed in the next section).

Conclusion

A series of samples with different $Al_{0.53}Ga_{0.47}N$ layer thicknesses was investigated and a decrease in $Al_xGa_{1-x}N$ NBE emission energy as well as FWHM with thickness was found. Multiple probable effects for the decreasing emission energy have been investigated and it was found that strain relief by inclined dislocations is the most likely cause. The decreasing FWHM of the $Al_xGa_{1-x}N$ NBE was found to be caused by an improved morphology.

4.4 Properties of Si-doped AlGaN

As discussed in section 2.4, the n-doping of group-III nitrides is realized by using silicon (Si). Silicon is amphoteric, which means that it can act both as an acceptor or as a donor, depending on the atom it substitutes. In GaN the incorporation of Si on a Ga site has the lowest formation energy and Si acts as a donor. The formation energy for incorporating Si on a Ga site is small because the covalent radii of Si and Ga atoms are similar. The incorporation of Si on nitrogen (N) sites or as interstitials is energetically unfavourable as the difference in the covalent radii would lead to a large distortion of the crystal lattice, inducing strain in the grown material.

Silicon has an activation energy of 12–17 meV in GaN [46] (on a Ga site), resulting in 70–80% of the donors being active at room temperature. The doping in GaN is well understood and carrier concentrations between 1×10^{17} and 4×10^{19} [47] with a mobility of $100-450\,cm^2/Vs$ can be achieved, which is sufficient for the operation of devices.

In contrast to the Si doping in GaN the Si doping of $Al_xGa_{1-x}N$ layers with a high AlN content ($x > 80\%$) is much more challenging. One challenge is that the activation energy of the Si donors increases with the AlN% up to 238–255 meV in AlN [84, 85], resulting in a much lower fraction of active donors (0.7% – 1%) contributing to the charge transport. Another challenge to overcome is a reduction of the formation energy of compensating and self-compensating defects [86, 87] which can further reduce the amount of active donors. Understanding the behaviour, incorporation and distribution of these defects is crucial in improving the quality of Si-doped high band gap $Al_xGa_{1-x}N$ layers and devices utilizing

these layers. In this section the incorporation of the Si-donor in $Al_xGa_{1-x}N$ (with $x > 80\%$) and its influence on luminescence properties and topography of a series of $Al_xGa_{1-x}N$:Si samples are investigated.

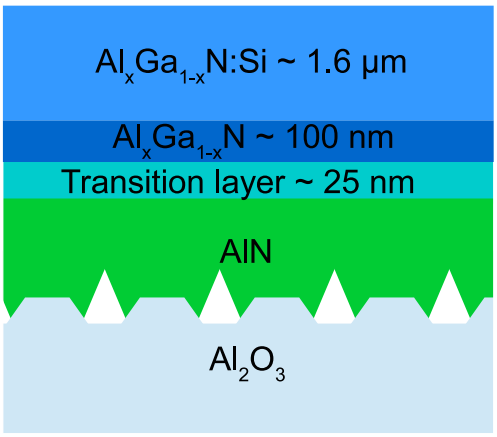

Figure 4.11: Layer structure of the investigated samples.

A number of samples were grown by MOVPE at TU-Berlin in order to determine the properties of the Si-donor in high band gap $Al_xGa_{1-x}N$ layers. The majority of these samples can be divided into four different groups, depending on their AlN% concentration and their SiH_4/III ratio. All samples are shown in table 4.2 and an overview over the 4 sample series is given in table 4.1. TMGa, TMAl, NH_3 and silane (SiH_4) were used as precursors, while H_2 was used as a carrier gas. Sample series 1 to 3 were grown with a constant AlN% fraction and varying SiH_4/III ratio, while sample series 4 was grown with varying composition and a near constant SiH_4/III ratio (see tables 4.2 and 4.1 for details). The thickness of the doped layers was kept constant at (1570±50) nm. The sample structure is shown in Fig. 4.11 and consists of an ELO AlN/Al_2O_3 template [78] on top of which 400 nm of AlN were grown, followed by a 25 nm thick transition layer and 120 nm undoped $Al_xGa_{1-x}N$ layer. On this structure the Si doped $Al_xGa_{1-x}N$ layer was deposited.

	AlN%	SiH_4/III ratio
Series 1	82	$1.9 \cdot 10^{-5}$–$1.8 \cdot 10^{-4}$
Series 2	86	$4.2 \cdot 10^{-5}$–$1.5 \cdot 10^{-4}$
Series 3	96	$9.7 \cdot 10^{-6}$–$6.6 \cdot 10^{-5}$
Series 4	82–95	$1.9 \cdot 10^{-5}$–$2.1 \cdot 10^{-5}$

Table 4.1: Different investigated $Al_xGa_{1-x}N$:Si series

Nr.	Series	SiH_4/III ratio (10^{-5})	AlN% XRD	AlN% WDX	Si WDX [$10^{18}\,cm^{-3}$]	Si SIMS [$10^{18}\,cm^{-3}$]
1	1,4	1.92	82.3 ± 1.0	82.2 ± 2.5	4.2 ± 0.4	
2	1	5.94	80.3 ± 1.0	80.1 ± 2.5	14 ± 2	7.0 ± 3.5[88]
2	1					4.1 ± 0.8[89]
3	1	17.7	82.7 ± 1.0	82.6 ± 2.5	28 ± 1	
4	2	4.16	86.8 ± 1.0	86.2 ± 2.6	6.3 ± 0.6	
5	2	6.00	84.7 ± 1.0	83.8 ± 2.6	9.0 ± 0.7	
6	2	7.06	84.2 ± 1.0	84.9 ± 2.6	11 ± 1	
7	2	10.1	85.1 ± 1.0	85.3 ± 2.6	14 ± 0.7	
8	2	14.8	86.3 ± 1.0	86.3 ± 2.6	25 ± 1	
9	3	0.972	95.9 ± 1.0	95.7 ± 2.9	3.0 ± 0.4	
10	3	2.14	93.7 ± 1.0	94.1 ± 2.8	5.7 ± 0.5	
11	3	3.50	94.7 ± 1.0	93.8 ± 2.9	7.0 ± 0.5	3.6 ± 0.7[89]
12	3	4.50	94.7 ± 1.0	94.5 ± 2.9	9.3 ± 0.7	
13	3	5.50	95.6 ± 1.0	94.8 ± 2.9	12 ± 0.7	
14	3	6.62	94.7 ± 1.0	94.7 ± 2.9	13 ± 0.6	
15	4	1.99	87.1 ± 1.0	87.2 ± 2.6	5.4 ± 0.6	
16	4	2.06	88.3 ± 1.0	91.7 ± 2.8	5.0 ± 0.4	
17	4	2.14	94.4 ± 1.0	94.8 ± 2.9	5.4 ± 0.5	
18		8.09	100 ± 1.0	99.9 ± 3.0	3.0 ± 0.5	
19			00.0 ± 1.0	00.0 ± 0.0		
20		28.5	100 ± 1.0			20 ± 10[88]
21		5.91	80.0 ± 1.0			8.3 ± 4[88]
22		5.91	80.0 ± 1.0			7.2 ± 4[88]
23		2.34	50.0 ± 1.0			2.2 ± 1[88]
24		6.35	100 ± 1.0			1.0 ± 0.5[88]
25		5.11	80.0 ± 1.0			4.1 ± 0.8[89]
26		5.85	90.0 ± 1.0			4.7 ± 0.9[89]
27		5.11	80.0 ± 1.0			3.8 ± 0.8[89]
28		5.85	90.0 ± 1.0			4.9 ± 1[89]

Table 4.2: Overview of the analysed samples, values are rounded to the last significant number.

4.4.1 Compositional characterization of $Al_xGa_{1-x}N$:Si

As small variations in the composition as well as doping and impurity concentration can have a strong effect on the performance of a device, reliable methods for determining these variables have to be used in order to underpin the optimization of growth conditions and achieve high quality devices. Here the determination of composition and doping concentration in high band gap $Al_xGa_{1-x}N$:Si layers was performed using wavelength dispersive X-ray measurements (WDX) in an electron probe microanalyser (EPMA, see Section 3.3).

All WDX measurements in the EPMA were conducted with the samples placed perpendicular to the incident electron beam, an acceleration voltage of 10 kV and a beam current of 40 nA. At this acceleration voltage 90% of the beam energy is deposited in the first 590 nm of an AlN sample, according to Monte Carlo simulations using the CASINO software [55]. The acceleration energy utilized is well above the minimal energy needed to excite the characterized elements while containing the interaction volume in the desired layer, as for lower AlN% (e.g. $Al_{0.82}Ga_{0.18}N$) the penetration depth of the electron beam will be smaller due to the higher material density.

Each of the plotted WDX measurement points consists of the mean of 10 measurements performed on a line on each of the samples. The errors shown consist of the standard error and an assumed systematic error of 3% of the measured signal which is well above the deviation from the weight total which was at $100 \pm 2\%$ for each investigated sample. For the XRD measurement an absolute error of 1% for the composition measurements was given by the collaborators.

Composition measurement

The composition of all samples was characterized using WDX and compared with results from high resolution X-ray diffraction (HR-XRD) which were supplied by TU-Berlin. For the WDX characterization the peak to background signals were compared with those from AlN and GaN standards to give the experimental k-ratios (sample intensity/standard intensity). The Ga L_α and Al K_α signals were recorded using a large TAP crystal (thallium acid phthalate, $2d = 25.75$ Å), for the N K_α signal a synthetic pseudocrystal (PC1 $2d = 60$ Å) was used. The measured k-ratios were automatically converted to atomic percentages and the measured composition agrees very well between both methods, showing only slight variations of the composition in each sample series.

In figure 4.12 the AlN content determined by WDX is plotted versus the AlN content determined by XRD (10.5) reciprocal space maps of all samples

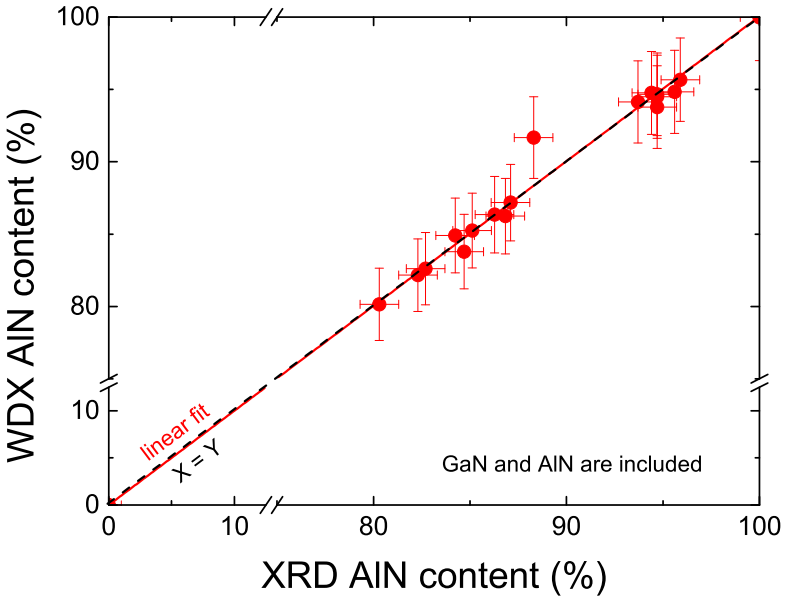

Figure 4.12: AlN content of samples determined by WDX plotted versus the AlN content determined by XRD (10.5) RSMs.

independent of the SiH_4/III ratio. Neglecting the one sample at an XRD AlN content of $x = 0.88$ (WDX $x = 0.92$), there is very good agreement between all of the WDX and XRD determined AlN compositions. The WDX measurement technique enables a fast, non destructive determination of the composition of wide bandgap $Al_xGa_{1-x}N$ alloys and is in good agreement with XRD measurements, well below the margin of error. Additionally, one can investigate quaternary InAlGaN alloys, as demonstrated by Bejtka et al. [90], which present further difficulties for XRD measurements due to the uncertainty of attributing lattice constants to compositions and strain.

Determination of the Si dopant concentration

For the WDX characterization of the Si-dopant concentration in the different sample series, a pure Si wafer was used as a standard to determine the k-ratios with a TAP crystal used to acquire the Si (K_α) signal and the counting time of the WDX detector was increased to accommodate for the lower concentrations. Each of the plotted WDX measurement points consists of the mean of 10 measurements performed on a line on each of the samples. The errors shown consist of the standard error and an assumed systematic error of 3% of the measured signal which is well above the deviation from the weight total which was at $100 \pm 2\%$

for each investigated sample.

Residual impurities were measured by secondary ion mass spectrometry (SIMS) (by [88, 89]), irrespective of their site in the crystal lattice, and lattice distortions. During SIMS of high band gap $Al_xGa_{1-x}N$ two effects influence the measurement. Firstly, matrix effects [91, 92] play an important role on the respective ion yield as only a few percent of the sputtered species are ionized. Therefore, reference samples of different $Al_xGa_{1-x}N$ composition for the respective impurity elements and sputtering ions were used to determine the relative sensitivity factors and the sputter rate. Secondly the accumulation of surface charges due to ion bombardment can strongly influence the secondary ion yield [93], this was partially mitigated by deposition of a conductive metal layer and electron beam irradiation. The impurity concentration was determined by the point-by-point correction (PCOR) protocol. Si relative sensitivity factors (RSF) are adjusted at each data point based on the AlN/GaN composition.

The detection limit, i.e. the lowest concentration measured of an element for a given set of analysis conditions, depends strongly on the AlN concentration. For example, in GaN the Si detection limit is 1×10^{16} atoms/cm^3 vs. in AlN the Si detection limit is 3×10^{17} atoms/cm^3. In $Al_{0.5}Ga_{0.5}N$ the detection limit for Si is between $\sim 6 \times 10^{16}$ atoms/cm^3 and 9×10^{16} atoms/cm^3. The error of the SIMS measurements was provided by the companies who executed the measurements and is 20% [89] and 50% [88] respectively, especially due to errors obtained from sample charging and possible matrix effects.

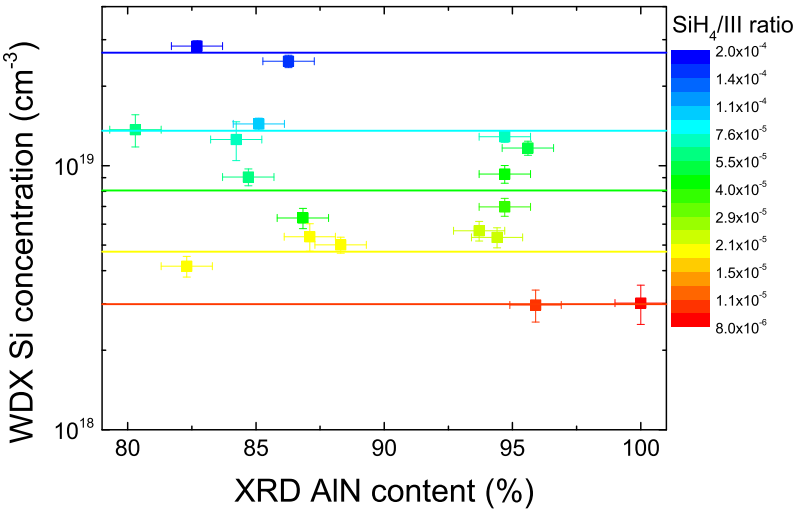

Figure 4.13: Si concentration measured by WDX in dependence of the AlN content and the SiH_4/III ratio.

In order to determine the Si concentration WDX measurements as well as SIMS measurements, on a very similar set of samples (see table 4.2), have been performed. Figure 4.13 shows the results of the WDX measurements on all investigated samples and how they depend on their AlN concentration as well as the SiH_4/III ratio. The results show that the Si incorporation of the investigated samples is independent of the composition of the sample and only depends on the SiH_4/III ratio that was used during the growth. This is in contrast to the findings by Junxue et al. [94] who proposed that an increased amount of TMAl in the gas-phase will lead to an increase in the Si incorporation ratio due to an increase in parasitic gas-phase reactions causing a local Ga-rich growth environment. We believe that the different observations made in this work stem from a much higher NH_3 flux and thus a higher V/III ratio, preventing the formation of a Ga-rich phase in the growth environment and keeping the growth under N-rich conditions for all samples.

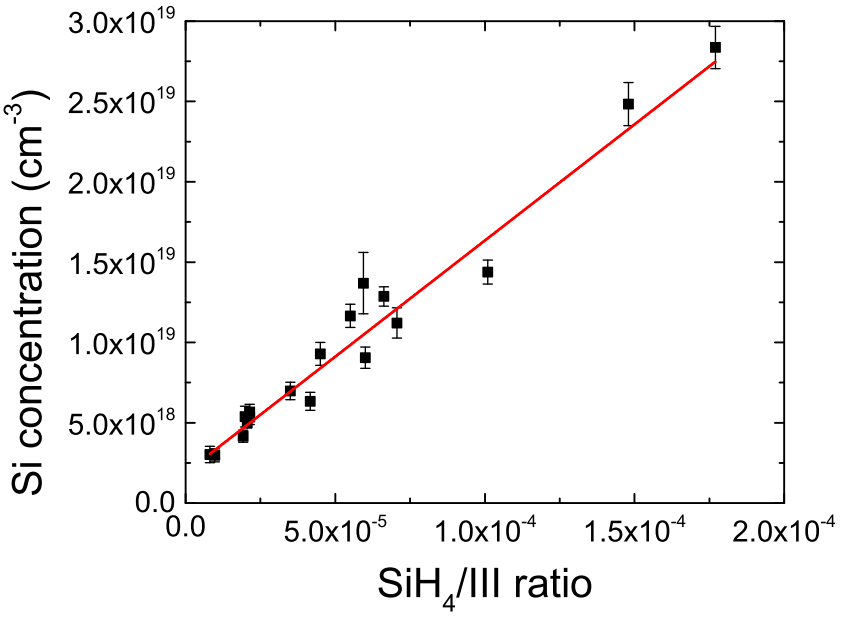

Figure 4.14: Si concentration measured by WDX in dependence of the SiH_4/III ratio. The linear fit of the data is shown as a red line.

In Fig. 4.14 the measured Si-concentration is plotted against the SiH_4 ratio. A linear function was fitted to the WDX data, with a gradient of $1.45\times10^{23}\,\mathrm{cm}^{-3}$ and an intercept with the Y-axis of $1.89\times10^{18}\,\mathrm{cm}^{-3}$. The good agreement between the measurement data and the linear fit ($\chi^2_{red} = 2.9$) shows that the the Si incorporation in wide band gap $Al_xGa_{1-x}N$ layers increases linearly with the

SiH_4/group-III ratio. This is in good agreement with findings of other groups [95, 96, 97]. In the investigated SiH_4/group-III ratio range no saturation could be observed. Determining the intercept of the linear fit with the Y-axis potentially allows one to obtain information about the desorption rate of the Si-donor. In the investigated series the intercept has a small positive value which would indicate Si incorporation without intentionally providing any SiH_4. This could be caused by a residual Si reservoir in the growth reactor due to prior growth of Si doped layers. However, the fitting error of the intercept is of the same order of magnitude as the obtained value of the intercept thus more precise conclusions cannot be drawn.

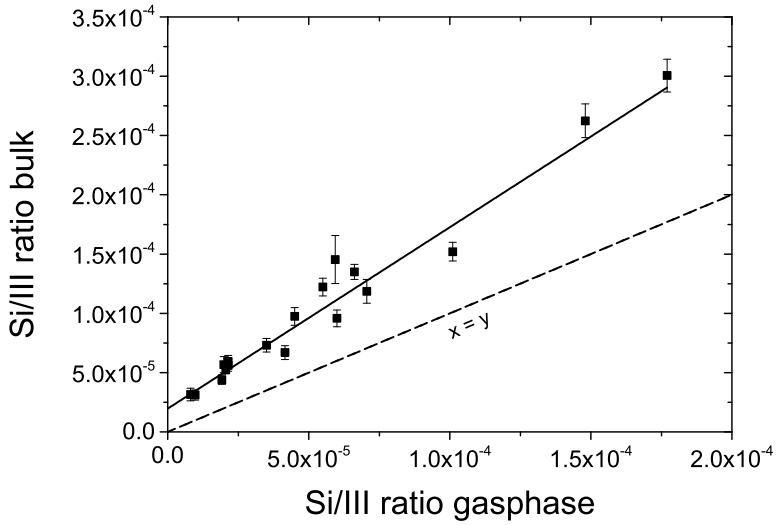

Figure 4.15: Comparison between Si/III ratio in gas-phase and bulk; the solid line is a linear fit over all data points, the dotted line shows equal Si/group-III ratio in gas-phase and bulk.

In Fig.4.15 the Si/group-III ratio in the bulk is plotted against the SiH_4/group-III ratio in the gas-phase. The incorporation increases linearly with the SiH_4/group-III, with a gradient of 1.46. As the Si incorporation on group-III lattice sites is strongly preferred over the incorporation on a N site it is possible to see that the incorporation of Si atoms is slightly preferred over the incorporation of group-III atoms [98, 99]. This is most likely a result of pre-reactions in the gas-phase which reduce the amount of available Ga and Al atoms for incorporation [100].

Comparing the WDX results on the Si concentration with commercially performed SIMS results [88, 89] (see figure 4.16) we found that both measurement methods show the same general trend: a linear increase in the Si concentration with increasing SiH_4/III ratio. Comparing the Si concentration values we find

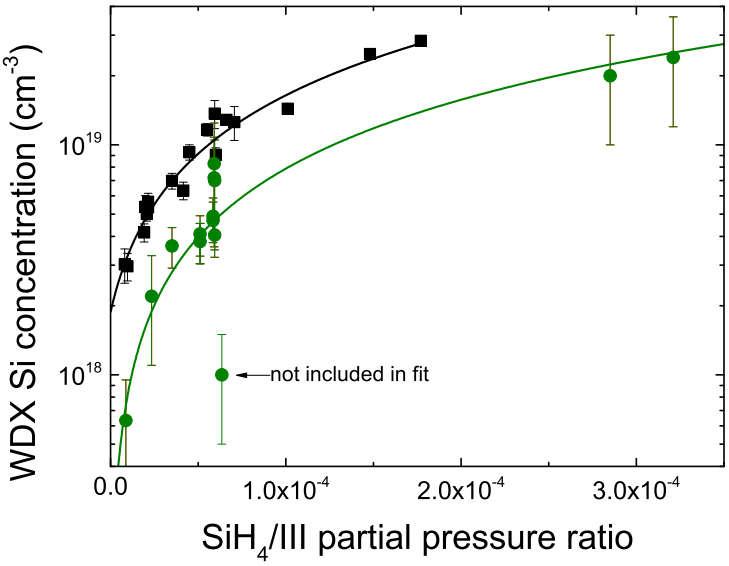

Figure 4.16: Si concentrations determined by WDX (black squares, independently of the aluminium content) as well as Si concentrations determined by SIMS (green circles) versus the SiH_4/III ratio. Linear fits of the data are shown as lines.

only partial agreement in the absolute concentration values between the two measurement methods. The linear fits of both measurement series show that the Si concentration differs by a factor of 2. For example for an $Al_{0.94}Ga_{0.06}N$ layer with a SiH_4/III ratio of 3.5×10^{-5} the Si concentration was determined to be $(36 \pm 7) \times 10^{17}\,\mathrm{cm}^{-3}$ by SIMS, whereas the Si concentration determined by WDX is $(70 \pm 5) \times 10^{17}\,\mathrm{cm}^{-3}$. For an $Al_{0.80}Ga_{0.20}N$ layer with a SiH_4/III ratio of 5.94×10^{-5} the discrepancy increases even further, for the measurements done by the same company, giving Si concentrations of $(14 \pm 2) \times 10^{18}$ and $(41 \pm 8) \times 10^{17}$[89] for WDX and SIMS, respectively. The SIMS measurements of the other employed company on the same sample resulted in a Si concentration of $(7 \pm 3.5) \times 10^{18}$[88].

The disagreement between the two measurement methods (and the two SIMS measurements) can be caused by a variety of effects including the matrix effect and sample charging. The matrix effect is a well known problem for SIMS measurements, changing the secondary ion yield depending on the matrix (i.e. composition of the sample) the ions are embedded in. To compensate for this SIMS standards with a known composition close to the investigated samples are needed. Standards fulfilling this criteria where utilized in these measurements reducing the possible influence of the matrix effect. The same effect can also

influence WDX measurements [101]. To reduce the influence of the matrix effect on the measured Si concentration a software correction was applied. It has to be noted that in previous measurements of Mg in GaN very good agreement between WDX and SIMS was found [102].

Sample charging provides another challenge to overcome in acquiring precise concentration measurements utilizing charged particles for the group-III nitride system. Although the investigated samples are all Si doped, charging effects were still observed, influencing the measured concentrations. An estimate of the charging on the WDX measurements can be gained by analysing the weight total, where a deviation from the optimum value (100%) can point out that the obtained data has been influenced by effects like sample charging. For these sample series all WDX measurements resulted in a weight total of $(100 \pm 2)\%$ indicating that sample charging had a negligible effect on the WDX measurement. SIMS measurements are expected to show a stronger dependence on sample charging effects than WDX as both the primary as well as the secondary ions will be affected by a built up surface charge. To reduce the effect of sample charging Au coating and electron bombardment were used for the SIMS measurements. However, even with the discrepancy of a factor of 2 between SIMS and WDX measurements (and no clear indication which technique is right) WDX provides a fast and accurate measurement with small errors and is capable to be established in measuring impurity concentrations above 3×10^{18}.

4.4.2 Luminescence Properties of $Al_xGa_{1-x}N$:Si

The influence of the Si doping concentration on the resistivity of the samples was investigated by Mehnke et al. [103] from TU-Berlin who found that the resistivity of Si doped $Al_xGa_{1-x}N$ increases with increasing AlN fraction x (shown in Fig. 4.17). They furthermore showed that the resistivity first decreases with increasing Si concentration and then increases again, giving an optimum doping concentration in dependence of the AlN composition of the $Al_xGa_{1-x}N$ layer.

The luminescence properties of these samples have been characterized by CL spectroscopy in order to better understand the reported behaviour of the resistivity with increasing AlN and Si concentration. We correlated the Si concentration to the luminescence properties of the different $Al_xGa_{1-x}N$:Si series by performing room temperature CL spectroscopy to better understand the reported behaviour with increasing AlN concentration and Si concentration. CL spectroscopy was conducted with an acceleration voltage of 15 kV in the setup described in section 3.2.2. At this acceleration voltages 90% of the beam energy is deposited within

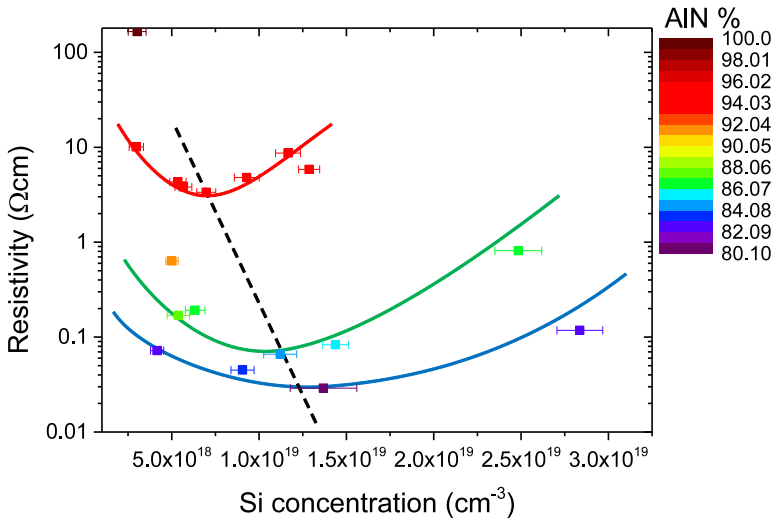

Figure 4.17: Resistivity as measured by TU-Berlin in dependence of the Si and AlN concentration. Two trends are clearly visible; with increasing AlN% the resistivity of the samples increases and the resistivity does have an optimum value for each AlN concentration. The dashed line shows the approximate optimum doping concentration, the coloured lines are guides to the eye only, showing the trends for sample series 1 (blue), 2 (green) and 3 (red)

a depth of 920 nm [55].

Influence of the AlN concentration on the luminescence properties of $Al_xGa_{1-x}N$:Si

To investigate the influence of the AlN fraction on the sample resistivity, sample series 4 has been characterized by room temperature CL spectroscopy. The samples in this series were grown with a near constant SiH_4/III ratio while changing the AlN fraction (see table 4.1 and table 4.2). The results of the investigation are shown in Fig. 4.18.

The recorded spectra of sample series 4 (Fig. 4.18) consists of three to four different peaks. All samples exhibit an $Al_xGa_{1-x}N$ near band edge (NBE) peak which blue-shifts with increasing AlN% from 5.36 eV (82.2% AlN) to 5.68 eV (94.8% AlN). In addition to the $Al_xGa_{1-x}N$ NBE peak, each spectrum shows different peaks associated with radiative recombinations involving defect centres in the bandgap.

The most prominent of these defect transitions for sample series 4 is the high energy peak between 4.40 eV and 4.55 eV. This peak features a strong blue-shift with increasing AlN% from 4.40 eV (82.2% AlN) to 4.55 eV (94.8% AlN) as well

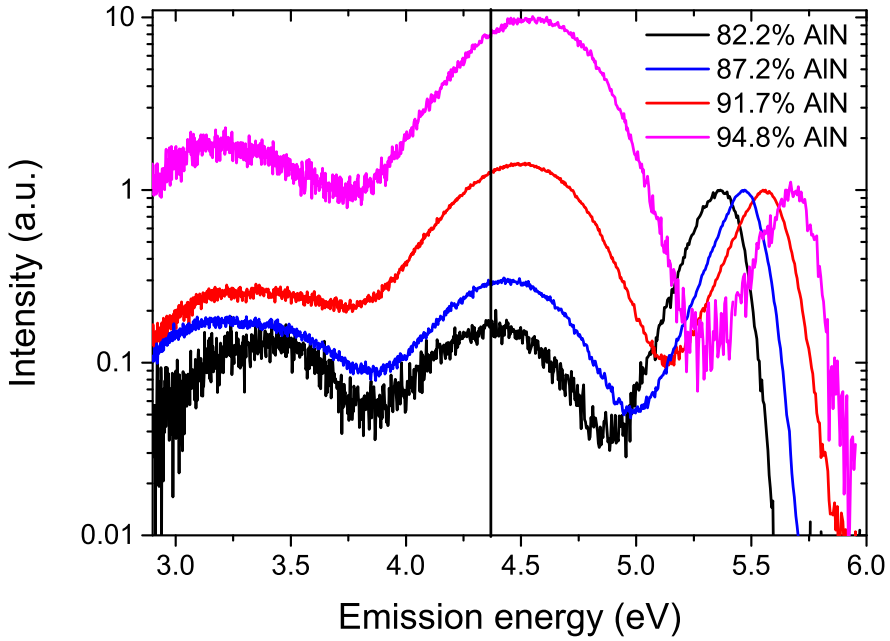

Figure 4.18: Room temperature CL spectra for sample series 4. The black line is set at the centre of the high energy defect peak for the 82.2% AlN sample.

as an increase in intensity in relation to the NBE peak (to illustrate the blue-shift of the defect peak, the peak position for the 82.2% AlN sample is marked with a black line in Fig. 4.18). This high energy peak was already observed by Nepal et al. [104] and was attributed to a recombination process involving a singly charged group-III vacancy complex e.g. $(V_{III}\text{-}2O_N)^-$. The blue-shift of this peak was attributed to a pinning of the singly charged acceptor level to the vacuum energy. The increase in emission intensity indicates an increased concentration of the related defect centre. For the investigated samples the increased incorporation is most likely caused by the increasing AlN% as WDX measurements (see Table 4.2 and Fig. 4.13) showed a near constant Si concentration in the sample series.

On the low energy side of the spectrum a broad luminescence band is visible; based on the work of Nam et al. [105] we attribute the broad defect band to two different optical transitions, the high energy side we attribute to a transition involving a doubly charged cation vacancy complex $(V_{III}\text{-}O_N)^{2-}$ and the low energy peak to a transition involving a triply charged cation vacancy $(V_{III})^{3-}$.

Two main characteristics of these peaks can be observed. Firstly, the relative strength of the two peaks changes with the composition of the layer, while for the 82% AlN sample the $(V_{III}\text{-}O_N)^{2-}$ dominates the low energy side of the spectrum,

the $(V_{III})^{3-}$ emission intensity increases with the AlN concentration, eventually dominating the low energy emission band.

The second characteristic that can be observed is a blue-shift of the luminescence band with increasing AlN concentration which was attributed to the same effect as for the high energy defect transition, namely a pinning of the related energy levels to the vacuum level due to strong localization of the defect centres [105].

The change in the emission intensity of the different defect peaks can be explained by taking the formation energy of these defects into account. Comparing calculations done for defects in GaN and AlN by Van de Walle et al. [39] and Hevia et al. [99], which are shown in Fig. 4.19 and Fig. 4.20 respectively, one can see that the group-III vacancy (V_{Ga} in GaN and V_{Al} in AlN) drastically changes its formation energy and thus its incorporation ratio, from GaN to AlN. Earlier calculations did not investigate the $(V_{III}\text{-}2O_N)^-$ complex or other complexes as the Si doping of GaN was easily achieved and presented no growth challenge, but as these complexes include a group-III vacancy it is reasonable to assume that their formation energy behaves in a similar way.

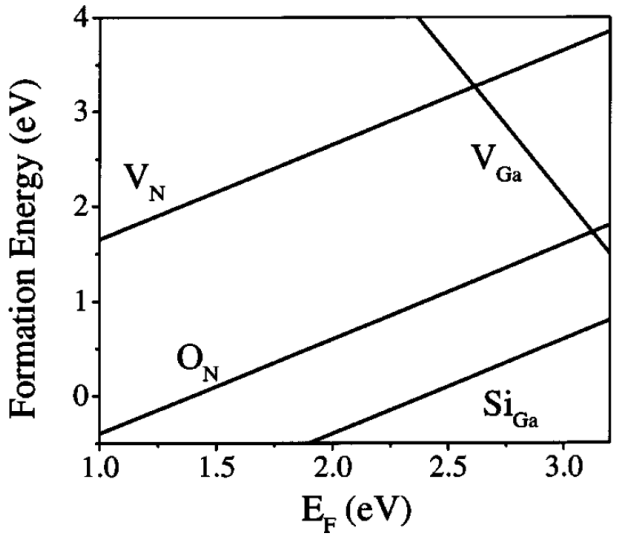

Figure 4.19: Formation energy as a function of the Fermi energy for O in GaN, the nitrogen vacancy and Si. Taken from Van de Walle et al. [39]. The zero of the Fermi energy is set at the valence-band maximum.

The reduced formation energy from GaN to AlN of the group-III vacancy explains the increase in luminescence intensity of the defect peaks with increasing AlN concentration in the recorded spectra. The change in the relative emission

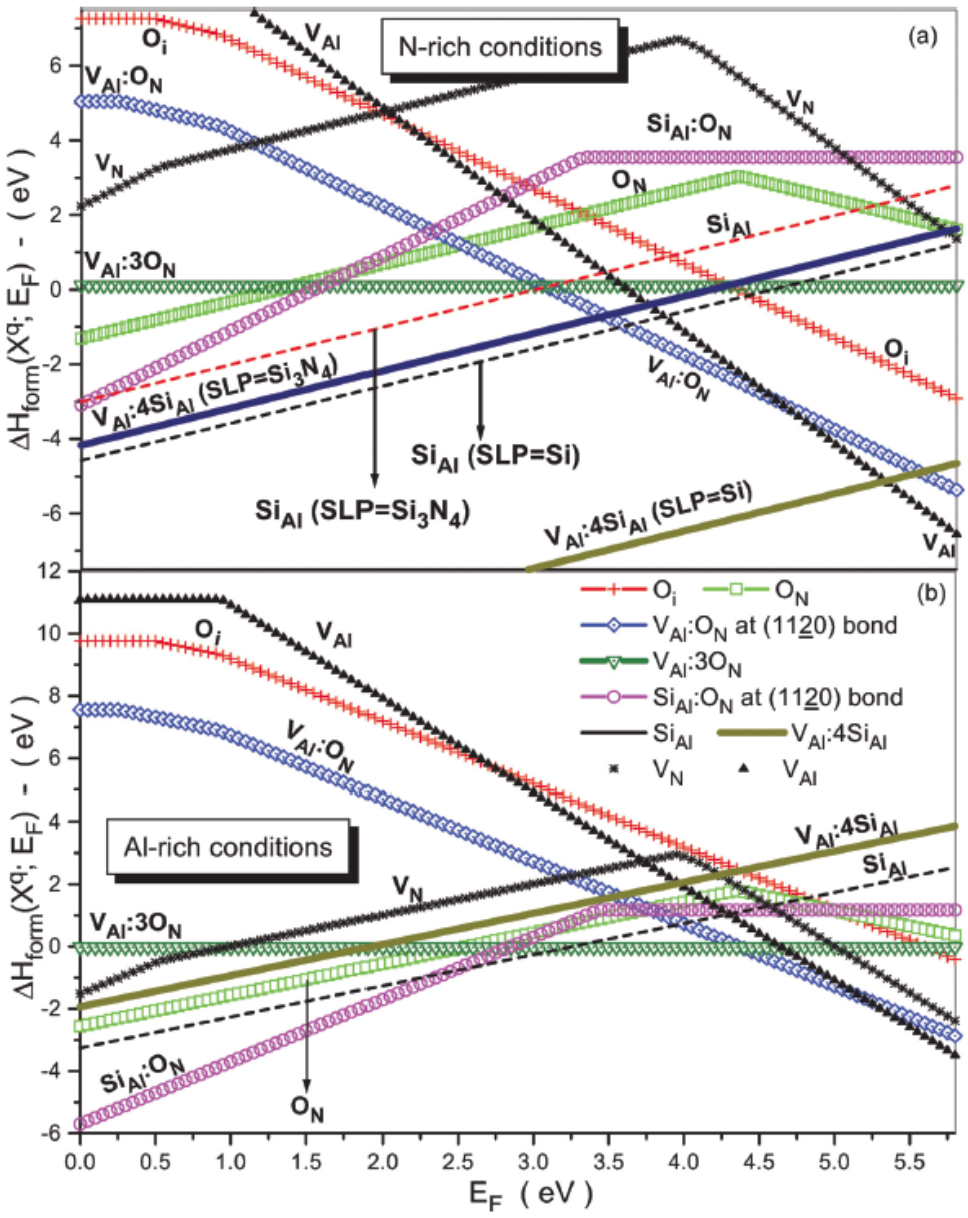

Figure 4.20: Formation energy of the Si donor and relevant defects in AlN for Al and N-rich conditions. Calculations done by Hevia et al. [99]. The zero of the Fermi energy is set at the valence-band maximum.

intensities of the two defect peaks observed in the low energy side of the spectrum (the peaks associated with the doubly charged $(V_{III}\text{-}O_N)^{2-}$ complex and the triply charged $(V_{III})^{3-}$) can also be explained with a change in the formation energy, showing that for the same Si concentration the $(V_{III}\text{-}O_N)^{2-}$ complex has the lower formation energy at 82.2% AlN while the group-III vacancy $(V_{III})^{3-}$ has the lower formation energy at 94.8% AlN.

Influence of the Si concentration on the luminescence properties of $Al_xGa_{1-x}N$:Si

The influence of the Si concentration on the luminescence properties of $Al_xGa_{1-x}N$:Si layers in sample series 1, 2 and 3 has been investigated by CL spectroscopy. The results of the investigation can be found in Fig. 4.21 for sample series 1 and in Fig. 4.22 for sample series 3. These two sample series were chosen as they represent the general trend of the luminescence properties of Si doped $Al_xGa_{1-x}N$ layers, the spectra of sample series 2 shows a mixture of both of these sample series.

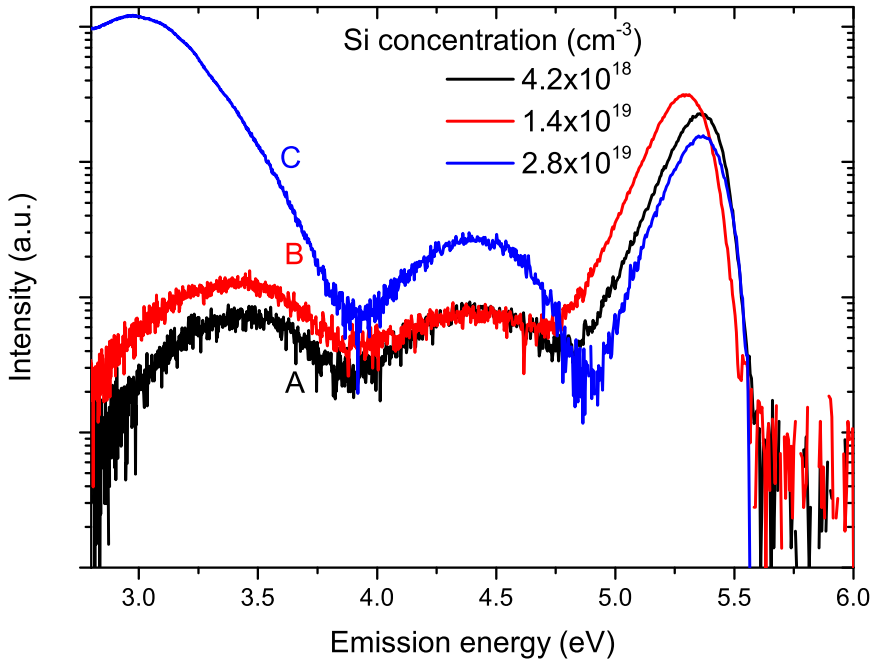

Figure 4.21: Room temperature CL spectra for sample series 1 with an AlN% of (81.5 ± 1.0)%, normalised on the $Al_xGa_{1-x}N$ NBE peak.

The CL spectra for samples A (black line) and B (red dashed) of sample series 1 (Fig. 4.21) consist of three main peaks. Sample A exhibits high energy near band edge (NBE) emission at 5.39 eV and two impurity transitions at 4.35 eV and

3.39 eV and the measurement additionally shows the second order of the NBE emission. The spectrum for sample B has the NBE emission at 5.32 eV and two impurity transitions at 4.35 eV and 3.36 eV. The CL spectrum for sample C (blue dotted) (Fig. 4.21) has a NBE emission peak at 5.39 eV and impurity transition at 4.38 eV as well as an additional strong peak at 3 eV. The impurity transition at 3.39 eV observed in the other samples (A and B) is most likely still present but is obscured by the high intensity and large FWHM of this additional peak. The variation in the NBE emission energy between the three samples can be explained by unintentional growth variations, as seen in the WDX measurement, leading to slightly different $Al_xGa_{1-x}N$ compositions as well as a small red-shift due to a narrowing of the band gap with increasing Si incorporation as observed by Monroy et al. [106]. The impurity transition at 4.35 eV is associated with recombination between a shallow donor (Si) and a singly-charged deep level acceptor [104]. This singly-charged acceptor is attributed to an acceptor complex $(V_{III}\text{-}2O_N)^-$. Alternatively oxygen on an interstitial site (O_i^-) would act as a singly-charged acceptor [99]. The low energy impurity transition at either 3.39 eV or 3.36 eV is attributed to recombination between a shallow donor (Si) and a doubly-charged deep level acceptor. The doubly-charged deep level acceptor is most likely another acceptor complex $(V_{III}\text{-}O_N)^{2-}$[105, 87]. The red-shift in the low energy defect emission (3.36 eV peak) with Si concentration is in good agreement with previous studies by Monroy et al.[106] and Nepal et al. [104] who attributed it to the increasing Si concentration and the variation in the bandgap energy respectively.

The origin of the 3 eV peak is assumed to be recombination between a shallow donor (Si) and a deep acceptor [105]. The deep acceptor is most likely a triply-charged cation vacancy $(V_{III})^{3-}$ [87, 99].

The relative intensities of the defect peaks give valuable information about the formation energy and incorporation of the different defect centres. The singly charged and the doubly charged defect peak have similar intensities for the two lower doped samples with a slight increase in intensity of the doubly charged defect with increasing Si concentration. Increasing the Si doping concentration further leads to a further shift of the Fermi level leading to the incorporation of an additional defect centre at 3 eV, the triply charged cation vacancy. The incorporation of this strongly compensating defect can explain the observed increase in the measured resistivity.

The spectra of sample series 3, with an AlN concentration of $(94.5 \pm 1.0)\%$ show a slightly different behaviour than sample series 1. The spectra of all samples consists of an $Al_xGa_{1-x}N$ NBE peak, the defect peak associated with the (V_{III}-

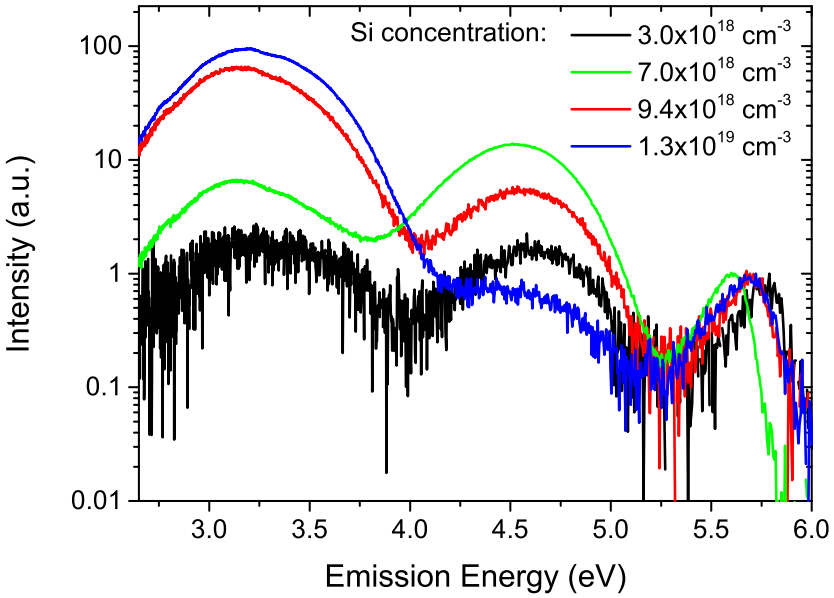

Figure 4.22: Room temperature CL spectra for sample series 3 with an AlN% of $(94.5 \pm 1.0)\%$, normalised on the $Al_xGa_{1-x}N$ NBE peak.

$2O_N)^-$ complex and a broad low energy defect band consisting of the emission from the $(V_{III}\text{-}O_N)^{2-}$ complex as well as the triply charged cation vacancy.

The defect peak associated with the triply charged cation vacancy is already present for the lowest doped sample with a Si concentration of $3\times10^{18}\,cm^{-3}$ which has not been observable for the similar doped sample of sample series 1 (with $81.5 \pm 1.0\%$ AlN). This is caused by the reduction of the formation energy of the triply charged cation vacancy with increasing AlN% as observed in sample series 4 (see Fig. 4.18). The increasing intensity of this peak with increasing doping concentration is caused by a reduction of the formation energy with increasing Si concentration.

The intensity of the defect peak associated with the $(V_{III}\text{-}2O_N)^-$ complex shows an interesting behaviour, first it increases with the doping concentration, reaching a maximum for the sample with a doping concentration of $7\times10^{18}\,cm^{-3}$ and then decreases with further increasing doping concentration. This behaviour is likely caused by a switch in the relative formation energy of the $(V_{III}\text{-}2O_N)^-$ complex and the $(V_{III}\text{-}O_N)^{2-}$ complex. For the lower doping concentration the singly charged complex will have the lower formation energy, which means that the available oxygen atoms favourably incorporate in this complex, while for higher doping concentration the doubly charged complex will have a lower forma-

tion energy, incorporating more of the available oxygen atoms in this complex, leaving fewer to incorporate in the singly charged one.

Conclusion

In conclusion, the luminescence properties of the different $Al_xGa_{1-x}N$:Si samples offer an explanation for the observed trends in the resistivity measurements by analysing the different peaks, present in these samples, and their relative intensities. The association of the different peaks with different acceptor states in the semiconductor offers valuable information in the optimization of the growth conditions for $Al_xGa_{1-x}N$:Si layers emphasizing the necessity of ultra pure precursors, to reduce the amount of available oxygen during the growth of these layers.

4.4.3 In depth analysis of $Al_{0.81}Ga_{0.19}N$:Si layers

Further analysis of these samples focussed on sample series 1 as it showed the lowest resistivity of all sample series, while at the same time offering a wide Si doping concentration to be investigated. The three samples of this series have been characterised by CL hyperspectral imaging and SE-imaging, further informations about the samples were provided by M. Nouf Allehiani who performed electron channelling contrast imaging (ECCI) as well as by TU-Berlin who performed atomic force microscopy (AFM) measurements on these samples.

Influence of the growth morphology on the luminescence properties

The sample morphology was characterized by SE-imaging as well as AFM measurements. The results of these investigation are shown in Fig. 4.23

SE and AFM images (Fig.4.23) reveal that the morphology of samples A and B mainly consists of different sized hexagonal domains while the morphology of sample C is dominated by step bunches with a periodicity of 3.5 µm, with hillocks on the terraces between the step bunches. The change in the surface morphology can be attributed to a different miscut angle of the underlying substrate as seen in section 4.2 and reported in literature [77, 61]. The periodicity of the step bunches reflects the periodicity of the underlying ELO-template, which was reported to us by the growers and can be seen in Fig. 4.26.

Low magnification room temperature CL NBE intensity maps of all three samples are shown in Fig.4.24. In these measurements a strong reduction of the NBE luminescence intensity along a periodic array of lines can be observed for samples A and B. The periodicity of these features is 3.5 µm. For sample

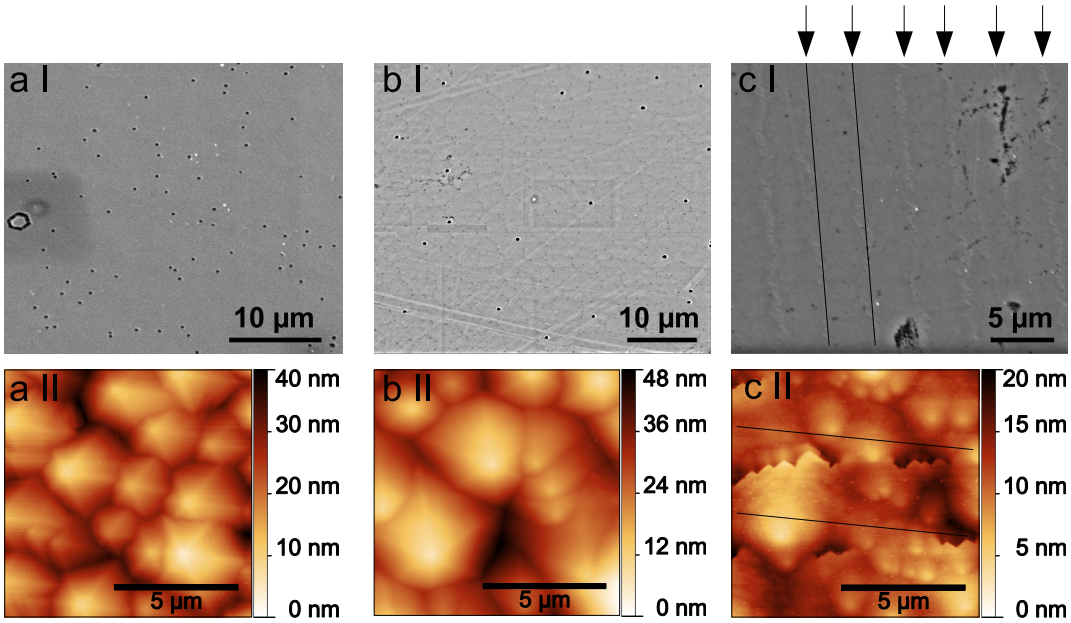

Figure 4.23: SE (I) and AFM (II) images of samples A(a), B(b) and C(c). AFM image courtesy of TU-Berlin. The step edges in sample C are marked with arrows and two lines are drawn in the SE and AFM image for clarity.

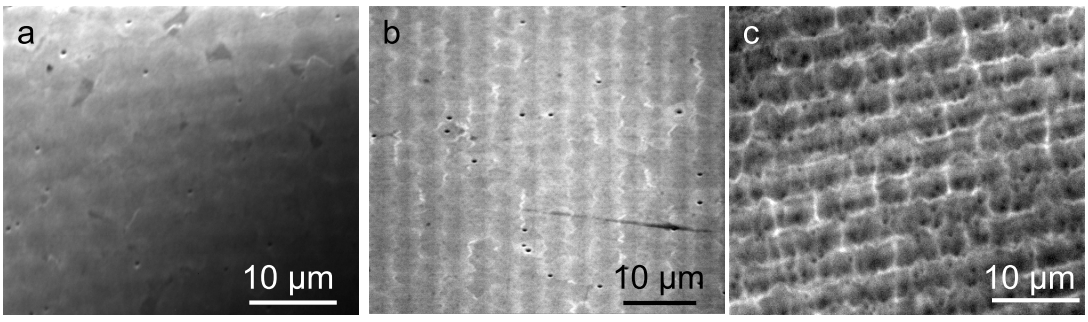

Figure 4.24: Low magnification room temperature $Al_xGa_{1-x}N$ NBE intensity maps of sample A (a), B (b) and C (c).

C the reduction of the NBE luminescence intensity is not as clearly visible in the low magnification measurement, thus a CL map has been taken at a higher magnification, the results of which are shown in Fig. 4.25. It is visible that in the step bunching area the bandgap is decreased. This can be due to a higher Ga incorporation along the step edges or a change in the local strain. It was found by Rieger et al. [107] that the bandgap of AlN changes with 24 meV/GPa and by Teisseyre et al. [108] that the bandgap of GaN changes with 40 meV/GPa. If the observed change in the emission energy of about 40 meV would be caused by strain this would indicate a local strain of 1 GPa which is about the strain expected for GaN grown fully strained on AlN [109] and thus highly unlikely. The enhanced Ga incorporation at the step edge should lead to an increase in the intensity along the step edges, but it is visible that the intensity peak is reduced right at the step edge.

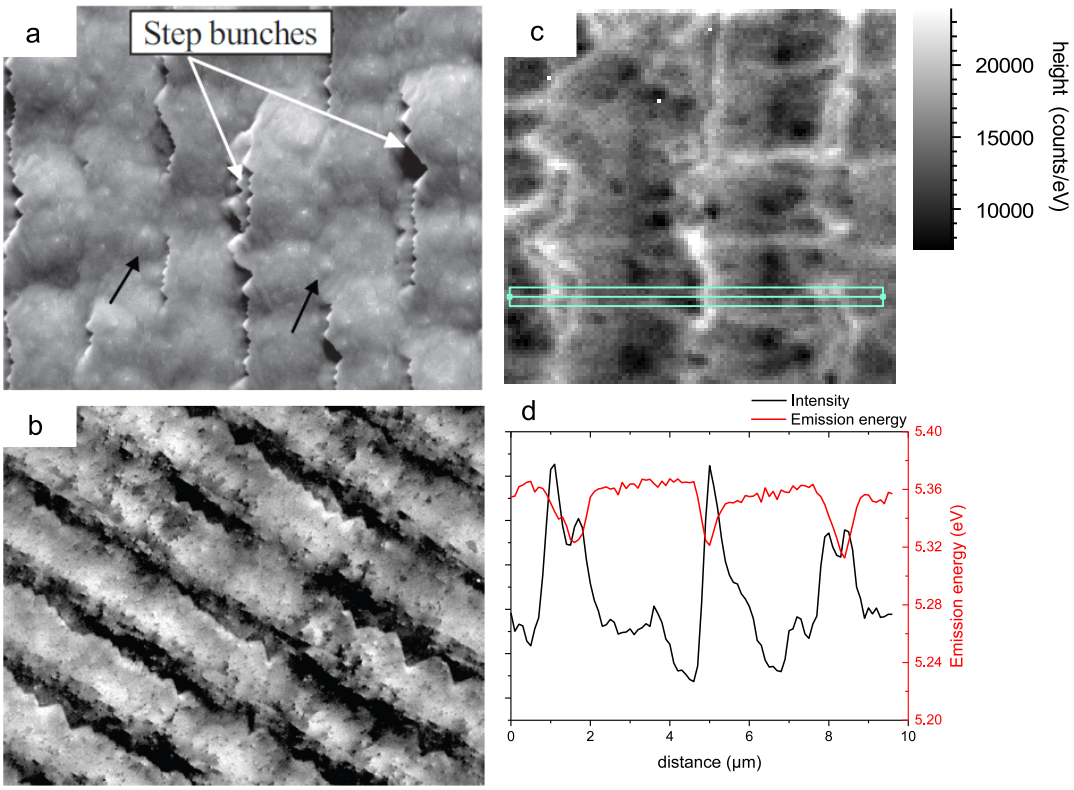

Figure 4.25: BSE topography image (a) and ECCI micrograph (b) as well as room temperature CL NBE intensity map (c) and line-scan (d) of the intensity (black) and emission energy (red) along the highlighted line of sample C. The BSE image and the ECCI micrograph are courtesy of Nouf M. Allehiani [110]

As the periodicity of the reduction in the NBE emission energy coincides with the periodicity of the underlying ELO-template it is safe to assume that the reason

for the observed reduction in the intensity is found in the vertical growth on top of the ELO-template. By performing cross-section CL imaging it was possible to investigate the vertical growth process. The results of the cross-section imaging for sample B are shown in Fig. 4.26.

The marked area in the SE-image (Fig. 4.26b) shows the area on which the CL images were acquired. In the SE-image the voids, generated by the ELO growth, the AlN template, the $Al_xGa_{1-x}N$:Si layer and the sample surface are all visible. The mean spectra of the recorded area (shown in Fig. 4.26a) reveals four different peaks, a peak at 5.92 eV associated with AlN near band edge emission from the AlN under-layer, a peak at 5.25 eV which we attributed to the $Al_xGa_{1-x}N$ layer and two defect peaks, associated with the singly and doubly-charged vacancy complexes. The AlN and $Al_xGa_{1-x}N$ peaks have been fitted to Gaussian functions for further analysis.

In the AlN intensity map (Fig. 4.26e) an increase in the AlN intensity is visible right after the coalescence of the AlN layer. This is most likely caused by an improvement in the crystalline quality of the grown layer. Furthermore dark vertical lines with a periodicity of 3.5 µm, originating from the voids can be observed.

TEM analysis performed at the Ferdinand Braun Institute für Höchstfrequenztechnik (FBH) (Fig. 4.27) and AFM imaging, done at the TU-Berlin, of this AlN layer explain the origin of these lines [111]. In the TEM image (Fig. 4.27) it can be seen that at the beginning of the growth threading dislocations are formed and propagate, during subsequent growth, in the [0001] direction. This continues until the layer coalesces. Step bunches, which can be seen in the AFM image, start from from the tip of the generated void and propagate over the sample surface. When a step bunch "moves" over a threading dislocation, the dislocation will change its angle of propagation [112]. This leads to the observed clustering of threading dislocation in the TEM image. As the spacing between that of the tips of the voids is 3.5 µm the periodicity of the step bunches as well as the clustered threading dislocations is 3.5 µm. This is also observable in the ECCI micrograph shown in Fig. 4.25 where an increased density of dislocations was found at the step edges.

In the $Al_xGa_{1-x}N$ NBE intensity CL image (Fig. 4.26c) the same observation can be made, a line with reduced intensity, compared to the surrounding area, propagates from the $Al_xGa_{1-x}N$/AlN interface to the surface of the layer. This indicates that the clustered threading dislocations stay clustered during the growth of the $Al_xGa_{1-x}N$ layer, resulting in a periodic array of areas with a higher

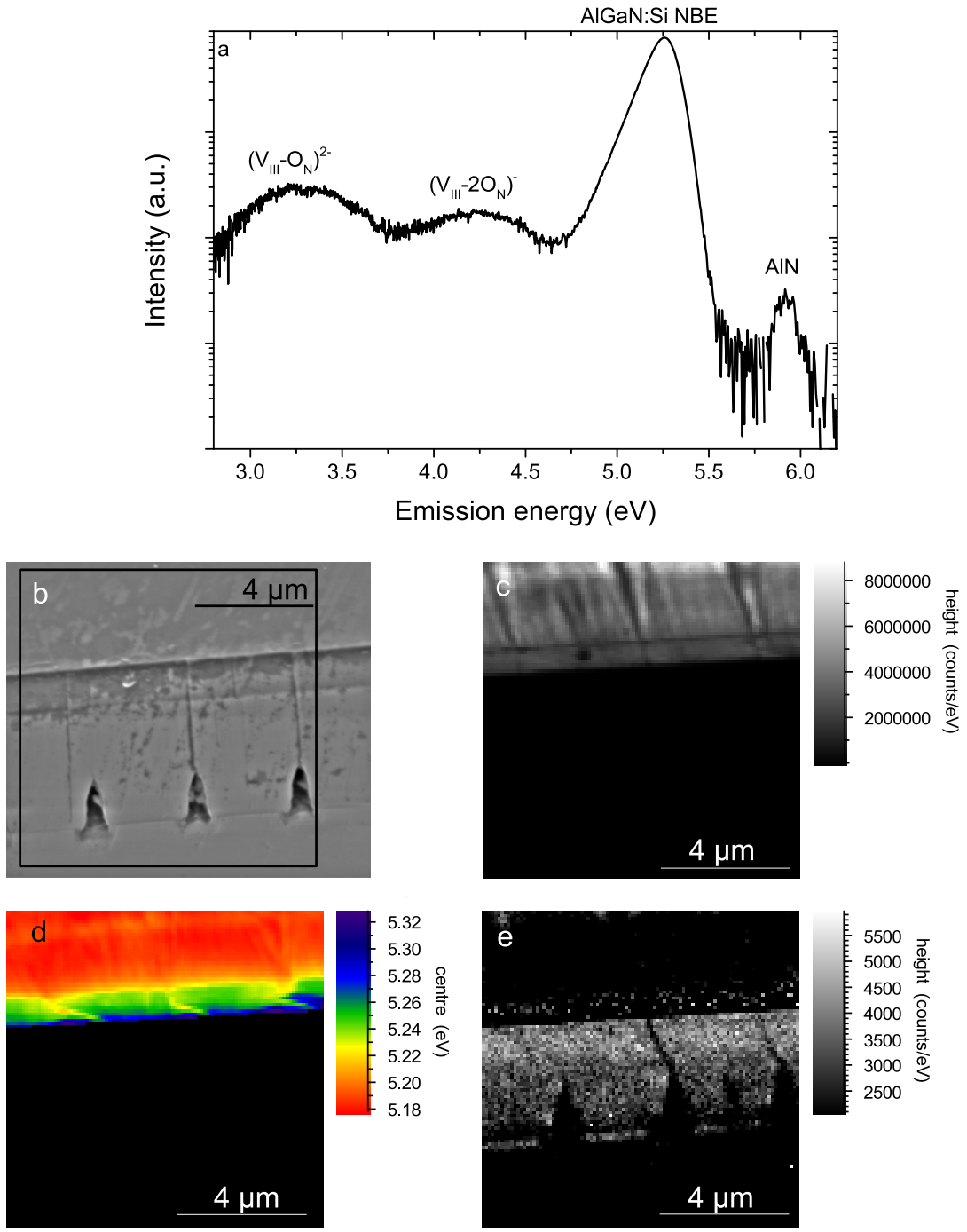

Figure 4.26: Mean room temperature CL spectra of the recorded area (a) cross-section SE-image (b) and fitted $10 \times 10\,\mu m^2$ room temperature CL-maps of the $Al_xGa_{1-x}N$ NBE-peak intensity (c), energy (d) and AlN intensity (e) of sample B. The marked area in the SE-image shows the area on which the CL images were acquired.

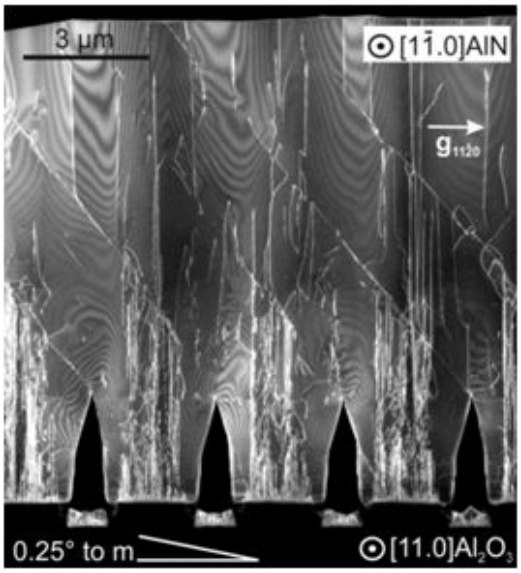

Figure 4.27: TEM cross-section, performed at the FBH, of an AlN/Al_2O_3 template [113].

threading dislocation density than the surrounding areas. This is the most likely explanation of the observed reduction in the NBE intensity for all samples in Fig. 4.24. This confirms, that threading dislocations act as non-radiative recombination centres in $Al_xGa_{1-x}N$ layers with high AlN%.

In the $Al_xGa_{1-x}N$ NBE emission energy map (Fig. 4.26d) two observations can be made. Firstly it is possible to observe a red-shift of the NBE emission energy from the $Al_xGa_{1-x}N$/AlN interface along the vertical growth direction towards the surface. This is in good agreement with the observations made for an increasing $Al_xGa_{1-x}N$ layer thickness in the previous section (section 4.3), indicating that the bending threading dislocations lead to a relief of compressive stress along the growth direction. Additionally it is possible to ascertain compositional inhomogeneities along the growth direction. The inhomogeneity starts at the $Al_xGa_{1-x}N$/AlN interface and is visible by tripod like patterns, with a clear energy shift to the surrounding material. The patterns consist of lines with a higher GaN content. It is observable that the pattern is formed by two lines originating from the interface, which then propagate in different directions. When both lines meet they nearly annihilate and form a new GaN rich line, propagating at a slightly changed angle through the material. This was already observed by Zeimer et al. [111] and attributed to the steps bunches on the AlN surface, with one of the lines originating at the bottom of a step edge of the AlN and the other line originating at the top of the step edge.

High magnification room temperature CL hyperspectral imaging was performed to investigate the influence of the surface morphology on the luminescence properties. It shows that there is a noticeable shift in the energy and intensity of the NBE emission across each sample. Samples A and B show a domain structure (Fig. 4.28 c,d), whereas sample C shows a strong shift in the emission energy along step bunches (Fig. 4.25). The energy variation in sample C is due to a higher GaN incorporation at the step edges which results in a lower bandgap compared to the surrounding material and explains the increase in the NBE intensity [111, 61], as was discussed in more detail in section 4.2. The variation in the emission energy between the different domains in samples A and B could be due to exciton localization at grain boundaries [114] or compositional inhomogeneity.

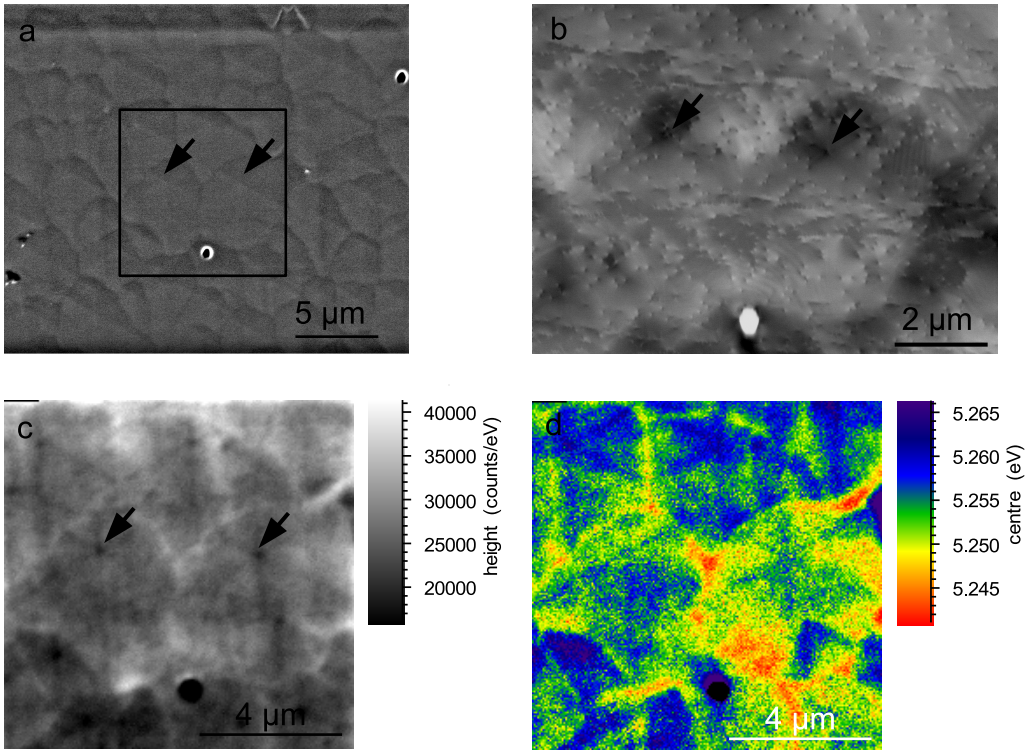

Figure 4.28: SE a) and ECCI image b) as well as room temperature CL $Al_xGa_{1-x}N$ NBE peak emission intensity c) and peak emission energy d) of sample B. The CL and the ECC image were taken in the boxed area in the SE-image.

SE-imaging, CL hyperspectral imaging and ECC imaging (by M. Nouf Allehiani) were performed on the same sample area (Fig. 4.28) to determine the cause of this effect. We found that the CL NBE intensity is reduced at the apex of each hillock, while ECCI reveals that a threading dislocation with a screw component is located at the apex of each hillock (arrows in Fig. 4.28 a,b,c). As a

result we conclude that the different domains are formed due to spiral growth around a dislocation with a screw component [115], which acts as a non-radiative recombination centre for the NBE emission. Threading dislocations with a screw component intersecting the surface of a layer can form a pinned step. Under favourable conditions this might bow out and form a spiral centred on the dislocation. The width of the spiral is determined by the progression of the pinned step (see section 2.2.2) around the dislocation and is limited by the critical curvature. The resulting hillock is formed from the spiral ramp created by the terrace associated with the pinned step [115]. The formation of the terraces during the during the spiral growth will introduce step edges on the surface, on which GaN is much more easily incorporated than AlN, due to the higher Ga atom mobility. This explains the differences in the emission energy between the hillocks, observed in Fig. 4.28 as the terrace width and step edge density will differ between the different hillocks. In contrast with ref. [114] grain boundaries can be excluded as the cause of this effect as an increased density of dislocations along the domain boundaries in these samples [116] was not observed. For the spiral growth to shape the morphology of a sample surface an additional criterion has to be met. The time for one full rotation of the spiral around the pinned step has to be smaller than the time between two free steps passing, as each free step passing the area of the hillock will annihilate one spiral [115, 117]. This means that an increase of the frequency of free steps passing an area will lead to a decreasing hillock height and can lead to hillocks vanishing from the surface. One way to increase the frequency of free steps is by changing the miscut angle of the underlying substrate. An increase in the miscut angle will, as discussed in section 4.2, lead to a decrease in the terrace width between the steps and thus increase the frequency of passing steps [117]. This explains the change of the morphology from sample A and B to sample C, sample C is most likely grown on a substrate with a higher miscut angle, which decreases the terrace width between steps and increases the frequency of free steps. For sample C the frequency of the free steps is higher than the angular frequency of the advancement of the spiral which leads to a morphology marked by step bunches instead of hillocks.

Influence of threading dislocations on the spatial distribution of defect luminescence

Fig. 4.29 shows the back scattered electron (BSE) image and the intensity distribution of the low energy (3.36 eV) defect CL for sample B. Clear regions with brighter defect luminescence can be observed. Correlation between the CL maps

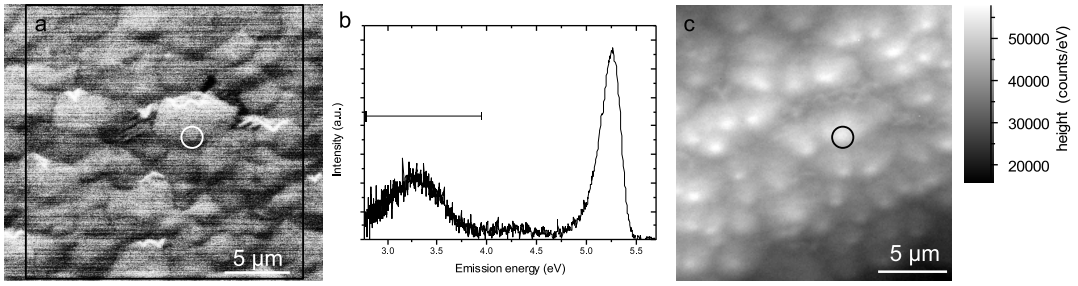

Figure 4.29: BSE image a), mean CL spectra of the marked region b) CL intensity map of the marked defect peak c) for sample B.

and the corresponding BSE images (one area of increased luminescence marked with circles in Fig. 4.29 for better visibility) reveals that the areas of increased defect luminescence intensity are located at and around the apex of each observed hillock. We concluded earlier that the hillocks form due to threading dislocations with a screw component as observed by ECCI.

This indicates that around screw dislocations the formation of compensating defect centres is enhanced. This could be caused by an increased oxygen incorporation around the screw dislocations, as oxygen is known to reduce the formation energy of V_{Al} leading to the formation of the observed $(V_{III}\text{-}2O_N)^-$ and $(V_{III}\text{-}O_N)^{2-}$ complexes or by the core structure of the dislocation itself, which could introduce deep level states in the band gap as calculated by Elsner et al. [118] and Belabbas et al. [119] for GaN. Different effects could lead to increased oxygen incorporation, namely the formation of a Cottrell atmosphere [26] or the preferential incorporation of oxygen at the inclined facets surrounding the screw dislocations. The formation of a Cottrell atmosphere is characterised by the drift and diffusion of impurities to a threading dislocation, reducing the strain field surrounding the dislocation. As no correlation between increased oxygen-related defect luminescence and pure edge type threading dislocations is observed, either the interaction energy between the impurities and dislocations with a screw component must be stronger or the formation of a Cottrell atmosphere is not the reason for the increased oxygen concentration. That no correlation between the pure edge dislocations and the defect luminescence is observed, is also in contrast to the calculations by Wright et al. [120] which predicted that edge dislocations decorated with V_{Al} would have lowest formation energy in AlN under nitrogen-rich conditions. Increased oxygen incorporation at different growth facets was observed by Hawkridge et al. [121] for open core screw dislocations in GaN and by Herro et al. [122] in AlN.

Conclusion

By combining the advantages of CL hyperspectral imaging and ECCI the influence of threading dislocations on the luminescence properties of $Al_xGa_{1-x}N$:Si was shown. This allows confirmation that threading dislocations act as non-radiative recombination centres for the NBE luminescence. The growth of hillocks has been attributed to threading dislocations with a screw component. Additionally the formation of hillocks leads to an increased defect luminescence intensity around the apices of the hillocks, indicating that both the incorporation of oxygen atoms and the formation of compensating defects are increased.

4.5 Summary

In this chapter the influence of various growth parameters on MOCVD grown $Al_xGa_{1-x}N$ layers was studied. In the first section two samples of $Al_xGa_{1-x}N$ grown on top of Al_2O_3 substrates with different miscut were investigated by CL in a low vacuum environment. SE and CL imaging showed that at higher miscut angles the sample surface changed from a hillock dominated morphology to a morphology dominated by step bunches, with smaller hillocks. It was found that these step-bunches introduce compositional inhomogeneities along step edges, where a higher GaN incorporation was measured. The increased GaN incorporation along the step bunches was attributed to the higher Ga atom mobility during growth.

In the second section the influence of the layer thickness on the luminescence properties of $Al_xGa_{1-x}N$ layers was characterized. The results of the SE and CL imaging showed a red-shift of the NBE emission, which was attributed to a relaxation of compressive stress in the layer through the bending of threading dislocations. Furthermore it was found that an increasing layer thickness leads to the coalescence of large hexagonal platelets, reducing the compositional inhomogeneity of the semiconductor, reducing the surface roughness and improving the crystal quality.

In the last section the Si doping of high AlN% $Al_xGa_{1-x}N$ layers was studied. The results show that the Si donor is incorporated linearly in $Al_xGa_{1-x}N$ and that the incorporation ratio does not depend on the AlN% of the layer. The dependence of the characteristics of the defect luminescence on the Si doping concentration was investigated and a clear correlation was found. Furthermore the effect of threading dislocations was investigated and it was found that all threading dislocations act as non-radiative recombination centres for the NBE emission. It was also shown that threading dislocations with a screw component

introduce spiral growth in the material as well as increase the incorporation of compensating and self-compensating defects.

Chapter 5

UV-LED structures

5.1 Introduction

There are many potential applications for semiconductor devices emitting in the UV spectral region, including: water purification [123], gas sensing and medical diagnostics. The most studied approach to realize these devices is by utilizing $Al_xGa_{1-x}N$ layers for the active zone as well as the device structure. Despite the significant boons of UV-LEDs there are many challenges remaining for highly efficient devices.

The doping of UV-LEDs, necessary to achieve a high carrier injection efficiency, is one of these challenges and has been discussed in section 4.4. Another challenge to overcome is the well documented phenomenon that with increasing AlN mole fraction in the QWs the external quantum efficiency drops (see Fig. 5.1). Additionally, the presence of non-radiative recombination centres as well as strain management in these devices presents challenges to overcome.

In the first section of this chapter, the behaviour of the luminescence intensity of $Al_xGa_{1-x}N$ QWs with increasing AlN concentration is studied and the most likely cause for the reduced intensity discussed.

A new approach for the realization of UV-LEDs is to replace the $Al_xGa_{1-x}N$ based active zone with an $In_xAl_{1-x}N$ based active zone. This new device design might be able to circumvent some of the efficiency limiting problems of traditional UV-LEDs. Due to the recent investigation of this device design the research is not as advanced and most of the current research efforts focus on reducing the challenges associated with the chosen material system, $In_xAl_{1-x}N$.

These challenges include the large difference in optimal growth temperature for InN ($\sim 550\,^{\circ}C$) [125] and AlN ($\sim 1100\,^{\circ}C$) [126], the large lattice mismatch of around 13.7% for the a-lattice constant and 14.5% for the c-lattice constant,

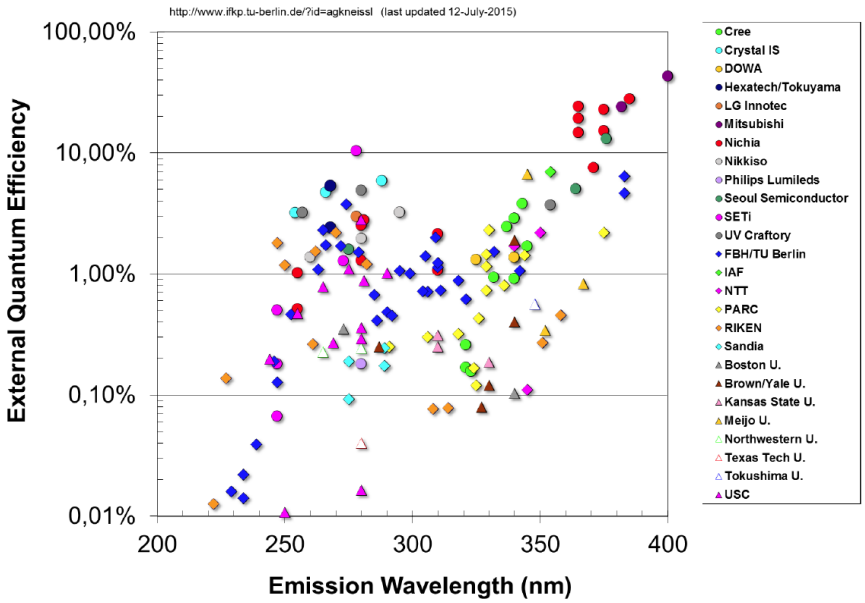

Figure 5.1: State of the art EQE for UV light emitting diodes. The original figure was published by Kneissl et. al [124] the updated version can be found on www.ifkp.tu-berlin.de/fileadmin/i1/thomsen/UV_LED_Efficiency_2015.pdf

reported reduction of the crystalline quality with increasing layer thickness, compositional splitting and a surface morphology consisting of hexagonal hillocks. Most of the research efforts put in the $In_xAl_{1-x}N$ focussed on the fabrication of lattice matched $In_xAl_{1-x}N$ layers on GaN which can be achieved for an In concentration of 17-18% [127]. In section 5.3 the influence of a number of growth conditions on the morphological and optical properties of $In_xAl_{1-x}N$ QWs has been investigated.

5.2 AlGaN UV-LED structures

In this section the well documented phenomenon of a reduced external quantum efficiency in $Al_xGa_{1-x}N$ UV-LEDs with increasing x (see Fig. 5.1) [128, 129, 130] is studied using CL hyperspectral imaging. For this purpose a series of samples was grown by the group of Prof. Michael Kneissl at TU-Berlin. All samples in the series were grown using a close coupled showerhead MOCVD reactor. TMGa, TMAl, NH_3 and SiH_4 were used as precursors for the investigated samples. The samples were grown on an AlN/Al_2O_3 template on which an AlN/GaN superlattice was deposited, followed by 650 nm undoped $Al_{0.5}Ga_{0.5}N$ and 4.8 µm Si-doped $Al_{0.5}Ga_{0.5}N$. On top of this 40 nm highly Si-doped $Al_xGa_{1-x}N$ as well as a 5 times $Al_yGa_{1-y}N/Al_xGa_{1-x}N$ QW/QB active zone were grown. The topmost layer consists of a 25 nm thick $Al_{0.7}Ga_{0.3}N$ electron blocking layer. The sample structure is schematically shown in Fig. 5.2. The QW composition of the samples in the series has been varied between 20% AlN and 45% AlN while the composition of the QB and the first barrier has been adjusted correspondingly from 33% AlN to 55.5% AlN, in order to keep the barrier height constant ($\Delta E_{QB-QW} = 0.29\,eV$) over the sample series (see table 5.1).

Sample Nr.	x (QB) [%]	y (QW) [%]	ΔE_{QB-QW} [eV]
1	55.5	45	0.29
2	51	40	0.29
3	39	27	0.29
4	33	20	0.29

Table 5.1: AlN concentration in the QB (x) and QW (y) for the $Al_yGa_{1-y}N$ QW sample series in percent.

The spectra of all samples were recorded with the CL setup described in section 3.2.2 using an acceleration energy of 5 keV which resulted in a penetration depth that allowed to obtain the luminescence properties of the QW region as well as the first barrier. The recorded spectra are shown in Fig. 5.3 and exhibit a QW emission wavelength between 322 nm and 279 nm as well as a clear intensity maximum for the sample with a QW containing 20% AlN. The measurement shows that an increasing AlN composition in the QWs from 20% to 45% leads to a strong reduction of the QW intensity. The low intensity peaks, for the two samples with the lowest AlN concentration, at the high energy side of the QW peaks are due to carriers recombining in the first 40 nm thick $Al_xGa_{1-x}N$:Si barrier.

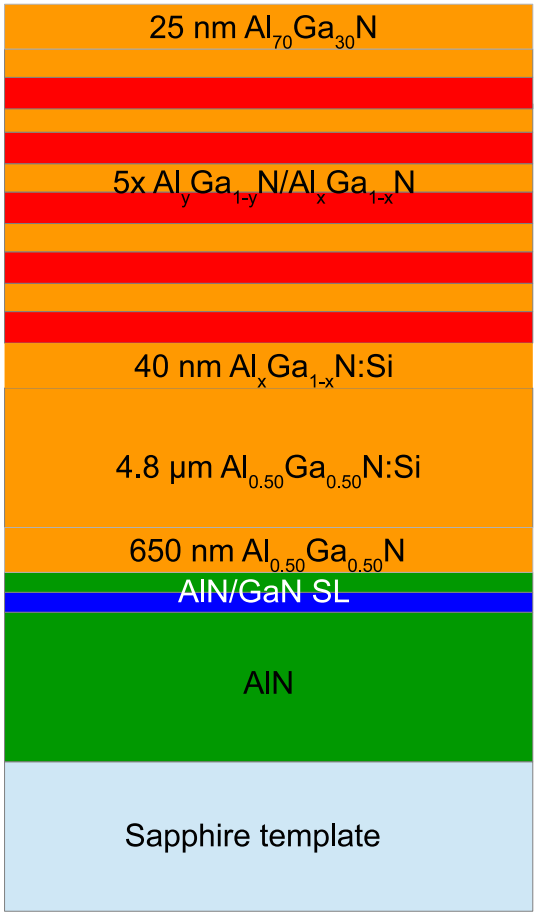

Figure 5.2: Layer structure of the investigated $Al_yGa_{1-y}N$ QW samples.

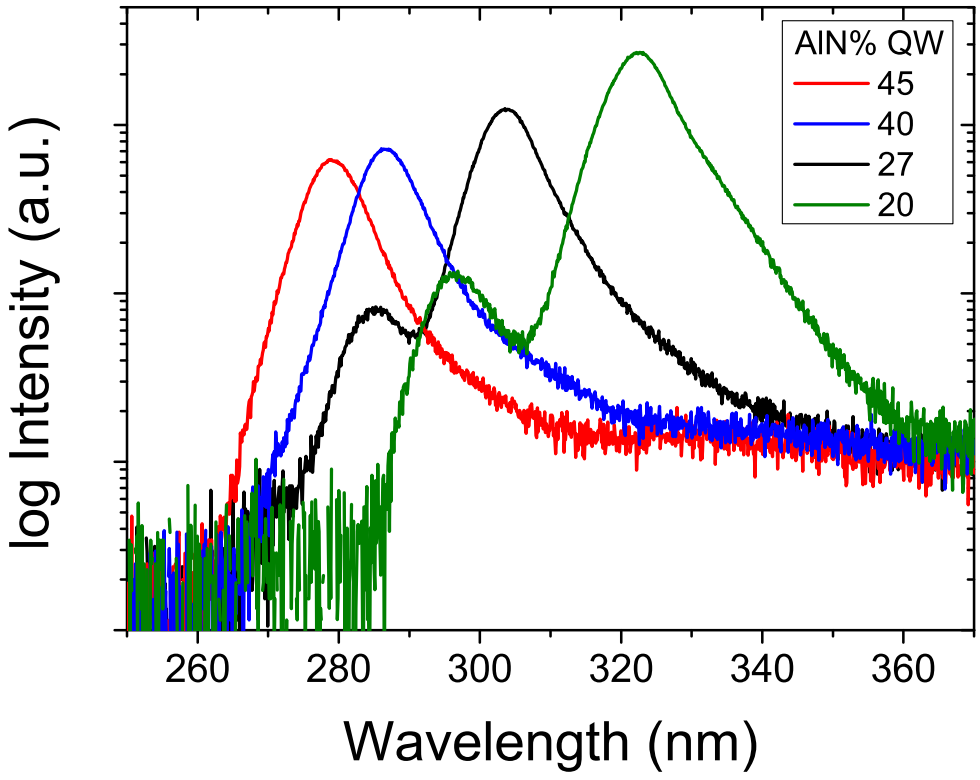

Figure 5.3: Spectra of the $Al_yGa_{1-y}N$ QW series with different QW and QB compositions. A reduction of the measured QW intensity with increasing AlN composition can be seen, the low intensity high energy peak, which can be observed for two of the samples, originates from the 40 nm thick first barrier.

The strong reduction of the emission intensity with decreasing emission wavelength has been observed by a number of groups [128, 129, 130] and attributed to a various different mechanisms, namely: an enhanced incorporation of non-radiative defect centres (e.g. threading dislocations); alloy broadening; and more recently a change in the optical polarization of the emitted light with increasing AlN composition [128, 129, 131, 132]. The present sample series has also been characterised with electron channelling contrast imaging (ECCI) by M. Nouf Allehiani and a near constant threading dislocation density has been found. This excludes an increased incorporation of these defects as the cause for the decreasing intensity. By analysing the recorded spectra shown in Fig. 5.3 a near constant FWHM of (9.5 ± 1) nm has been found, evidencing that the effect of alloy broadening is negligible for this sample series. This suggest that the observed decrease in intensity is caused by the change in the optical polarization.

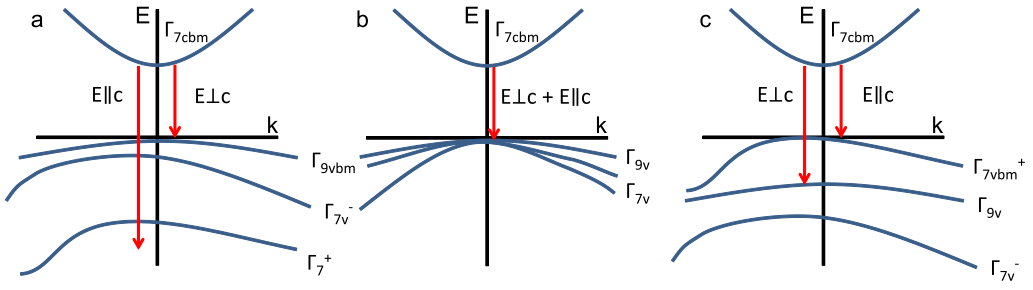

Figure 5.4: Schematic bandstructure of GaN (a) $Al_{0.25}Ga_{0.75}N$ (b) and AlN (c) according to [128].

Wurtzite crystals are of C_{6v}^4 symmetry which means that the conduction band forms of s-orbitals and transforms the Γ point congruent with the Γ_7 representation of that space group. The valence bands are formed out of combinations of products of p^3 like (p_x,p_y,p_z-like) orbitals with spin functions. Under the influence of crystal field splitting the sixfold degenerate Γ_{15} level associated with the cubic system splits into the Γ_{6v} and Γ_{1v} valence bands which seperate into the Γ_{9v}, Γ_{7v}^+ and Γ_{7v}^- bands due to spin-orbit coupling [133]. Since the splitting of the p-like states at the VBM is affected by the crystal-field, the optical transition matrix elements are strongly related to the crystal symmetry [134]. The small spin-orbit coupling in the nitrides makes it possible to approximate the hole bands as follows:

$$
\begin{aligned}
|\Gamma_{9v}; \pm 3/2> &= \frac{1}{\sqrt{2}}|X \pm iY, \pm 1/2> \\
|\Gamma_{7v}^{-}; \pm 1/2> &\sim \frac{1}{\sqrt{2}}|X \pm iY, \mp 1/2> \\
|\Gamma_{7v}^{+}; \pm 1/2> &\sim |Z, \pm 1/2>
\end{aligned}
$$

As can be seen from this equation, the Γ_{7v}^{+} band is composed only of the $|Z>$ component which shows that only optical transitions with TM polarization are allowed as only those conserve angular momentum. [134]. More information is found in the books of Morkoc [133], Nakamura et al. [134] and Cardona et al.[135].

Light emitted from GaN layers has been found to be primarily TE polarized [136], meaning that the electric field of the emitted light is perpendicular to the (0001) c-axis, labelled E$\perp$c in Fig. 5.4. This allows photons to be easily extracted from the top surface of substrate of the devices [129, 137]. For AlN and $Al_xGa_{1-x}N$ layers (with $x > 0.25$) on the other hand it was found that the emitted light is mostly TM polarized, having the electric field parallel to the (0001) c-axis, labelled E$\|$c in Fig. 5.4. This prevents an easy extraction of the generated photons from the top surface or substrate of the devices and results in a strong reduction of the measured intensity [128].

This change is attributed to a change in the internal bandstructure between GaN and AlN. The bandstructure of GaN (schematically shown in Fig. 5.4a) at the Γ-point is determined by crystal field splitting and spin-orbit coupling [136]. The topmost valence band is the Γ_{9vbm} band to which electrons from the conduction band can recombine by emitting TE polarized photons. The second valence band is a Γ_{7v}^{-} band which mainly allows recombination processes including TE polarized photons, this band is located 6 meV below the Γ_{9vbm} band [136]. The third valence band is the Γ_{7v}^{+} band , separated by 43 meV from Γ_{9vbm} band and mostly allows recombination processes with TM polarized photons (see table 5.2). With the Γ_{9vbm} only allowing TE polarization it is easy to understand that light generated in GaN layers is to a high degree TE polarized [128].

In comparison to the bandstructure of GaN the bandstructure of AlN exhibits vastly different properties. Due to a negative crystal field splitting in AlN the topmost band is the Γ_{7vbm}^{+} band, separated by 213 meV from the Γ_{9v} band and by 226 meV from the Γ_{7v}^{-} band (see Fig. 5.4c) [130]. The negative crystal field

	relative square of the transition dipole matrix element	
Transition	E‖c	E⊥c
$E_1(\Gamma_{7cbm} \rightarrow \Gamma_{9vbm})$	0	1
$E_2(\Gamma_{7cbm} \rightarrow \Gamma_{7v}^{-})$	0.053	0.974
$E_3(\Gamma_{7cbm} \rightarrow \Gamma_{7v}^{+})$	1.947	0.026

Table 5.2: Calculated relative square of the transition dipole matrix element I_v of GaN for light polarized parallel and perpendicular to the (0001) c-axis. Calculated by Chen et. al [136]

splitting was found to be due to AlN having a smaller c_0/a_0 lattice constants ratio and a larger u parameter, which is a dimensionless cell-internal coordinate that distinct the two nearest-neighbour anion-cation bind lengths [130]. The large negative crystal field splitting not only influences the order of the valence bands but also strongly influences the optical properties of AlN. Namely that the $E(\Gamma_{7cbm} \rightarrow \Gamma_{7vbm}^{+})$ recombination process dominates the emission of AlN layers which is thereby mainly TM polarized.

Knowing the bandstructure of GaN and AlN and the resulting optical properties helps in understanding the optical properties and emission characteristics of $Al_xGa_{1-x}N$ layers. For $Al_xGa_{1-x}N$ it was found that for $x < 0.25$ the emitted light is mostly TE polarized, while for $x > 0.25$ TM polarized light has a higher intensity, with both polarizations being equal at $x = 0.25$ where all three bands are degenerated [128] (see Fig. 5.4b).

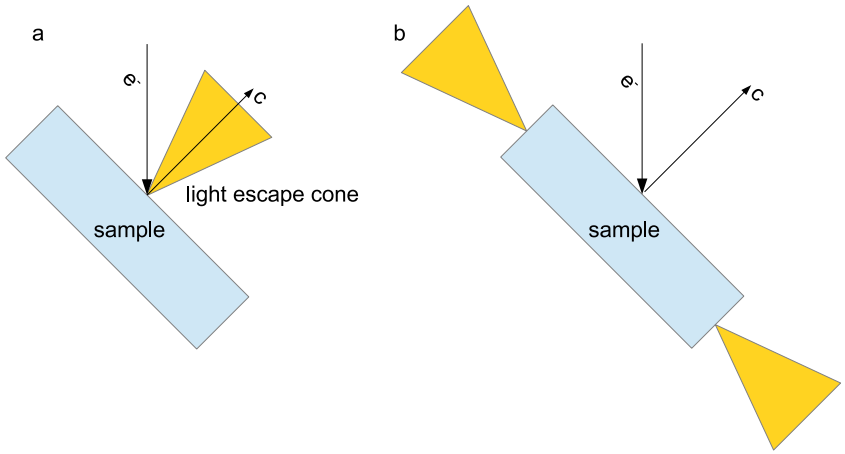

Figure 5.5: Light extraction for TE (a) and TM (b) polarized light for samples grown along the (0001) c-axis. The e^- denotes the excitation source.

This means that for $Al_xGa_{1-x}N$ layers the intensity of TE polarized light will decrease with increasing AlN% while the intensity of TM polarized light increases

with increasing AlN composition. This behaviour will cause reduced measured intensities for increasing AlN% due to the light propagation of TM polarized light in a semiconductor crystal and our measurement setup (see Fig. 5.5). While it would generally be possible to correct measured intensities for the polarization switch, this would need exact information about the strain state as well as the temperature in QWs as both parameters were found to have an effect on the degree of polarization as investigated by Kolbe et. al [138].

The change in the polarization with increasing AlN content provides a great challenge for the fabrication of $Al_xGa_{1-x}N$ based UV LEDs as most LED design currently in use are surface-bottom emitters. This means that the light extraction is done from the surface or through the substrate of the grown devices. The light propagation of TM polarized light on the other hand will only allow a fraction of the generated light to be extracted in this way which means that either new LED designs have to be found in order to extract light with high efficiency from the edge of the sample or new geometries have to be utilized which allow for a top extraction, as proposed by Zhao et al [139].

5.3 InAlN LED structures

5.3.1 QW growth temperature

To investigate the influence of the QW growth temperature, on the luminescence properties of $In_xAl_{1-x}N$ UV-LEDs, a sample series was grown by MOCVD at Tyndall. The growth temperature of the QWs was changed between the different samples from 710 °C to 790 °C. The sample structure is shown in Fig. 5.6 and consists of an AlN layer grown on top of a c-plane Al_2O_3 substrate followed by a 2 µm $Al_{0.53}Ga_{0.47}N$ buffer layer. The active region was grown on top of the buffer layer and consist of a 5× $In_xAl_{1-x}N/Al_{0.59}Ga_{0.41}N$ QW/QB structure. The final layer is an $Al_{0.83}Ga_{0.17}N$ cap layer grown on the last QW. The composition of the buffer layer, the barriers and the cap were determined by HR-XRD in Tyndall.

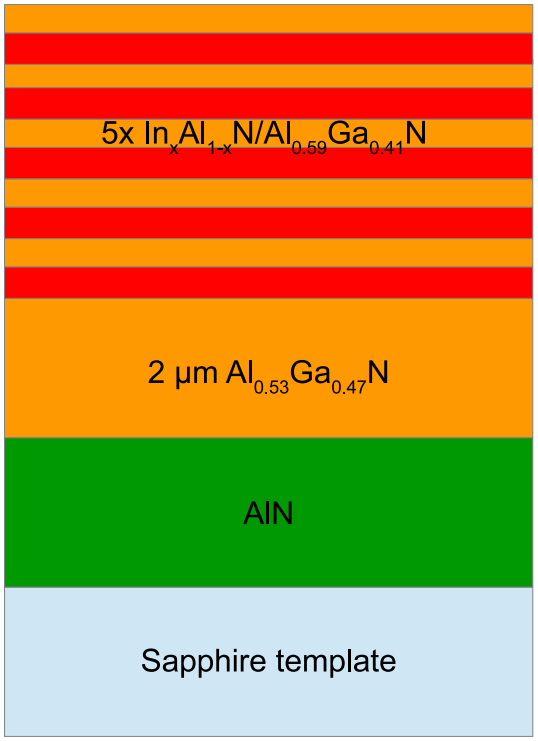

Figure 5.6: Layer structure of the investigated samples.

Luminescence properties

The normalised emission spectra of these samples, shown in Fig. 5.7, were measured using the CL setup described in section 3.2.2 with a beam energy of 5 keV. The spectra consist of an $Al_xGa_{1-x}N$ NBE peak centred around (258 ± 2) nm and

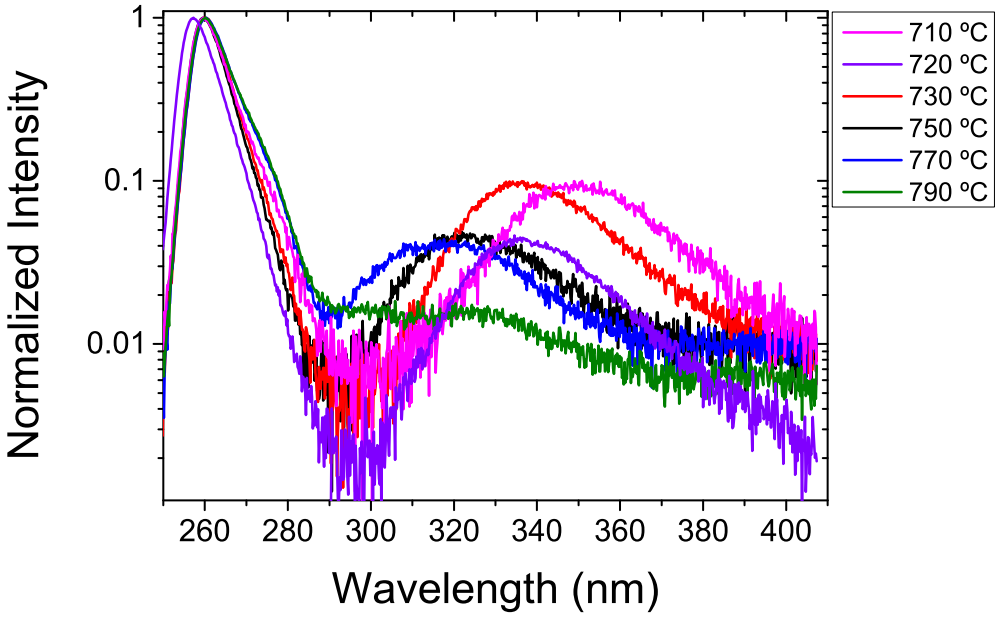

Figure 5.7: Normalised roomtemperature CL emission spectra of samples with a 5 period $In_xAl_{1-x}N/Al_{0.59}Ga_{0.41}N$ QW/QB structure with QW growth temperatures from 710 °C to 790 °C

a broad QW luminescence peak. The emission energy of the QW peak strongly depends on the growth temperature, blue shifting from 351 nm for 710 °C to 317 nm for 770 °C. At a growth temperature of 790 °C the quantum well peak is split into a double peak emitting at 300.5 nm and 330 nm. The $Al_xGa_{1-x}N$ NBE CL emission originates from the underlying buffer layer and the observed emission energy variation is most likely caused by unintentional growth variations.

By extracting the QW emission energy for each of the samples it is possible to observe a correlation between the emission energy and the growth temperature (shown in Fig.5.8), where the emission energy blueshifts with increasing growth temperature. This is caused by an enhanced In desorption rate, leading to a decreasing InN fraction within the QWs and thus an increasing bandgap. Calculating the InN concentration, using Vegards law and a bowing parameter of 3 [13], while disregarding the effect of electric fields, a decrease of the InN concentration of the grown structure by about 1% per 10 °C can be found. This value is considerably lower than values stated in literature, where an InN% change of approximately 2.5% per 10 °C is stated [140]. This apparent discrepancy could be caused by the difference in growth parameters between both series. It was for example found that a higher NH_3 flow rate increases the InN incorporation [140]

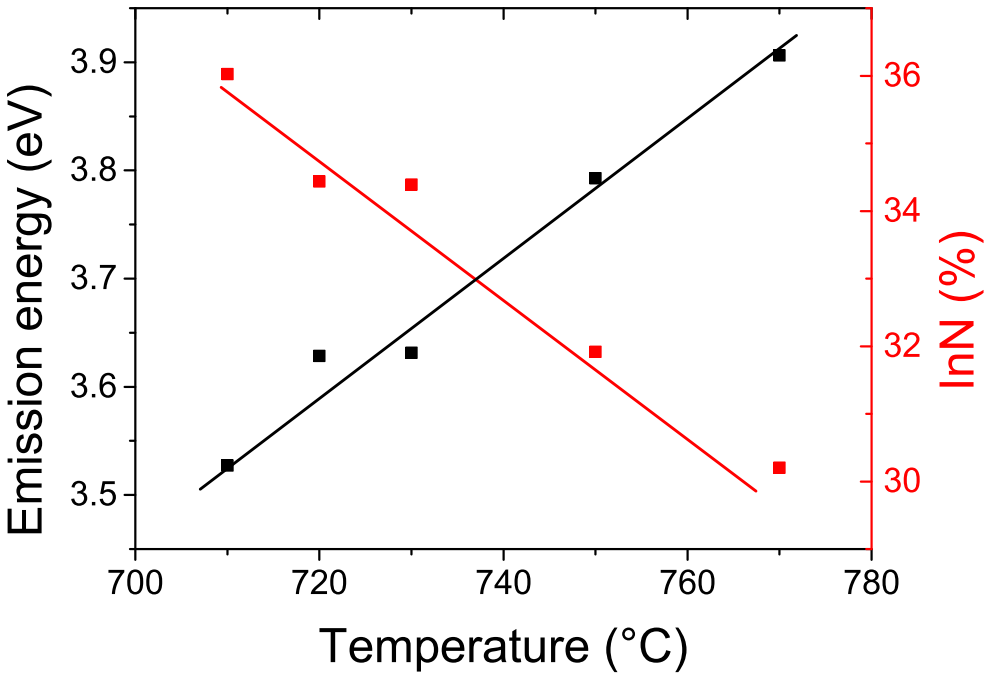

Figure 5.8: Extracted QW emission energy (black squares) and calculated InN concentration (red dots) in the QW for samples with a growth temperature between 710 °C and 770 °C. The InN concentration was calculated using Vegards Law [11] and a bowing parameter of 3. The lines are guides to the eye only.

while other studies found that an increase in reactor pressure can lead to a higher InN incorporation [141]. The sample grown at 790 °C was not included in this analysis due to the appearance of a double peak emitting at 300.5 nm and 330 nm. The appearance of the double peak is an indication for compositional splitting in the QW. This has already been observed by Fujimori et. al. [142] who attributed it to a possible phase separation or a strong compositional inhomogeneity.

To assess the possible influence of the QW growth temperature on the sample morphology and the compositional homogeneity of the QWs, SE-imaging and CL hyperspectral imaging were performed.

Morphology

The same sample morphology was found, by SE-imaging, for all samples. An example of the morphology at two different magnifications, for the sample with a QW growth temperature of 750 °C, is shown in Fig. 5.9.

A non-uniform morphology was found for all investigated samples. The morphology consists of two different well defined features, elevated hillocks as well as hexagonal domains. The hillocks as well as the domains exhibit one or more dark spots in their centres. The observed surface morphology is similar to the morphology discussed in section 4.3 indicating that the formation of the elevated hillocks as well as the hexagonal domains is not caused by the growth of the MQW structure but rather caused by the growth conditions used for the $Al_xGa_{1-x}N$ buffer layer. The main difference between the morphology of the samples under discussion and the morphology shown in section 4.3 are the dark features, which are not visible in the morphology shown in Fig. 4.10. This difference could indicate that these are caused by the deposition of the active region.

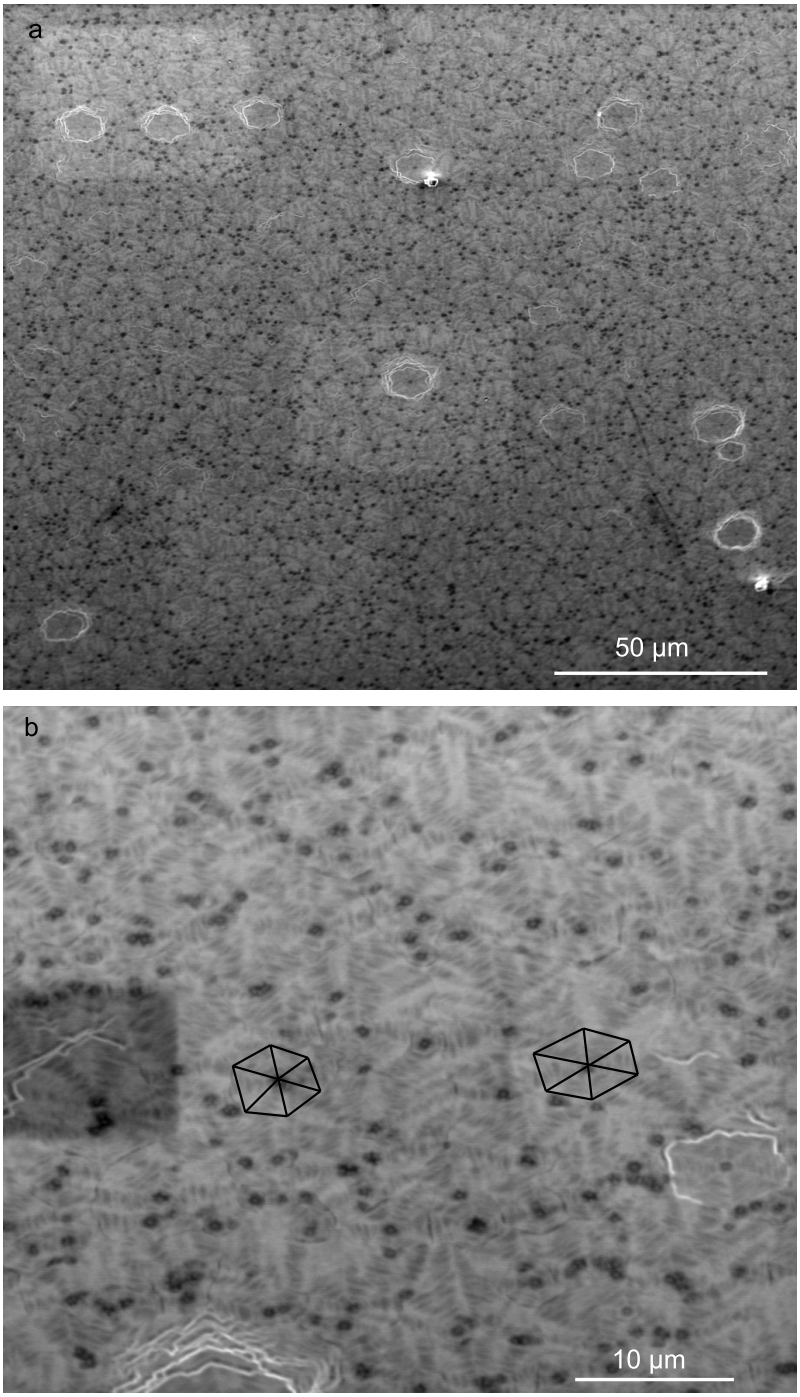

Figure 5.9: SE-image of the morphology of the sample with a QW growth temperature of 750 °C at two different magnifications. In both magnifications elevated hillock structures as well as hexagonal domains can be observed. Each of the structures features one or more dark circular spots in the middle.

CL hyperspectral imaging

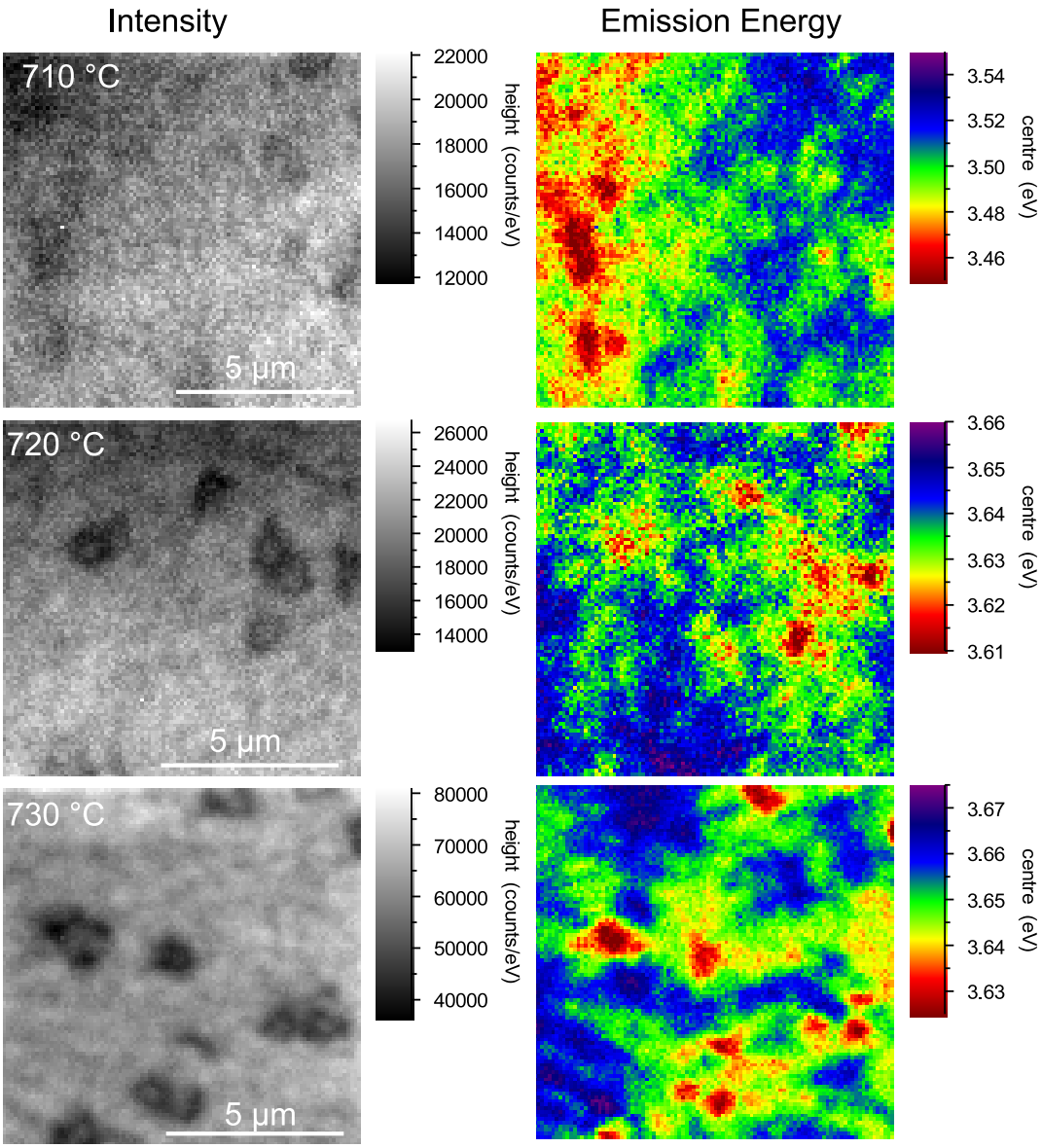

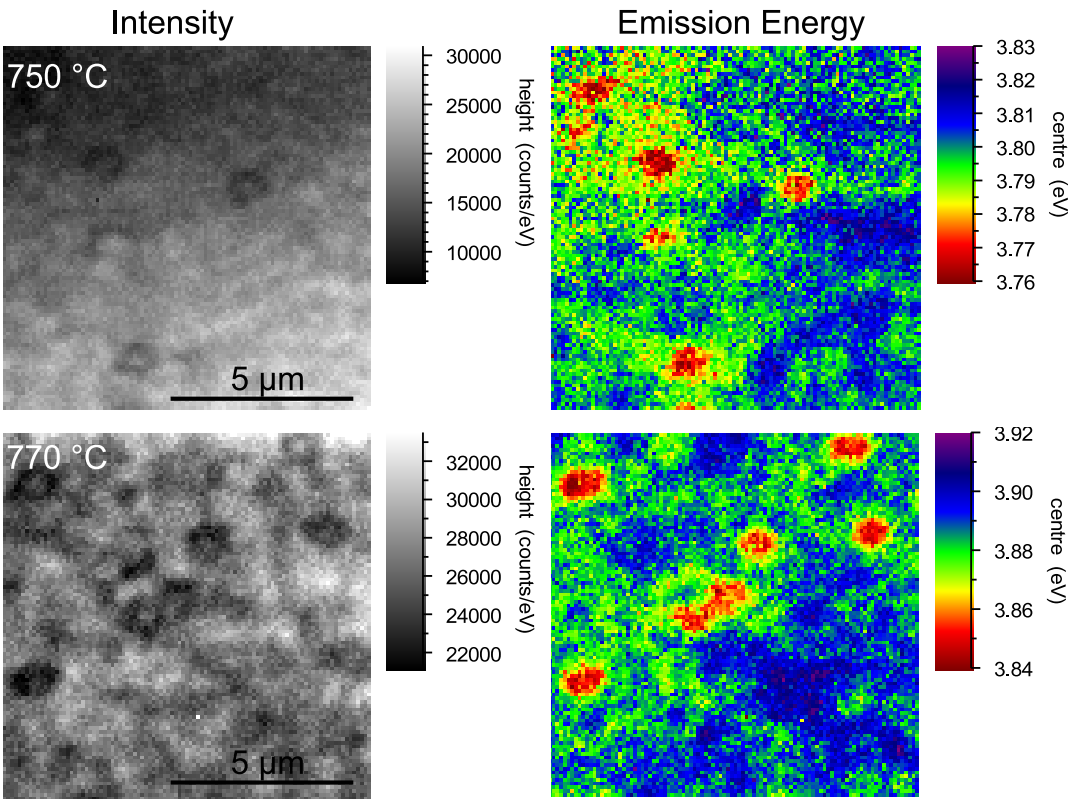

Figure 5.10: Intensity distribution and emission energy of the $In_xAl_{1-x}N$ QW for all samples with a QW growth temperature between 710 °C and 770 °C. All of the samples show a similar uniform intensity distribution apart from circular areas of decreased intensity. The emission energy of all investigated samples shows a strong red-shift in the areas where the intensity is reduced.

A Gaussian function was fitted to the $In_xAl_{1-x}N$ QW emission peak of the recorded CL spectra (shown in Fig. 5.7) for all samples to derive intensity as well as emission energy variations over the measured area. The results are shown for all samples in Fig. 5.10. The CL hyperspectral imaging of the sample series reveals that changing the QW growth temperature does not have a drastic impact on the luminescence properties apart from the emission energy. For all samples between 710 °C and 770 °C the intensity map shows a uniform intensity distribution with a strong reduction of the emission intensity at the circular features, indicating that they are caused by defects acting as non-radiative recombination centres. Examining the emission energy maps of each of the samples one finds that the variation in the emission energy between the different samples is similar, with a value of (70 ± 10) meV. Looking at the correlation between the intensity and the emission energy maps for each sample it becomes apparent that the circular areas in which the intensity is strongly reduced are also marked by a strong red-shift

of the emission energy. This indicates a preferential InN incorporation at these centres of non-radiative recombination. As all samples show the same general behaviour, a more in depth investigation will be performed on only one of the samples (QW temperature of $720\,°C$) at a higher magnification. The SE-image as well as the CL maps for the $Al_xGa_{1-x}N$ NBE peak and the $In_xAl_{1-x}N$ QW peak for this sample are shown in Fig. 5.11.

The high magnification SE-image shown in Fig. 5.11a depicts one of the smaller hexagonal domains observed in Fig. 5.9 with one of the dark circular spots in the centre of the domain. At this magnification it is possible to see that these smaller domains also exhibit a hillock structure. The terrace steps of the hillock as well as the ridges are clearly visible. The $Al_xGa_{1-x}N$ NBE CL intensity map (Fig. 5.11b) shows no correlation to this hillock structure whereas the CL emission energy is modulated by the hillock, with emission energy variations along the ridges and the terrace steps. The CL emission energy variation of the $Al_xGa_{1-x}N$ NBE emission (Fig. 5.11c) is caused by the different mobilities of Ga and Al adatoms which lead to a preferential incorporation of GaN at step edges and kinks provided by the hillock and thus a reduced emission energy at these sites. The $In_xAl_{1-x}N$ CL intensity (Fig. 5.11d) shows the same behaviour as shown for all samples in Fig. 5.10, a uniform intensity distribution with a strong reduction of intensity at a circular feature where the CL emission energy map (Fig. 5.11e) of the QW peak shows a strong red-shift. Matching the $In_xAl_{1-x}N$ CL maps with the SE-image it becomes apparent that the circular feature corresponds to the dark circular spot observed in the apex of the hillock.

The presence of hillocks on the sample surface offers a possible explanation for the observed strong compositional inhomogeneity (visible in Fig. 5.10) in the investigated samples. Hillocks can form, as discussed in section 4.4, due to spiral growth around a threading dislocation with a screw component in the apex of the hillocks. Assuming that the hillocks observed in these samples are formed due to this mechanism it is reasonable to assume that the dark spot observed in the SE-images corresponds to the location of the threading dislocation. This implies that in $In_xAl_{1-x}N$ layers the InN incorporation is increased around threading dislocations with a screw component, leading to the measured compositional inhomogeneity. The influence of threading dislocations on the compositional homogeneity of $In_xAl_{1-x}N$ and $In_xGa_{1-x}N$ layers has been studied by a number of authors.

Kehagias et al. [143] found an increased InN concentration in V-defects in $In_xAl_{1-x}N$ layers, forming a star like pattern with the increased InN concentration

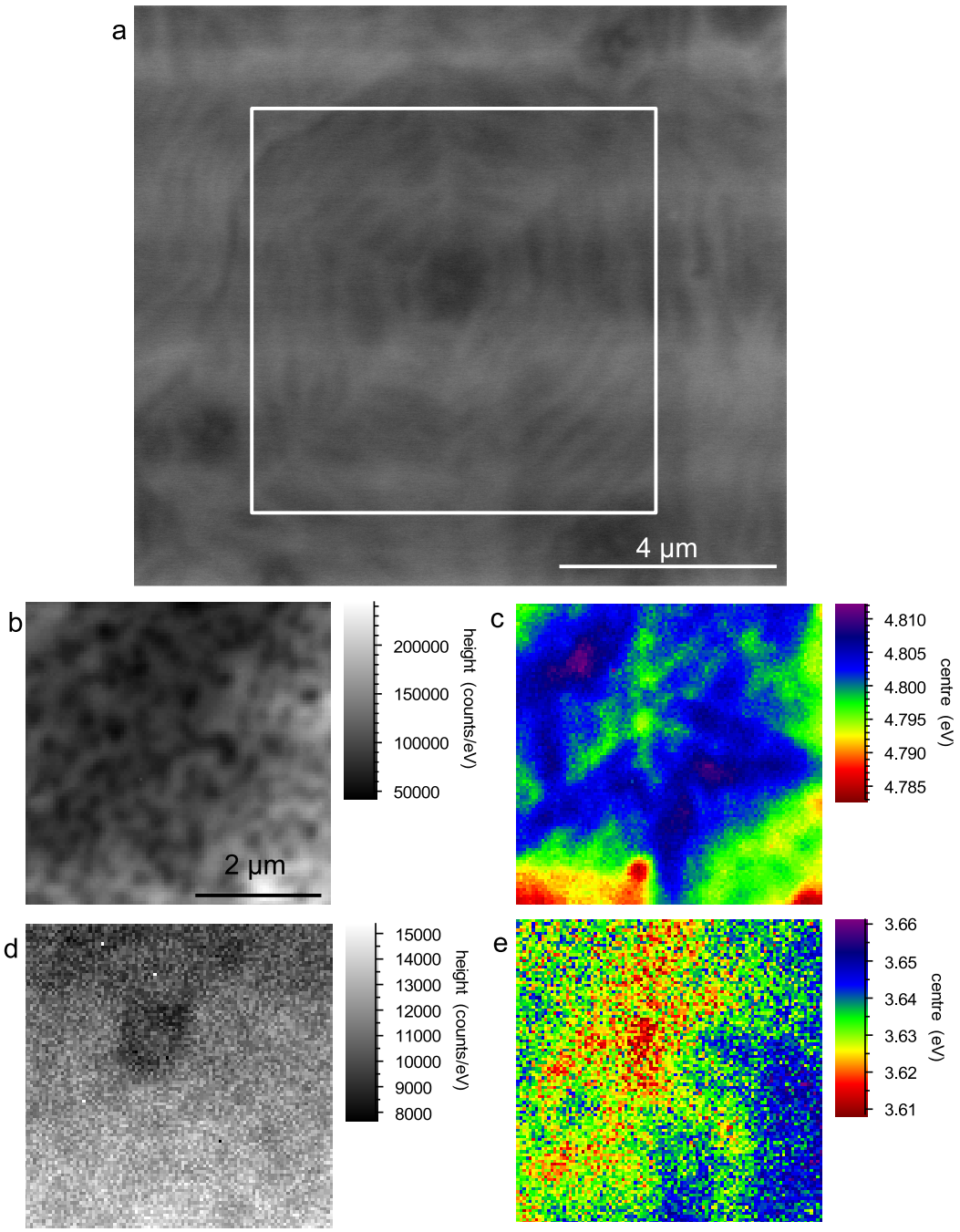

Figure 5.11: SE-image a), $Al_xGa_{1-x}N$ NBE intensity b) and emission energy c) as well as $In_xAl_{1-x}N$ QW intensity d) and emission energy e) of the sample with a QW growth temperature of 720 °C.

in the centre of the pyramid as well as on the ridges of the side walls. This observation is similar to the CL emission energy map of the $In_xAl_{1-x}N$ QWs in Fig. 5.11e in which a red-shifted emission energy was found at the apex of the hillock as well as lines with a red-shifted emission energy originating from the the apex.

The cause for InN agglomeration at screw dislocations has been studied by theoretical modelling by Lei et. al. [144]. They calculated the inner core energy of screw dislocations in AlN, GaN and InN and found that the core energy is lowest for screw dislocations in InN. They further found that by incorporating In atoms into the core of screw dislocations in GaN or AlN the dislocation energy significantly reduces and therefore their stability is increased. This study also showed that a large interaction energy between the dislocation and In atoms is the driving force for the compositional inhomogeneity in $In_xGa_{1-x}N$ and $In_xAl_{1-x}N$ alloys.

Mouti et al. [145] investigated the effect of strain fields caused by threading dislocations on composition modulations and surface morphology of $In_xAl_{1-x}N$ layers. They have investigated the influence of edge dislocations, screw dislocations and mixed dislocations and found that only threading dislocations with a screw component lead to the formation of pits.

For edge dislocations, which are characterised by small regions of opposite strain (tensile and compressive) on either side of the dislocation, they found that InN should segregate towards the tensile strained half of the strain field and away from the compressively strained half. This would reduce the relative strain fields as increasing the InN composition on the tensile strained half might reduce the strain field introduced by the dislocation. This effect is neither clearly visible in the CL emission energy maps of the $In_xAl_{1-x}N$ QWs nor can we observe edge dislocations in the QW CL intensity maps despite edge dislocations acting most likely as non-radiative recombination centres [146]. The lack of visibility of this effect in the CL maps might be due to the small lateral extension of the increased InN composition which should be in the range of a few nm and the large excitation volume of the chosen beam conditions which is in the range of 150 nm. Nevertheless, the InN segregation around edge dislocations could be the cause for the small InN variation generally observed in $In_xAl_{1-x}N$ layers.

For screw dislocations Mouti et al. [145] found the same star shaped variation in the local InN composition as reported by Kehagias et al. [143]. They explained the formation of this pattern by InN segregation to the dislocation core which causes the dislocation to open up, forming a pit in the surface of the $In_xAl_{1-x}N$

layer. The formation of the pit will then provide additional lattice sites in the <11-20> direction between (10-11) planes onto which InN preferentially bonds eventually forming the star shaped pattern. The deviation from a perfect pattern as observed in Fig. 5.11e can be explained if mixed dislocations are taken into account. Mixed dislocations introduce the same general pattern as screw dislocations which is then modulated by the edge component of the dislocation. The tensile and compressive half strain fields of the edge dislocation can influence the branches of the star. Branches which lie in the region with tensile stress were found to bend towards the axis of maximum stress, while branches lying in the compressive region will bend away from this axis, which leads to a less perfect star shaped pattern of the InN concentration around the dislocation.

Thus the compositional inhomogeneities observed in the QW CL emission energy maps in Fig. 5.10 and Fig. 5.11e can be explained by the presence of threading dislocations with a screw component. These were shown to lead to InN segregation into their core in order to reduce the core energy of the dislocation [144]. This will then in turn lead to the formation of a surface pit (dark features in Fig. 5.11a and Fig. 5.9) which provide lattice sites onto which InN is favourably incorporated, leading to the star shaped feature with an increased InN concentration as observed in Fig. 5.11e. The difference in morphology observed for this sample series (Fig. 5.9) to the sample surface observed in section 4.3 is caused by the deposition of the $In_xAl_{1-x}N$ active zone. Northrup et. al [147] showed that for $In_xGa_{1-x}N$ layers on GaN, the presence of InN at a dislocation core strongly favours the formation of a pit with the dislocation core at its centre.

In addition to the effect of the InN segregation to the screw dislocation, the strain field of the dislocation itself could have an impact on the emission energy. The strength of the strain field surrounding a mixed dislocation in $In_xAl_{1-x}N$ has been calculated by Mouti et al. [145] to be around 0.04 GPA. Furthermore, it was found by Kamińska et al. [148] that the bandgap shows a dependence on the pressure between 13-29 meV/GPa. Thus we would only expect a minimal change in the bandgap energy due to the strain of the observed dislocations, even for edge dislocations which show a strain field with a calculated strength of 0.1 GPa we would only expect a change in the emission energy by 1-3 meV which is considerably lower than the observed variation of 30 meV.

Conclusion

The results presented in this analysis show that the QW growth temperature has a strong effect on the emission energy of $In_xAl_{1-x}N$ QWs, which blueshift by

6 meV/K with increasing growth temperature due to an increased In desorption rate. The morphology of the investigated samples was dominated by the morphology of the underlying layer structure thus no clear influence of the growth temperature on the morphology was found. The analysis of the samples furthermore showed that threading dislocations with a screw component can have a major impact on the compositional homogeneity of $In_xAl_{1-x}N$ QWs, inducing an InN segregation towards the dislocation core and facilitating pit formation as well as acting as non-radiative recombination centres. This shows that reducing the threading dislocation density in $In_xAl_{1-x}N$ based light emitting devices is an important task for future growth efforts in order to achieve high quality devices.

5.3.2 QW thickness

To characterise the influence of the QW thickness, on the properties of $In_xAl_{1-x}N$ UV-LEDs, a series of four different samples was grown by MOCVD at the Tyndall National Institute. To manipulate the QW thickness the QW growth time was varied between 20 s and 46.8 s with a constant growth temperature of 730 °C. According to the grower QW thicknesses between 1.1 nm and 2.8 nm were achieved. The structure of the samples consists of an Al_2O_3 substrate on top of which a 2 µm thick AlN layer and a 2 µm $Al_{0.53}Ga_{0.47}N$ buffer layer were grown. The active region was deposited on top of the buffer layer and consists of a 5 period QW/QB $In_{0.18}Al_{0.82}N/Al_{0.53}Ga_{0.47}N$ structure. Photoluminescence (PL) spectroscopy was performed at Tyndall to investigate the influence of the well thickness on the emission wavelength and intensity of the active region. The PL results are depicted in Fig. 5.13. A red-shift of the emission wavelength with increasing quantum well thickness as well as a maximum of the intensity for a quantum well thickness of 1.4 nm can be observed.

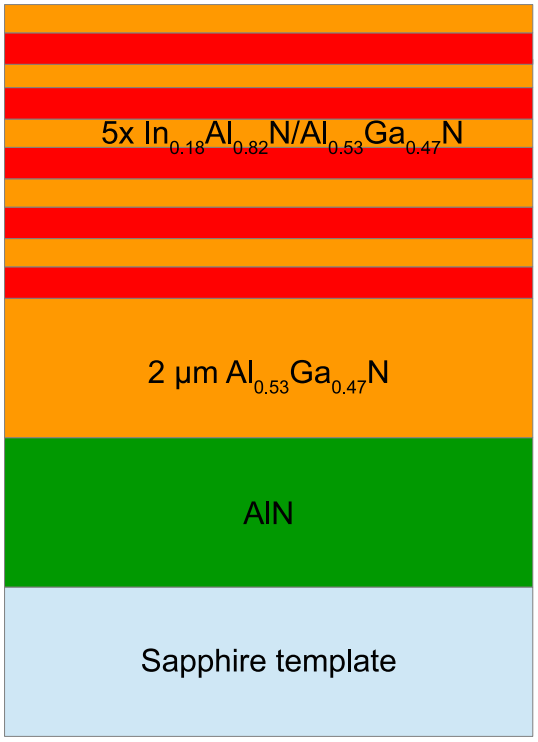

Figure 5.12: Layer structure of the investigated samples.

SE-imaging and room temperature CL spectroscopy were performed on these samples in order to characterise the influence of the quantum well thickness on the surface morphology and luminescence properties of the QW. In Fig. 5.14 the

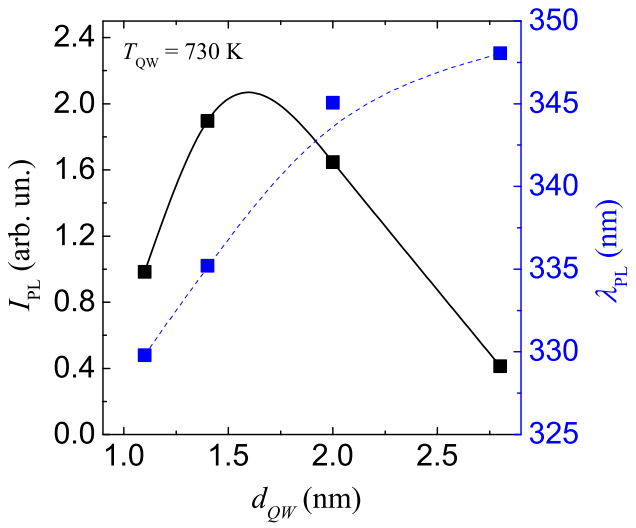

Figure 5.13: Intensity (black) and emission wavelength (blue) measured by PL, at Tyndall National Institute, in dependance of the QW thickness. The lines are guides to the eye only.

normalized CL spectra for each of the different samples is shown. The spectra consist of an $Al_xGa_{1-x}N$ NBE peak and a broad QW peak. The $Al_xGa_{1-x}N$ NBE peak originates from the buffer layer underlying the active zone and has a peak emission wavelength of (260±1) nm. The variation of the peak emission wavelength of the $Al_xGa_{1-x}N$ layer is believed to be due to unintentional growth variations.

For further investigation Gaussian functions have been fitted to the $Al_xGa_{1-x}N$ NBE and the QW peak in order to extract the peak wavelength and the QW/NBE integrated intensity ratio. Fig. 5.15 shows the dependence of the emission wavelength of the QWs on the thickness (red circles). The CL measurements show the same behaviour as the PL measurements, with the emission wavelength exhibiting a red shift for increasing quantum well thickness.

This is caused by two different effects. One is a direct function of the dependence of the energy levels in a QW on the QW thickness, the second is the influence of polarization fields in group-III nitrides. The energy level in the quantum wells can be approximated by the particle in a box solution with: $E \sim (\frac{1}{d})^2$ with d the thickness of the quantum well, resulting in a emission energy well above the actual material bandgap for thin QWs, converging towards the bandgap energy

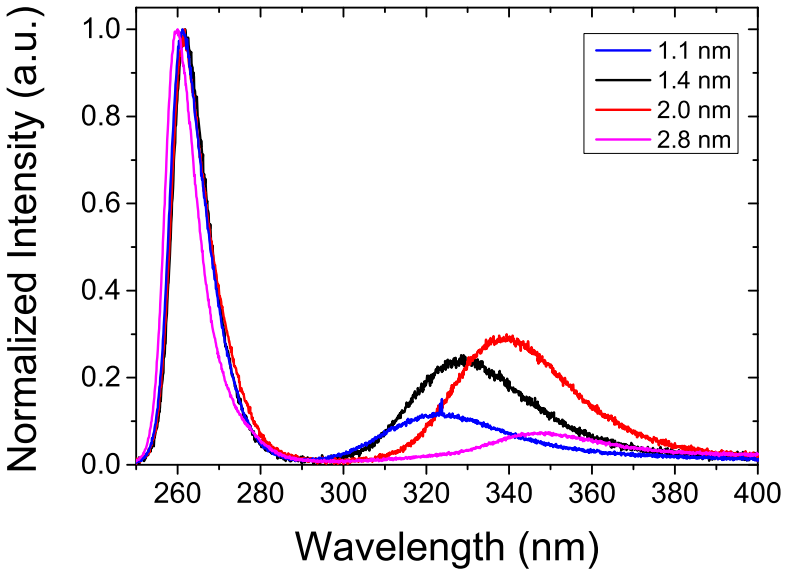

Figure 5.14: Room temperature CL spectra of the samples with different quantum well thicknesses.

of the material for increasing QW thickness. This inherent red-shift of the emission energy with increasing QW thickness is further enhanced by the effects of internal electric fields which can lead to a quantum confined Stark effect (QCSE). The internal electric fields consist of a piezoelectric field and a field caused by spontaneous polarization. The piezoelectric fields along the growth direction are caused by the inherent lattice mismatch between the QWs and the underlying structure, causing the QWs to grow biaxially strained, as discussed in section 2.3. The spontaneous polarization field along the c-direction is an inherent property of the group-III nitrides. These electric fields tilt the electric bands, forming triangular wells for electrons and holes respectively. This induces a red-shift of the emission energy by separating the electron and hole wavefunctions in the order of $e(E_{pz} + E_{sp})d$ [149, 150], as discussed in 2.3, with E_{pz} the piezoelectric polarization field and E_{sp} the spontaneous electric field. This effect is more pronounced in thicker QWs leading to a stronger separation of the wave-functions and thus a stronger red-shift [151, 152].

In Fig. 5.15 the intensity ratio I_{QW}/I_{AlGaN} as measured by CL is depicted (black squares). An increase in the intensity ratio is observed for an increasing quantum well thickness up to a thickness of 1.4 nm, where the measured intensity ratio has a maximum. For higher quantum well thicknesses the intensity ratio decreases again. The intensity of the QW is maximal for intermediate quantum

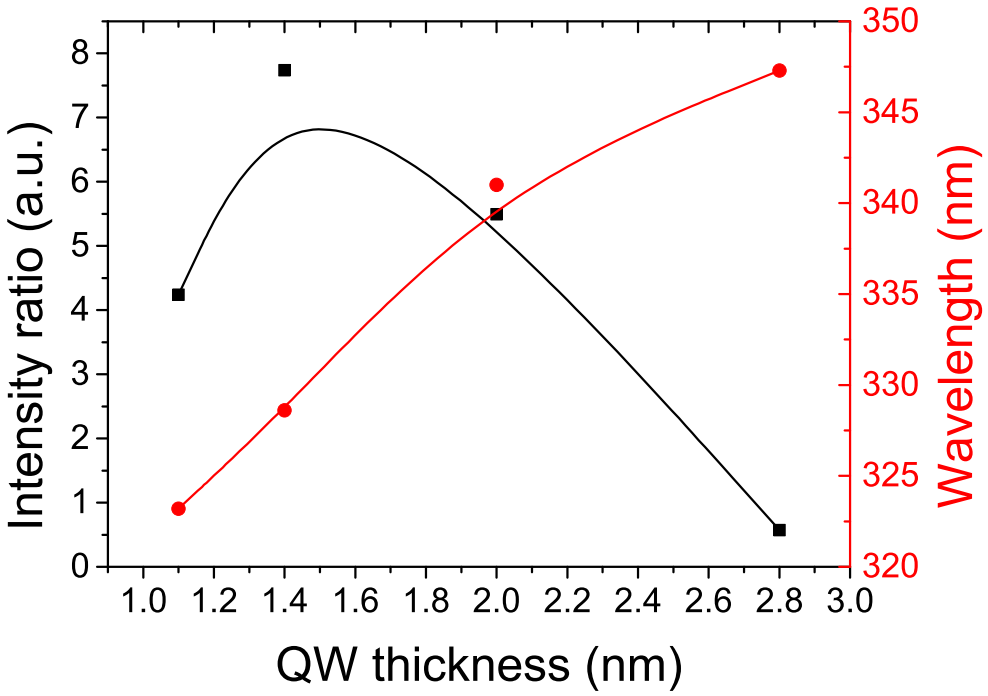

Figure 5.15: Plot of the fitted values for the intensity ratio between the $In_xAl_{1-x}N$ QW peak and the $Al_xGa_{1-x}N$ NBE (black squares) as well as the emission energy of the QW peak against the QW thickness (red circles). The lines are guides to the eye only.

well thicknesses due to a trade off between different competing mechanisms. For low quantum well thicknesses the non-radiative recombination of carriers at defects at hetero-interfaces and the extension of the electron wave function outside the quantum well limits the achievable intensity [153]. For high quantum well thicknesses the influence of the QCSE, namely the separation of the electron and hole wavefunctions, is more pronounced, leading to a stronger charge separation reducing the recombination probability and thus causing a strong reduction in emission intensity [54, 152].

To study the effect of the internal electric fields on the emission energy, excitation dependent CL measurements were performed. The results are shown in Fig. 5.16, the power dependent values for the thickest sample series are not shown as the QW intensity for low excitation currents was too low to be investigated.

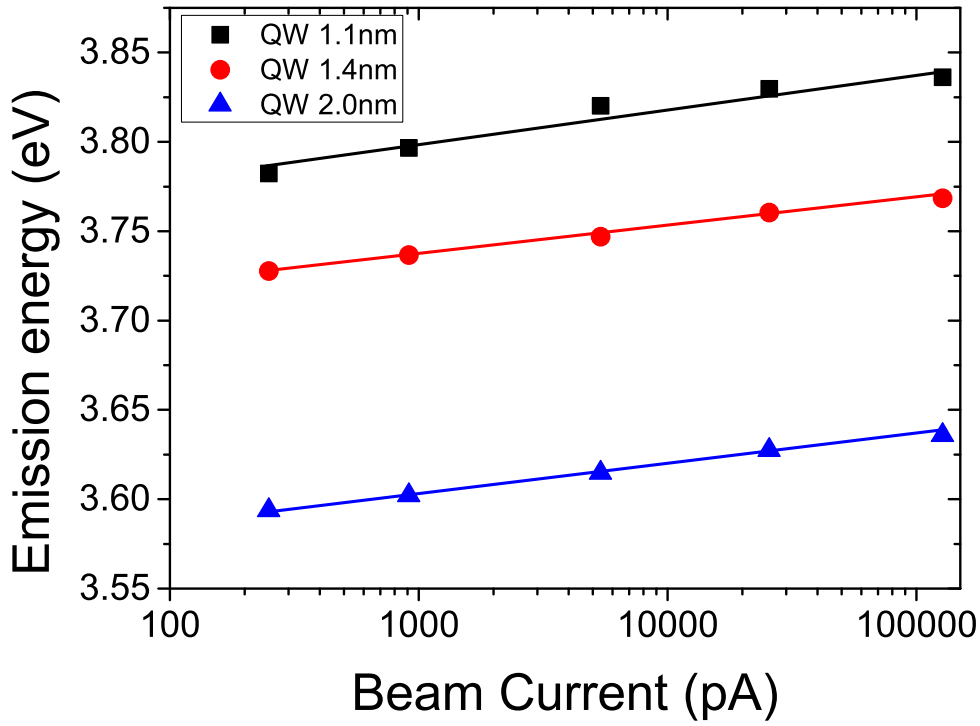

Figure 5.16: Plot of the fitted values for the QW emission energy against the excitation current.

It was found that the excitation current has a strong influence on the QW emission energy inducing a blueshift in the QW emission for all investigated samples (Fig. 5.16). A blueshift of the quantum well emission energy can be caused by two major effects [154]. I) Filling of the energetic ground states in the quantum well resulting in the emission from higher QW states and II) screening of the

electric fields causing the QCSE and thus countering the tilt of the bandstructure.

In Fig. 5.17 the room temperature CL spectra for the sample with a QW thickness of 1.4 nm at different excitation currents are shown. It can be seen that the FWHM of the QW peak does not increase with increasing excitation current, but rather decreases from 44 nm to 34 nm from the lowest to the highest excitation current. This indicates that the screening of the internal electric fields is the dominant effect in causing a blueshift of the QW emission energy. The electric fields in the active region are screened by electrons injected in the QW, reducing the effective field strength. Injecting more carriers in the active region will lead to a stronger field screening and thus to a re-normalization of the quantum well as well as a reduction of the influence of the electric fields on the emission energy, i.e. causing a blueshift with increasing excitation density [152]. In contrast to literature [152] we do not observe a stronger blueshift for thicker quantum wells instead each sample shows a similar shift of $(45 \pm 5)\, meV$.

SE and CL images were recorded in order to determine the compositional homogeneity of the different QWs as well as their possible influence on the surface topography. The measurements were performed with an acceleration energy of 5 keV and a chamber pressure between 2×10^{-5} mbar and 0.3 mbar. The utilization of the low vacuum mode was necessary as the samples exhibited strong charging effects. For this acceleration energy, 90% of the energy is deposited in a depth of 100 nm, which allowed light to be generated in the QWs as well as the underlying $Al_xGa_{1-x}N$ buffer.

The SE-images for these samples reveal a surface morphology dominated by two different features: A low density of large hillocks and a high density of smaller domains. Both features have a hexagonal shape and feature a dark spot in the middle, similar to the topography observed in the previous section (Fig. 5.9). A typical SE-image is shown in Fig. 5.18.

All CL-maps of these samples show the same features in the emission energy and intensity. In Fig. 5.19 the results of the SE and CL imaging for the sample with a QW thickness of 2.4 nm are shown. The $10\,\mu m$ CL image was measured in the marked area in the centre of Fig. 5.19a . The emission energy of the $Al_xGa_{1-x}N$ buffer (Fig.5.19b) shows a domain like behaviour, with a constant emission energy for each of the domains and a difference of up to 50 meV between the domains. The QW emission intensity (Fig.5.19c) reveals large localized drops in the intensity. These areas of lower intensity coincide with the position of the black dots seen in the SE-image. This indicates that the black dots are defects in the sample, acting as non-radiative recombination centres. The QW CL emission

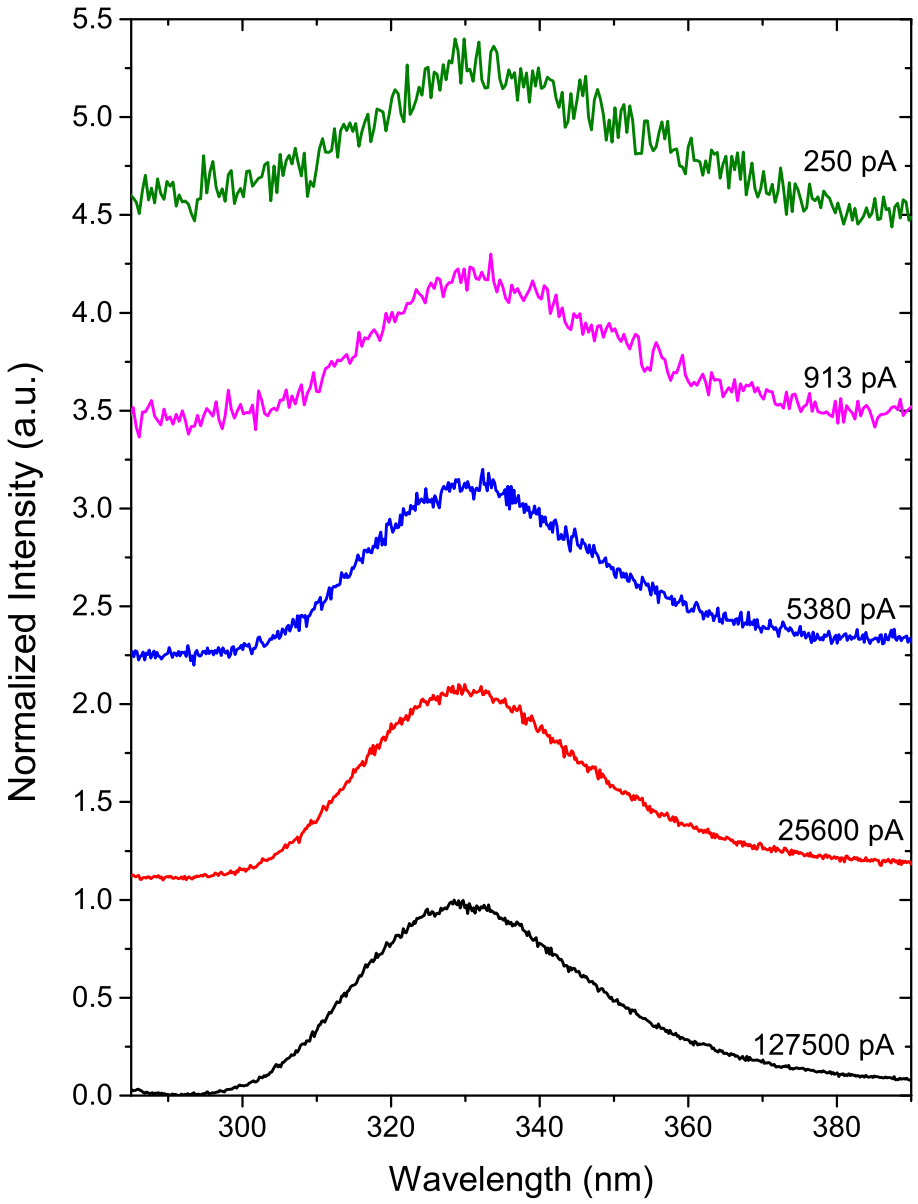

Figure 5.17: Room temperature CL spectra of the sample with a QW thickness of 1.4 nm at different excitation currents.

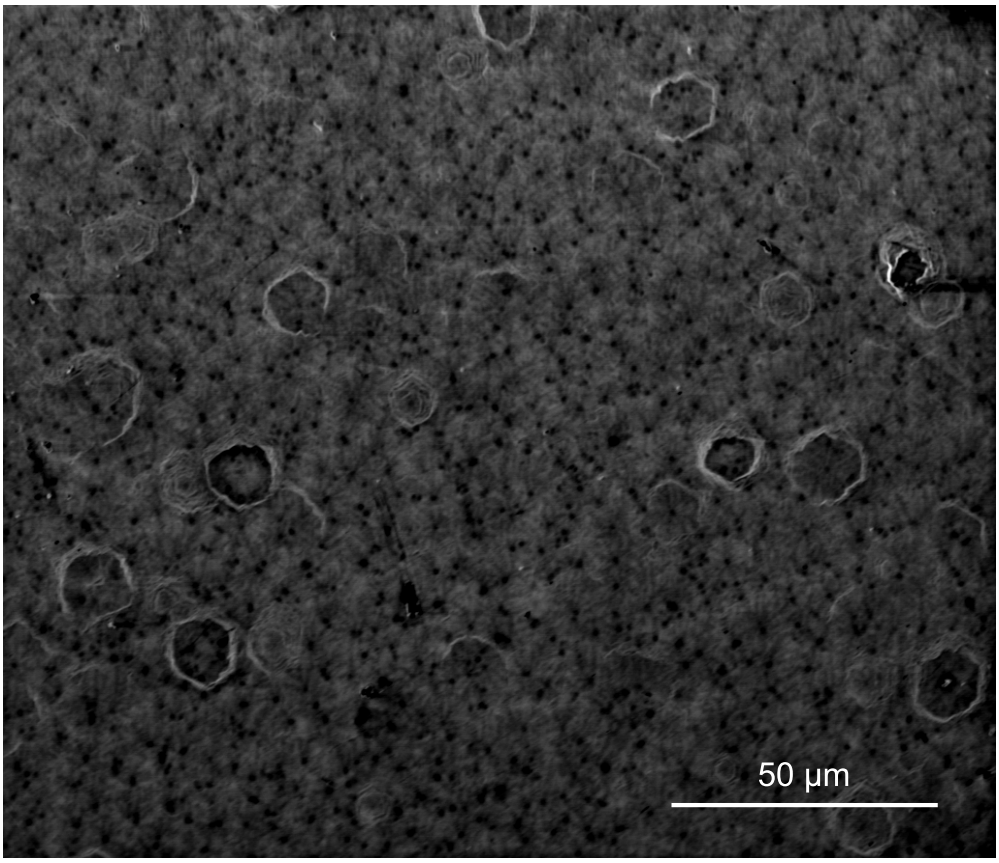

Figure 5.18: SE-image of the sample topography. Two features form the sample morphology, low density of elevated hillock structures as well as a high density of domains.

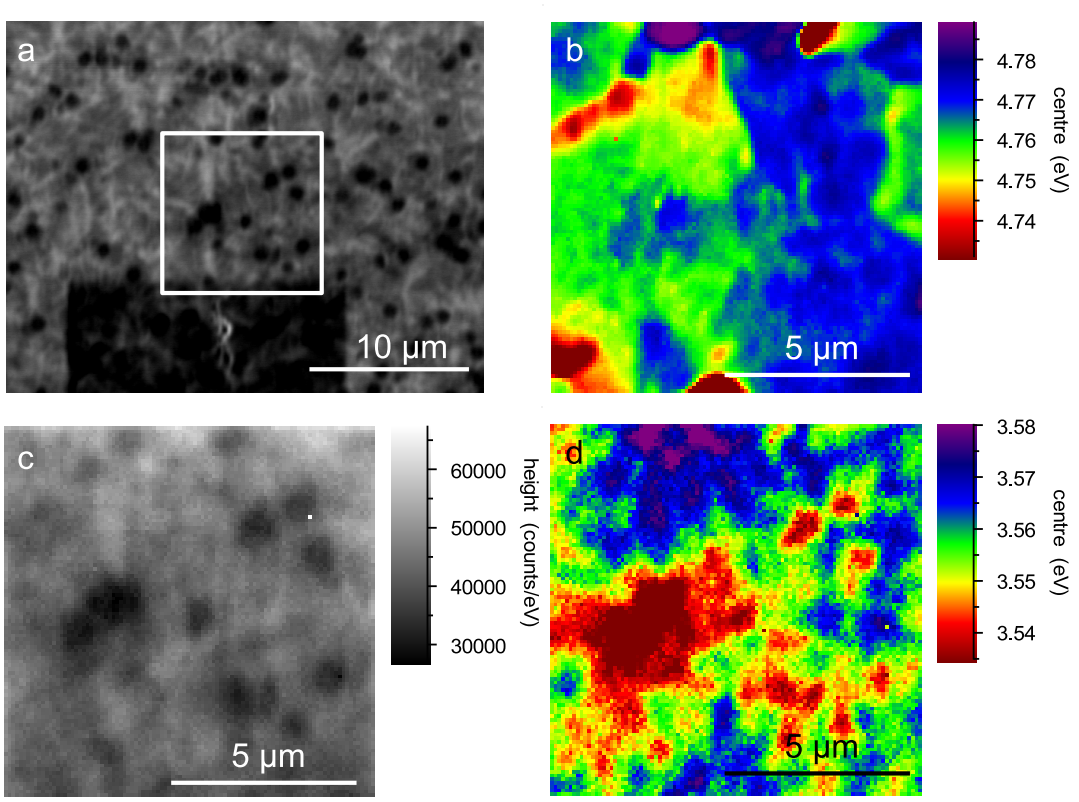

Figure 5.19: SE-image a) and CL emission energy for $Al_xGa_{1-x}N$ buffer b) $In_xAl_{1-x}N$ QW c) intensity distribution and QW emission energy d) for the sample with a QW thickness of 2.4 nm. The CL hyperspectral image was acquired in the boxed area of the SE-image.

energy (Fig. 5.19d) exhibits a variation of about 50 meV and a red-shift of the emission energy is observable at areas with a lower emission intensity. These results show that the CL maps for this sample series behave in the same way observed in the CL maps shown and discussed in the previous section (section 5.3.1). The strong influence of the underlayer is prohibiting the analysis of the influence of the QW thickness on the morphology and compositional inhomogeneity.

Conclusion

According to the results presented here the quantum well thickness influences the emission wavelength and the intensity of the emission. Quantum well thicknesses of 1.4 nm seem to give the highest intensity. The surface of the samples exhibited two different features which might indicate unfavourable growth conditions of the $Al_xGa_{1-x}N$ buffer layer. The spatial homogeneity of the QW emission is poor with emission energy variations of up to 50 meV and there are regions where the intensity of the quantum wells is reduced due to non-radiative recombination centres. The emission energy variation of the QW shows no observable dependence on the QW thickness and is most likely caused by the low homogeneity of the $Al_xGa_{1-x}N$ buffer layer which shows clear domains of different emission energies.

5.3.3 Buffer and Barrier composition

The aluminium nitride composition of the $Al_xGa_{1-x}N$ buffer layer and the $Al_xGa_{1-x}N$ quantum barrier was altered by variation of the precursor flux. Three samples were grown at Tyndall National Institute with a variation of the TMGa/TMAl flux ratio between 0.9 and 3.44 , the growth temperature was kept constant at $1110\,°C$. The V/III ratio was 781 except for the barrier of the the sample with the highest Ga/Al ratio were it was reduced to 523. The reactor pressure was 50 mbar for the buffer growth and 70 mbar for the barrier growth. The samples were grown on *c*-plane sapphire substrates with a miscut of 0.1°. The active regions of the samples consist of a 5 period QW/QB $In_{0.23}Al_{0.77}N/Al_xGa_{1-x}N$ MQW structure.

XRD and PL measurements were conducted on these samples in Tyndall. XRD measurements were used to determine the composition of the buffer layer and the quantum barrier, which was varied between 36% AlN and 65% AlN. PL was performed to investigate the influence of the different aluminium nitride composition on the emission energy and intensity of the $In_xAl_{1-x}N$ quantum wells.

Luminescence Properties

Room temperature CL-spectroscopy was conducted on these samples. The results of the CL measurement for each of the samples are depicted in Fig. 5.20. We were able to measure the NBE emission of $Al_xGa_{1-x}N$ (between 4.27 eV and 4.92 eV) as well as the quantum well emission ($\sim 3.55\,eV$). As expected the $Al_xGa_{1-x}N$-NBE emission energy shifts significantly with the AlN composition. Calculating the AlN composition from the CL spectra using Vegard's law with a bowing parameter of 1 shows good agreement between CL and XRD. Furthermore, we observe an increase in the FWHM of the $Al_xGa_{1-x}N$-NBE with increasing AlN composition, which is depicted in Fig. 5.21. This behaviour can have different causes, alloy broadening due to random distribution fluctuations of the Al and Ga atoms [155], decreasing crystalline quality or compositional inhomogeneity due to morphological effects. The PL measurements provided by the workgroup of Prof. P. J. Parbrook are in good agreement with the findings of the CL spectroscopy.

The measured quantum well emission energy changes only slightly with the AlN composition (between 3.46 eV and 3.55 eV) while the intensity ratio I_{QW}/I_{AlGaN} strongly increases with increasing AlN content (Fig.5.21). The increase of the intensity ratio with an increasing AlN content in the sample can be explained by a better carrier confinement in the quantum wells due to higher potential barriers between quantum well and quantum barrier.

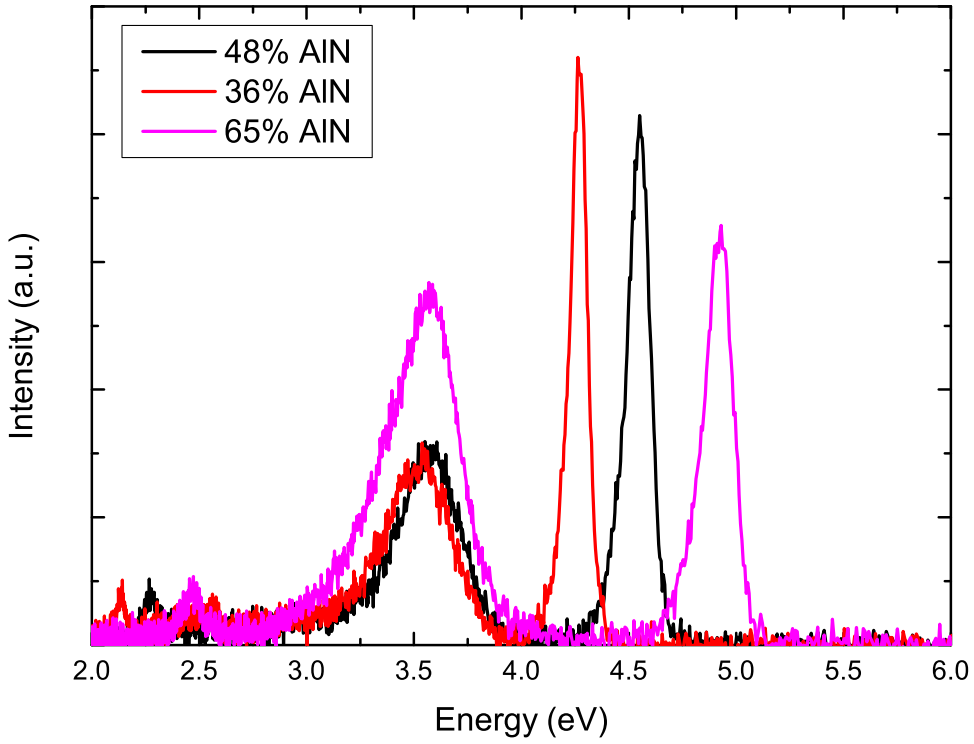

Figure 5.20: CL spectra of the three investigated samples with buffer and barrier composition of 36;48 and 65% AlN respectively.

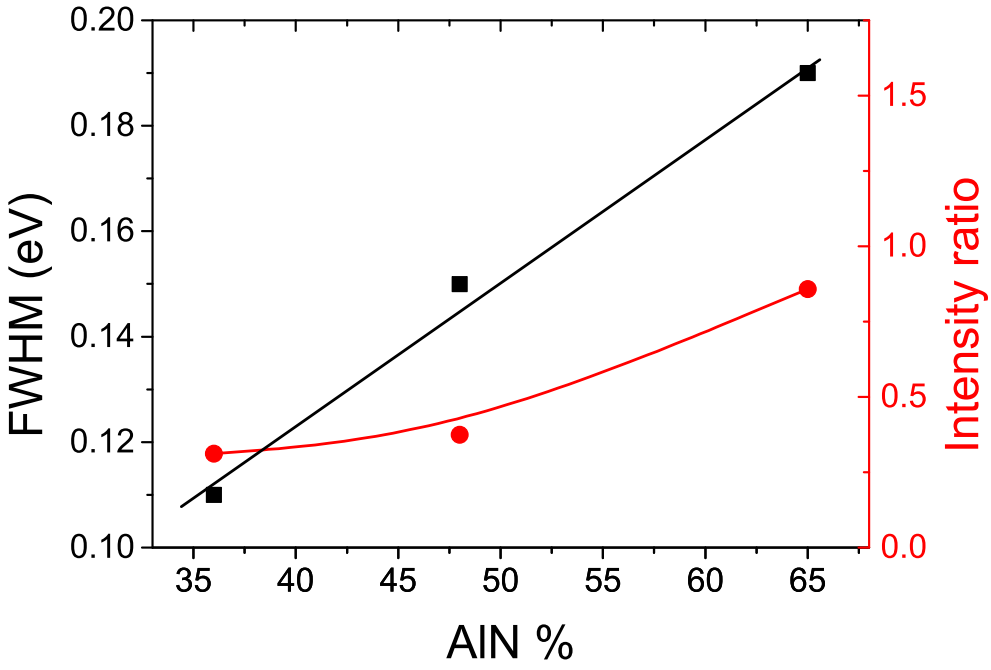

Figure 5.21: FWHM of the $Al_xGa_{1-x}N$-NBE peak (black, squares) and intensity ratio I_{QW}/I_{AlGaN} (red, circles) of three samples with different buffer compositions. The lines are guides to the eye only.

Morphology and CL mapping

In order to investigate the influence of the changing AlN composition on the surface morphology and the spatial homogeneity of the luminescence, SE and CL hyperspectral imaging were performed with high magnification in the ESEM. The results of the investigation are presented below, the energy scale of the CL emission energy maps has been kept constant at $\Delta 0.1$ eV for the $Al_xGa_{1-x}N$ maps for better comparison.

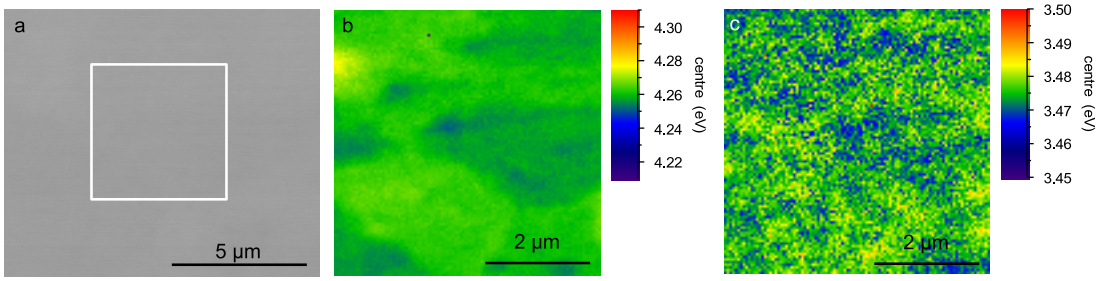

Figure 5.22: SE-image a) and emission energy of $Al_xGa_{1-x}N$ NBE b) and $In_xAl_{1-x}N$ QW c) for the 36% AlN sample. The CL hyperspectral image was acquired in the boxed area of the SE-image.

The measurement on the sample with the lowest AlN composition is depicted in Fig. 5.22. The SE-image shows a very smooth surface with only very few features visible. The $5 \times 5\,\mu m$ CL-map for the $Al_xGa_{1-x}N$ NBE emission energy (Fig. 5.22b) reveals a domain like behaviour while the CL-map for the emission energy of $In_xAl_{1-x}N$ QW (Fig.5.22c) shows no such behaviour. The emission energy of the $Al_xGa_{1-x}N$ NBE varies between $4.25\,eV$ and $4.27\,eV$ in total with the emission energy of each of the domains remaining fairly constant. The probable causes for this kind of behaviour were already discussed in chapter 4. Contrary to that the emission energy of the QW shows no structure and varies randomly between $3.46\,eV$ and $3.47\,eV$. This means that for a low aluminium nitride composition the spatial inhomogeneity of the buffer layer has no observable influence on the QW.

The same kind of behaviour can be observed in the measurements performed on the 48% AlN sample which are depicted in Fig. 5.23. The surface is again featureless and the CL maps of the emission energy again show a domain like behaviour for the $Al_xGa_{1-x}N$ NBE emission with a larger emission energy variation, ranging from $4.53\,eV$ to $4.58\,eV$ and small random fluctuations for the emission energy of the QW (varying between 3.54 eV and 3.56 eV). Additionally, a hexagonal structure in the emission energy of the $Al_xGa_{1-x}N$ NBE can be observed,

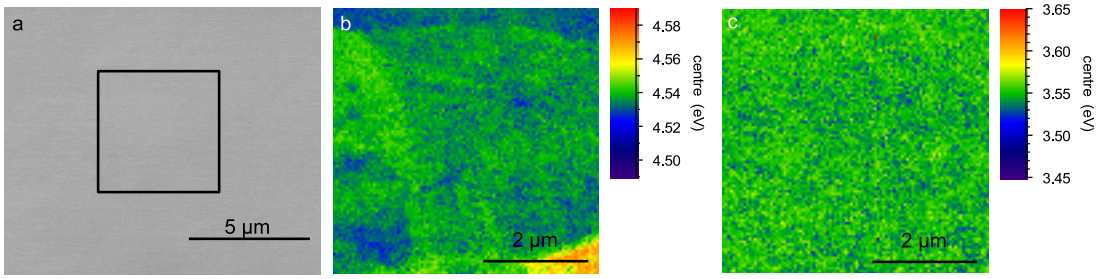

Figure 5.23: SE-image a) and emission energy of $Al_xGa_{1-x}N$ NBE b) and $In_xAl_{1-x}N$ QW c) for the 48% AlN sample. The CL hyperspectral image was acquired in the boxed area of the SE-image.

indicating that the morphology of the $Al_xGa_{1-x}N$ buffer layer showed hexagonal domains before the deposition of the active zone.

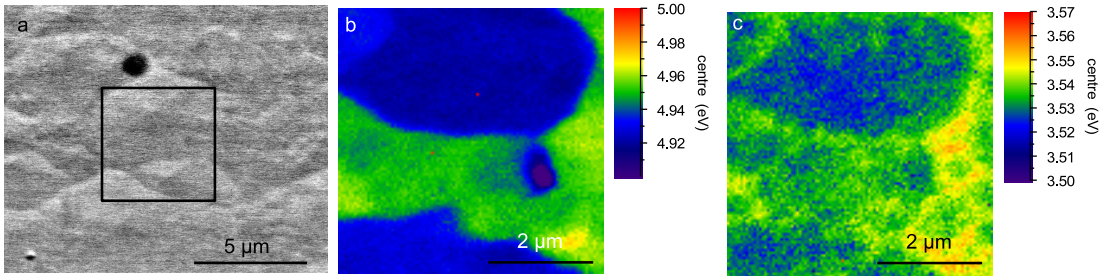

Figure 5.24: SE-image a) and emission energy of $Al_xGa_{1-x}N$ NBE b) and $In_xAl_{1-x}N$ QW c) for the 65% AlN sample.

The results for the sample with the highest AlN composition, shown in Fig. 5.24, differ greatly from the previous two samples. In the SE-image we can clearly observe a rough surface with pyramidal surface features (hillocks). The CL-map for the emission energy of the $Al_xGa_{1-x}N$ peak again shows distinctive domains with different emission energies, centred around 4.9 eV and around 4.98 eV. The observed domains match features measured on the surface of the sample. The CL-map for the QW emission energy reveals that the spatial homogeneity of the QW emission is reduced, compared to the previous samples. Instead of random fluctuations the emission energy depends on the domains observed in the $Al_xGa_{1-x}N$ CL-map.

Comparing the three different samples it is apparent that the morphology of the underlying $Al_xGa_{1-x}N$ buffer layer changes with increasing AlN% evidenced by the increasing emission energy difference between the observed domains as well as a change in the overall morphology for the last sample, which exhibited a

dominant hillock structure on the surface.

This change is caused by the fluctuation in the growth kinetics due to the variation of the diffusion length. Al adatoms have a smaller diffusion length compared to Ga adatoms so that increasing the Al% in the growth environment will change the overall diffusion length during the growth. Due to the high sticking coefficient of Al atoms they are often incorporated in the lattice near the point where they where deposited which leads to an increase in surface roughness by reduction of step flow growth. The high diffusion length of Ga atoms on the other hand leads to their increased mobility over a given range (depending on the growth conditions e.g. growth temperature) on the sample surface, incorporating favourably at kinks and edges, which results in a smoother surface morphology. Thus, the same growth conditions which give a smooth surface at a certain Al% will produce an increased surface roughness and hillocks when the Al% is increased as was observed in the investigated samples [156].

This change of the $Al_xGa_{1-x}N$ buffer morphology was found to influence the compositional homogeneity of the active region grown on top of it. The hillock morphology promotes a variation in the In incorporation across the sample surface by providing a different density of kinks and edges onto which In atoms prefer to incorporate. For the 36% and the 48% AlN samples the density of these favoured lattice sites is too small to cause an observable incorporation variation and the emission energy fluctuation is dominated by random alloy scattering. The sample with 65% AlN, on the other hand, offers a high density of kinks and edges, such that the In incorporation is dominated by surface effects rather than random fluctuations.

5.4 Summary

In this chapter the properties of MOVPE grown UV-LED structures have been studied. In the first section the intensity reduction observed in $Al_xGa_{1-x}N$ UV LEDs with decreasing wavelength has been investigated. It was found that the reduction of measured intensity is caused by a change of the internal bandstructure of $Al_xGa_{1-x}N$, changing from having the Γ_{9v} as the valence band maximum for GaN to the Γ_{7v}^{+} band. This influences the optical polarization of generated photons and their propagation through the grown material. Light emitted from GaN and low AlN concentration $Al_xGa_{1-x}N$ layers is mostly TE polarized, allowing for an easy extraction through the sample surface or the substrate, while $Al_xGa_{1-x}N$ QWs with an AlN composition larger than 25% emit mostly TM po-

larized light reducing the extraction efficiency and thus the measured intensity. This behaviour was found as a challenge to overcome in future design of UV LEDs either changing the LED design or utilising new geometries to allow for top extraction, as proposed by Zhao et al [139].

In the second section UV LEDs with an $In_xAl_{1-x}N$ based active zone have been studied. The influence of three different growth parameter on the optical and morphological properties of these devices were investigated.

The results of the investigation of the influence of the growth temperature show that the QW growth temperature has a strong effect on the emission energy of $In_xAl_{1-x}N$ QW, leading to an increased InN desorption rate with increasing temperature, which induces a blueshift of the QW emission. The thickness of the QW was shown to have a strong influence on the QW emission intensity and to a lesser degree on the emission energy. This was attributed to the effect of spontaneous and piezoelectric fields in the QW, separating the electron and hole wavefunctions. Investigation of the buffer and barrier composition showed that an increased confinement due to a larger bandoffset between the QW and QB results in a higher QW intensity.

The morphology of the investigated samples was dominated by the morphology of the underlying layer structure and no clear influence of the QW growth parameter on the morphology was found. The analysis of the samples furthermore showed that threading dislocations with a screw component can have a major impact on the composition homogeneity of $In_xAl_{1-x}N$ QWs, inducing an InN segregation towards the dislocation core and facilitating pit formation as well as acting as non-radiative recombination centres. This shows that reducing the threading dislocation density in $In_xAl_{1-x}N$ based light emitting devices is an important task for future growth efforts in order to achieve high quality devices.

Chapter 6

Low dimensional semiconductor structures

6.1 Introduction

Solid state lighting utilizing planar GaN LEDs emitting in the blue spectral region is one of the the key technologies for reducing the world wide emission of CO_2, while simultaneously providing access to ambient lightning to a wider number of households. These devices are already widely commercially available but their efficiency is still limited by a number of physical effects.

Efficient carrier injection for electrically driven operation of these devices, for example, is limited by the low achievable hole concentration in GaN:Mg layers. The quantum confined stark effect (QCSE) is another well known phenomenon that reduces the efficiency of GaN based planar LEDs by reducing the overlap of the electron and hole wave-functions (as described in section 2.3). Point defects and dislocations acting as non-radiative recombination centres are an additional observed and well documented phenomenon that can strongly reduce the efficiency (as described in section 2.2.2)[24, 25].

Some of these effects can be circumvented by increasing the amount of nano-structuring of LEDs. In this chapter $In_xGa_{1-x}N$/GaN nanorods will be discussed as one example of these nano-structures, in which the diameter of the whole LED structure is being reduced to a few 100 nm. Other examples of nano structures would be quantum dots and nanowires. In quantum dots the spatial dimensions of the active zone are smaller than the de-Broglie wavelength of electrons and holes in the material, thus confining the carriers spatially in all three dimensions leading to an icnrease of the overlap of the wavefunctions. Nanowires are structures with a diameter of a few nanometer due to their small dimensions carriers can be

confined in two dimensions in the active zone, leading to an increased overlap of the electron and hole wavefunction. Furthermore, the growth of nanowires allows for defect and strain free material growth which provides further improvement for optical devices.

Nanorods have been found to reduce the threading dislocation density by offering extra surfaces on which they can terminate (see Fig. 6.1b) [157]. Furthermore, nanorods offer easy access to non and semipolar planes on which the QCSE is strongly reduced or not present at all (see Fig. 6.1a) [158]. Additionally, nanorods offer a higher active zone volume, which increases the light output per surface area, potentially reducing the manufacturing costs and reducing the size making them more suitable for compact devices (e.g. mobile phones) [159].

While the shape of the nanorods provides solutions to the aforementioned issues of planar LEDs, the growth process of highly homogeneous nanorod arrays still poses significant challenges. There exist various techniques for the growth of nanorods arrays which provide different sets of advantages and difficulties. These approaches are generally divided into top-down and bottom-up methods. The top-down method involves growing the full LED structure, then depositing a mask and etching down. While this approach can achieve a reduced threading dislocation density [160] at a high array uniformity it does not provide access to planes with a reduced QCSE (see Fig. 6.1b). The bottom-up method on the other hand achieves low dislocation densities while giving access to the non and semipolar planes but is more limited in the variation of the growth parameters (see Fig. 6.1a). In this method a mask is deposited before growth, achieving nanorod formation by selective area growth out of the mask windows. More information about these techniques can be found in Reference [159].

In this chapter an approach for the fabrication of nanorod LEDs is studied, which combines the advantages of the two previously described methods, by fabricating a nanorod template in a top-down approach and growing the active zone in a bottom-up method on this template [161, 162]. For this purpose a series of samples has been grown by MOCVD at the Tyndall National Institute in Cork, by Michele Conroy and Haoning Li in the group of Prof. Peter Parbrook. The sample series consists of two GaN nanorod templates (A and B) which have been prepared differently and two $In_xGa_{1-x}N$/GaN MQW nanorod structures (samples A-1 and B-1) which were grown on parts of these nanorod templates. All four samples were investigated by SE and CL hyperspectral imaging. For in-depth analysis single nanorods were removed from one of the samples, deposited on a copper transmission electron microscope (TEM) grid and investigated using

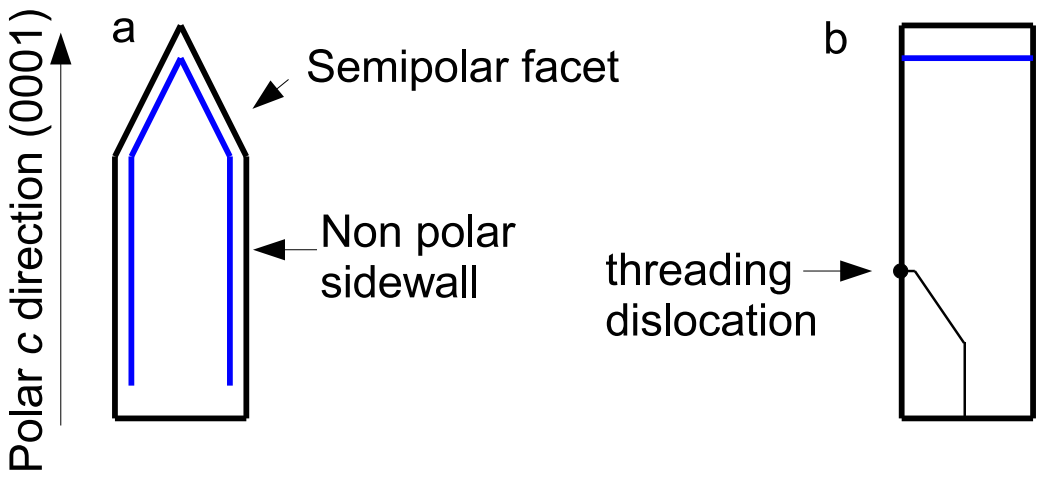

Figure 6.1: Schematics of two example nanorod LEDs grown with the bottom-up (a) and the top-down (b) method. The active region is marked in blue and the termination of a threading dislocation at a sidewall is shown in (b).

SE and CL hyperspectral imaging as well as scanning transmission electron microscopy (STEM) which was performed by researchers from the King Abdullah University of Science and Technology.

6.2 GaN Nanorod Templates

The GaN nanorod templates were prepared by a top-down approach (schematically shown in Fig. 6.2). At first a thick GaN layer was grown on top of an AlN/Al_2O_3 template. The samples where then removed from the growth reactor and a SiO_2 sphere mask was deposited on top of the GaN layer (Fig. 6.2a). This mask was then etched with CF_4, which partially dissolves the SiO_2 spheres but not the GaN, in order to obtain the desired sphere dimensions (Fig. 6.2b). In the next step Cl_2 was used to etch into the GaN layer (Fig. 6.2c). In the last step the SiO_2 mask was removed by soaking the samples in a buffered oxide etch (BOE) bath (Fig. 6.2d). The etching times between template A and template B have been varied and the influence of this variation was studied by SE and CL hyperspectral imaging. Template A was etched for 35 s in CF_4 and 2 minutes in Cl_2 and template B for 70 s in CF_4 and 2.5 minutes in Cl_2.

Morphology

In figure 6.3 the acquired SE-images for both templates are shown. The diameter of the nanorods can be determined from the SE-image and is ≈500 nm for both

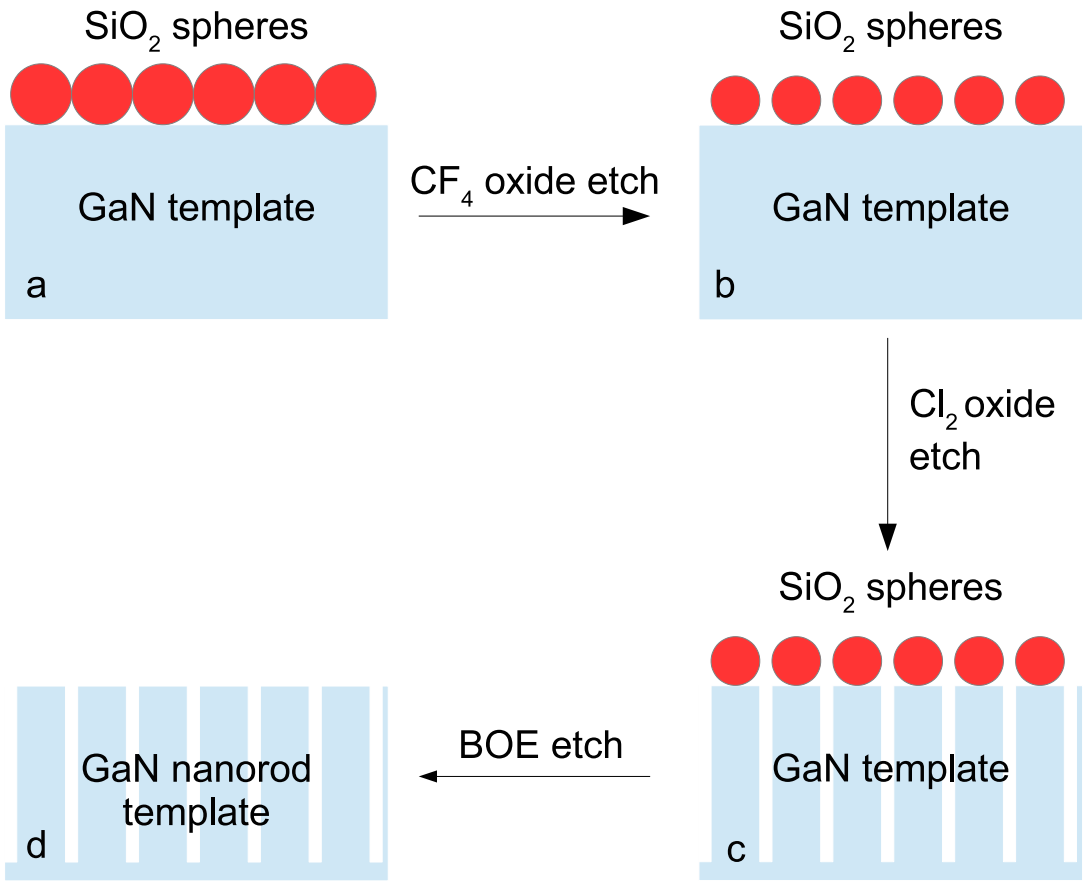

Figure 6.2: Schematic of the etching process of a nanorod template. First a SiO_2 sphere mask is deposited on top of the GaN template (a), in the first etching process the spheres are etched down to the desired size (b), in the next etching step the GaN material not protected by the mask is removed by etching (c), in the last step the mask is removed (d) and the GaN nanorod template obtained.

templates. The two samples show partially connected nanorods. As no growth was taking place after the fabrication process, this can be attributed to a non uniform deposition of the mask used for the selective area etching. Both templates exhibit a strong difference in the morphology of the nanorods, especially in the top.

The nanorods in template A, with the lower etching time, have a cylindrical form with a circular shaped top and a flat *c*-plane plateau, whilst the nanorods from template B exhibit a conical shape with a hexagonal pyramidal top and only a small *c*-plane facet on the plateau. The difference in the morphology is most likely caused by the different etching times (at step b and c in Fig. 6.2).

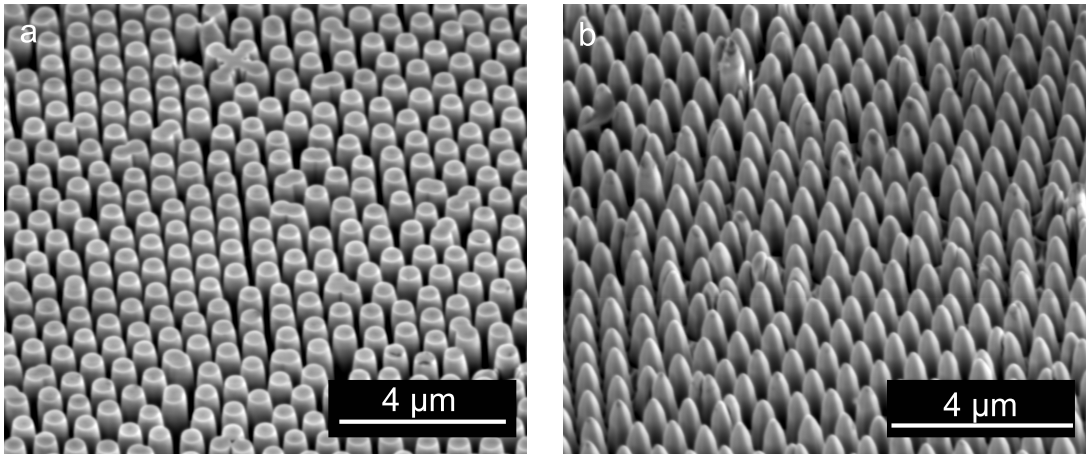

Figure 6.3: SE-images of GaN nanorod template A (a) and B (b) after removal of the mask.

As described in Fig. 6.2, during the fabrication of the nanorod template, etch resistant spheres are deposited on top of the semiconductor surface, to act as a mask for the etching process. For small etching times the etching process will only take part in the unmasked area, resulting in a nanorod surface shape dominated by the shape of the deposited droplets as seen for template A which shows circular tops (Fig. 6.3a and Fig.6.4a). During longer etching times, the mask deteriorates (the diameter of the SiO_2 sphere shrinks) exposing more and more of the GaN surface, with increasing time, to the etch solution. This means that parts that were protected by the sphere at the beginning of the etching process might see the etch solution at a later time and will then be also etched although at a lower rate, producing the conical morphology observed in template B (Fig. 6.3b and Fig.6.4b). The remaining c-plane facet of the conical nanorods indicates the remaining diameter of the SiO_2 sphere that acted as a mask.

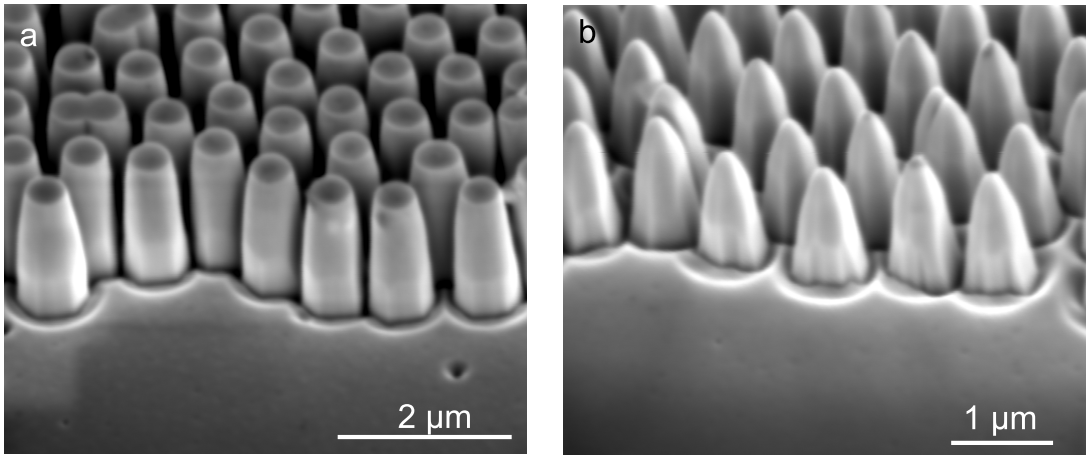

Figure 6.4: Cross-section SE-images of GaN nanorod templates A (a) and B (b) after removal of the mask.

Cross-section SE-imaging of the templates was performed to determine the height of the nanocolumns. The SE-images can be seen in figure 6.4 and a nanorod height of ≈1300 nm has been determined for both templates. This indicates that for template B only parts of the mask were dissolved during the etching process as a full dissolution of the mask would result in a measurable difference of the nanorod height. The SE-images reveal a good homogeneity in width and size as well as distribution of the nanorods; no surface defects like V-pits are visible on any of the nanorods.

Luminescence Properties

By performing room temperature CL hyperspectral imaging on the areas shown in Fig. 6.4, information about the material properties in the nanorod was obtained. For the acquisition of the CL image a beam energy of 5 keV was used. The results of the CL investigation of template A and B are shown in Fig. 6.5 and Fig. 6.6.

The acquired CL spectra for template A (black) and B (red) are shown in Fig. 6.5. The spectra taken from both samples are near identical, exhibiting a GaN peak at 3.4 eV and a broad defect band between 1.9 eV and 2.5 eV. The observed defect band is commonly observed in intentionally or unintentionally n-doped GaN layers and called yellow luminescence (YL), with a band centre of approximately 2.2 eV. This deep level luminescence band is of high importance for GaN based structures as the deep level defects associated with it can act as efficient carrier traps and re-absorption centres, possibly decreasing the output power of an LED structure. The origin of this defect band is highly disputed

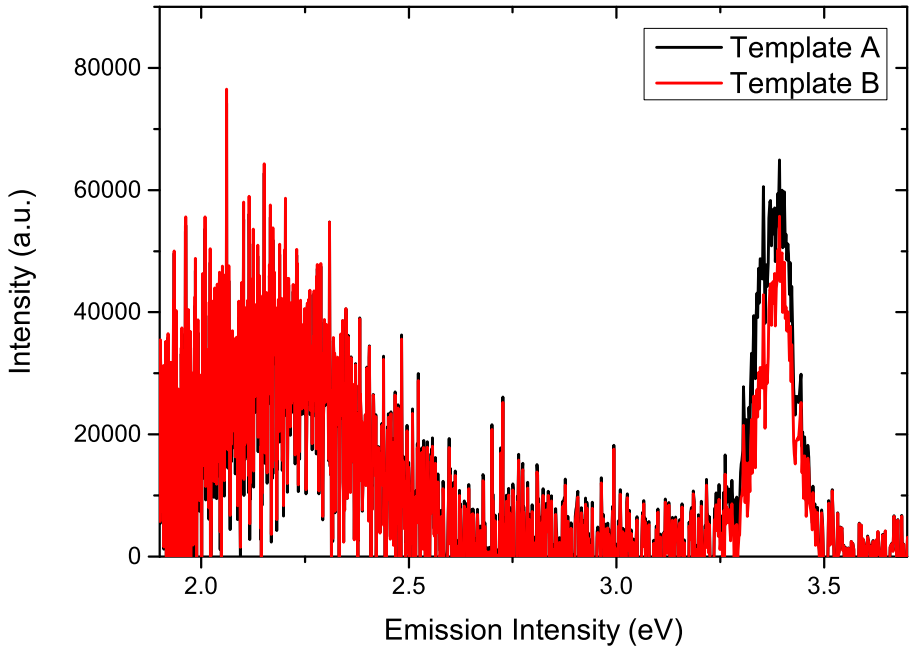

Figure 6.5: Room temperature CL spectra taken from template A (black) and template B (red)

and different deep level defects have been associated with it [163]. Defect centres associated with the yellow luminescence are the gallium vacancy (V_{Ga}) and related complexes such as V_{Ga}-O_N [164, 165]; carbon atoms on nitrogen sites (C_N) [166] and carbon related complexes [167]; others associate edge dislocations with the YL [168, 169]. For further investigation the CL map for template A, recorded over the area shown in Fig. 6.4, was analysed using principal component analysis.

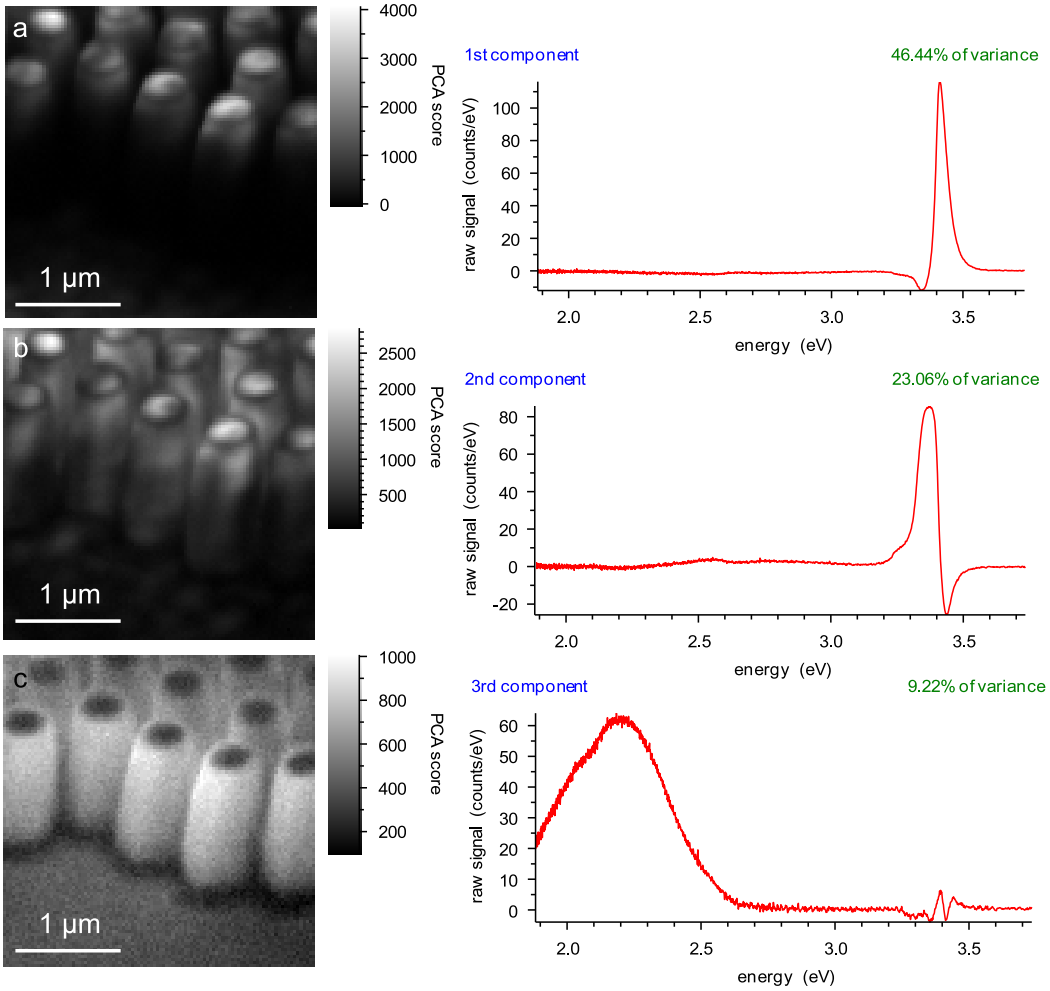

Figure 6.6: Result of principal component analysis for template A. The first three components are shown.

The first three principal components are shown in Fig. 6.6. The first two components are the high (Fig. 6.6 a)) and low energy (Fig. 6.6 b)) side of the GaN peak observed in the recorded spectra for both samples (Fig. 6.5). Comparing the intensity maps of both components it can be seen that the high energy emission is strongest at the *c*-plane top and strongly reduced towards the

base of the nanorod while the intensity distribution of the lower energy component is distributed more uniformly with a slight increase at the top of the nanorod. The intensity variation on the *c*-plane facet of the nanorod, visible in the first and second component, is most likely caused by non-radiative recombination centres, like threading dislocations, propagating along the nanorod growth direction. The degradation of the NBE emission intensity along the nanorod and the presence of the low energy second component is caused by effects of the etching process. One such effect is that due to the randomness of impinging etch ions the nanorod sidewalls will be left with an increased surface roughness compared to the *c*-plane facet reducing the emission intensity [170]. The second effect is that during the etching process the removal of N atoms is enhanced compared to Ga atoms [171]. This leaves Ga-rich nanorod sidewalls to which either impurities or excitons can bind [172, 173]. Excitons bound to surface states (Y_4 line) have previously been reported [163, 174]to cause a low energy shoulder as observed in the presented samples.

Incorporated defects and vacancies can either act as non radiative recombination centres or emit YL. Especially O bound to Ga atoms has been reported to degrade the luminescence intensity [171]. The peak observed in the second component has been attributed to a recombination process involving oxygen atoms on a nitrogen site as recombination processes involving bound excitons are unlikely to be observed at room temperature.

The enhanced incorporation of impurities along the sidewalls becomes apparent if one takes the third principal component into account, which consists of the YL component of the spectra. The intensity plots shows a strong anti correlation between the GaN NBE and the YL emission intensity. The YL intensity is high at the nanorod sidewalls where the GaN NBE is reduced and weak on the top *c*-plane facet of the nanorod where the GaN NBE is increased. This indicates that during the etching process defect centres responsible for the YL have been incorporated into the nanorod sidewalls, causing a high defect density on the sidewalls. The top *c*-plane facet was protected from the incorporation of the defect centres due to the etch resistant mask.

6.3 MQW Arrays

After the etching process parts of the templates were used to grow a subsequent structure of 300 nm GaN followed by an array of 5 $In_{0.16}Ga_{0.84}N$ quantum wells and 5 GaN quantum barriers in a bottom-up approach. The quantum wells

were grown at a temperature of 750 °C, the barriers at 850 °C. A quantum well thickness of 2 nm with an InN content of 16% and a barrier thickness of 4 nm were aimed at. The samples where characterized by SE and CL hyperspectral imaging.

Morphology

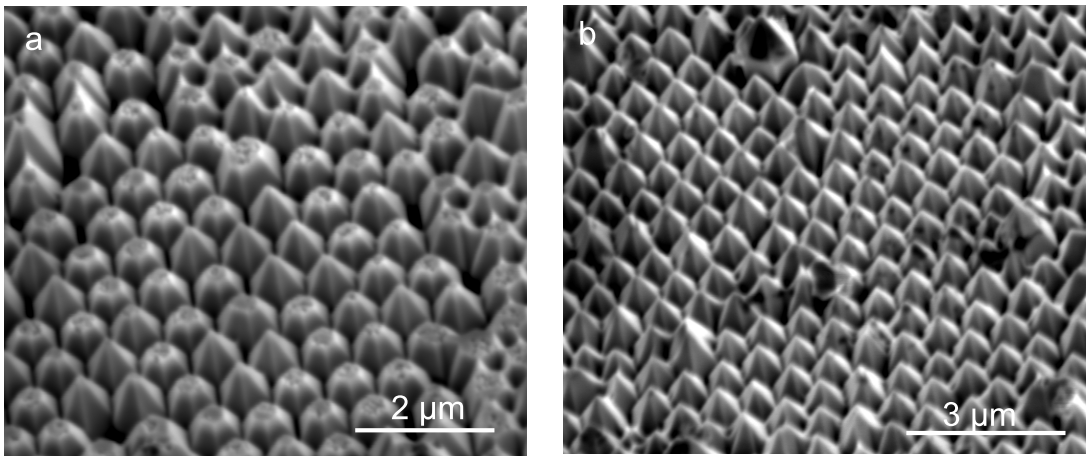

Figure 6.7: SE-images of $In_xGa_{1-x}N$/GaN nanorods grown on template A (a) and template B (b)

By comparing the SE-images in Fig. 6.7 for both samples after the growth of the $In_xGa_{1-x}N$/GaN MQW structure it is possible to observe the influence of the template morphology on the morphology of the subsequently grown structure. For template A which had flat *c*-plane tops only about 50% of the nanorods have formed a pyramidal top, with a small remaining *c*-plane facet, while the remaining nanorods exhibit a large flat *c*-plane top (Fig. 6.7a) with semipolar sidewalls. The SE-image shows a sizeable height difference between the two types of rods observable for template A. Furthermore, on the majority of the nanorods with a flat top, as well as on some pyramidal rods, surface defects can be observed. The SE-image for the overgrown structure (Fig. 6.7b), that was deposited on template B, shows a more homogeneous surface morphology, all of the nanorods retained the pyramidal form observed in the SE-image for the template (Fig. 6.3b), the already small *c*-plane facet on top of the pyramid is further reduced. The prevalence of the pyramidal shaped top of the nanorods is caused by the different growth rates of polar and semipolar planes [175]. No surface defects have been observed for the nanorods grown on template B. In the SE-images of both samples, in the upper right corner, areas in which the nanorods started

to coalesce are visible. This is caused by a deviation from the hexagonal closed packed distribution of the SiO_2 mask. During the GaN growth, after the etching process, the nanorod will grow in vertical as well as lateral size, which can lead to coalescence of nanorods if the distance between the etched rods was smaller than the now commencing lateral growth.

Luminescence Properties

The luminescence properties of these nanorods have been studied by room temperature CL hyperspectral imaging in the centre of the SE-images shown in Fig. 6.7, the spectra of both samples are shown in Fig. 6.8. The spectra and images were recorded with a beam energy of 5 keV at room temperature.

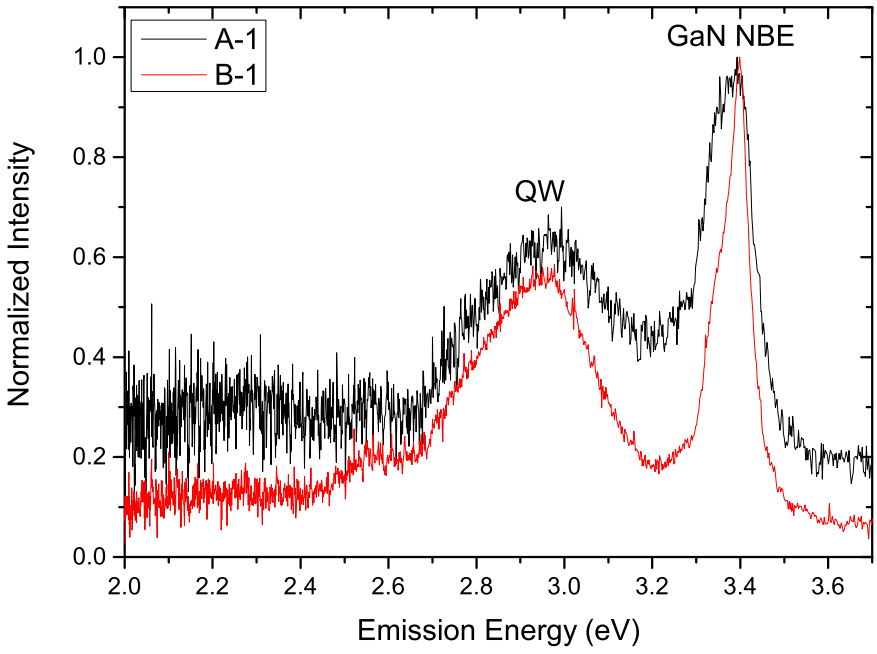

Figure 6.8: Room temperature CL spectra of the two overgrown samples; A-1 (black) and B-1 (red)

Both spectra show a strong GaN NBE peak at 3.4 eV, a low energy shoulder, a broad peak at 2.95 eV and a peak at 2.56 eV. Analysing the spectra of both samples, it is evident that sample A-1 has a higher background count, a broader GaN NBE peak as well as a lower signal to noise ratio, suggesting a reduced material quality compared to sample B-1. Comparison between the GaN peak of both samples shows that the low energy shoulder of sample A-1 is much more

pronounced than for sample B-1, which could be caused by the higher crystalline quality of sample B-1 or an additional luminescent region close to the GaN band edge for sample A-1. The broad peak at 2.95 eV has been attributed to the MQW emission from the semipolar sidewalls. Calculating the InN% in the QWs from the peak position, while disregarding any strain and confinement effects, leads to a QW composition of approximately $In_{0.14}Ga_{0.86}N$ assuming a bowing parameter of 1.4 eV [176]. A notable feature of the recorded spectra is that no YL was measured. This indicates that in the treatment of the nanorods after the etching process no defect centres causing the YL were incorporated.

To study the spatial distribution of the different luminescence peaks, the CL hyperspectral images were numerically fitted to the different components of the spectra using Gaussian peaks and the results of this are shown in Fig. 6.9.

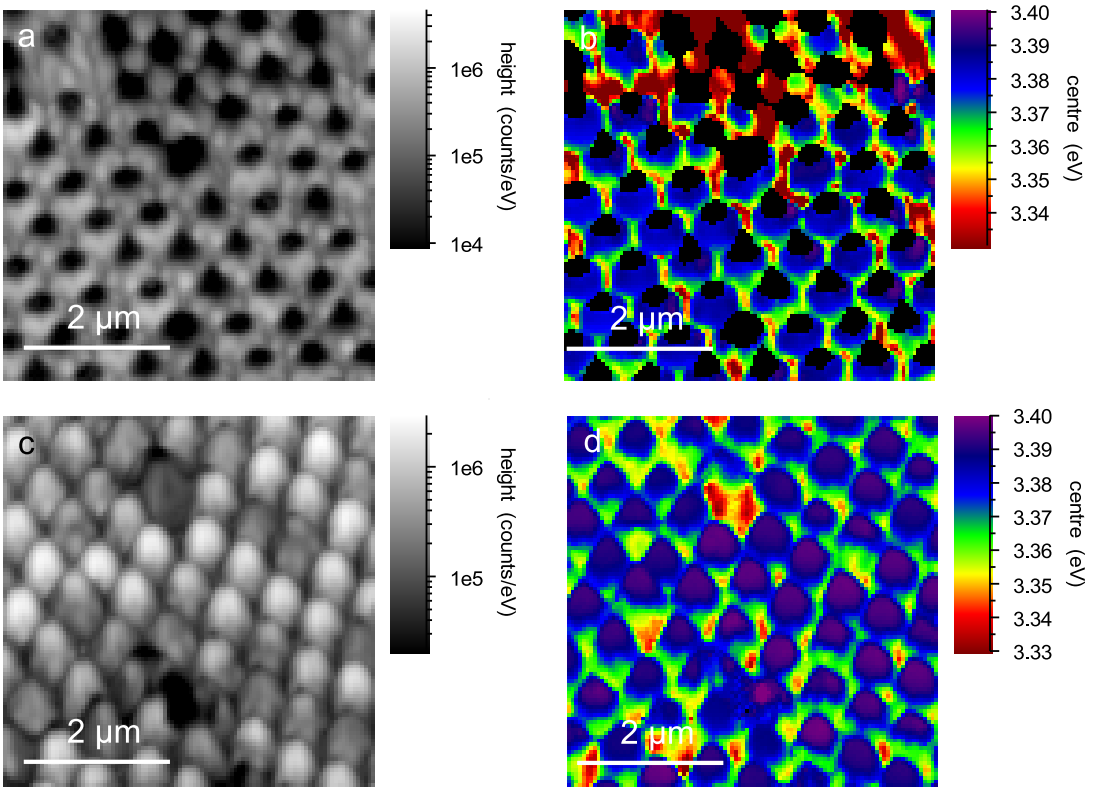

Figure 6.9: GaN NBE Emission intensity and emission energy for $In_xGa_{1-x}N$/GaN nanorod samples A-1 (a),(b) and B-1 (c),(d)

The plot of the fitted intensity for sample A-1 (Fig. 6.9a) reveals high GaN NBE emission intensity along the visible part of the semipolar sidewalls and a strong reduction in the emission intensity on the top part, regardless of the morphology of the top. This is most likely caused by the defects visible in the

SE-image for sample A-1 which are likely to act as non-radiative recombination centres, reducing the GaN NBE intensity. In the GaN NBE emission energy map for sample A-1 (Fig. 6.9b) a large variation in the emission energy of up to 60 meV can be observed. This is most likely rather a variation in the relative height of the two GaN peaks and a shift of the peak centre of the fitted Gaussian peak than a real variation in the GaN emission energy. These samples were grown on top of an AlN/Al_2O_3 template which would induce compressive strain into a GaN layer which should induce a blueshift of the emission energy. An increase in the compressive strain from the bottom towards the top of the nanorod is highly unlikely and thus it is more probable that the energy shift is caused by the prevalence of surface state emission over NBE emission on the semipolar and non-polar planes of the nanorod.

The GaN intensity map for sample B-1 (Fig. 6.9 c) differs from the intensity map of sample A-1, the GaN intensity shows a more homogeneous intensity distribution in each of the nanorods, with only a small area, located at the tip of the pyramidal nanorod, where the intensity is strongly reduced. Slight differences in the GaN NBE intensity can be found between the various nanorods which is most likely caused by a difference in the density of non-radiative recombination centres like impurities, vacancies and threading dislocations. The GaN emission energy image shown in Fig. 6.9 d) shows the same general behaviour as the emission energy for sample A-1.

Fitting the acquired CL hyperspectral image to show the QW emission intensity and emission energy for sample A-1 (Fig. 6.10) reveals strong inhomogeneities. The intensity of the QW emission (Fig. 6.10a) is generally higher on the sidewalls of the nanorods and strongly reduced at the pyramidal top of the nanorod. In the top right of the measured area the region with the highest emission intensity can be found, showing a difference in emission intensity of at least an order of magnitude higher than the rest of the investigated area.

The fitted emission energy of the QW emission (Fig. 6.10b) reveals strong difference in the emission energy of the QWs across the investigated area. In the top right, where the highest intensity was measured, the emission energy is about 2.95 eV as expected from the spectra shown in Fig. 6.8, with a red shift towards the apex of the nanorods. The fitted emission energy of the rest of the investigated area is approximately 0.1 eV shifted from this top right area, indicating a strong inhomogeneity of the QWs across the characterised region.

By analysing the extracted spectra from three different points of the maps one can see that the emission in the top right (Fig. 6.10c Pos.1) of the sample

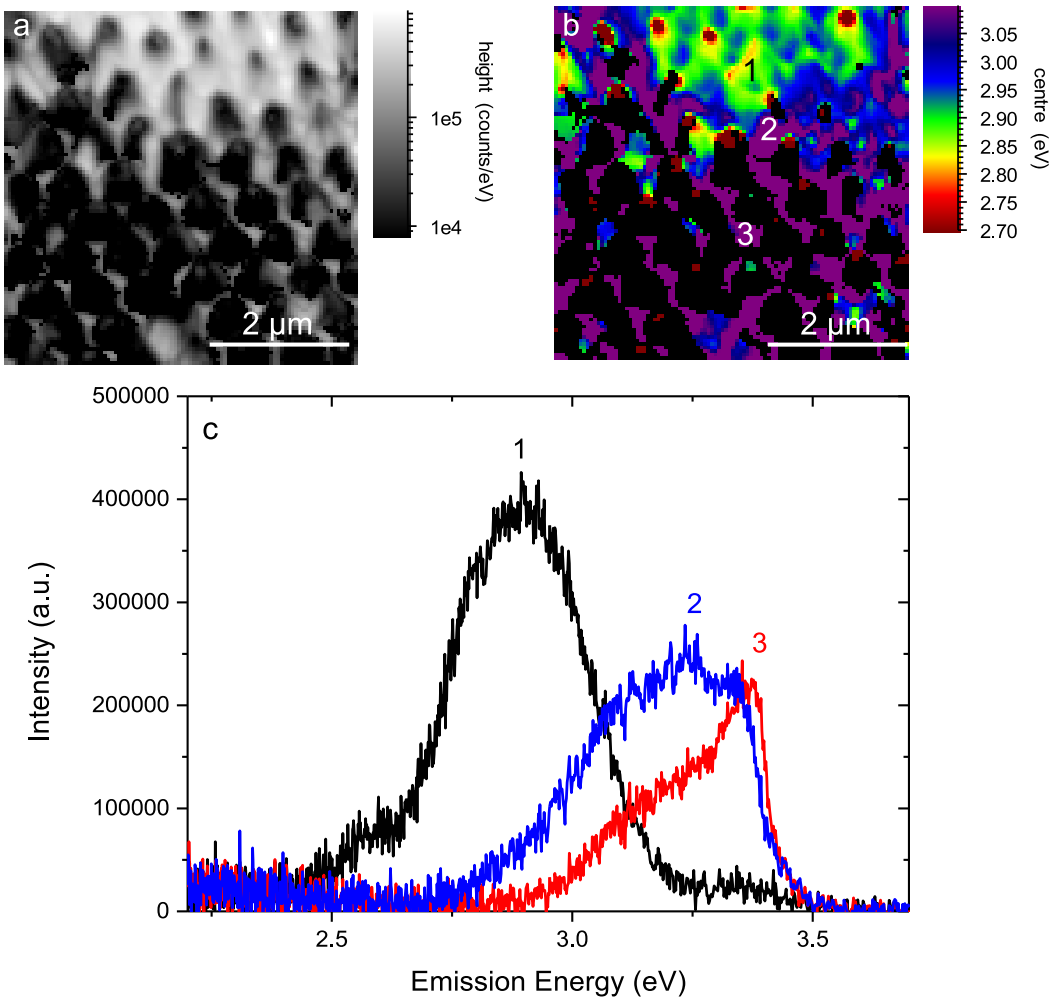

Figure 6.10: $In_xGa_{1-x}N$ MQW emission intensity (a), emission energy (b) for $In_xGa_{1-x}N$/GaN nanorod sample A-1 and extracted spectra from three positions (1,2,3) (c).

shows the same behaviour as in the previously shown spectra. A clearly resolved broad QW peak with an emission energy of 2.9 eV was measured. The spectra extracted from positions two and three (Fig. 6.10c Pos.2 and Pos.3) strongly differ from the spectra measured at position one. The emission energy is blue shifted compared to the QW peak, emitting at 3.2 eV, partially merging with the GaN NBE peak. The existence of a layer emitting in this region might explain the broader NBE peak observed for sample A-1 compared to sample B-1 as seen in Fig. 6.8 and also strongly suggests an inhomogeneity in the InN incorporation over the measured area.

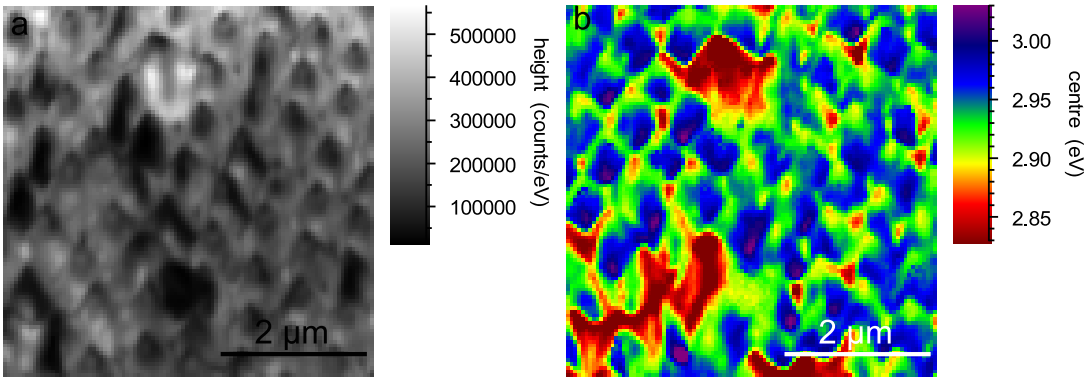

Figure 6.11: $In_xGa_{1-x}N$ MQW emission intensity (a) and emission energy (b) for $In_xGa_{1-x}N$/GaN nanorod sample B-1.

The extracted emission intensity and energy maps of sample B-1 (Fig. 6.11a,b) show homogeneous luminescence properties of the QW emission. The emission intensity distribution (Fig. 6.11a) shows a clear correlation to the morphology of the sample (Fig. 6.7), with high intensity along the pyramidal tops of the nanorods and a reduced intensity in the apices.

The QW emission energy of sample B-1 (Fig. 6.11b) is more homogeneous over the investigated area than the QW emission energy of sample A-1. The emission energy is at ~ 2.95 eV over most of the investigated area, with a redshift at the apices of the nanorods as well as on areas where a reduced intensity on the sidewalls of the nanorods can be observed.

Comparing the intensity distribution of the MQW emission intensity between samples A-1 and B-1 one can find that the emission intensity is much more homogeneous for sample B-1 and that both samples show a reduced emission intensity at the top of the nanorods. The same observation can be made when comparing the emission energy of both samples. Sample B-1 shows a much more homogeneous emission energy distribution while both samples show a redshift of

the emission energy at the apices of the nanorods. This indicates that the overall InN incorporation for sample B-1 is more homogeneous than for sample A-1 and that an effect causes the reduced InN incorporation on the semipolar QWs for sample A-1.

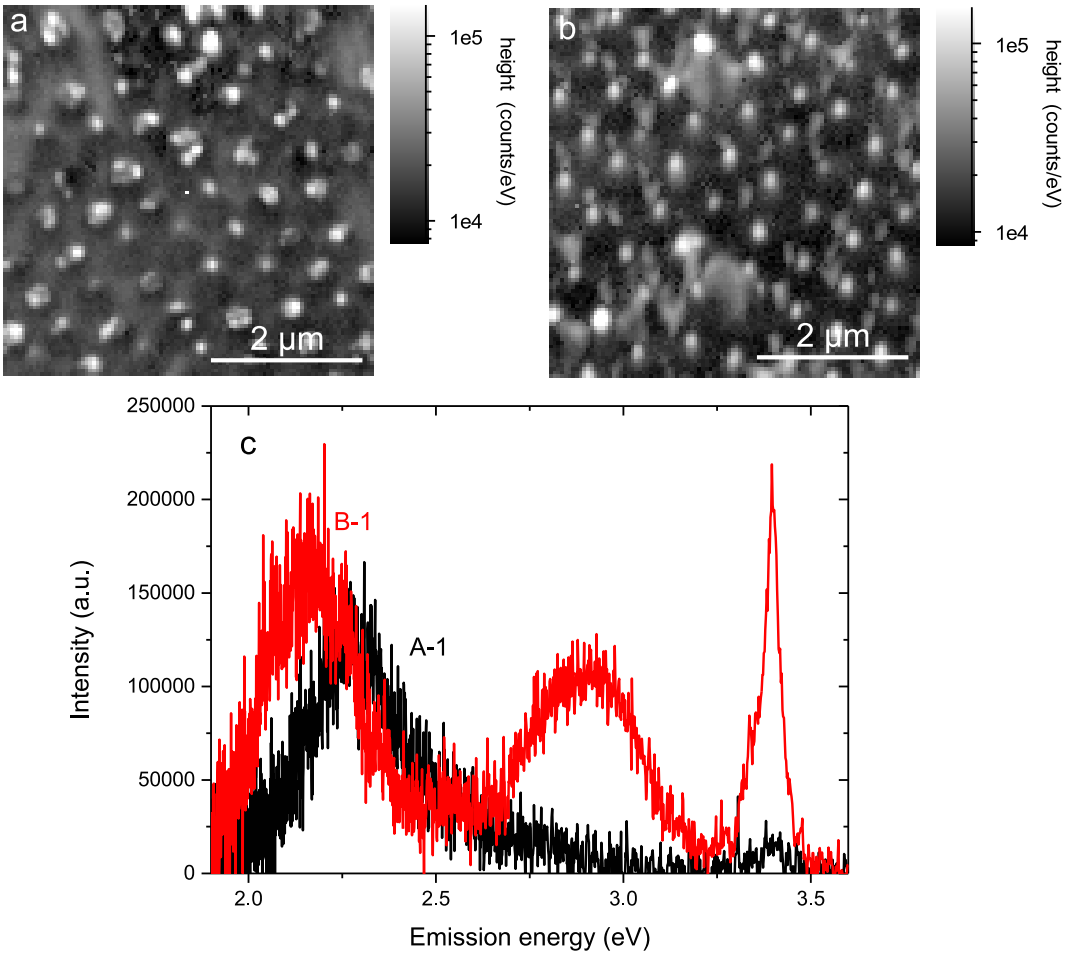

Figure 6.12: Intensity maps of the luminescence originating from the *c*-plane facet of the nanorods for sample A-1 (a) and B-1 (b) as well as spectra extracted from a *c*-plane facet for both samples (c).

By investigating the top of the nanorods, another luminescence active region was found. Plotting the intensity distribution and extracting spectra from the top of the nanorods (Fig. 6.12) the luminescence properties of this region can be investigated. The additional luminescence band of sample A-1 shows one broad peak centred at 2.26 eV while the additional luminescence band of sample B-1 emits at a lower energy of 2.16 eV. The presence of an additional $In_xGa_{1-x}N$ layer on the *c*-plane facets most likely accounts for the observed reduced intensity of the GaN and QW emission intensity observed in the apex of each of the nanorods

and furthermore, it explains the observed reduced emission energy of the QW fits (see Figs. 6.10 and 6.11) at the apex of the nanorods.

This additional $In_xGa_{1-x}N$ layer also most likely caused the strong inhomogeneities in QW emission energy and emission intensity observed for sample A-1. InN has different incorporation rates on different crystal planes, strongly favouring the incorporation on the *c*-plane facet compared to the semipolar *r*-plane [177], this coupled with the longer diffusion length of In adatoms compared to Ga adatoms [178][179] leads to an agglomeration of InN on the *c*-plane facet, forming an additional $In_xGa_{1-x}N$ layer with a higher InN concentration than the *r*-plane QWs.

The growth of these two layers is essentially a competing mechanism where both facets compete for the available InN. For sample A-1 with the much larger *c*-plane facets on the template (Fig. 6.3) this competition between the layers results in the *c*-plane facets soaking up most of the offered InN, strongly reducing the available InN for incorporation on the semipolar QWs, causing QWs with an emission energy much higher than aimed for.

The same effect can be observed, to an extent, for sample B-1 where the QW emission energy corresponds to a QW composition of $In_{0.14}Ga_{0.86}N$ instead of the aimed one of $In_{0.16}Ga_{0.82}N$, with the difference in InN being incorporated on the *c*-plane facets.

The higher emission energy of the extra $In_xGa_{1-x}N$ layer in sample A-1 compared to sample B-1 can also be explained by the larger *c*-plane facets. For sample A-1 the available InN has to cover a larger area than that of sample B-1 leading to a reduced InN concentration despite soaking up more InN.

6.4 Characterisation of a Single Nanorod

To further investigate the behaviour of the additional luminescence band as well as the distribution of the MQW luminescence single nanorods were removed from the nanorod array of sample B-1 , deposited on a copper TEM grid and investigated by room temperature CL hyperspectral imaging, SE-imaging as well as by scanning transmission electron microscopy (STEM). The investigation details of the best nanorod are presented in this section. The results of the SE and CL hyperspectral imaging are shown in Fig.6.13.

The structure of the nanorod can be clearly seen in the SE-image. It consists of a base with $\{10\bar{1}0\}$ (*m*-plane) side-walls and a pyramidal top with semipolar $\{10\bar{1}1\}$ facets. The panchromatic CL intensity map in Fig. 6.13b shows a re-

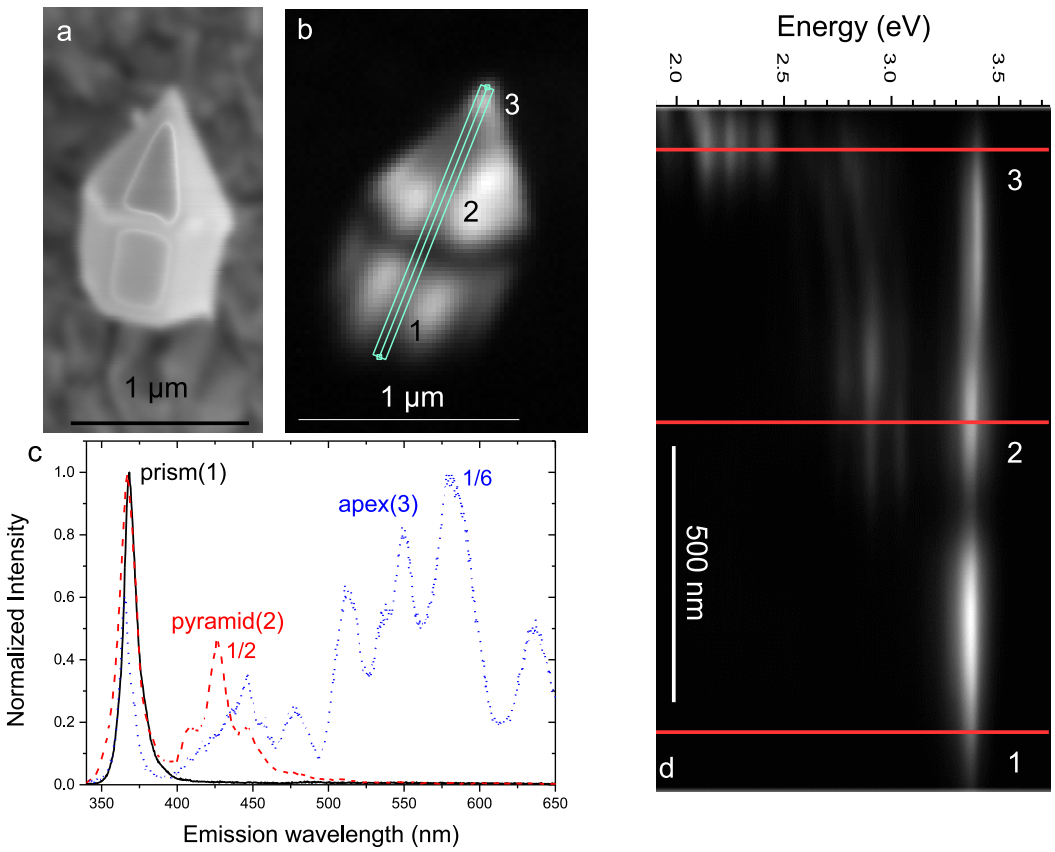

Figure 6.13: SE-image (saturated due to the current needed for CL) of the nanorod (a), Panchromatic CL intensity (b) and spectra (c) from selected spots of the nanorod as well as line spectra (d), taken along the line shown on the panchromatic image, of the investigated nanorod. In the spectra the maximum intensity of the spectra taken from the pyramid and the apex relative to the the maximum of the spectra taken from the prism is marked.

duction in the luminescence intensity at the point where the top (pyramid) and bottom (prism) of the nanorod meet. The intensity variations at the pyramidal top of the nanorod are due to re-absorption effects (see section 3.2.5) and the geometry of the measurement setup additionally a higher point defect density in this area could cause a reduction of the emission intensity. Extracting the spectral information along the line shown in Fig. 6.13b generates a spectral line scan of the nanorod. The spectral line scan is shown in Fig.6.13d and three distinct regions with different optical properties can be identified.

The first region (Fig. 6.13c prism(1)) is in the base of the nanorod, where only the GaN near band edge (NBE) signal can be measured, showing that no $In_xGa_{1-x}N$ growth occurred on the *m*-plane side walls during the deposition of the $In_xGa_{1-x}N$/GaN active zone. This is expected given the ultradense nature of the array from which the individual rod was extracted and in contrast to nanorods with a wider spacing where $In_xGa_{1-x}N$ growth could be found on the *m*-plane [180, 181]. The small FWHM (12 nm) of the GaN NBE peak and the absence of any yellow luminescence on the *m*-plane sidewalls indicate that damage introduced during the etching process was successfully healed during the regrowth and the material is of high optical quality [130, 154, 182, 183].

The second region with distinct optical properties is dominated by a broad luminescence band (395 – 465 nm) consisting of a main peak with an emission wavelength of 426 nm and two satellite peaks on the high and low energy side of the main peak, with emission wavelengths of 409 nm and 446 nm respectively (Fig. 6.13c pyramid(2)). The three peaks are separated by an energy of approximately 150 meV. Applying a digital bandpass to the hyperspectral image to only show the luminescence intensity between 395 nm and 465 nm (Fig. 6.15a) it is possible to see that the luminescence of this region is emitted from the pyramidal top of the nanorod. We attribute the luminescence in this range to the semipolar QWs. As the growth conditions for the active zone have not been varied throughout the growth process, only minimal variations are expected in each subsequent quantum well, thus the origin of the satellite peaks is believed to be due to optical modes such as Fabry-Perot modes or whispering gallery modes (WGM). In Fig. 6.14 different possible optical modes in the horizontal plane of a hexagonal nanorod are shown.

To determine which mode is causing the additional satellite peaks the energy spacing between different modes is calculated using $\Delta E = hc/nL$ with L the optical path length and n the refractive index. Assuming a constant refractive index of 2.615 [184] and a hexagonal side length l with a value of 350 nm,

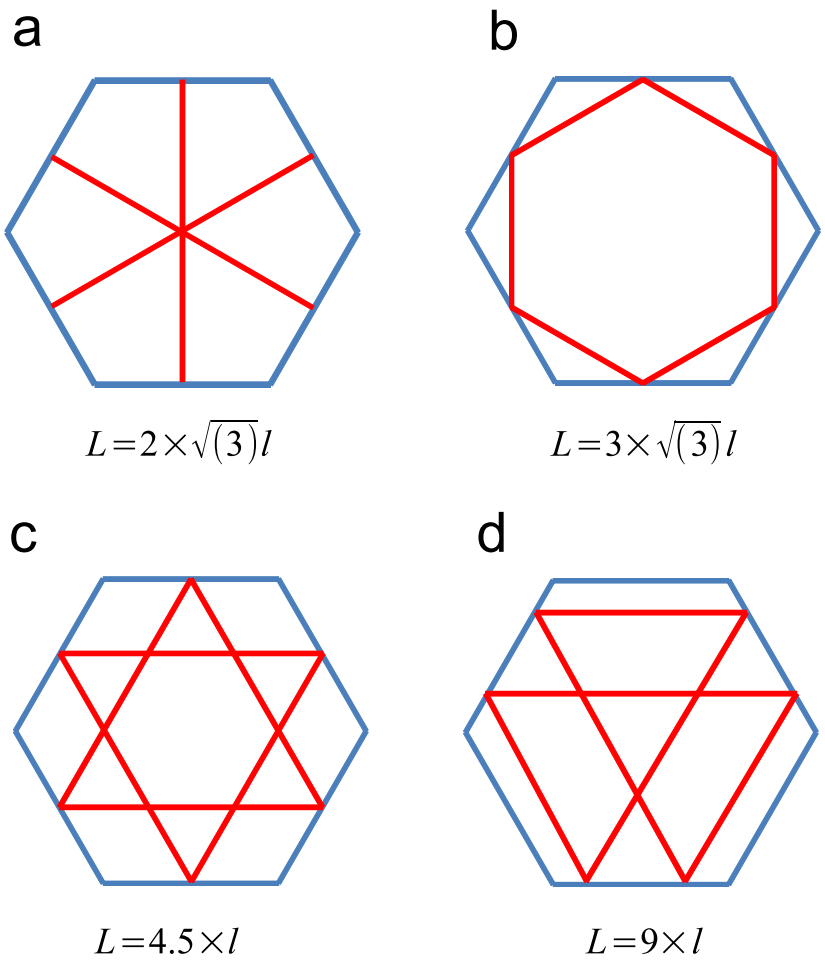

Figure 6.14: Optical modes in the horizontal plane of a hexagonal nanorod, Fabry-Perot modes (a), WGM (b), triangular quasi-WGMs (c), quasi-WGMs (d) with their corresponding optical path lengths L, with l the hexagonal side length.

the path length L, of the different optical modes can be determined in order to identify which of the different modes results in the energy separation closest to the one experimentally observed. Four different optical modes have been investigated: Fabry-Perot modes (Fig.6.14a), where the light strikes the sidewalls of the nanorod twice per cycle; WGM (Fig. 6.14b) where the light propagates around the periphery of the nanorod in a hexagonal pattern, being reflected six times; triangular quasi-WGMs (Fig. 6.14c) where the light is reflected three times and quasi-WGMs (Fig. 6.14d) where the light is reflected six times in a round trip. Energy separations of 350 meV; 260 meV; 306 meV and 150 meV for the investigated modes in situations a,b,c and d respectively have been found. The best agreement between the experimental energy separations and the calculated ones is found for the quasi-WGMs shown in Fig.6.14d.

Using the following formula obtained from a plane wave model it is possible to calculate the peak emission wavelengths for the different quasi-WGMs [185]:

$$9l = \frac{\lambda_{\text{mode}}}{n}\left[N + \frac{6}{\pi}\arctan\left(\beta\sqrt{\frac{1}{3}n^2 - \frac{4}{3}}\right)\right] \tag{6.1}$$

The left side of the equation is the optical path for the quasi-WGM, N is the mode number, n is the refractive index, which depends on the wavelength and was obtained using the values published by Adachi [184]. The last term corrects for the phase shift occurring at total internal reflection, where β is $1/n$ for the TM modes and n for TE modes [185]. The calculated values in the spectral range of the observed peaks are plotted in Fig. 6.15b.

Comparing the calculated peak wavelengths for the quasi-WGMs with the measured spectra (Fig. 6.15b) it is possible to see that the calculated mode peak wavelengths fits the measured data very well for the case of TM modes with mode numbers N=17,18,19; the small deviation between the experimental and the calculated mode wavelengths can be explained by a small uncertainty in the measured nanorod diameter or refractive index. The good agreement with the TM polarized modes indicates that the light in the quasi-WGMs is preferentially TM polarized. The influence of TE polarized modes is considerably weaker, observable in small shoulders of the three main peaks. Similar observations have been made for hexagonal and triangular ZnO cavities [186, 187]. These modes stay constant over a large area of the pyramidal top of the nanorod, despite the diameter of the top constantly changing. This is due to the light not coupling into possible modes in the pyramidal top but instead into the base of the nanorod, which can be exemplary seen in Fig. 6.17.

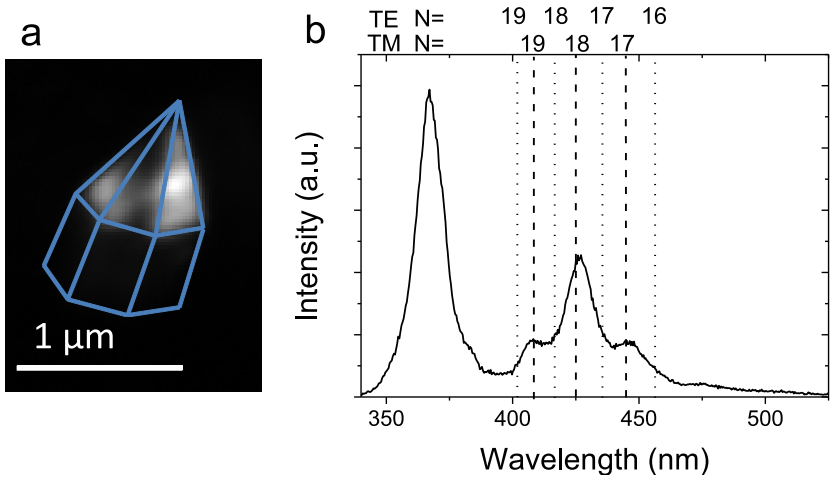

Figure 6.15: Intensity plot of the emission between 395 nm and 465 nm (a) and calculated quasi-WGMs with the experimental spectrum from Position 2 (b). TM modes are dashed, TE dotted.

In the spectral linescan in Fig. 6.13d we can observe that in the transition area between the second and the third optical region, the emission energy of the semipolar QWs shift to lower energies. This is most likely caused by an InN and thickness variation of the semipolar QWs when the semipolar facet and the *c*-plane facet meet (see Fig. 6.16). Similar behaviour was observed by Chang et al. [162] who observed a reduced emission energy from deposited QWs in an area where *m*-plane QWs meet a semipolar facet. This was attributed by them to the different InN incorporation on the different crystal facets. A related observation was made by Le Boulbar et al. who found evidence for an increased InN incorporation at the apex between two facets (in their case the *m*-plane facet and the semipolar $1\bar{1}01$) [180].

The third optical region exhibits a broad luminescence band consisting of multiple peaks from 490 nm to 650 nm covering the visible spectral range from green to red (Fig. 6.13d apex(3)). Applying a digital bandpass filter to the CL data to only show the luminescence intensity in this spectral range it is possible to see that this region is spatially confined to the tip of the nanorod, starting at 150 nm below the apex as shown in Fig.6.16a).

Scanning transmission electron microscope (STEM) imaging, shown in Fig. 6.16b), performed on a nanorod from the same array, reveals that five *c*-plane QWs have been grown at the tip of the nanorod. The growth of the *c*-plane QWs is caused by the presence of a *c*-plane facet on the top of the nanorod before the growth of the $In_xGa_{1-x}N$/GaN active zone. There are multiple effects which can combine to account for the very long wavelength emission from the

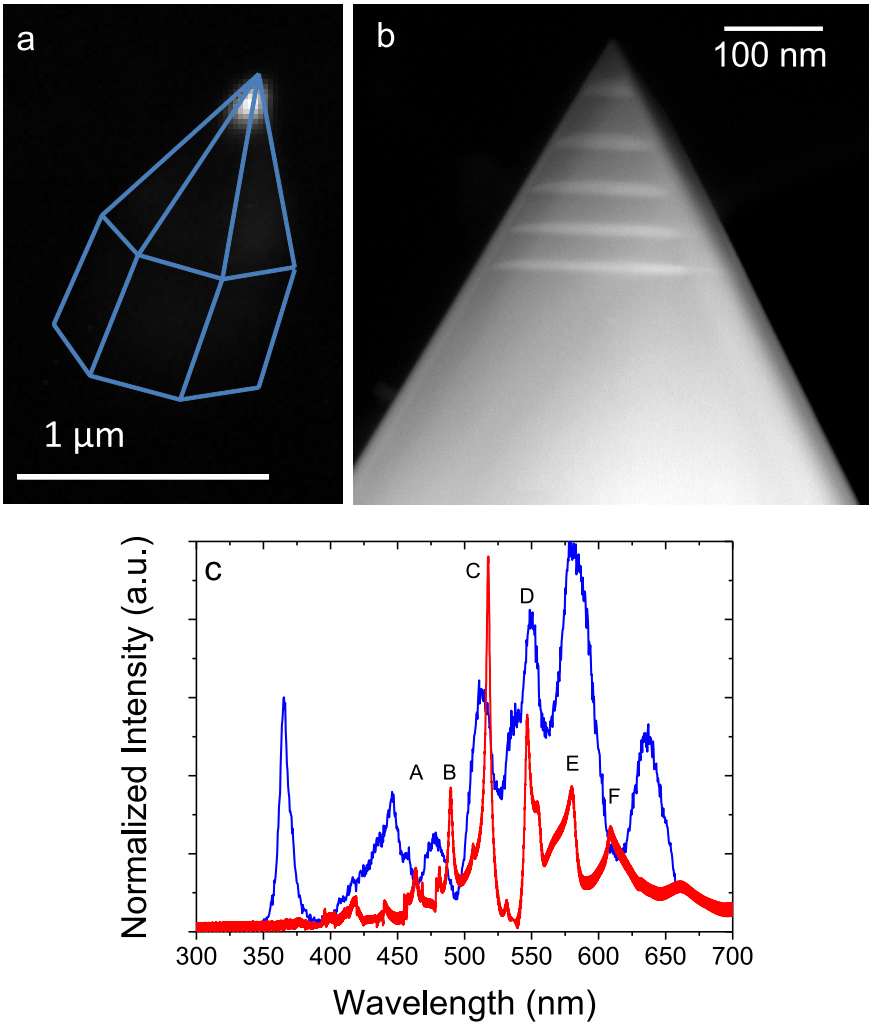

Figure 6.16: Intensity plot of the emission between 490 nm and 650 nm (a) and STEM image of the tip of a similar nanorod (b) as well as measured (blue, dotted) and simulated (red) spectra from the apex of the nanorod (c).

apex, as discussed further in a paper by Conroy et al. [188]. Firstly, due to the enhanced effect of electric fields on *c*-plane QWs the emission energy of these quantum wells will be red shifted compared to the semipolar QWs [36]. This is further enhanced by a reduced confinement of electric carriers in the QWs as the *c*-plane QWs have an increased thickness compared to the semipolar QWs. Furthermore the growth on a different crystal plane will also lead to a difference of the composition between the semipolar and *c*-plane QWs which is caused by the different diffusion length of In adatoms compared to Ga adatoms [178, 179] and the different In incorporation rates on the *c*-plane and *r*-plane crystallographic orientation [177] visible by the contrast difference between the semipolar QWs and the c-plane QWs in Fig. 6.16b. Comparing the relative intensity of this spectral region (see Fig. 6.13) with the relative intensity of both other regions, one can see that the optical quality is strongly reduced. This might be caused by an enhanced incorporation of point defects at interfaces (see Section 5.3.2) or a strong QCSE (see Section 2.3) due to the high QW thickness (see Fig. 6.16).

3D finite difference time domain modelling [189] simulations have been performed to investigate the influence of possible optical modes on the emission of the *c*-plane QWs. The results of the simulation are shown in Fig. 6.16c and Fig. 6.17. The simulated spectrum shows good agreement with the spectrum acquired from the apex of the nanorod. We attribute the small deviation between them to small deviations in the simulation parameters (e.g. height and width) from the actual parameters. Figure 6.17 shows the nanorod structure with a dipole source emitting at the apex of the nanorod, representing emission from the *c*-plane QWs. The results show frequency domain snapshots of the total electric field intensity for different mode numbers (peaks labelled A-F in Fig. 6.16c) at a fixed horizontal plane. For example, the third panel in Fig. 6.17 shows the the field intensity for the 5^{th}-order vertical mode and 10^{th}-order horizontal mode which lies at 518 nm (peak labelled C in Fig. 6.16c). This shows the very complex 3D nature of the vertical and horizontal modes within the structure.

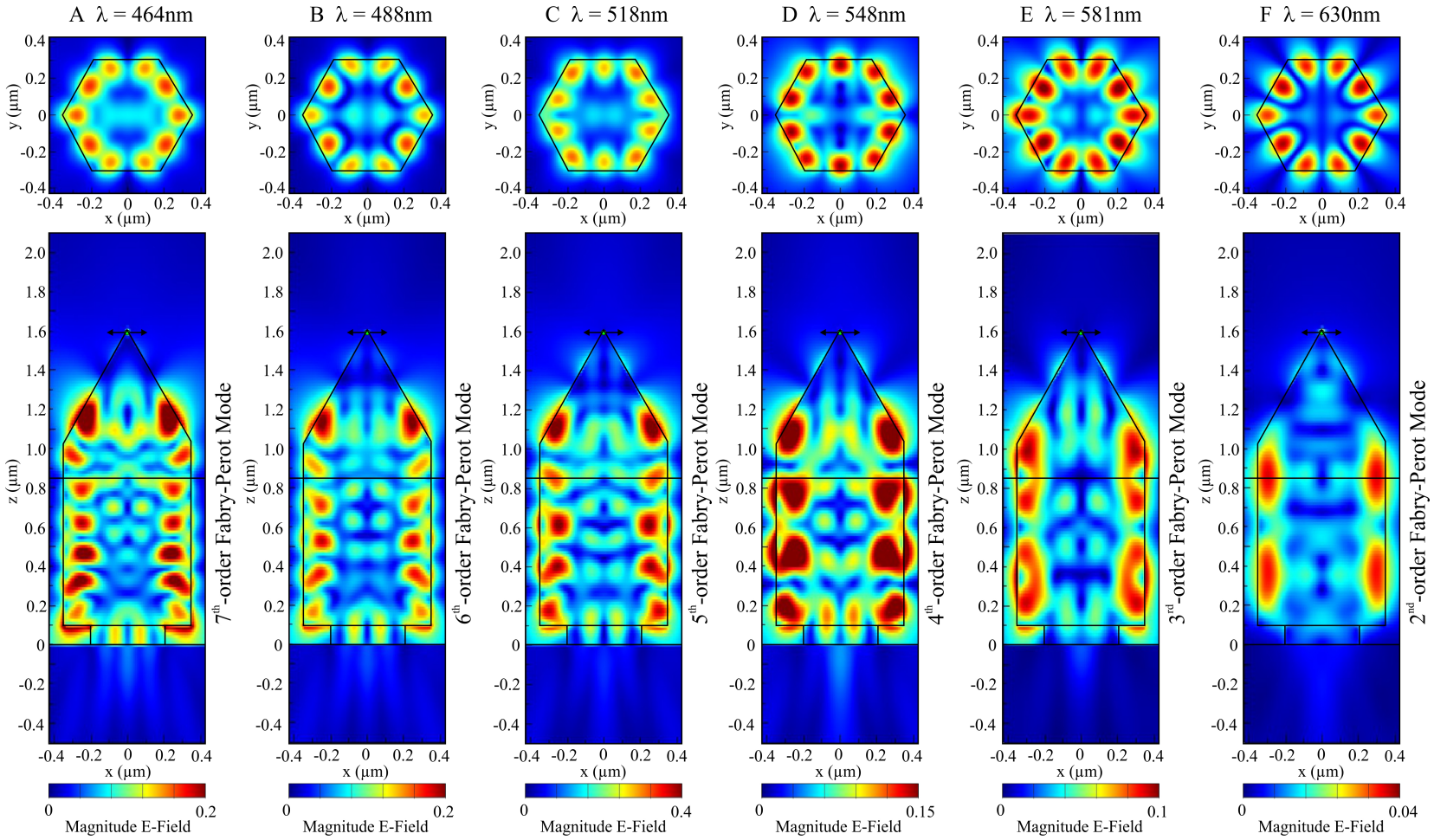

Figure 6.17: Modelled 3D optical modes at different wavelengths in a GaN nanorod: the horizontal modes from the marked plane are shown on top, the vertical modes on the bottom.

In conclusion, the luminescence properties of a single $In_xGa_{1-x}N$/GaN nanorod have been investigated by a combination of SE and CL hyperspectral imaging with STEM measurements and FDTD simulations. It was found that the growth resulted in the deposition of semipolar as well as polar QWs, the latter being attributed to the presence of a *c*-plane facet prior to deposition of the active region. FDTD simulation as well as plane wave modelling show that the QW emission is strongly influenced by optical modes propagating through the nanorod. The findings presented here show that nanorod LED structures offer an array of advantages over planar LED structures. The presence of optical modes, which can easily be engineered by changing the diameter and height of the nanorod, as well as two QW regions emitting from the blue to the red spectral region, potentially allows the design of true white LEDs without the need of light conversion using phosphors.

6.5 Summary

In this chapter the luminescence properties of $In_xGa_{1-x}N$/GaN MQW nanorods have been investigated. Characterization of the two different templates in section 6.2 revealed the influence of the etching time on the resulting morphology of the GaN nanorod templates. The resulting morphology was found to strongly influence the luminescence properties of $In_xGa_{1-x}N$/GaN MQWs grown on top of the nanorods. The best homogeneity in emission intensity and energy was found for the sample with a higher etching time. It was also found that the presence of *c*-plane facets on the nanorods before the $In_xGa_{1-x}N$/GaN MQW growth leads to the formation of *c* -plane QWs on the tip of the nanorods. The formation of this additional luminescent active region was found to have a detrimental effect on the luminescence properties of the sample with a shorter etching time and larger *c*-plane facets. By analysing a single nanorod from the sample with a longer etching time it was possible to see the influence of optical modes in the nanostructure on the optical properties of the QW luminescence from both the semipolar QWs and the *c* -plane QWs.

The findings presented here show that nanorod LED structures offer an array of advantages over planar LED structures. The presence of optical modes, which can easily be engineered by changing the diameter and height of the nanorod, as well as two QW regions emitting from the blue to the red spectral region, potentially allows the design of true white LEDs without the need of light conversion using phosphors. In these LED structures the warmth of the light could

be engineered by changing the dimensions of the nanorods, shifting the resonant modes.

Another prospective application of the findings presented in this chapter is utilizing the enhanced c-plane QW growth to fabricate $In_xGa_{1-x}N/GaN$ quantum dots which could be used for a wide range of applications, eg. single photon emitters.

Chapter 7

Conclusions and Future Work

This summary chapter recaps the experimental work presented in this thesis and provides summaries of the different experimental chapters. In the second section of this chapter possible future work based on the reported experimental work is discussed.

7.1 Conclusions

7.1.1 Techniques and samples

This thesis presented work on the analysis of low conductivity wide band gap semiconductors by the SEM based techniques of CL hyperspectral imaging, SE-imaging and WDX. Other measurement techniques were provided by collaborators, these include: Nouf M. Allehiani[1],the group of Prof. M. Kneissl at TU-Berlin[2] and the group of Prof. P. J. Parbrook at Tyndall National Institute[3]. Different series of samples were analysed and the results combined in three chapters depending on their structure: "Analysis of AlGaN layers" for samples where the main research interest was focussed on the properties of $Al_xGa_{1-x}N$ layers; "UV-LED structures" for samples where the investigation centred on the luminescence properties of the active region of UV-light emitting semiconductor structures and "Low dimensional semiconductor structures" where the properties of nanorod structures and their influence on the luminescence properties of MQW $In_xGa_{1-x}N$/GaN nanorod LEDs were discussed.

[1]providing ECCI images
[2]providing AFM, HR-XRD, SIMS and resistivity measurements
[3]providing AFM, HR-XRD, TEM images and PL

7.1.2 Analysis of AlGaN layers

In chapter 4 the influence of various growth parameters on MOCVD grown $Al_xGa_{1-x}N$ layers was studied in three sections on sample series provided by Prof. P. J. Parbrook (the miscut sample series as well as the sample series of $Al_xGa_{1-x}N$ layers with different thicknesses) from the Tyndall National Institute and by Prof. M. Kneissl from TU-Berlin (the investigated $Al_xGa_{1-x}N$:Si samples).

In the first section "Influence of miscut angle on AlGaN layers" (section 4.2) two samples of $Al_xGa_{1-x}N$ grown on top of Al_2O_3 substrates with different miscuts where investigated by CL in a low vacuum environment. CL and SE-imaging showed that at higher miscut angles the sample surface changed from a hillock dominated morphology to a morphology dominated by step bunches. It was found that this change introduces compositional inhomogeneities along step edges, where a higher GaN incorporation was measured. The increased GaN incorporation along the step bunches was attributed to the higher Ga atom mobility during growth.

In the second section "Influence of AlGaN layer thickness" (section 4.3) the influence of the thickness of $Al_xGa_{1-x}N$ layers on their luminescence properties was characterized. The results of the CL and SE-imaging showed a redshift of the $Al_xGa_{1-x}N$ NBE emission, which was attributed to a relaxation of compressive strain in the layer due to the bending of threading dislocations. Furthermore it was found that an increasing layer thickness leads to the coalescence of large hexagonal platelets, improving the compositional homogeneity of the semiconductor, decreasing the surface roughness and improving the crystal quality.

In the last section "Properties of Si-doped AlGaN" (section 4.4) the Si doping of high AlN% $Al_xGa_{1-x}N$ layers was studied. WDX results showed that Si is incorporated linearly with increasing SiH_4/III ratio and that the incorporation of the Si donor is independent of the AlN concentration. The analysis of room temperature CL spectra of $Al_xGa_{1-x}N$:Si with different AlN and doping concentrations revealed that the observed behaviour of the resistivity is caused by the incorporation of defect centres, it was also found that the type and concentration of the different defect centres depends on the AlN concentration as well as on the Si concentration. Furthermore, the effect of threading dislocations was investigated and it was found that all threading dislocations act as non-radiative recombination centres for the $Al_xGa_{1-x}N$ NBE emission. It was also shown that threading dislocations with a screw component introduce spiral growth in the material as well as increase the incorporation of compensating and self-compensating point defects. The spiral growth was found to cause hillocks on the sample sur-

face which introduce small step edges and kins onto which Ga atoms preferably bond and thus cause a compositional inhomogeneity.

7.1.3 UV-LED structures

In chapter 5 the properties of MOVPE grown UV-LED structures have been studied on $Al_xGa_{1-x}N$ UV-LEDs provided by the group of Prof. M. Kneissl from TU-Berlin and $In_xAl_{1-x}N$ UV-LEDs provided by the group of Prof. P. J. Parbrook from the Tyndall National Institute.

In the section "AlGaN UV-LED structures" (section 5.2) the intensity reduction observed in $Al_xGa_{1-x}N$ UV-LEDs with decreasing wavelength has been investigated. It was found that the reduction of measured intensity is caused by a change of the internal band structure of $Al_xGa_{1-x}N$. This behaviour was shown to be a challenge to overcome in future design of UV LEDs and will require changes in the LED design or utilisation of new geometries to allow for top extraction, as proposed by Zhao et al [139].

In the section "InAlN LED structures" (section 5.3) UV LEDs with an $In_xAl_{1-x}N$ based active zone have been studied. The influence of three different growth parameter on the optical and morphological properties of these devices was investigated.

The results of the investigation of the influence of the growth temperature shows that the QW growth temperature has a strong effect on the emission energy of $In_xAl_{1-x}N$ QW, leading to an increased InN desorption rate with increasing temperature, which induces a blueshift of the QW emission. The thickness of the QW was shown to have a strong influence on the QW emission intensity and to a lesser degree on the emission energy. Investigation of the buffer and barrier composition showed that an increased confinement due to a larger bandoffset between the QW and QB results in a higher QW intensity.

The surface morphology of the investigated samples was dominated by the morphology of the layer structure grown prior to the deposition of the active zone and no clear influence of the QW growth parameter on the morphology was found. The analysis of the samples furthermore showed that threading dislocations with a screw component can have a major impact on the compositional homogeneity of $In_xAl_{1-x}N$ QWs, inducing an InN segregation towards the dislocation core and facilitating pit formation as well as acting as non-radiative recombination centres.

7.1.4 Low dimensional semiconductor structures

In chapter 6 the luminescence properties of $In_xGa_{1-x}N$/GaN MQW nanorods have been investigated with the help of samples grown by the group of Prof. P. J. Parbrook. Characterization of the two different templates in section 6.2 revealed the influence of the etching time on the resulting morphology of the GaN nanorod templates. This morphology was found to strongly influence the luminescence properties of $In_xGa_{1-x}N$/GaN MQWs grown on top of the nanorods. The best homogeneity in emission intensity and energy was found for the sample with a higher etching time. It was also found that the presence of *c*-plane facets on the nanorods before the $In_xGa_{1-x}N$/GaN MQW growth leads to the formation of *c* -plane QWs on the tip of the nanorods. The formation of this additional luminescent active region was found to have a detrimental effect on the luminescence properties of the sample with a shorter etching time and larger *c*-plane facets. Additionally, by analysing a single nanorod from the sample with a longer etching time it was possible to see the influence of optical modes in the nano-structure on the optical properties of the QW luminescence from both the semipolar QWs and the *c* -plane QWs.

7.2 Future Work

Future research on $Al_xGa_{1-x}N$:Si is required in order to optimize the electrical properties of LED structures based on these layers. This includes furthering the understanding of the incorporation of compensating and self-compensating defect centres, which could potentially be achieved by growing in an Al-rich environment, for which calculations done by Hevia et al. [99] showed a higher formation energy of the triply charged cation vacancy. A downside of growing in this environment would that a dependence of the Si incorporation on the AlN concentration in this layer was reported by Junxue et al. [94] although they only studied a limitied amount of samples. Thus a careful consideration of both effects has to be done in order to achieve the optimal solution. Furthermore, the role of threading dislocations on the spatial distribution of dopants should be more intensively studied, for example by a combination of CL, WDX and ECCI, as studies suggest an increased Si incorporation around edge dislocations [190].

$Al_xGa_{1-x}N$ based UV-LEDs require future work in order to improve the extraction efficiency of TM-polarized light, which could be done by using alternative LED geometries to allow for top extraction, as proposed by Zhao et al [139]. Zhao et al. suggested utilizing nanowire geometries for UV-LEDs to circumvent the

downside of in-plane propagation of TM polarized light in surface-bottom emitters, they found that for certain nanowire dimensions the TM polarized light would be emitted from the top surface due to light coupling and scattering processes in the nanowire array. This research can be underpinned by utilizing the high spatial resolution of CL for detailed analysis of the nanowire as well as by performing polarization dependent CL in order to determine the polarization of the emitted light. Collaboration with other groups for the growth of these structures and for advanced modelling techniques to understand the the influence of the various growth parameters would be essential.

$In_xAl_{1-x}N$ based UV-LED devices need considerable research effort in order to achieve a device quality comparable to $Al_xGa_{1-x}N$ based UV-LEDs, this is mostly a task for growers which can be aided, as demonstrated, by utilizing multi-mode SEM based techniques. More importantly it is necessary to study the behaviour of the light polarization of $In_xAl_{1-x}N$ based LEDs with increasing AlN concentration, in order to prove that these LEDs offer an alternative to the established $Al_xGa_{1-x}N$ system, this can for example be achieved by polarization dependent CL measurements.

The findings presented in this thesis indicate a promising future for nanorod based LED devices. The influence of optical modes in these nano-structures on the luminescence profiles of the active region can offer an additional engineering parameter to further optimize LEDs. Furthermore, by exploiting the unique properties found in these nanorods one could achieve white light emitting LEDs without the need to use phosphors for colour conversion or one could fabricate single photon emitting QDs in the tip of the nanorod. To achieve all of these possibilities further research effort is needed, in understanding which parameter influences the optical modes and which growth parameters result in the highest quality nanorod structures. This can be accomplished by collaboration with groups utilising advanced modelling techniques (e.g. FDTD) to further the understanding of the coupling of light emitted from the different active zones in the nanorods with the optical modes. Additionally, the role of different QWs has to be further investigated to better understand differences between non-polar, semi-polar and polar QWs and their interaction with optical modes. The role of the QWs which formed at the tip of the nanorod should also be further investigated, for example by studying samples in which the parameters of the active zone has been varied (QW number, QW thickness and composition). SEM based techniques are especially suited for underpinning any research efforts in this area, as they can easily characterize single nanorods as well as nanorod arrays. Longterm research in this

area should also include the investigation how these nanorod structures can be efficiently processed as the commonly used approaches for planar LEDs will have to be changed due to the 3D nature of the nanorods.

List of Figures

List of Tables

Bibliography

[1] E.R. Blatchley, C. Shen, O.K. Scheible, J.P. Robinson, K. Ragheb, D.E. Bergstrom, and D. Rokjer. Validation of large-scale, monochromatic UV disinfection systems for drinking water using dyed microspheres. *Water research*, 42(3):677–688, 2008.

[2] R.Z. Chen, S.A. Craik, and J.R. Bolton. Comparison of the action spectra and relative {DNA} absorbance spectra of microorganisms: Information important for the determination of germicidal fluence (UV dose) in an ultraviolet disinfection of water. *Water Research*, 43(20):5087–5096, 2009.

[3] A. Khan, H. Seongmo, J. Lowder, V. Adivarahan, and Q. Fareed. Reliability issues in AlGaN based deep ultraviolet light emitting diodes. In *Reliability Physics Symposium, 2009 IEEE International*, pages 89–93, 2009.

[4] Y. Xie, Y. Qian, S. Zhan, W. Wang, and X. Liu et al. Band parameters for nitrogen containing semiconductors. *Appl. Phys. Lett.*, 69:334, (1996).

[5] F. Hasegawa, M. Minami, K. Sunaba, and T. Suemasu. Thick and smooth hexagonal GaN growth on GaAs (111) substrates at $1000°C$ with Halide Vapor Phase Epitaxy. *Jpn. J. Appl. Phys.*, 38:L700, (1999).

[6] O. Ambacher. Growth and applications of group III-nitrides. *Journal of Physics D: Applied Physics*, 31(20):2653, 1998.

[7] M. Frentrup. Epitaxie und Charakterisierung von nicht- und semipolaren Galliumnitrid-Heterostrukturen. Diplomarbeit, Technische Universität Berlin, (2010).

[8] S.Nakamura, S. Pearton, and G. Fasol. *The blue laser Diode*. Springer, 2 edition, (2000).

[9] V. Y. Davydov, A. A. Klochikhin, V. V. Emtsev, D. A. Kurdyukov, S. V. Ivanov, V. A. Vekshin, F. Bechstedt, J. Furthmüller, J. Aderhold, J. Gaul,

A.V. Mudryi, H. Harima, A. Hashimoto, A. Yakamoto, and E. E. Haller. Band Gap of Hexagonal InN and InGaN Alloys. *Phys. stat. sol. (b)*, 234:787, (2002).

[10] Q. Guo and A. Yoshida. Temperature dependence of band gap change in InN and AlN. *Physica*, 34(1):149 – 154, 1967.

[11] L. Vegard. Die Konstitution der Mischkristalle und die Raumfüllung der Atome. *Zeitschrift für Physik*, 5:17–26, 1921.

[12] I. Vurgaftman and J. R. Meyer. Band parameters for nitrogen-containing semiconductors. *J. Appl. Phys.*, 94:3675, (2003).

[13] J. Wu, W. Walukiewicz, K.M Yu, J. W. Ager III, S. X. Li, E. E. Haller, Hai Lu, and W. J. Schaff. Universal bandgap bowing in group-III nitride alloys. *Solid State Communications*, 127(6):411 – 414, 2003.

[14] Aixtron SE. Dornkaulstr. 2, 52134 Herzogenrath, Germany, 2016.

[15] M. A. Herman, W. Richter, and H. Sitter. *Epitaxy.* Springer, 1 edition, (2004).

[16] A. Saxler, P. Kung, C.J. Sun, E. Bigan, and M. Razeghi. High quality aluminum nitride epitaxial layers grown on sapphire substrates. *Applied Physics Letters*, 64(3):339–341, 1994.

[17] C.-H. Lee, G. C. Chi, C. F. Lin, M. S. Feng, and J. D. Guo. X-ray crystallographic study of GaN epitaxial films on Al_2O_3(0001) substrates with GaN buffer layers. *Applied Physics Letters*, 68(24):3440–3442, 1996.

[18] H. Amano, N. Sawaki, I. Akasaki, and Y. Toyoda. Metalorganic vapor phase epitaxial growth of a high quality GaN film using an AlN buffer layer. *Applied Physics Letters*, 48(5):353–355, 1986.

[19] S. Nakamura. Gan growth using gan buffer layer. *Japanese Journal of Applied Physics*, 30(10A):L1705, 1991.

[20] S. Figge, T. Böttcher, S. Einfeldt, and D. Hommel. In situ and ex situ evaluation of the film coalescence for GaN growth on GaN nucleation layers. *Journal of Crystal Growth*, 221(1-4):262 – 266, 2000.

[21] M. Leyer, J. Stellmach, Ch. Meissner, M. Pristovsek, and M. Kneissl. The critical thickness of InGaN on (0 0 0 1)GaN. *Journal of Crystal Growth*, 310:4913, (2008).

[22] S. R. Lee, D. D. Koleske, K. C. Cross, J. A. Floro, K. E. Waldrip, A. T. Wise, and S. Mahajan. In situ measurements of the critical thickness for strain relaxation in AlGaN/GaN heterostructures. *Appl. Phys. Lett.*, 85:6164, (2004).

[23] J. A. Floro, D. M. Follstaedt, P. Provencio, S. J. Hearne, and S. R. Lee. Misfit dislocation formation in the AlGaN-GaN heterointerface. *J. Appl. Phys.*, 96:7087, (2004).

[24] T. Sugahara, H. Sato, M. Hao, Y. Naoi, S. Kurai, S. Tottori, K. Yamashita, K. Nishino, L. T. Romano, and S. Sakai. Direct evidence that dislocations are non-radiative recombination centers in GaN. *Japanese Journal of Applied Physics*, 37(4A):L398, 1998.

[25] G. Kusch, M. Nouf-Allehiani, F. Mehnke, C. Kuhn, P.R. Edwards, T. Wernicke, A. Knauer, V. Kueller, G. Naresh-Kumar, M. Weyers, M. Kneissl, C. Trager-Cowan, and R.W. Martin. Spatial clustering of defect luminescence centers in Si-doped low resistivity $Al_{0.82}Ga_{0.18}N$. *Applied Physics Letters*, 107(7), 2015.

[26] A. H. Cottrell and B. A. Bilby. Dislocation theory of yielding and strain ageing of iron. *Proc. Phys. Soc. London Sect. A*, 62(1):49–62, 1949.

[27] A.P. Zhang, L.B. Rowland, E.B. Kaminsky, V. Tilak, J.C. Grande, J. Teetsov, A. Vertiatchikh, and L.F. Eastman. Correlation of device performance and defects in AlGaN/GaN high-electron mobility transistors. *Journal of Electronic Materials*, 32(5):388–394, 2003.

[28] X.A. Cao, E.B. Stokes, P.M. Sandvik, S.F. LeBoeuf, J. Kretchmer, and D. Walker. Diffusion and tunneling currents in GaN/InGaN multiple quantum well light-emitting diodes. *Electron Device Letters, IEEE*, 23(9):535–537, 2002.

[29] N. Sharma, P. Thomas, D. Tricker, and C. Humphreys. Chemical mapping and formation of V-defects in InGaN multiple quantum wells. *Applied Physics Letters*, 77(9):1274–1276, 2000.

[30] S. Suihkonen, T. Lang, O. Svensk, J. Sormunen, P.T. Törmä, M. Sopanen, H. Lipsanen, M.A. Odnoblyudov, and V.E. Bougrov. Control of the morphology of InGaN/GaN quantum wells grown by metalorganic chemical vapor deposition. *Journal of Crystal Growth*, 300(2):324 – 329, 2007.

[31] D. Hull and D.J. Bacon. Chapter 2 - observation of dislocations. In *Introduction to Dislocations (Fifth Edition)*, pages 21 – 41. Butterworth-Heinemann, fifth edition, 2011.

[32] B. Beaumont, P. Vennéguès, and P. Gibart. Epitaxial Lateral Overgrowth of GaN. *physica status solidi (b)*, 227(1):1–43, 2001.

[33] P. Vennéguès, B. Beaumont, V. Bousquet, M. Vaille, and P. Gibart. Reduction mechanisms for defect densities in GaN using one- or two-step epitaxial lateral overgrowth methods. *Journal of Applied Physics*, 87(9):4175–4181, 2000.

[34] E. F. Schubert. *Light-Emitting Diodes*. Cambridge University Press, 1 edition, (2005).

[35] F. Bernardini, V. Fiorentini, and D. Vanderbilt. Spontaneous polarization and piezoelectric constants of iii-v nitrides. *Phys. Rev. B*, 56:R10024–R10027, 1997.

[36] M. Leroux, N. N. Grandjean, M. Laügt, J. Massies, B. Gil, P. Lefebvre, and P. Bigenwald. Quantum confined Stark effect due to built-in internal polarization fields in (Al,Ga)N/GaN quantum wells. *Phys. Rev. B*, 58:R13371–R13374, 1998.

[37] C. Kittel. *Einfürung in die Festkörperphysik*. Oldenbourg Verlag München Wien, 14 edition, (2006).

[38] E. Calleja, F.J. Sánchez, D. Basak, M.A. Sánchez-García, E. Mu noz, I. Izpura, F. Calle, J.M.G. Tijero, J.L. Sánchez-Rojas, B. Beaumont, P. Lorenzini, and P. Gibart. Yellow luminescence and related deep states in undoped GaN. *Phys. Rev. B*, 55:4689–4694, 1997.

[39] C. G. Van de Walle, C. Stampfl, and J. Neugebauer. Theory of doping and defects in III-V nitrides. *Journal of Crystal Growth*, 189-190:505–510, 1998.

[40] S. Nakamura, T. Mukai, M. Senoh, and N. Iwasa. Thermal annealing effects on p-type Mg-doped GaN films. *Japanese Journal of Applied Physics*, 31(2B):L139, 1992.

[41] H. Amano, M. Kito, K. Hiramatsu, and I. Akasaki. P-type conduction in Mg-doped GaN treated with low-energy electron beam irradiation (LEEBI). *Japanese Journal of Applied Physics*, 28(12A):L2112, 1989.

[42] L.T. Romano and T.H. Myers. The influence of inversion domains on surface morphology in GaN grown by molecular beam epitaxy. *Appl. Phys. Lett.*, 71:3486, (1997).

[43] P. Vennéguès, M. Leroux, S. Dalmasso, M. Benaissa, P. De Mierry, P. Lorenzini, B. Damilano, B. Beaumont, J. Massies, , and P. Gibart. Atomic structure of pyramidal defects in Mg-doped GaN. *Phys. Rev. B*, 68:235214, (2003).

[44] L.T. Romano, J.E. Northrup, A.J. Ptak, and T.H. Myers. Faceted inversion domain boundary in GaN films doped with Mg. *Appl. Phys. Lett.*, 77:2479, (2000).

[45] S. Figge, R. Kröger, T. Böttcher, P.L. Ryder, and D. Hommel. Magnesium segregation and the formation of pyramidal defects in p-GaN. *Appl. Phys. Lett.*, 81:4748, (2002).

[46] W. Götz, N. M. Johnson, C. Chen, H. Liu, C. Kuo, and W. Imler. Activation energies of Si donors in GaN. *Appl. Phys. Lett.*, 68:3144, (1996).

[47] L. B. Rowland, K. Doverspike, and D. K. Gaskill. Silicon doping of GaN using disilane. *Appl. Phys. Lett.*, 66:1495, (1995).

[48] S. Fischer, C. Wetzel, E.E. Haller, and B.K. Meyer. On p-type doping in GaN-acceptor binding energies. *Appl. Phys. Lett.*, 67:1298, (1995).

[49] A. Salvador, W. Kima, Ö. Aktas, A. Botchkarev, Z. Fan, and H. Morkoç. Near ultraviolet luminescence of Be doped GaN grown by reactive molecular beam epitaxy using ammonia. *Appl. Phys. Lett.*, 69:2692, (1996).

[50] P.J. Goodhew, J. Humphreys, and R. Beanland. *Electron microscopy and analysis*. Taylor and Francis, 3 edition, (2001).

[51] P.E.J. Flewitt and R.K. Wild. *Physical methods for materials characterisation*. Institute of Physics Publishing, 1 edition, (1994).

[52] K. Thonke, I. Tischer, M. Hocker, M. Schirra, K. Fujan, M. Wiedenmann, R. Schneider, M. Frey, and M. Feneberg. Nanoscale characterisation of semiconductors by cathodoluminescence. *IOP Conf. Series: Materials Science and Engineering*, 55:012018, 2014.

[53] Y.P. Varshni. Temperature dependence of the energy gap in semiconductors. *Physica*, 34(1):149 – 154, 1967.

[54] N. Grandjean, B. Damilano, S. Dalmasso, M. Leroux, M. Laügt, and J. Massies. Built-in electric-field effects in wurtzite AlGaN/GaN quantum wells. *Journal of Applied Physics*, 86(7):3714–3720, 1999.

[55] D. Drouin, A. R. Couture, D. Joly, X. Tastet, V. Aimez, and R. Gauvin. Casino v2.42 fast and easy-to-use modeling tool for scanning electron microscopy and microanalysis users. *Scanning*, 29(3):92–101, 2007.

[56] K. Kumakura, T. Makimoto, N. Kobayashi, T. Hashizume, T. Fukui, and H. Hasegawa. Minority carrier diffusion length in GaN: Dislocation density and doping concentration dependence. *Applied Physics Letters*, 86(5), 2005.

[57] K. Kanaya and S. Okayama. Penetration and energy-loss theory of electrons in solid targets. *Journal of Physics D: Applied Physics*, 5(1):43, 1972.

[58] K. Knobloch, P. Perlin, J. Krueger, E.R. Weber, and C. Kisielowski. Effect of internal absorption on cathodoluminescence from GaN. *MRS Internet Journal of Nitride Semiconductor Research*, 3, 1 1998.

[59] A.A. Allerman, M.H. Crawford, A.J. Fischer, K.H.A. Bogart, S.R. Lee, D.M. Follstaedt, P.P. Provencio, and D.D. Koleske. Growth and design of deep-UV (240-290 nm) light emitting diodes using AlGaN alloys. *Journal of Crystal Growth*, 272(1-4):227–241, 2004.

[60] T. Wang, Y.H. Liu, Y.B. Lee, Y. Izumi, J.P. Ao, J. Bai, H.D. Li, and S. Sakai. Fabrication of high performance of AlGaN/GaN-based {UV} light-emitting diodes. *Journal of Crystal Growth*, 235(1-4):177–182, 2002.

[61] G. Kusch, H. Li, P.R. Edwards, J. Bruckbauer, T.C. Sadler, P.J. Parbrook, and R.W. Martin. Influence of substrate miscut angle on surface morphology and luminescence properties of AlGaN. *Appl. Phys. Lett.*, 104(9):092114, 2014.

[62] X.L. Wang, D.G. Zhao, D.S. Jiang, H. Yang, J. W. Liang, U. Jahn, and K. Ploog. Al compositional inhomogeneity of AlGaN epilayer with a high Al composition grown by metal-organic chemical vapour deposition. *Journal of Physics: Condensed Matter*, 19(17):176005, 2007.

[63] M. Iwaya, S. Terao, T. Sano, T. Ukai, R. Nakamura, S. Kamiyama, H. Amano, and I. Akasaki. Suppression of phase separation of AlGaN during lateral growth and fabrication of high-efficiency UV-LED on optimized AlGaN. *Journal of Crystal Growth*, 237-239, Part 2:951–955, 2002.

[64] Q. Sun, Y. Huang, H. Wang, J. Chen, R.Q. Jin, S.M. Zhang, H. Yang, D.S. Jiang, U. Jahn, and K.H. Ploog. Lateral phase separation in AlGaN grown on GaN with a high-temperature AlN interlayer. *Applied Physics Letters*, 87(12), 2005.

[65] P. Perlin, G. Franssen, J. Szeszko, R. Czernecki, G. Targowski, M. Kryśko, S. Grzanka, G. Nowak, E. Litwin-Staszewska, R. Piotrzkowski, M. Leszczyński, B. Łucznik, I. Grzegory, R. Jakieła, M. Albrecht, and T. Suski. Nitride-based quantum structures and devices on modified GaN substrates. *Phys. stat. sol. (a)*, 206(6):1130–1134, 2009.

[66] V. Kueller, A. Knauer, U. Zeimer, M. Kneissl, and M. Weyers. Controlled coalescence of MOVPE grown AlN during lateral overgrowth. *Journal of Crystal Growth*, 368(0):83 – 86, 2013.

[67] T. Someya, K. Hoshino, and Y. Arakawa. Misorientation-angle dependence of GaN layers grown on a -plane sapphire substrates by metalorganic chemical vapor deposition. *Appl. Phys. Lett.*, 13(0):1992, 2001.

[68] N.A.K. Kaufmann, L. Lahourcade, B. Hourahine, D. Martin, and N. Grandjean. Critical impact of Ehrlich-Schwöbel barrier on GaN surface morphology during homoepitaxial growth. *J. of Crystal Growth*, 433:36–42, 2016.

[69] J. Tersoff, Y. H. Phang, Zhenyu Zhang, and M. G. Lagally. Step-Bunching Instability of Vicinal Surfaces under Stress. *Phys Rev. Lett.*, 75(14):2730–2733, Oct 1995.

[70] S. Stoyanov. Electromigration induced step bunching on Si surfaces - how does it depend on the temperature and heating current direction? *Japanese Journal of Applied Physics*, 30(1R):1, 1991.

[71] H.Y. Lin, Y.F. Chen, T.Y. Lin, C.F. Shih, K.S. Liu, and N.C. Chen. Direct evidence of compositional pulling effect in $Al_xGa_{1-x}N$ epilayers. *J. Crystal Growth*, 290(1):225–228, Apr 2006.

[72] J.R. Gong, W.T. Liao, S.L. Hsieh, P.H. Lin, and Y.L. Tsai. Strain-induced effect on the Al incorporation in AlGaN films and the properties of AlGaN/GaN heterostructures grown by metalorganic chemical vapor deposition. *J. Crystal Growth*, 249(1-2):28–36, Feb 2003.

[73] Y. Koide, N. Itoh, N. Sawaki, and I. Akasaki. Effect of AlN Buffer Layer on AlGaN/α-Al_2O_3 Heteroepitaxial Growth by Metalorganic Vapor Phase Epitaxy. *Jpn. J. App. Phys*, 27(7):1156–1161, July 1988.

[74] M. Asif Khan, M. Shatalov, H. P. Maruska, H. M. Wang, and E. Kuokstis. III–Nitride UV Devices. *Japanese Journal of Applied Physics*, 44(10):7191–7206, Oct 2005.

[75] D.G. Zhao, D.S. Jiang, J.J. Zhu, Z.S. Liu, S.M. Zhang, Hui Yang, U. Jahn, and K.H. Ploog. Al composition variations in AlGaN films grown on low-temperature GaN buffer layer by metalorganic chemical vapor deposition. *Journal of Crystal Growth*, 310(24):5266 – 5269, Dec 2008.

[76] T. Y. Chang, M. A. Moram, C. McAleese, M. J. Kappers, and C. J. Humphreys. Inclined dislocation arrays in AlGaN/AlGaN quantum well structures emitting at 290 nm. *J. App. Phys.*, 108(12):–, Dec 2010.

[77] S. Keller, C. S. Suh, N. A. Fichtenbaum, M. Furukawa, Z. Chen R. Chu, K. Vijayraghavan, S. Rajan, S. P. DenBaars, J. S. Speck, and U. K. Mishra. Influence of the substrate misorientation on the properties of N-polar InGaN/GaN and AlGaN/GaN heterostructures. *J. App. Phys.*, 104(9):–, Nov 2008.

[78] A. Knauer, V. Kueller, U. Zeimer, M. Weyers, C. Reich, and M. Kneissl. AlGaN layer structures for deep UV emitters on laterally overgrown AlN/sapphire templates. *phys. stat. sol. (a)*, 210(3):451–454, Dec 2013.

[79] A.Shikanai, T. Azuhata, T. Sota, S. Chichibu, A. Kuramata, K. Horino, and S. Nakamura. Biaxial strain dependence of exciton resonance energies in wurtzite GaN. *Journal of Applied Physics*, 81(1):417–424, 1997.

[80] P. Cantu, F. Wu, P. Waltereit, S. Keller, A. E. Romanov, U. K. Mishra, S. P. DenBaars, and J. S. Speck. Si doping effect on strain reduction in compressively strained $Al_{0.49}Ga_{0.51}N$ thin films. *Applied Physics Letters*, 83(4):674–676, 2003.

[81] Z. Ren, Q. Sun, S.-Y. Kwon, J. Han, K. Davitt, Y.K. Song, A.V. Nurmikko, H.-K. Cho, W. Liu, J. A. Smart, and L.J. Schowalter. Heteroepitaxy of AlGaN on bulk AlN substrates for deep ultraviolet light emitting diodes. *Applied Physics Letters*, 91(5):–, 2007.

[82] D. M. Follstaedt, S. R. Lee, P. P. Provencio, A. A. Allerman, J. A. Floro, and M. H. Crawford. Relaxation of compressively-strained AlGaN by inclined threading dislocations. *Applied Physics Letters*, 87(12):–, 2005.

[83] A. E. Romanov and J. S. Speck. Stress relaxation in mismatched layers due to threading dislocation inclination. *Applied Physics Letters*, 83(13):2569–2571, 2003.

[84] R. Collazo, S. Mita, J. Xie, A. Rice, J. Tweedie, R. Dalmau, and Z. Sitar. Progress on n-type doping of AlGaN alloys on AlN single crystal substrates for UV optoelectronic applications. *physica status solidi (c)*, 8(7-8):2031–2033, 2011.

[85] X.T. Trinh, D. Nilsson, I.G. Ivanov, E. Janzén, A. Kakanakova-Georgieva, and N.T. Son. Stable and metastable Si negative-U centers in AlGaN and AlN. *Appl. Phys. Lett.*, 105(16):162106, 2014.

[86] C.G. van de Walle and J. Neugebauer. First-principles calculations for defects and impurities: Applications to III-nitrides. *J. Appl. Phys.*, 95:3851, 2004.

[87] Q. Yan, A. Janotti, M. Scheffler, and C.G. Van de Walle. Origins of optical absorption and emission lines in AlN. *Appl. Phys. Lett.*, 105(11):111104, 2014.

[88] RTG. Schwarzschildstr. 1, 12489 Berlin, Germany, 2015.

[89] Evans Analytical Group. 2710 Walsh Ave., Santa Clara, CA 95051, United States of America, 2013.

[90] K. Bejtka, P.R. Edwards, R.W. Martin, S. Fernández-Garrido, and E. Calleja. Composition and luminescence of AlInGaN layers grown by plasma-assisted molecular beam epitaxy. *Journal of Applied Physics*, 104(7), 2008.

[91] G. Blaise and M. Bernheim. Proceedings of the third symposium on surface physics university of Utrecht, The Netherlands 26-28 june 1974: Adsorption of gases studied by secondary ion emission mass spectrometry. *Surface Science*, 47(1):324 – 343, 1975.

[92] V.R. Deline, W. Katz, C.A. Evans, and P. Williams. Mechanism of the SIMS matrix effect. *Applied Physics Letters*, 33(9):832–835, 1978.

[93] K. Wittmaack. Primary-ion charge compensation in SIMS analysis of insulators. *Journal of Applied Physics*, 50(1):493–497, 1979.

[94] J. Ran, X. Wang, G. Hu, J. Li, J. Wang, C. Wang, Y. Zeng, and J. Li. The difference of Si doping efficiency in GaN and AlGaN in GaN-based HBT structure. *physica status solidi (c)*, 3(3):490–493, 2006.

[95] G. Parish, S. Keller, S.P. Denbaars, and U.K. Mishra. SIMS investigations into the effect of growth conditions on residual impurity and silicon incorporation in GaN and $Al_xGa_{1-x}N$. *Journal of Electronic Materials*, 29(1):15–20, 2000.

[96] Y. Taniyasu, M. Kasu, and N. Kobayashi. Intentional control of n-type conduction for Si-doped AlN and $Al_xGa_{1-x}N(0.42 \leq x \geq 1)$. *Applied Physics Letters*, 81(7):1255–1257, 2002.

[97] A. Kakanakova-Georgieva, D. Nilsson, X.T. Trinh, U. Forsberg, N.T. Son, and E. Janzén. The complex impact of silicon and oxygen on the n-type conductivity of high-Al-content AlGaN. *Applied Physics Letters*, 102(13), 2013.

[98] C. Stampfl, J. Neugebauer, and C. G. Van de Walle. Doping of $Al_xGa_{1-x}N$ alloys. *Materials Science and Engineering: B*, 59(1-3):253–257, 1999.

[99] D.F. Hevia, C. Stampfl, F. Vi nes, and F. Illas. Microscopic origin of n-type behavior in Si-doped AlN. *Phys. Rev. B*, 88:085202, 2013.

[100] J. Stellmach, M. Pristovsek, Ö. Savaş, J. Schlegel, E.V. Yakovlev, and M. Kneissl. High aluminium content and high growth rates of AlGaN in a close-coupled showerhead {MOVPE} reactor. *Journal of Crystal Growth*, 315(1):229 – 232, 2011.

[101] C.-U. Ro, J. Osán, and R. Van Grieken. Determination of low-Z elements in individual environmental particles using windowless EPMA. *Analytical Chemistry*, 71(8):1521–1528, 1999.

[102] C.J. Deatcher, K. Bejtka, R.W. Martin, S. Romani, H. Kheyrandish, L.M. Smith, S.A. Rushworth, C. Liu, M.G. Cheong, and I. M. Watson. Wavelength-dispersive X-ray microanalysis as a novel method for studying magnesium doping in gallium nitride epitaxial films. *Semiconductor Science and Technology*, 21(9):1287, 2006.

[103] F. Mehnke, T. Wernicke, H. Pingel, C. Kuhn, C. Reich, V. Kueller, A. Knauer, M. Lapeyrade, M. Weyers, and M. Kneissl. Highly conductive n-$Al_xGa_{1-x}N$ layers with aluminium mole fractions above 80%. *Applied Physics Letters*, 103(21), 2013.

[104] N. Nepal, M. L. Nakarmi, J. Y. Lin, and H. X. Jiang. Photoluminescence studies of impurity transitions in AlGaN alloys. *Applied Physics Letters*, 89(9):092107, 2006.

[105] K. B. Nam, M. L. Nakarmi, J. Y. Lin, and H. X. Jiang. Deep impurity transitions involving cation vacancies and complexes in AlGaN alloys. *Applied Physics Letters*, 86(22):222108, 2005.

[106] E. Monroy, J. Zenneck, G. Cherkashinin, O. Ambacher, M. Hermann, M. Stutzmann, and M. Eickhoff. Luminescence properties of highly Si-doped AlN. *Appl. Phys. Lett.*, 88(7):071906, 2006.

[107] W. Rieger, T. Metzger, H. Angerer, R. Dimitrov, O. Ambacher, and M. Stutzmann. Influence of substrate-induced biaxial compressive stress on the optical properties of thin GaN films. *Applied Physics Letters*, 68(7):970–972, 1996.

[108] H. Teisseyre, T. Suski, P. Perlin, I. Grzegory, M. Leszczynski, M. Bockowski, S. Porowski, J. A. Freitas, R. L. Henry, A. E. Wickenden, and D. D. Koleske. Different character of the donor-acceptor pair-related 3.27 ev band and blue photoluminescence in mg-doped gan. hydrostatic pressure studies. *Phys. Rev. B*, 62:10151–10157, 2000.

[109] A. Reiher, J. Bläsing, A. Dadgar, A. Diez, and A. Krost. Efficient stress relief in gan heteroepitaxy on si(1 1 1) using low-temperature aln interlayers. *Journal of Crystal Growth*, 248:563 – 567, 2003.

[110] N. M. Allehiani, G. Kusch, G. Naresh-Kumar, F. Mehnke, J. Enslin, T. Wernicke, A. Knauer, V. Kueller, P. R. Edwards, E. Pascal, R. Johnston, S. Kraeusel, B. Houraine, M. Weyers, M. Kneissl, C. Trager-Cowan, and R. W. Martin. Quantitative analysis of threading dislocations in $al_{0.82}ga_{0.18}$n:si layers grown on laterally overgrown aln/sapphire template. 2016. to be submitted.

[111] U. Zeimer, V. Kueller, A. Knauer, A. Mogilatenko, M. Weyers, and M. Kneissl. High quality AlGaN grown on {ELO} AlN/sapphire templates. *Journal of Crystal Growth*, 377(0):32 – 36, 2013.

[112] X. Q. Shen, H. Matsuhata, and H. Okumura. Reduction of the threading dislocation density in GaN films grown on vicinal sapphire (0001) substrates. *Applied Physics Letters*, 86(2), 2005.

[113] A. Mogilatenko, V. Küller, A. Knauer, J. Jeschke, U. Zeimer, M. Weyers, and G. Tränkle. Defect analysis in AlGaN layers on AlN templates obtained by epitaxial lateral overgrowth. *Journal of Crystal Growth*, 402:222 – 229, 2014.

[114] I.A. Ajia, P.R. Edwards, Z. Liu, J.C. Yan, R.W. Martin, and I.S. Roqan. Excitonic localization in AlN-rich $Al_xGa_{1-x}N/Al_yGa_{1-y}N$ multi-quantum-well grain boundaries. *Appl. Phys. Lett.*, 105(12):122111, 2014.

[115] B. Heying, E. J. Tarsa, C. R. Elsass, P. Fini, S. P. DenBaars, and J. S. Speck. Dislocation mediated surface morphology of GaN. *Journal of Applied Physics*, 85(9):6470–6476, 1999.

[116] W. Qian, M. Skowronski, M. De Graef, K. Doverspike, L.B. Rowland, and D.K. Gaskill. Microstructural characterization of α-GaN films grown on sapphire by organometallic vapor phase epitaxy. *Appl. Phys. Lett.*, 66(10):1252, 1995.

[117] R. M. Farrell, E. C. Young, F. Wu, S. P. DenBaars, and J. S. Speck. Materials and growth issues for high-performance nonpolar and semipolar light-emitting devices. *Semicond. Sci. Technol.*, 27(2):024001, 2012.

[118] J. Elsner and R. Jones and P.K. Sitch and V. D. Porezag and M. Elstner and Th. Frauenheim and M. I. Heggie and S. Öberg and P. R. Briddon. Theory of threading edge and screw dislocations in GaN. *Phys. Rev. Lett.*, 79(19):3672–3675, 1997.

[119] I. Bellabas, M. A. Belkhir, Y.H. Lee, J. Chen, A. Béré, P. Ruterana, and G. Nouet. Local electronic structure of threading screw dislocation in wurtzite GaN. *Computational Materials Science*, 37(3):410–416, 2006.

[120] A.F. Wright and J. Furthmüller. Theoretical investigation of edge dislocations in AlN. *Appl. Phys. Lett.*, 72(26):3467, 1998.

[121] M.E. Hawkridge and D. Cherns. Oxygen segregation to dislocations in GaN. *Appl. Phys. Lett.*, 87(22):221903, 2005.

[122] Z.G. Herro, D. Zhuang, R. Schlesser, and Z. Sitar. Growth of AlN single crystalline boules. *J. Crystal Growth*, 312(18):2519–2521, 2010.

[123] M.A. Würtele, T. Kolbe, M. Lipsz, A. Külberg, M. Weyers, M. Kneissl, and M. Jekel. Application of GaN-based ultraviolet-C light emitting diodes–UV LEDs–for water disinfection. *Water Research*, 45(3):1481–1489, 2011.

[124] M. Kneissl, T. Kolbe, C. Chua, V. Kueller, N. Lobo, J. Stellmach, A. Knauer, H. Rodriguez, S. Einfeldt, Z. Yang, N. M. Johnson, and M. Weyers. Advances in group III-nitride-based deep UV light-emitting diode technology. *Semiconductor Science and Technology*, 26(1):014036, 2011.

[125] B. Maleyre, O. Briot, and S. Ruffenach. MOVPE growth of InN films and quantum dots. *Journal of Crystal Growth*, 269(1):15 – 21, 2004.

[126] A.V. Lobanova, K.M. Mazaev, R.A Talalaev, M. Leys, S. Boeykens, K. Cheng, and S. Degroote. Effect of V/III ratio in AlN and AlGaN {MOVPE}. *Journal of Crystal Growth*, 287(2):601 – 604, 2006.

[127] R. Buttè, J-F. Carlin, E. Feltin, M. Gonschorek, S. Nicolay, G. Christmann, D. Simeonov, A. Castiglia, J. Dorsaz, H. J. Buehlmann, S. Christopoulos, G. Baldassarri Höger von Högersthal, A. J. D. Grundy, M. Mosca, C. Pinquier, M. A. Py, F. Demangeot, J. Frandon, P. G. Lagoudakis, J. J. Baumberg, and N. Grandjean. Current status of AlInN layers lattice-matched to GaN for photonics and electronics. *Journal of Physics D: Applied Physics*, 40(20):6328, 2007.

[128] K.B. Nam, J. Li, M.L. Nakarmi, J.Y. Lin, and H.X. Jiang. Unique optical properties of AlGaN alloys and related ultraviolet emitters. *Applied Physics Letters*, 84(25):5264–5266, 2004.

[129] T. Kolbe, A. Knauer, C. Chua, Z. Yang, S. Einfeldt, P. Vogt, N.M. Johnson, M. Weyers, and M. Kneissl. Optical polarization characteristics of ultraviolet (In)(Al)GaN multiple quantum well light emitting diodes. *Applied Physics Letters*, 97(17), 2010.

[130] J. Li, K.B. Nam, M.L. Nakarmi, J.Y. Lin, H.X. Jiang, P. Carrier, and S.-H. Wei. Band structure and fundamental optical transitions in wurtzite AlN. *Applied Physics Letters*, 83(25):5163–5165, 2003.

[131] A. Khan, K. Balakrishnan, and T. Katona. Ultraviolet light-emitting diodes based on group three nitrides. *Nature Photonics*, 2(77):84, 2008.

[132] H.S. Kim, R.A. Mair, J. Li, J.Y. Lin, and H.X. Jiang. Time-resolved photoluminescence studies of $Al_xGa_{1-x}N$ alloys. *Applied Physics Letters*, 76(10):1252–1254, 2000.

[133] H. Morkoç. *Nitride Semiconductor Devices*. Wiley-VCH, (2013).

[134] S. Nakamura and S. F. Chichibu. *Introduction to nitride semiconductors, blue lasers and light emitting diodes*. CRC press, (2000).

[135] Peter Y. Yu and M. Cardona. *Fundamentals of Semiconductors*. Springer, 4 edition, (2010).

[136] G.D. Chen, M. Smith, J.Y. Lin, H.X. Jiang, S.-H. Wei, M.A. Khan, and C.J. Sun. Fundamental optical transitions in GaN. *Applied Physics Letters*, 68(20):2784–2786, 1996.

[137] H. Morkoç, S. Strite, G.B. Gao, M.E. Lin, B. Sverdlov, and M. Burns. Large-band-gap SiC, III-V nitride, and II-VI ZnSe-based semiconductor device technologies. *Journal of Applied Physics*, 76(3):1363–1398, 1994.

[138] T. Kolbe, A. Knauer, C. Chua, Z. Yang, V. Kueller, S. Einfeldt, P. Vogt, N.M. Johnson, M. Weyers, and M. Kneissl. Effect of temperature and strain on the optical polarization of (In)(Al)GaN ultraviolet light emitting diodes. *Applied Physics Letters*, 99(26), 2011.

[139] S. Zhao, M. Djavid, and Z. Mi. Surface emitting, high efficiency near-vacuum ultraviolet light source with aluminum nitride nanowires monolithically grown on silicon. *Nano Letters*, 0(0):null, 2015.

[140] T.C. Sadler, M.J. Kappers, and R.A. Oliver. The effect of temperature and ammonia flux on the surface morphology and composition of $In_xAl_{1-x}N$ epitaxial layers. *Journal of Crystal Growth*, 311(13):3380 – 3385, 2009.

[141] H. Kim-Chauveau, P. de Mierry, J-M. Chauveau, and J-Y. Duboz. The influence of various MOCVD parameters on the growth of $Al_{1-x}In_xN$ ternary alloy on GaN templates. *Journal of Crystal Growth*, 316(1):30 – 36, 2011.

[142] T. Fujimori, H. Imai, A. Wakahara, H. Okada, A. Yoshida, T. Shibata, and M. Tanaka. Growth and characterization of AlInN on AlN template. *Journal of Crystal Growth*, 272(1-4):381–385, 2004.

[143] T. Kehagias, G.P. Dimitrakopulos, J. Kioseoglou, H. Kirmse, C. Giesen, M. Heuken, A. Georgakilas, W. Neumann, T. Karakostas, and P. Komninou.

Indium migration paths in V-defects of InAlN grown by metal-organic vapor phase epitaxy. *Applied Physics Letters*, 95(7), 2009.

[144] H. Lei, J. Chen, and P. Ruterana. Role of c-screw dislocations on indium segregation in InGaN and InAlN alloys. *Applied Physics Letters*, 96(16), 2010.

[145] A. Mouti, J.-L. Rouvière, M. Cantoni, J.-F. Carlin, E. Feltin, N. Grandjean, and P. Stadelmann. Stress-modulated composition in the vicinity of dislocations in nearly lattice matched $Al_xIn_{1-x}N$/GaN heterostructures: A possible explanation of defect insensitivity. *Phys. Rev. B*, 83:195309, 2011.

[146] D. Cherns, S.J. Henley, and F.A. Ponce. Edge and screw dislocations as nonradiative centers in InGaN/GaN quantum well luminescence. *Applied Physics Letters*, 78(18):2691–2693, 2001.

[147] J. E. Northrup, L. T. Romano, and J. Neugebauer. Surface energetics, pit formation, and chemical ordering in InGaN alloys. *Applied Physics Letters*, 74(16):2319–2321, 1999.

[148] A. Kamińska, G. Franssen, T. Suski, E. Feltin, and N. Grandjean. Pressure-induced piezoelectric effects in near-lattice-matched GaN/AlInN quantum wells. *Journal of Applied Physics*, 104(6), 2008.

[149] H. Teisseyre, T. Suski, S. P. Łepkowski, S. Anceau, P. Perlin, P. Lefebvre, L. Kończewicz, H. Hirayama, and Y. Aoyagi. Determination of built-in electric fields in quaternary InAlGaN heterostructures. *Applied Physics Letters*, 82(10):1541–1543, 2003.

[150] P. Perlin, C. Kisielowski, V. Iota, B.A. Weinstein, L. Mattos, N.A. Shapiro, J. Kruger, E.R. Weber, and J. Yang. InGaN/GaN quantum wells studied by high pressure, variable temperature, and excitation power spectroscopy. *Applied Physics Letters*, 73(19):2778–2780, 1998.

[151] T. Kuroda and A. Tackeuchi. Influence of free carrier screening on the luminescence energy shift and carrier lifetime of InGaN quantum wells. *Journal of Applied Physics*, 92(6):3071–3074, 2002.

[152] J. Bai, T. Wang, and S. Sakai. Influence of the quantum-well thickness on the radiative recombination of InGaN/GaN quantum well structures. *Journal of Applied Physics*, 88(8):4729–4733, 2000.

[153] M.D. Craven, P. Waltereit, J.S. Speck, and S.P. DenBaars. Well-width dependence of photoluminescence emission from a-plane GaN/AlGaN multiple quantum wells. *Applied Physics Letters*, 84(4):496–498, 2004.

[154] J. Zhang, J. Yang, G. Simin, M. Shatalov, M. A. Khan, M.S. Shur, and R. Gaska. Enhanced luminescence in InGaN multiple quantum wells with quaternary AlInGaN barriers. *Applied Physics Letters*, 77(17):2668–2670, 2000.

[155] G. Steude, B. K. Meyer, A. Göldner, A. Hoffmann, F. Bertram, J. Christen, H. Amano, and I. Akasaki. Optical investigations of AlGaN on GaN epitaxial films. *Appl. Phys. Lett.*, 74:2459, (1999).

[156] F. Fedler, R.J. Hauenstein, H. Klausing, D. Mistele, O. Semchinova, J. Aderhold, and J. Graul. Strain, morphological, and growth-mode changes in AlGaN single layers at high AlN mole fraction. *Journal of Crystal Growth*, 241(4):535 – 542, 2002.

[157] D. Zubia and S.D. Hersee. Nanoheteroepitaxy: The application of nanostructuring and substrate compliance to the heteroepitaxy of mismatched semiconductor materials. *Journal of Applied Physics*, 85(9):6492–6496, 1999.

[158] U.T. Schwarz and M. Kneissl. Nitride emitters go nonpolar. *physica status solidi (RRL)-Rapid Research Letters*, 1(3):A44–A46, 2007.

[159] S. Li and A. Waag. GaN based nanorods for solid state lighting. *Journal of Applied Physics*, 111(7), 2012.

[160] Q. Li, K. R. Westlake, M. H. Crawford, S. R. Lee, D. D. Koleske, J. J. Figiel, K. C. Cross, S. Fathololoumi, Z. Mi, and G. T. Wang. Optical performance of top-down fabricated InGaN/GaN nanorod light emitting diode arrays. *Opt. Express*, 19(25):25528–25534, 2011.

[161] S.D. Hersee, X. Sun, and X. Wang. The controlled growth of GaN nanowires. *Nano Letters*, 6(8):1808–1811, 2006.

[162] J.-R. Chang, S.-P. Chang, Y.-J. Li, Y.-J. Cheng, K.-P. Sou, J.-K. Huang, H.-C. Kuo, and C.-Y. Chang. Fabrication and luminescent properties of core-shell InGaN/GaN multiple quantum wells on GaN nanopillars. *Applied Physics Letters*, 100(26), 2012.

[163] M.A. Reshchikov and H. Morkoç. Luminescence properties of defects in GaN. *Journal of Applied Physics*, 97(6), 2005.

[164] H. Lei, H.S. Leipner, J. Schreiber, J.L. Weyher, T. Wosiński, and I. Grzegory. Raman and cathodoluminescence study of dislocations in GaN. *Journal of Applied Physics*, 92(11):6666–6670, 2002.

[165] J. Mickevičius, R. Aleksiejūnas, M.S. Shur, S. Sakalauskas, G. Tamulaitis, Q. Fareed, and R. Gaska. Correlation between yellow luminescence intensity and carrier lifetimes in GaN epilayers. *Applied Physics Letters*, 86(4), 2005.

[166] J.L. Lyons, A. Janotti, and C.G. Van de Walle. Carbon impurities and the yellow luminescence in GaN. *Applied Physics Letters*, 97(15), 2010.

[167] S.O. Kucheyev, M. Toth, M.R. Phillips, J.S. Williams, C. Jagadish, and G. Li. Chemical origin of the yellow luminescence in GaN. *Journal of Applied Physics*, 91(9):5867–5874, 2002.

[168] C. Grazzi, H.P. Strunk, A. Castaldini, A. Cavallini, H.P.D. Schenk, and P. Gibart. Optoelectronic properties of GaN epilayers in the region of yellow luminescence. *Journal of Applied Physics*, 100(7), 2006.

[169] D.G. Zhao, D.S. Jiang, H. Yang, J.J. Zhu, Z.S. Liu, S.M. Zhang, J.W. Liang, X. Li, X.Y. Li, and H.M. Gong. Role of edge dislocations in enhancing the yellow luminescence of n-type GaN. *Applied Physics Letters*, 88(24), 2006.

[170] H. W. Choi, S. J. Chua, and S. Tripathy. Morphological and structural analyses of plasma-induced damage to n-type GaN. *Journal of Applied Physics*, 92(8):4381–4385, 2002.

[171] H. W. Choi, S. J. Chua, A. Raman, J.S. Pan, and A. T. S. Wee. Plasma-induced damage to n-type GaN. *Applied Physics Letters*, 77(12):1795–1797, 2000.

[172] S. Xu, Y. Hao, J. Zhang, T. Jiang, L. Yang, X. Lu, and Z. Lin. Yellow luminescence of polar and nonpolar GaN nanowires on r-plane sapphire by metal organic chemical vapor deposition. *Nano Letters*, 13(8):3654–3657, 2013.

[173] C.-Y. Wang, L.-Y. Chen, C.-P. Chen, Y.-W. Cheng, M.-Y. Ke, M.-Y. Hsieh, H.-M. Wu, L.-H. Peng, and J. J. Huang. Gan nanorod light emitting diode arrays with a nearly constant electroluminescent peak wavelength. *Opt. Express*, 16(14):10549–10556, 2008.

[174] C.-C. Tsai, G.-H. Li, Y.-T. Lin, C.-W. Chang, P. Wadekar, Q. Chen, L. Rigutti, M. Tchernycheva, F. Julien, and L.-W. Tu. Cathodoluminescence spectra of gallium nitride nanorods. *Nanoscale Research Letters*, 6(1):631, 2011.

[175] B. O. Jung, S.-Y. Bae, Y. Kato, M. Imura, D.-S. Lee, Y. Honda, and H. Amano. Morphology development of GaN nanowires using a pulsed-mode MOCVD growth technique. *CrystEngComm*, 16:2273–2282, 2014.

[176] J. Wu, W. Walukiewicz, K.M. Yu, J.W. Ager, E.E. Haller, H. Lu, and W.J. Schaff. Small band gap bowing in $In_{1-x}Ga_xN$ alloys. *Applied Physics Letters*, 80(25):4741–4743, 2002.

[177] T. Wernicke, L. Schade, C. Netzel, J. Rass, V. Hoffmann, S. Ploch, A. Knauer, M. Weyers, U. Schwarz, and M. Kneissl. Indium incorporation and emission wavelength of polar, nonpolar and semipolar InGaN quantum wells. *Semiconductor Science and Technology*, 27(2):024014, 2012.

[178] B. Neubert, P. Brückner, F. Habel, F. Scholz, T. Riemann, J. Christen, M. Beer, and J. Zweck. GaInN quantum wells grown on facets of selectively grown GaN stripes. *Applied Physics Letters*, 87(18), 2005.

[179] K. Nishizuka, M. Funato, Y. Kawakami, Y. Narukawa, and T. Mukai. Efficient rainbow color luminescence from $In_xGa_{1-x}N$ single quantum wells fabricated on $11\bar{2}2$ microfacets. *Applied Physics Letters*, 87(23), 2005.

[180] E.D. Le Boulbar, P.R. Edwards, S.H. Vajargah, I. Griffiths, I. Girgel, P. M. Coulon, D. Cherns, R.W. Martin, C.J. Humphreys, C.R. Bowen, D.W.E. Allsopp, and P.A. Shields. Structural and optical emission uniformity of m-plane InGaN single quantum wells in core-shell nanorods. *Crystal Growth and Design*, 16(4):1907–1916, 2016.

[181] I. Girgel, P.R. Edwards, E. LeBoulbar, P.M. Coulon, S. L. Sahonta, D. W. E. Allsopp, R.W. Martin, C. J. Humphreys, and P. A. Shields. Investigation of indium gallium nitride facet-dependent nonpolar growth rates and composition for core-shell light-emitting diodes. *Journal of Nanophotonics*, 2016. in press.

[182] H. Lee, D.B. Oberman, and J.S. Harris. Reactive ion etching of GaN using CHF_3/Ar and C_2ClF_5/Ar plasmas. *Applied Physics Letters*, 67(12):1754–1756, 1995.

[183] C.R. Eddy Jr. and B. Molnar. Plasma etch-induced conduction changes in gallium nitride. *Journal of Electronic Materials*, 28(3):314–318, 1999.

[184] S. Adachi. *Optical Constants of Crystalline and Amorphous Semiconductors: Numerical Data and Graphical Information*. Kluwer Academic, 1999.

[185] C. Tessarek, C. Dieker, E. Spiecker, and S. Christiansen. Growth of GaN nanorods and wires and spectral tuning of whispering gallery modes in tapered GaN wires. *Japanese Journal of Applied Physics*, 52(8S):08JE09, 2013.

[186] X. Zhang, X. Zhang, J. Xu, X. Shan, J. Xu, and D. Yu. Whispering gallery modes in single triangular ZnO nanorods. *Opt. Lett.*, 34(16):2533–2535, 2009.

[187] T. Nobis, E.M. Kaidashev, A. Rahm, M. Lorenz, and M. Grundmann. Whispering gallery modes in nanosized dielectric resonators with hexagonal cross section. *Phys. Rev. Lett.*, 93:103903, 2004.

[188] M. Conroy, H. Li, G. Kusch, P.R. Edwards, C. Zhao, B. Ooi, R.W. Martin, J.D. Holmes, and P.J. Parbrook. Site controlled red-yellow-green light emitting InGaN quantum disks on nano-tipped GaN rods. *Nanoscale*, 2016. to be published.

[189] Lumerical Solutions, 2015.

[190] K. Forghani, L. Schade, U.T. Schwarz, F. Lipski, O. Klein, U. Kaiser, and F. Scholz. Strain and defects in Si-doped (Al)GaN epitaxial layers. *Journal of Applied Physics*, 112(9), 2012.